Contribution of plasma membrane lipid domains to red blood cell (re)shaping

Léonard Catherine

Décembre 2017

Thèse présentée en vue de l'obtention
du grade de docteur en sciences biomédicales
et pharmaceutiques

Promotor: Prof. Mingeot-Leclercq Marie-Paule
Co-promotor: Prof. Tyteca Donatienne
President of the jury: Prof. Muccioli Giulio
Members of the jury:
Prof. Alsteens David
Prof. Dupont Christine
Prof. Delcorte Arnaud
Prof. Ruysschaert Jean-Marie
Prof. De Almeida Rodrigo

Faculté de pharmacie et des sciences biomédicales
Université catholique de Louvain

Table of content

List of abbreviations

AFM	atomic force microscopy
BCR	B-cell receptor
BODIPY	4,4-difluoro-5,7-dimethyl-4-bora-3a,4a-diaza-s-indacene
Ca^{2+}	calcium ion
Chol	cholesterol
CL	cardiolipin
CTxB	cholera toxin B-subunit
DPH	diphenylhexatriene
ER	endoplasmic reticulum
FCS	fluorescence correlation spectroscopy
FRAP	fluorescence recovery after photobleaching
GP	generalized polarization
GPI	glycosylphosphatidylinositol
GPMV	giant plasma membrane vesicle
GSL	glycosphingolipid
GUV	giant unilamellar vesicle
HC	high curvature area
LC	low curvature are
Ld	liquid-disordered
$L_{domains}$	domain boundary length
Lo	liquid-ordered
Lysenin*	His-mCherry-NT-Lysenin
MV	microvesicle
mβCD	methyl-β-cyclodextrin
PC	phosphatidylcholine
PDMS	Polydiméthylsiloxane
PE	phosphatidylethanolamine
PI	phosphatidylinositol
PIP_2	PI(4,5)P2, phosphatidylinositol-4,5-bisphosphate
PIPs	phosphoinositides
PKC	protein kinase C
PLL	poly-L-lysine
PM	plasma membrane
PMCA	Plasma membrane Ca^{2+} ATPase
POPC	palmitoyl-oleoyl-PC
PS	phosphatidylserine
RBC	red blood cell
SDS	sodium dodecyl sulfate
SIM	structured illumination microscopy
SIMS	secondary ion mass spectrometry
SL	sphingolipid
SM	sphingomyelin
SMase	sphingomyelinase

STED	stimulated emission depletion microscopy
Theta*	His-mCherry-Theta-D4
Tm	melting temperature
TRPC	transient receptor potential cation channels

CHAPITRE 1

Lipid domains and membrane (re)shaping: from biophysics to biology

Abstract

The surface of living cells provides an interface that not only separates the outer and inner environments but also contributes to several functions, including regulation of solute influx and efflux, signal transduction, lipid metabolism and trafficking. To fulfill these roles, the cell surface must be tough and plastic at the same time. This could explain why cell membranes exhibit a so large number of different lipid species and why some lipids form membrane domains. Besides the transient nanometric lipid rafts, morphogical evidence for stable submicrometric domains has been recently reported for a variety of living cells. Such complexity in lipid distribution has been reported to contribute to immune signaling or host–pathogen interactions. However, whether lipid domains could participate in cell shaping and reshaping (*e.g.* deformation and vesiculation) remains to be demonstrated. In this chapter, we highlight the main actors involved in cell (re)shaping, including the cytoskeleton, membrane-bending proteins and membrane biophysical properties. Based on integration of theoretical work and data obtained on model membranes, highly specialized cells and living cells (from prokaryotes to yeast and mammalian cells), we then discuss recent evidences supporting the existence of submicrometric lipid domains and documented mechanisms involved in their control. Finally, we provide lines of evidence supporting the potential implication of lipid domains in cell (re)shaping and suggesting the need for further investigation.

1. Introduction

The surface of living cells is a complex assembly of a variety of molecules that provides an interface separating the outer and the inner environments. It is also responsible for a number of important functions, including regulation of solute influx and efflux, signal transduction, lipid metabolism and trafficking, and represents the target of infectious agents such as bacteria and their associated toxins, viruses and parasites, *a.o.*. To fulfill these functions, the cell surface must be tough and plastic at the same time. This could explain why cell membranes exhibit a so large number of different lipid species that are heterogeneously distributed, both transversally and laterally.

Glycerophospholipids, sphingolipids and sterols are the main lipids found in biological membranes. Glycerophospholipids include phosphatidylcholine (PC), phosphatidylethanolamine (PE), phosphatidylserine (PS), phosphatidic acid (PA) and phosphatidylinositol (PI) and its phosphorylated derivatives (PIP, PIP_2 and PIP_3; collectively PIPs). Sphingolipids are derived from ceramide, which is decorated with a phosphocholine headgroup in the case of sphingomyelin (SM) or with saccharides in the case of glycosphingolipids (GSLs). Sterols constitute apolar membrane lipids with an inflexible core formed by four fused rings, with cholesterol predominating in mammals. Several features indicate remarkable membrane lipid diversity. Thus, even within the same lipid class, lipids can differ regarding headgroup structures and length and degree of unsaturation of the hydrophobic chains, creating thousands of combinations. Whether each lipid species has a defined biological function or whether cell function is modulated by structural organization of membrane lipids remain to be elucidated. In favour of the second hypothesis, lipid diversity could guarantee a much more stable, robust membrane that can withstand changes in the surrounding pH, temperature and osmolarity (Thomas and Rana, 2007). In this context, diversity could be intrinsically related to the different functions assumed by cell membranes including ligand binding, endocytosis, intracellular transport, cell migration or squeezing *e.g.*. Whatever the hypothesis, the lipid diversity allows for different non-covalent forces, *i.e.* van der Waals, electrostatic, solvation (hydration, hydrophobic), steric, entropic, *e.g.*, which are critical for membrane structure, organization and functions through modulation of biophysical membrane properties including lipid packing, membrane curvature and asymmetry (Bigay and Antonny, 2012; Janmey and Kinnunen, 2006; Sodt et al., 2016).

Current views on structural and dynamical aspects of biological membranes have been strongly influenced by the homogenous fluid mosaic model of Singer and Nicolson in 1972 (Singer and Nicolson, 1972). Today, this basic model remains relevant (Nicolson, 2014), although it is widely accepted that it cannot explain the role of mosaic, aggregate and domain structures in

membranes and the lateral mobility restriction of many membrane proteins (Goni, 2014). In the 90's, Simons and coll. proposed the lipid raft hypothesis (Simons and Ikonen, 1997), where GSLs form detergent-resistant membranes (DRMs) enriched in cholesterol and glycosylphosphatidylinositol (GPI)-anchored proteins in cold non-ionic detergents. In 2006, lipid rafts were redefined as: "small (20-100nm), heterogeneous, highly dynamic, sterol- and sphingolipid-enriched domains that compartmentalize cellular processes. Small rafts can sometimes be stabilized to form larger platforms through protein-protein and protein-lipid interactions" (Pike, 2006). However, the raft hypothesis is still up for debate (Bagatolli et al., 2010b; Bagatolli and Mouritsen, 2013). This could arise from its original definition experiments using the controversial detergent extraction method in combination with cholesterol and/or sphingolipid depletion. It should be nevertheless noticed that recent progress in microscopy, such as combined fluorescence correlation spectroscopy (FCS) with stimulated emission depletion microscopy (STED) (Vicidomini et al., 2015) or super-resolution microscopy (Stone et al., 2017a), provides strong evidence for the existence of transient, nanoscale, cholesterol- and sphingolipid-enriched membrane clusters, giving new insight in the raft hypothesis. Controversial opinions regarding the raft hypothesis could also arise from its restricted definition as compared to the high diversity of lipid composition among cellular membranes and the wide amount of factors regulating lipid clustering. Yet, the original definition of rafts is often revisited. In 2010, lipid rafts were redefined as "fluctuating nanoscale assemblies of sphingolipids, cholesterol and proteins that can be stabilized to coalesce, forming platforms that function in membrane signaling and trafficking" (Lingwood and Simons, 2010), taking into account the dynamical aspect of membranes.

In addition to rafts, other nanoscale domains, *i.e.* <100nm in diameter, have been described at the PM of eukaryotes: caveolae (Parton and del Pozo, 2013) and tetraspanin-rich domains (Yanez-Mo et al., 2009), *a.o.*. Moreover, morphological evidence for stable (min *vs* sec) submicrometric (>200nm *vs* <100nm) lipid domains was reported in artificial (Baumgart et al., 2007; Bernardino de la Serna et al., 2004; Kahya et al., 2003) and highly specialized biological membranes (Bernardino de la Serna et al., 2004; Plasencia et al., 2007). In the past decades, owing to the development of new probes and imaging methods, several groups have presented evidence for submicrometric domains in a variety of cells from prokaryotes to yeast and mammalian cells (Bach and Bramkamp, 2013; Carquin et al., 2015; Carquin et al., 2014; D'Auria et al., 2013b; Grossmann et al., 2007; Sanchez et al., 2012; Tyteca et al., 2010).

Such complexity in lipid distribution could play a role in cell physiology, including in cell shaping and reshaping processes. However, whereas the traction by the cytoskeleton, the action of membrane-bending proteins and transversal asymmetry have been shown to contribute to cell reshaping (Lux,

2016; McMahon and Gallop, 2005; Waugh, 1996), the importance of membrane lateral heterogeneity remains to be clearly determined. In this chapter, we highlight the main actors involved in membrane deformation (Section 4.), provide evidence for lipid domains in living cells (Section 5.) and a summary of their regulation mechanisms (Section 6.). In chapter, we also provide lines of evidence supporting the potential implication of lipid domains in cell (re)shaping (Section 7.).

2. Membrane shaping & reshaping – role in physiopathology

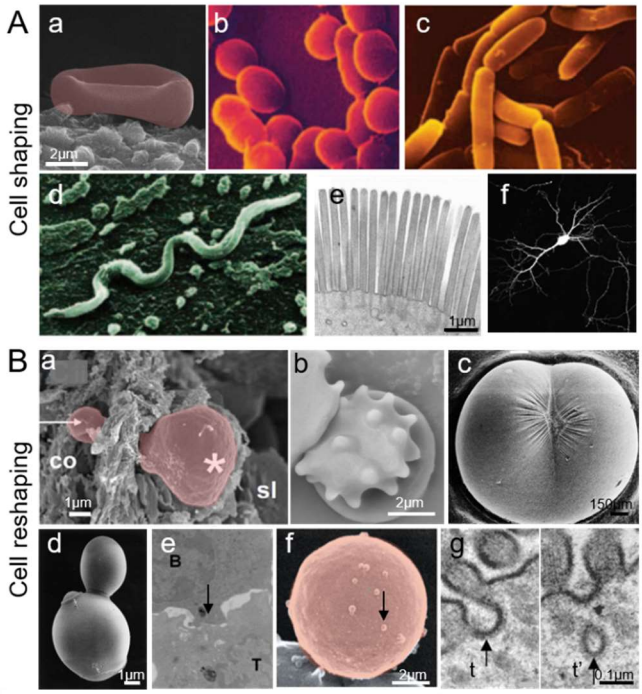

Figure 1. Physiological importance of cell (re)shaping. A. Shape of (a) a biconcave RBC; (b-d) cocci, rods and spirochetes; (e) enterocyte brush border of mouse intestinal explant; (f) growing neuron branches into dendrite. Adapted from: (a) our unpublished data; (b-d) (Zimmerberg and Kozlov, 2006); (e) (Hansen et al., 2007); (f) (Andreae and Burrone, 2015). B. Reshaping upon (a) RBC crossing from the splenic cord to sinus; (b) platelet activation; (c) cleavage furrow initiation in *Xenopus*; (d) yeast *S. cerevisiae* budding; (e) formation of the immunological synapse (arrow); (f) RBC vesiculation upon senescence (arrow); (g) vesicle endocytosis (arrow) in mouse intestinal explants during fat absorption. Adapted from: (a) (Deplaine et al., 2011); (c) (Danilchik et al., 2006); (d) (Osumi, 1998); (e) (Singleton et al., 2006); (f) our unpublished data; (g) (Hansen et al., 2007).

Membranes are at the centre of cell shaping and reshaping processes. For examples, RBC exhibits a biconcave shape needed for its optimal deformation and function (see Section 4.), while bacteria can be cocci, rods and spirochetes (Fig. 1Aa-d). Epithelial cells and neurons are other examples of cells showing 'special' shapes needed for their functions (Fig. 1Ae,f). In their environment, cells face a variety of stimuli and stresses, either chemical/biochemical (*e.g.* hormones, ligands, toxins, ions) or physico-mechanical (*e.g.* temperature, pH, pressure, sheer stress, stretching). Examples include squeezing of RBCs in the narrow pores of spleen sinusoids, pressure exerted by tumors on surrounding cells, sheer stress by the blood stream on endothelial cells, stretching of muscle cells during contraction, gathering of blood platelets to stop bleeding, cell division and formation of the immunological synapse (Fig. 1Ba-e). As opposed to global cell deformability, local budding and vesicle formation can also occur from the PM, allowing for endocytosis (Fig. 1Bg) or microvesicle (MV) formation. While considered for a long time as inert cellular fragments, MVs are nowadays recognized to play crucial roles in both physiological and pathological processes, such as intercellular communication (Turturici et al., 2014), coagulation (Yuana et al., 2013), inflammation (Gupta and Pulliam, 2014), tumorigenesis (Muralidharan-Chari et al., 2010) and migration (Shen et al., 2011), *a.o.*. MVs are also released from RBCs upon normal senescence (Fig. 1Bf), a process accelerated in RBC membrane fragility diseases, leading to loss of biconcavity and deformability. It is thus important to decipher molecular details of membrane structure and mechanisms involved in cell (re)shaping. In Section 7., we focus on the potential implication of lipid domains in cell shaping, squeezing, vesiculation and division.

3. Membrane shaping & reshaping – measurement

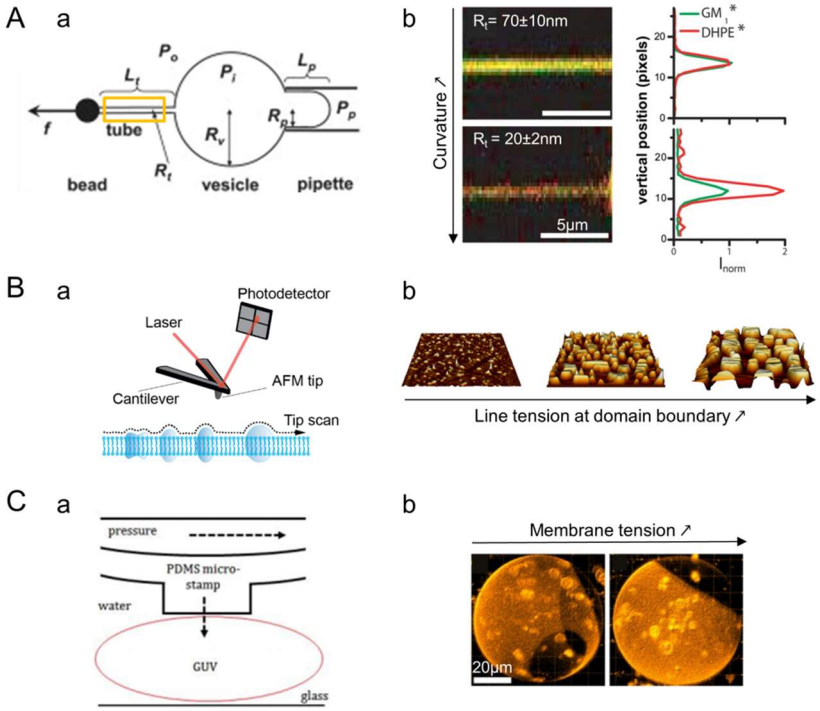

Figure 2. Principles of some methods used to evaluate lipid domain organization upon deformation. A. Micropipette aspiration. (a) Experimental apparatus for GUV aspiration and tube pulling. Pi, Po & Pp: pressures inside vesicle, outside vesicle & in the micropipette; Rt, Rv & Rp: radius of tube, vesicle & pipette; Lt & Lp: length of tube and vesicle projection in pipette; f: pulling force; I_{norm}: normalized intensity (Tian and Baumgart, 2009). (b) Confocal equatorial section showing the partitioning of fluorescent lipids in membrane nanotubes of different radii (yellow box in a) pulled out from a GUV (Sorre et al., 2009). B. AFM. (a) The AFM consists in an AFM tip positioned at the end of a flexible cantilever and brought in contact with the sample. During scanning, the applied force is maintained constant thanks to an optical system based on a laser focused at the end of the cantilever and reflected into a photodetector. The tip contours the surface and its movement results in a height image. (b) Three-dimensional AFM images of phase-separated membranes of differential composition and domain height mismatch (Garcia-Saez et al., 2007a). C. Microfluidics. (a) Side view of a microfluidic device composed of a pressure layer with integrated microstamps situated above a fluidic layer containing a GUV. (b) Induced tension by the microfluidic device causes lipid lateral sorting in GUVs: 0min, one Ld and two Lo phases (left); after 45min, lipid sorting into one Lo patch to reduce the tension (right) (Robinson et al., 2012).

Cell mechanical properties involved in deformation can be studied by several biophysical methods. These can be classified into two categories, based on measurements on individual or multiple cells. Biophysical techniques devoted to individual cells include micropipette aspiration, atomic force microscopy (AFM), optical tweezers or microfluidics, *a.o.*. Measurement on multiple cells can be performed by cell separation (by filtration through polycarbonate membrane or a mixture of microbeads) or microfluidics. Based on their ability to image lipid domains in relation to cell deformation, we decided to focus in this Section on the micropipette aspiration, AFM and microfluidics. For optical tweezers, we recommend (Henon et al., 1999); for cell separation by filtration through polycarbonate membrane or a mixture of microbeads, see (Deplaine et al., 2011; Reid et al., 1976).

Micropipette aspiration was initially developed to measure the RBC elastic properties (Rand and Burton, 1964). Briefly, a micropipette is manipulated towards a cell, usually in suspension, and a small suction pressure is applied, partially aspirating the cell inside the micropipette. Upon increasing the suction pressure, the cell deforms and either completely flows into the micropipette or increases the length of projection of the aspirated portion (Fig. 2Aa). This deformation is then analyzed to determine the cell elastic property, *i.e.* the Young's modulus. The technique can be used to apply forces over a range of three orders of magnitude from 10pN to 1nN (Hochmuth, 2000). It has been applied to various cells including red cell membranes (Hosseini and Feng, 2012) and cancer cells (Chivukula et al., 2015; Lee and Liu, 2015). In the context of lipid domains, it can be used to test whether these exhibit a gradient along the deformation projection (Fig. 2Aa,b).

AFM was invented 30 years ago to image at high-resolution non-conductive sample. Key developments now allow AFM to investigate biological sample, *i.e.* imaging in buffer solution and maintaining the native state of the biological system (Müller et al., 2009). Briefly the principle of AFM is to scan a tip over the sample while using an optical detection system to measure with high-sensitivity the force applied on the sample (Gerber and Lang, 2006). This detection system is based on a laser focused at the end of the cantilever and deflected into a photodiode. This electric signal is then converted into a force using calibrated parameters. By maintaining the applied force constant, the height of the tip is adjusted and its movement results in the height image that resembles the sample topography with the resolution depending on the radius of the tip, the applied force, the physical properties of the sample, and how precisely the feedback system acts (Fig. 2B). AFM rapidly evolved from an imaging tool to a multifunctional tool that, simultaneously to the topography, is also capable to probe biophysical properties (Butt et al., 2005). By recording force-distance curves, *i.e.* by monitoring the variation of the force while approaching the AFM tip and retracting it away from the biological sample, various properties can be quantified either during the approach curve or during the retraction curve. Approach curve allows the extraction of properties

including mechanical deformation of the sample, elastic modulus and energy dissipation. The dissipation is the area of the hysteresis between the approach and the retract curve. Retraction curve can quantify adhesion forces established between the tip and the sample. Modern AFM instruments can acquire several hundreds of thousands of force-distance curves while imaging the biological sample, allowing mapping physical properties and interactions to the sample topography. Force-distance based AFM (or multiparametric imaging) opens the door to image complex biological systems and simultaneously quantify and map their properties. Nowadays, multiparametric imaging allows investigating native biosystems with a resolution approaching 1nm on purified membrane proteins and simultaneously mapping their mechanical properties (Dufrêne et al., 2013). Force-distance based AFM was also used to map the mechanical properties of heterogeneous membranes (Sullan et al., 2009), RBCs (Bremmell et al., 2006), human keratinocytes (Heu et al., 2012) or bacteria (Alsteens et al., 2013). Besides mechanical properties, force-distance based AFM also enables to map specific receptors. Using functionalized AFM tips with specific chemical groups or ligands, the adhesion and mechanical strength of specific bonds can be measured. Furthermore recording these forces while imaging the biological systems allows detecting and localizing specific interaction of biological samples ranging from antibodies to living cells (Baumgartner et al., 2000; Grandbois et al., 2000; Thie et al., 1998). Biospecific AFM mapping has proven useful to map receptor sites on animal cells (Grandbois et al., 2000; Kim et al., 2006; Roduit et al., 2008).

Microfluidic technologies can also be used to investigate cell mechanical properties upon deformation. These can be classified according to the mechanical stimuli used to deform the cell (for review (Zheng et al., 2013)): constriction channel (Fig. 2Ca), shear stress, voltage shock, optical stretcher, electric field or micropipette aspiration. Microfluidics have been used to measure the deformability of RBCs (Lee et al., 2007), leukocytes (Rosenbluth et al., 2008), human cancer cell lines (Guck et al., 2005) and patient oral squamous cells (Remmerbach et al., 2009). Furthermore, their development in pathological contexts gives promising perspectives for labelled-free clinical diagnostic. For example, breast cancer cells were distinguished from non-malignant cells (Hou et al., 2009), malignant cells were identified in human pleural fluid sample (Gossett et al., 2012) and RBCs with deficiencies of cytoskeletal protein network were detected (Bao et al., 2011). Although cost-effective, microfluidics is biocompatible, requires small sample volume and gives fast responses. In addition, its "tune-ability" makes it adaptable to any cell type, permits to recreate specific environmental deformation conditions and to record electrical or biochemical properties besides mechanical parameters. Furthermore, as microfluidics can be coupled to fluorescence microscopy, it has been used to evaluate reorganization of lipid domains under

stretching of model membranes (Fig. 2Cb) (Robinson et al., 2012; Robinson et al., 2013).

4. Membrane shaping & reshaping – regulation

In this Section we will deepen three key determinants for cell (re)shaping, *i.e.* the cytoskeleton (Section 4.2.), membrane shaping proteins (Section 4.3.) and intrinsic membrane properties (Section 4.4.).

4.1 Cytoskeleton

As highlighted above, the RBC cytoskeleton strengthens the lipid bilayer end endows the membrane with durability and flexibility to survive in the circulation (Lux, 2016). It is made of a pseudohexagonal meshwork of spectrin, actin, protein 4.1R, ankyrin and actin-associated proteins, attached to the membrane via multiprotein complexes, centered on ankyrin and protein 4.1R. For readers interested in the anatomy of the red cell membrane skeleton, an excellent recent review is recommended (Lux, 2016).

It is well established that the RBC membrane is not static and ATP allows maintaining the RBC biconcave shape and dynamic characteristics. For instance, intracellular ATP increases the compliance of the membrane, as revealed by AFM upon small compression of subcellular components (Picas et al., 2013) and through fluctuation analysis (Betz et al., 2009; Park et al., 2010). Mechanical measurements using optical tweezers has however led to the opposite conclusion (Yoon et al., 2008). Thus, while it is clear that phosphorylation directly modulates the mechanical stability of the RBC membrane, the response is complex due to the fact that many cytoskeleton components are phosphoproteins. Among those, phosphorylation of the 4.1R by PKC triggers the relaxation of the RBC membrane through loosening the link between membrane and spectrin (Manno et al., 2005) whereas phosphorylation of β-spectrin through the membrane-bound casein kinase I (Manno et al., 1995) could enhance the maintenance of stable network interaction by increasing the spectrin-ankyrin affinity (Picas et al., 2013). Besides phosphoproteins, PIPs are alternative candidates. While PIP_2 enhances the binding of 4.1R to glycophorin C, it inhibits the binding to Band 3 *in vitro* (An et al., 2006).

In nucleated mammalian cells, the cytoskeletal network scaffolding the PM at the macroscopic level is a heterogeneous system consisting of actin fibers, intermediate filaments and microtubules. This elaborate protein organization mediates and controls membrane shaping and organization through the continuous dynamic interplay between the PM and the cortical network underlying it. Adhesion between the cytoskeleton and the lipid bilayer maintains membrane tension, while membrane shape and cytoskeletal assembly/disassembly processes are also strongly intertwined. The

cytoskeleton is known to regulate several essential cell processes as follows: cortical actin supports the macroscopic curvature of the membrane during mitosis, membrane ruffling is involved in phagocytosis, while actin dynamics (treadmilling, branching and bundling) provides the mechanical force needed for endocytosis, migration (formation of filopodia and lamellopodia) and morphogenesis. Additionally, molecular motors such as kinesins, dynein and myosin support some organelle morphologies and promote the reorganization of the membrane (McMahon and Gallop, 2005).

Cortical actin is tightly bound to the PM *via* actin binding proteins, such as α-actinin domain, the ERM (Ezrin/Radixin/Moesin) domain (Anthony Bretscher et al., 2000; Saleh et al., 2009), the calponin homology (CH) domain (Gimona et al., 2002) and the Wiskott-Aldrich syndrome (WASP) homology domain-2 (WH2) (Paunola et al., 2002). More commonly, linker proteins act as crosslinkers between the actin architecture and membrane proteins by means of protein-protein interactions motifs such as PDZ or ankyrin. PIPs are major regulatory factors of actin-membrane interactions (Fukami et al., 1992; Fukami et al., 1996), playing several roles in actin dynamics regulation by controlling the localization and activity of actin-binding proteins, *a.o*. Interactions between proteins and PIPs are mainly mediated by pleckstrin homology (PH) domains (Feeser and Ostap, 2010; Liu et al., 2016b; McKenna and Ostap, 2009; Yu et al., 2012). In addition, many actin binding and actin modulating proteins get activated through the interaction with PIP_2-containing membranes (*e.g.* α-actinin, vinculin, talin or ezrin). Moreover, PIP_2 stimulates actin polymerization activators (*e.g.* WASP, WAVE), while it inhibits proteins that break and depolymerize actin (*e.g.* gelsolin, cofilin, villin, profilin) (Köster and Mayor, 2016). Some studies also proposed the connection between actin cytoskeleton and PS to induce nanoclustering of GPI-anchored proteins *via* transbilayer lipid interactions (Raghupathy et al., 2015).

4.2 Membrane shaping proteins

Remodeling of cell shape is accomplished by recruiting specialized proteins, which contain motifs able to generate, sense or stabilize membrane curvature. The synergistic actions of membrane shaping proteins along with changes in the lipid bilayer and the cytoskeleton enable numerous cellular processes like division, migration and intracellular trafficking.

Three key mechanisms underlying membrane shaping are currently known. The first mechanism acts at the nanoscopic level and is a result of protein crowding and partitioning of transmembrane domains. Molecular crowding by protein-protein interactions has been recently pinpointed as a mechanism for altering the effective bending modulus and the curvature of the membrane (Stachowiak et al., 2012). Transmembrane proteins with a conical or inverted-conical shape can also mold their associated membranes around their shapes,

as in voltage-dependent K^+ channels (MacKinnon, 2003) or the nicotinic acetylcholine receptor (Unwin, 2005). Additionally, transmembrane receptors clustering, such as transferrin or low-density lipoprotein, results in endocytic clathrin-coated pit formation (Ehrlich et al.).

The second mechanism involves the direct insertion of small hydrophobic protein motifs between the lipid headgroups. The hydrophobic surface insertion into the membrane hemilayer enlarges the surface of the inner leaflet, thus causing membrane curvature. Numerous proteins playing key roles in membrane shaping are known to present amphiphatic helices (endophilin, amphipysin, epsin, Bin2 *a.o.* (Drin and Antonny, 2010)), but the most well-known classes leading to this type of electrostatic interactions are the endosomal sorting complexes required for transport (ESCRT) and Bin/Amphiphysin/RVS (BAR) domain containing proteins. The electrostatic interactions between ESCRT proteins are involved in membrane budding during virus infection, membrane scission in the multivesicular body pathway and cytokinesis (Hurley and Hanson, 2010; Raiborg and Stenmark, 2009). The BAR domain protein superfamily includes dimeric banana shaped structures, which bind electrostatically to the membrane through their concave face. Binding is thought to be mediated by the interaction between positively-enriched areas of the BAR module (membrane contact site) and negatively-charged lipids like PIPs (Mim and Unger, 2012; Rao and Haucke, 2011). BAR proteins can also target negative PIPs through pleckstrin homology (PH) or PhoX (PX) domains. The fact that BAR domains interact preferentially with curved membranes makes them a sensor of high positive curvature (Hinshaw and Schmid, 1995; Peter et al., 2004). The F-BAR (FCH-BAR) domains recognize shallow positive curvature, while I-BAR (Inverse-BAR) domains interact with shallow negatively curved membranes. BAR domain proteins have been implicated in many cellular functions involving sensing or induction of membrane curvature, such as endocytosis and membrane trafficking, podosome and filopodia formation, or mitochondria and autophagosome shape (reviewed in (Frost et al., 2009)). BAR domain proteins can be seen as a signaling 'hub' connecting membrane geometry and/or lipid composition to actin cytoskeleton regulation and to different signaling pathways (Aspenstrom, 2014; Sit and Manser, 2011).

The last mechanism of membrane deformation is the scaffold mechanism by peripheral proteins at the nanoscopic level and their oligomeric assemblies at the microscopic level. Clathrin, COPI and COPII are coat proteins recruited from the cytosol during vesicle budding. They have the capacity to bend membranes by relying on adaptor proteins. After the spherical coated vesicle pinches off, these proteins are released back into the cytosol and can be recycled (McMahon and Boucrot, 2011; Zanetti et al., 2012). Oligomerization of caveolin is linked to the formation of caveolae (Parton and del Pozo, 2013), while reticulons and flotilins stabilize the ER curvature (Shibata et al., 2009).

4.3 Intrinsic membrane properties

Several intrinsic membrane properties contribute to cell (re)shaping. We here provide information on their regulation and physiological implication, with specific focus on the molecular level. Membrane properties and regulation at the larger scale of lipid domains and resulting from collective lipid behaviour will be discussed in more details in Section 6.

The cellular membrane exhibits transbilayer asymmetry, first hypothesized in the 70's by Bretscher (Bretscher, 1972). This asymmetry contributes to PM complexity and diversity by the differential repartition between the two leaflets of lipid (i) order and packing (Section 4.4.1.), (ii) charge and dipole (Section 4.4.2.) and (iii) molecular shape (Section 4.4.3.), thereby leading to optimal physiological output. The inner monolayer contains most of PS and PE whereas PC and SM are mostly located within the outer leaflet. Whereas lipid PM asymmetry has been largely reported including in human RBCs (Daleke, 2008) and platelets (Lhermusier et al., 2011), it is cell type-dependent (Murate et al., 2015; Murate and Kobayashi, 2015). The asymmetric distribution of phospholipids is accompanied by asymmetry of fatty acid chains. For example, in human RBCs, the double bond index is 1.54 for the inner face *vs* 0.78 for the outer face (Elani et al., 2015). In contrast to phospholipids, transbilayer distribution of cholesterol is highly debated (Liu et al., 2016a). Recently, cholesterol has been shown to inhibit phospholipid scrambling (Arashiki et al., 2016), an unsuspected function that could be critical for cell deformation. Membrane proteins (with their preferred orientation) and communication with the exterior and interior aqueous compartments (which contain different concentrations of ions, small molecules, and/or proteins) also contribute to the bilayer asymmetry. Rapid exchanges between leaflets are presumed to be prohibited by the large enthalpic barrier associated with translocating hydrophilic materials, such as a charged lipid headgroup, through the hydrophobic membrane core. The mechanism underlying transbilayer asymmetry involves specific flippase (inward moving), floppase (outward moving) and scramblase (bidirectional) enzymes that assist in the movement of lipids between the two leaflets of cellular membranes (Pomorski and Menon, 2016). The coupling may be also an intrinsic property of the lipid themselves (Chiantia and London, 2012) *via* interdigitation through long acyl chain (C22-C24) (Lin and London, 2015; Raghupathy et al., 2015).

(i) Lipid order and packing

Lipid packing depends on the ratio between small and large polar heads and the ratio between unsaturated and saturated acyl chains. The usual cis-unsaturated oleyl chain (C18:1) occupies a larger volume than the palmitoyl chain (C16:0) because the double bond induces a ''kink'' in the middle of the chain which lowers the packing density of the acyl chains, thereby increasing membrane fluidity (Koynova and Caffrey, 1998). Owing to its acyl chain

composition, SM forms a taller, narrower cylinder than PC, increasing its packing density in the membrane. Consequently, at physiological temperature, a SM bilayer exists in a solid gel phase with tightly packed, immobile acyl chains (Slotte, 2013; van Meer et al., 2008). By interfering with acyl chain packing, sterols inhibit the transition of the membrane to the solid gel state. At the same time, sterols rigidify fluid membranes by reducing the flexibility of neighbouring unsaturated acyl chains, thereby increasing membrane thickness and impermeability to solutes (the so-called condensing effect of sterols) (Brown and London, 1998).

Based on membrane packing criteria, membrane can be viewed as a patchwork with areas characterized by differences in membrane fluidity. The areas of low fluidity are named the solid phase (Lβ) (or solid-ordered (So) phase). In these areas the lipid acyl chains are tightly packed and there is a low rate of lateral diffusion. In contrast, the more fluid areas are named the liquid crystalline (Lα) phase (McConnell and Vrljic, 2003) (more commonly called the liquid-disordered (Ld) state) which exhibits both low packing and high lateral diffusion. In addition, at the proper concentration, cholesterol may facilitate lateral segregation of lipids into cholesterol-depleted and -enriched regions, such as liquid-ordered (Lo) lipid domains, which expose high packing and high lateral diffusion. Lipid phase behavior is temperature-dependent and the Lβ phase transition into Ld phase occurs when temperature increases. The temperature at which this transition occurs is known as the gel-to-liquid transition temperature (T*m*) and depends on lipid acyl chains. Lipids with long saturated fatty acyl chains (*e.g.* most sphingolipids) have high T*m*, whereas lipids with fatty acids having cis double bonds (*e.g.* most phospholipids) have low T*m*.

Membrane fluidity is critical to warrant proper protein sorting and membrane trafficking required during adaptive responses. For example, organelles of the secretory pathway differ in lipid composition, resulting into gradual increase of molecular packing density and membrane rigidity from the ER toward the PM (Holthuis and Menon, 2014; van Meer et al., 2008). Thus, modulation of lipid composition and fluidity seems critical for adaptive responses even though cytosolic proteins and integral membrane sensors also contribute to regulate fluidity (Bigay and Antonny, 2012; Ernst et al., 2016; Puth et al., 2015). As a consequence of membrane transbilayer asymmetry, membrane physical properties are also asymmetrical, the outer monolayer being more packed and rigid than the inner one (Elani et al., 2015). How differential order of lipid domains in one leaflet can affect the order of the opposite leaflet is highlighted in Section 6.2.

(ii) Lipid dipole

Most of the phospholipids and sphingolipids are zwitterionic and exhibit a significant permanent electric dipole moment (Gawrisch et al., 1992). Cell membrane transversal asymmetry thus creates a permanent dipole potential,

leading to a significant difference in electric potential across the membrane that can vary from 100 to 400mV and is positive in the membrane interior (Schamberger and Clarke, 2002). The dipole potential arises from the water dipole of the hydrated lipid bilayer (Gawrisch et al., 1992; Zheng and Vanderkooi, 1992), the carbonyl groups of the ester linkages between the headgroup and the hydrocarbon chains (Clarke, 1997; Gawrisch et al., 1992) and the lipid headgroup (Starke-Peterkovic and Clarke, 2009). Cholesterol increases the membrane dipole potential by impacting the orientation, strength and packing density of the molecular dipoles at the membrane surface (McIntosh et al., 1989; Szabo, 1974) and *via* its own dipole moment, which depends on its membrane orientation and membrane packing (Haldar et al., 2012; Starke-Peterkovic et al., 2006). How membrane and domain dipole potential can affect lipid domain size and topography and how electrostatic interactions modulate and reorganize lipid domains are developed in Sections 6.2. & 6.3.

(iii) Lipid molecular shape

Moving to lipid molecular shape, *i.e.* ratio of head-to-tail area, some lipids like PC show comparable lateral areas in the head and tail regions with an overall cylindrical molecular geometry, forming a planar bilayer. In contrast, PE have a small headgroup relative to the cross-sectional area of the hydrocarbon tails (conical shape) whereas lysophospholipids are characterized by tail regions of bigger lateral cross-section than the headgroups (inverted conical shape). The cylindrical, conical and inverted-conical lipids have zero, negative and positive spontaneous curvatures, respectively.

Generation of membrane shape by lipids is generally attributed to intrinsic lipid molecular shapes (lipid morphism (Cullis and De Kruijff, 1979)) and lipid membrane transversal asymmetry (bilayer couple hypothesis (Sheetz and Singer, 1974)) and this specific molecular lipid sorting is usually associated to a substantial and persistent energy input mediated by proteins (Zimmerberg and Kozlov, 2006). The asymmetry between the inner and outer leaflets results in spontaneous bending of originally flat membrane. This can be ascribed by an elastic parameter, named the spontaneous curvature which corresponds to the curvature that an unconstrained monolayer would adopt. It can be positive (if the membrane prefers to bulge toward the exterior compartment) or negative. When a system is forced to adopt a curvature different from the spontaneous curvature, the curvature elastic stress is considered. Examples include cellular processes that require membrane bending like endocytosis, budding or cell deformation. Since these processes are highly sensitive to changes in lipid composition and to the presence of specific lipids (Ailte et al., 2016; Chernomordik and Kozlov, 2008), subtle modifications in lipid composition may have major implications for lipid and protein sorting under a curvature-based membrane-sorting model (Holdbrook et al., 2016;

McMahon and Boucrot, 2015; McMahon and Gallop, 2005). How membrane curvature can affect lipid domain sorting and topography is discussed in Section 6.2, and how lipid domains could be involved in the generation of membrane shape is discussed in Section 7.1.

5. Lipid domains – evidence

The concept of lipid rafts is used to describe unstable nanoscale assemblies (20-100nm) enriched in sphingolipid, cholesterol and GPI-anchored proteins (Lingwood and Simons, 2010; Simons and Ikonen, 1997). Besides rafts, there are various types of membrane domains that are characterized by their enrichment in specific proteins, such as caveolae and tetraspanin-enriched domains (Parton and del Pozo, 2013; Yanez-Mo et al., 2009). Rafts can sometimes be stabilized to form larger platforms through protein:protein and protein:lipid interactions (Pike, 2006). Morphological evidence for stable (min *vs* sec for rafts) submicrometric domains (>200nm in diameter *vs* <100nm) has been reported in artificial (Baumgart et al., 2007; Bernardino de la Serna et al., 2004; Kahya et al., 2003) (Section 5.1.) and highly specialized biological membranes (Bernardino de la Serna et al., 2004; Plasencia et al., 2007) (Section 5.2.).

However, there is an intensified debate on the real existence of stable submicrometric lipid domains in cells. This can result from three main features. First, whereas some groups have provided evidences for stable submicrometric lipid domains in physiological conditions (Sections 5.3. & 5.4. for examples), there are cases in which they have not been detected. For example, whereas submicrometric domains enriched in sphingolipids have been demonstrated by secondary ion mass spectrometry (SIMS) at the fibroblast PM, cholesterol is uniformly distributed throughout (Frisz et al., 2013a; Frisz et al., 2013b). Likewise, using protein micropatterning combined with single-molecule tracking, Schutz and coll. have shown that GPI-anchored proteins do not reside in ordered domains at the PM of living cells (Sevcsik et al., 2015). Differences between studies can be explained by several reasons. Thus, analysis of lipid lateral heterogeneity suffers from technical issues such as lipid unresponsiveness to chemical fixation, fast translational movement, small molecular size and high packing density. As a consequence, it is a big challenge to design small specific fluorescent tools that can be used to analyze lipid organization by microscopic methods with resolution approaching the nanometer-scale under poor lipid fixation. Moreover, imaging artefacts could arise from non-resolved membrane projections and domain abundance strongly varies with temperature, another possible cause of non-reproducibility. Despite these limitations, which are also discussed elsewhere (Carquin et al., 2016; Takatori et al., 2014), novel specific probes have recently been developed and validated (reviewed in (Carquin et al., 2016; Maekawa and Fairn, 2014; Maekawa et al., 2016; Skocaj et al., 2013)).

Membrane composition and biophysical properties also strongly influence lipid lateral distribution. Finally, living cells are far from equilibrium and are instead constantly reorganized by energy-driven processes, including motor-driven constriction of the cytoskeleton, membrane trafficking, lipid metabolism and exchanges of ions and molecules with the environment. A second reason alimenting the debate is that submicrometric lipid domains have sometimes been reported under non-physiological conditions: (i) in RBCs after alteration of membrane ceramide or cholesterol contents upon treatment with a toxin from *Pseudomonas aeruginosa* (Montes et al., 2008) or methyl-β-cyclodextrin (mβCD) (Cai et al., 2012), respectively; and (ii) in CHO cells upon cholesterol depletion (Hao et al., 2001). Third, lipid domains could be not stably present but transiently generated by the hydrolysis of specific lipids. One can cite the ceramide-rich domains with diameters of ~200nm up to several micrometers that can be formed upon SM degradation by acid SMase in response to stress (Grassme et al., 2003; Stancevic and Kolesnick, 2010).

Therefore, one major challenge will be to evaluate whether submicrometric lipid domains can be generalized or if they are restricted to cells exhibiting particular membrane lipid composition, biophysical properties and membrane:cytoskeleton anchorage. The rest of this book chapter is dedicated to this crucial question.

5.1 Membrane models

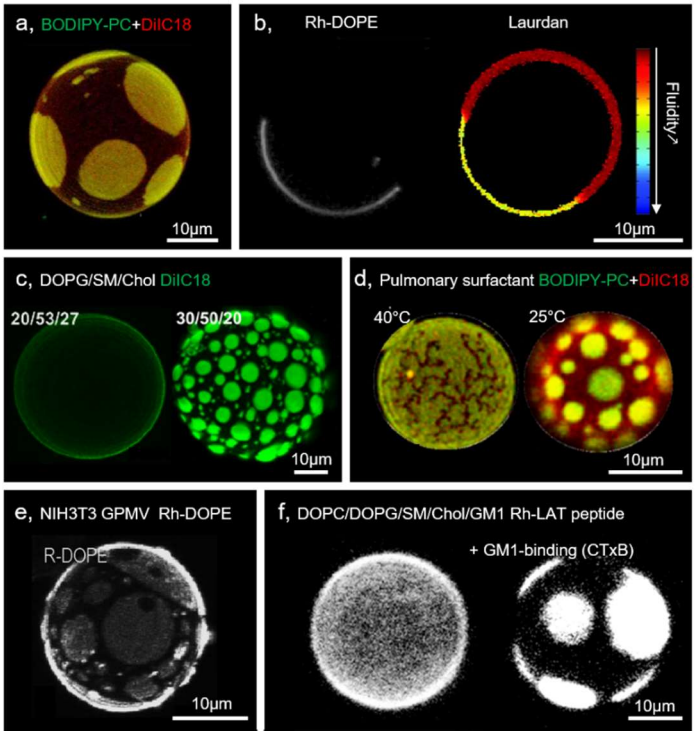

Figure 3. Visualization of phase coexistence in model membranes. (a) GUV (DOPC/DPPC/Chol) labelled with BODIPY-PC and DiIC18 showing Lo and Ld phases. (b) GUV (DOPC/SSM/Chol) labelled with Rhodamine-DOPE (Ld phase) or Laurdan (fluidity). (c) GUVs of DOPG/eSM/Chol in different ratios labeled with the Ld phase marker DiIC18. (d) GUV produced from native pulmonary surfactant labelled with BODIPY-PC and DiIC18 and examined at 40°C and 25°C. (e) GPMV from NIH 3T3 cells labeled with Rhodamine-DOPE, showing fluid/fluid phase coexistence. (f) GUVs (DOPC/DOPG/SM/Chol/GM1) labelled with Rhodamine-LAT peptides examined before and after addition of CTxB (dark areas, Lo phase). Adapted from: (a) (Bernardino de la Serna et al., 2004); (b) (Kaiser et al., 2009); (c) (Pataraia et al., 2014); (d) (Bernardino de la Serna et al., 2009); (e); (Baumgart et al., 2007) ; (f) (Hammond et al., 2005).

Different types of model membranes have been developed to study phase separation, including planar supported bilayers (Fidorra et al., 2006) and giant unilamellar vesicles (GUVs) (Bagatolli, 2006) made from lipid mixtures as well as giant PM vesicles (GPMVs) isolated from cellular PMs after chemical treatment (Levental et al., 2011). All these models are useful to perform systematic analysis of the impact of lipid composition on phase separation, like in model membranes mimicking the composition of the PM outer leaflet (Fig. 3a,b). They show liquid-liquid phase separations, with domains of variable sizes depending on lipid composition and temperature (Fig. 3c,d). Planar supported bilayers are useful for methods requiring rigid planar

surfaces like AFM and ToF-SIMS. With a size of 15-30µm, GUVs are more suitable to approach the PM morphology. However, even if proteins can be incorporated (Girard et al., 2004), GUV composition remains far from the complex PM composition. GPMVs also exhibit phase separation (Fig. 3e). However, whereas they contain both PM lipids and proteins, several factors that are known to modulate phase separation are still missing, including cytoskeleton anchorage, active cellular processes and cross-binding proteins (Fig. 3f). These differences, which must be considered when studying phase separation, are reflected in the differential T*m* in living cells and isolated GPMVs (Veatch et al., 2008).

5.2 Highly-specialized biological membranes

The question is whether and how lipid organization in model membranes can be extrapolated to PMs. Indeed, in contrast to model membranes, PMs (i) are complex in lipid composition and intrinsic membrane properties, (ii) exhibit a high diversity of membrane proteins and a more or less anchored cytoskeleton, and (iii) are out of thermodynamic equilibrium. It is thus interesting to first describe lipid lateral distribution in membranes in which local equilibrium conditions are prone to occur, *i.e.* the pulmonary surfactant and the skin stratum corneum membranes, due to a relatively slow molecular turnover (Bernardino de la Serna et al., 2004; Plasencia et al., 2007). Pulmonary surfactant membranes contain an important quantity of DPPC, cholesterol and unsaturated lipids and a low fraction of membrane proteins. These membranes show the coexistence of two liquid domains at physiological temperature that was linked with their spreading capacity at the air-water interface (Bernardino de la Serna et al., 2009; Bernardino de la Serna et al., 2004). Whereas extraction of the surfactant proteins does not alter phase coexistence, partial cholesterol depletion leads to elongated irregular domains, typical of gel/fluid phase coexistence. Domain organization is also strongly affected by temperature (Bernardino de la Serna et al., 2004). In the skin stratum corneum membrane, the lipid composition is also unique with mainly unusually long chain ceramides and free fatty acids as well as cholesterol (Bouwstra et al., 2003; Downing, 1992). Using GUVs composed of lipid mixtures extracted from human skin stratum corneum, Plasencia et al have shown a pH- and temperature-dependent membrane lateral organization. At pH 5, membranes exhibit a Ld phase at temperature >70°C, a Ld/gel phase coexistence between 40 and 70°C and a gel/gel-like phase coexistence at temperature <40°C (relevant since skin physiological temperature is ~30°C). At pH 7, the coexistence of these two distinct micrometric gel-like domains disappears and has been linked to the permeability properties of the skin stratum corneum (Plasencia et al., 2007).

Thus, these two specialized membranes highlight three important features regarding membrane lateral distribution. First, they represent alternative models besides model membranes in which equilibrium thermodynamic lipid

phases have been evidenced. Second, lipid domains could be favored by the exceptional lipid composition of these membranes. It is thus crucial to consider this parameter when discussing the existence of lipid domains. Third, domains seem to be physiologically relevant.

5.3 Prokaryotes & yeast

In contrast to mammalian cells, membrane domains are understudied in bacteria. This could be explained by three main reasons. First, the presence of lipid domains in cell membranes was for a long time thought to be a step during the course of evolution of cellular complexity. Second, the formation of lipid rafts requires sterols, which are missing from the membrane of most bacteria. Third, taking into account the small size of bacteria and the resolution limits of conventional confocal microscopy, exploring lipid domains in bacteria is particularly difficult. Biophysical methods such as FRET and fluorescence anisotropy have nevertheless provided a significant amount of information.

Cardiolipin-enriched domains have been evidenced in bacteria with the fluorescent dye 10-N-nonylacridine orange (NAO). This probe, which was initially developed to visualize cardiolipin-rich mitochondria in eukaryotic cells, was also used to localize cardiolipin at the polar and septal poles of *E. coli* and *B. subtilis* (Kawai et al., 2004; Mileykovskaya and Dowhan, 2000). More recently, it has been shown that bacteria have the capacity to organize protein transport, secretion and signal transduction cascade in functional membrane microdomains (FMMs) (Lopez, 2015). Whereas FMMs have been suggested to be equivalent to eukaryotic lipid rafts (Bramkamp and Lopez, 2015), they exhibit differential composition. Indeed, bacterial membranes are enriched in phospholipids, lipopolysaccharides and various lipoproteins (Huijbregts et al., 2000; Lopez-Lara and Geiger, 2016) but most of them do not have sphingolipids (Parsons and Rock, 2013) and only a few contain sterols (Huang and London, 2016; Lin and Rikihisa, 2003). It should be stressed that some bacteria synthesize hopanoids, which have a chemical structure similar to that of cholesterol (Saenz et al., 2012) and which could form nanometric domains by self-aggregation (Bramkamp and Lopez, 2015). A nanoSIMS technique was employed to probe the existence of hopanoid lipid domains in cyanobacterium *Nostoc punctiforme (Doughty et al., 2014)*. Bacterial flotillin FloT and FloA proteins along with squalene biosynthesis were found to play key roles in the formation of lipid domains. Heterogeneous distribution of flotillin-like proteins in *B. subtilis* was directly visualized by fluorescence microscopy upon labelling with the translational fusion FloT-GFP (Donovan and Bramkamp, 2009; López and Kolter, 2010). The question of lipid composition of the flotillin-enriched structures still remains.

In contrast to bacteria, yeast represents a powerful system to explore lipid domain organization based on genetic approaches. In addition, like plants,

yeast exhibits membranes which appear highly heterogeneous and can be imaged with conventional methods (Malinska et al., 2003). As indirect evidence for lipid domains in yeast, a Lo/Ld phase coexistence has been shown on model membranes either prepared from yeast total lipid extracts or with defined composition including ergosterol and inositolphosphoceramide (Klose et al., 2010). Then, *sterol-enriched submicrometric compartments containing the eisosome protein Sur7 and proton symporters* Can1, Fur4, Tat2 and HUP1 have been evidenced thanks to filipin labelling (Spira et al., 2012). More recently, major redistribution of PIP_2 into membrane clusters has been evidenced upon osmotic stress in both fission and budding yeast cells (Guiney et al., 2015; Kabeche et al., 2015). Such PIP_2 clusters are spatially organized by eisosomes, protein-based structures of the yeast PM. After perturbation of sphingolipids, sterol, PS or PIP_2 levels, patchwork protein distribution is modified, suggesting a relation between proteins and lipids at the yeast PM domains. Besides PM, the yeast vacuole membrane proteins also segregate in two large stable membrane domains exhibiting differential ordering properties in response to nutrient deprivation, changes in pH of the medium and other stresses (Toulmay and Prinz, 2013).

5.4 Animal cells

In the past decades, submicrometric lipid domains have been documented at the outer and/or inner PM leaflet of various cell types, using several tools and methods. A substantial, albeit non-exhaustive, list of examples is presented in (Carquin et al., 2016). We will here select some cells based on their need to reshape during essential physiopathological processes, *i.e.* RBC (squeezing in narrow pores), platelet (spreading during coagulation), neutrophil (chemotaxis), neuron and glial cell (shape adaptation), epithelial cell (polarization) and cancer cell (squeezing to invade tissues). Images are provided in Figs. 4 & 5.

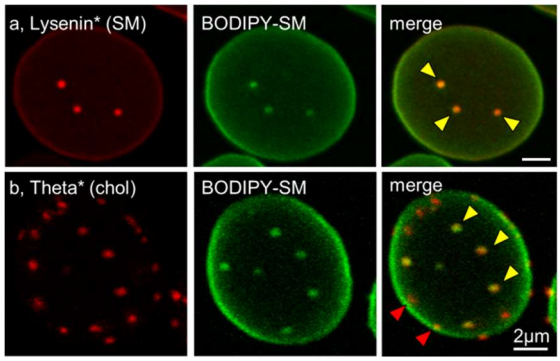

Figure 4. Evidence for submicrometric lipid domains in RBCs. RBCs labelled by Lysenin* (a; endogenous SM) or Theta* (b; endogenous cholesterol), then by exogenous BODIPY-SM. Whereas Lysenin* and BODIPY-SM perfectly co-localize (a), two types of cholesterol domains, enriched in either both cholesterol and SM

(yellow arrowheads, b) or cholesterol mainly (red arrowheads, b), coexist (Carquin et al., 2015; Carquin et al., 2014).

Human RBCs are the simplest and best characterized eukaryotic cell system both at lipid and protein levels (Goodman et al., 2013; Zachowski, 1993), present biconcavity and are submitted to strong deformability during their 120-days lifetime. Moreover, for practical purposes, RBCs are a model of choice because they (i) are easily available and robust, (ii) exhibit high homogeneity in size and shape due to rapid clearance of damaged RBCs by the spleen, (iii) present a flat surface without membrane projections or protrusions, avoiding confusion between domains and lipid enrichment in membrane ruffles, and (iv) do not make endocytosis, avoiding any confusion between domains and endosomes. We first revealed submicrometric domains by vital confocal imaging of spread RBCs upon trace insertion in the outer PM leaflet of fluorescent lipid analogs (*e.g.* BODIPY-SM) (D'Auria et al., 2011; Tyteca et al., 2010). Similar domains have then been observed upon direct labeling of endogenous SM and cholesterol using specific fluorescent toxin derivatives, Lysenin and Theta (Carquin et al., 2015; Carquin et al., 2014) (Fig. 4). Double labeling of RBCs with the SM-specific Lysenin, then with BODIPY-SM, reveals perfect colocalization, suggesting the relevance of BODIPY-SM to study its native counterpart (Carquin et al., 2014). In contrast, double labeling with BODIPY-SM and the cholesterol-specific probe Theta leads to partial dissociation, indicating the coexistence of two types of domains at the RBC surface (see below). Submicrometric lipid domains have been confirmed on RBCs suspended in a 3D-gel, thus without artificial stretching, suggesting a genuine feature of RBCs *in vivo.* Mechanistically, lipid domains of RBCs are governed by temperature, lipid content, membrane:cytoskeleton anchorage and membrane tension (Carquin et al., 2015; Carquin et al., 2014) (see Fig. 6). In agreement with our confocal imaging data, Scheuring and coll. revealed by AFM the structural and mechanical heterogeneity of the RBC membrane (Picas et al., 2013). These studies contrast with the random distribution of SM clusters observed by Kobayashi and coll. using SDS-digested freeze-fracture replica labelling (Murate et al., 2015; Murate and Kobayashi, 2015). Whether this discrepancy reflects differences in methodology (imaging approach, fixation, labelling efficiency) or in parameters that are known to regulate domains (temperature, membrane tension,

Human platelets are central to hemostasis. Using 4-dimensional live-cell imaging and electron microscopy, Agbani et al have recently shown that platelets adherent to collagen are transformed into PS-exposing balloon-like structures with expansive macro/microvesiculate contact surfaces, by a process called procoagulant spreading (Agbani et al., 2015). Whereas platelet activation is known to critically depend on PS surface exposure (Heemskerk et al., 1997), the importance of lipid lateral distribution is less understood. On one hand, using the artificial lipid probe DiIC18, Gousset et al have shown

submicrometric domains in platelets upon activation, suggesting regulated raft coalescence into larger domains under appropriate conditions (Bali et al., 2009; Gousset et al., 2002). On the other hand, random distribution of SM clusters has been revealed by SDS-digested freeze-fracture replica labelling in both non-stimulated and stimulated platelets (Murate et al., 2015; Murate and Kobayashi, 2015).

Upon recruitment to sites of inflammation *via* chemotaxis, neutrophils rapidly change their morphology, from roughly spherical resting to migratory cells with distinct leading and trailing edges. Maxfield and coll. have proposed that membrane lipid organization is critical for human neutrophil, through the formation of submicrometric domains that help in amplifying the chemoattractant gradient and maintaining cell polarization (Pierini et al., 2003). However, this suggestion was mainly based on disruption of lipid organization using mβCD and morphological evidence for lipid domains was not provided. Recently, STED has revealed that the two main neutrophil GSLs, phosphatidylglucoside and lactosylceramide, form distinct domains in their outer PM (Fig. 5a). Moreover, lactosylceramide domains associate with the Src family kinase Lyn and could thereby participate in chemotaxis (Ekyalongo et al., 2015; Sonnino et al., 2009). Evidence for domains in the inner leaflet of neutrophil PM has also been provided, with diameter >200nm and enrichment in SM (Murate et al., 2015) (Fig. 5b).

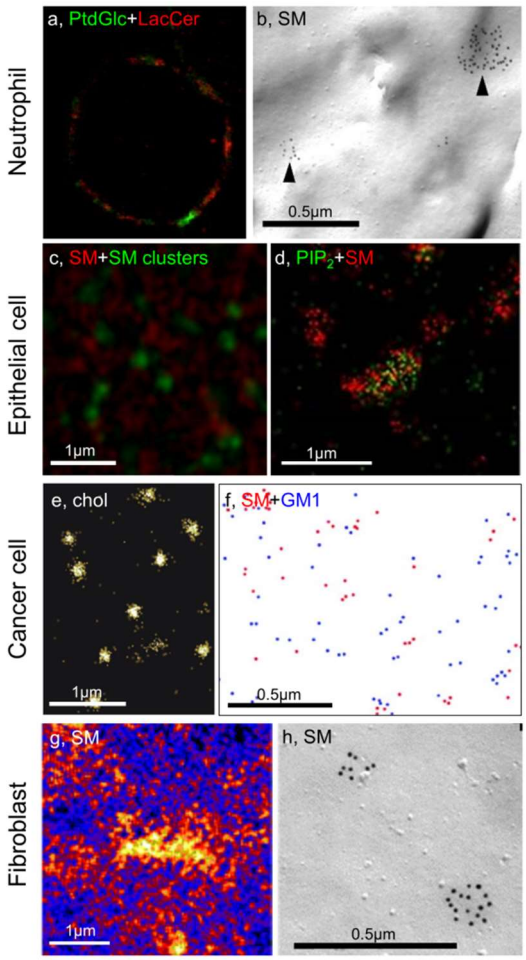

Figure 5. Evidence for submicrometric lipid domains in nucleated mammalian cells. (a) Human neutrophil stained for phosphatidylglucoside (PtdGlc) and lactosylceramide (LacCer) and examined by STED microscopy. (b) Human neutrophil analyzed for SM at the inner face by SDS-digested freeze-fracture replica labelling with a Lysenin fragment. (c) LLC-PK1 cell labeled for SM (Equinatoxin) and SM clusters (Lysenin) and analyzed at their apical surface by structured illumination microscopy (SIM). (d) LLC-PK1 cell expressing Dronpa-PH (PIP_2), stained with Lysenin (SM) and analyzed by PALM/dSTORM. (e) HeLa cell labeled for cholesterol (Theta toxin fragment) and analyzed by PALM. (f) Jurkat cell labeled with a Lysenin fragment (SM) and biotinylated CTxB (GM1). (g) Fibroblast labeled with ^{15}N-sphingolipid precursors and examined by SIMS combined with TIRF. (h) Human skin fibroblast labeled and imaged as in (b). Adapted from (a) (Ekyalongo et al., 2015); (b) (Murate et al., 2015); (c) (Makino et al., 2015); (d) (Abe et al., 2012); (e) (Mizuno et al., 2011); (f) (Kiyokawa et al., 2005); (g) (Frisz et al., 2013b); (h) (Murate et al., 2015).

Neurons can also adopt a variety of shapes to adapt to the region and function in the nervous system. By characterizing by AFM the elastic properties of specific membrane domains in living hippocampal neurons, it was demonstrated that GPI-anchored proteins reside within domains of ~70nm size that are stiffer than the surrounding membrane. Upon inhibition of actin filament formation, the size of the GPI-enriched domains increases without change in stiffness (Roduit et al., 2008). During the development of the central nervous system, the reciprocal communication between neurons and oligodendrocytes is essential for the generation of myelin. Oligodendrocytes exhibit a differential relative abundance of specific lipids during differentiation (Jackman et al., 2009) and a high global lipid content (Aggarwal et al., 2011). Several reports have shown that some of these lipids cluster into domains. First, galactosylceramide and sulfatides form submicrometric domains (Boggs and Wang, 2004), mutually interacting at the apposed membranes of wrapped myelin (Boggs et al., 2010), regulating PM organization and myelin protein lateral diffusion (Ozgen et al., 2014). Second, GM1-enriched domains are essential for oligodendrocyte precursor survival by providing signaling platforms for growth factor-mediated integrin activation (Decker and ffrench-Constant, 2004).

Lipid domains could also play a role in epithelial cell polarization. By FRAP of several membrane proteins, Meder and coll. revelead the coexistence of at least two different lipid phases in the apical PM of epithelial cells, but not in fibroblasts (Meder et al., 2006). In differentiated MDCK cells, SM-enriched domains have been evidenced at the basolateral membrane (Makino et al., 2015). In contrast, the SM-specific probe Lysenin selectively stains the apical PM of Eph4 cells, a cell line derived from mouse mammary gland epithelial cells (Ikenouchi et al., 2012), and SIM evidences SM clusters in the apical PM of LLC-PK1 cells (Makino et al., 2015) (Fig. 5c). Such differences in lipid lateral distribution should be discussed in light of epithelial cell biochemical and morphological characteristics, as proposed in (Fanning et al., 2012; Umeda et al., 2006).

Lipid domains are also relevant to cancer cells. First, imaging by AFM of membranes purified by ultracentrifugation from human breast cancer cells (MDA-MB-231) has revealed the presence of submicrometric domains (Orsini et al., 2012). Second, super-resolution fluorescence microscopy of HeLa cells labeled with fluorescent Lysenin and Theta has demonstrated two types of lipid domains of ~250nm in diameter and differentially enriched in cholesterol and SM (Mizuno et al., 2011) (Fig. 5e). Third, electron microscopy of Jurkat T-cells (an immortalized line of human T lymphocyte cells) double labeled with Lysenin and CTxB indicates the coexistence of SM- and GM1-enriched domains (Kiyokawa et al., 2005) (Fig. 5f). Upon labeling of the same cells with Laurdan, Dinic and coll. have shown the association of TCR with small ordered actin-dependent PM domains in resting T cells that can aggregate upon TCR engagement (Dinic et al., 2015). Acquisition of a motile

phenotype in T lymphocytes results in the redistribution of ganglioside GM3- and GM1-enriched raft domains to the leading edge and to the uropod, respectively, in a cholesterol- and actin-dependent process. It was suggested that segregation of membrane proteins between distinct lipid domains allows mediating redistribution of specialized molecules needed for T cell migration (Gomez-Mouton et al., 2001).

Lipid domains have also been observed in other cells such as fibroblasts and myoblasts. At the PM of fixed mouse embryo fibroblasts labeled with Lysenin, SM clusters that appear to be membrane lipid trafficking-dependent have been observed (Paparelli et al., 2016). In contrast to cholesterol which is uniformly distributed throughout, evidence for submicrometric sphingolipid-enriched domains has been provided at the NIH3T3 mouse embryo fibroblast PM using SIMS (Fig. 5g). These domains are only reduced in abundance upon cholesterol depletion but fully eliminated upon cytoskeleton disruption, suggesting they are not lipid rafts (Frisz et al., 2013a; Frisz et al., 2013b). SM domains (Murate et al., 2015) (Fig. 5h) and restriction of PIP_2 diffusion have also been shown in the inner leaflet of fibroblasts (Golebiewska et al., 2008). At the lateral PM of living C2C12 myoblasts, which exhibit a ~40mol% cholesterol (Perkins and Scott, 1978) and a strong membrane:cytoskeleton anchorage, we revealed heterogeneous distribution of cholesterol upon decoration by Theta (Carquin et al., 2015).

Thus, stable lipid domains can be evidenced in a large diversity of living cells but the concept is still difficult to generalize. As recently proposed by Kobayashi and coll. for asymmetric lipid distribution across the PM, we suggest that the lateral distribution of lipids is highly regulated and cell-dependent. It is thus crucial to integrate PM lipid composition and membrane properties, cytoskeleton:membrane coupling as well as membrane trafficking and lipid turnover while discussing lipid domains (see Section 6.).

Another important challenge is to evaluate lipid domain diversity, both at the inner and the outer leaflets, and to establish whether there is a correspondence between lipid domains in the two leaflets. Several studies based on multiple labeling using validated probes, combined or not with specific lipid depletion, report for the coexistence of distinct lipid domains in the PM. First, sterol- and sphingolipid-enriched domains only partially overlap in several PMs. For instance, by double labeling experiments in RBCs, we showed the coexistence of two types of domains, one enriched in SM and cholesterol *vs* another mainly enriched in cholesterol (Carquin et al., 2015). SIMS in mouse fibroblasts revealed that partial cholesterol depletion does not eliminate the sphingolipid domains but reduces their abundance (Frisz et al., 2013b). The structure and abundance of sphingolipid domains at the yeast PM seem independent of ergosterol (Aresta-Branco et al., 2011). Second, one (class of) lipid can even be distributed in several different pools. Thus, the dissociation of SM- and GM1-rich domains in the outer PM leaflet of Jurkat T-cells has been shown

by electron microscopy (Kiyokawa et al., 2005) (Fig. 5f). GM1 and GM3 clusters at the fibroblast PM largely dissociate and are redistributed upon actin cytoskeleton disruption, indicating that their distribution not only depends on phase separation but also on cytoskeleton (Fujita et al., 2009). By confocal vital imaging of the RBC PM, we evidenced two types of cholesterol-enriched domains (Carquin et al., 2015). Using a toxin that binds to cholesterol-rich membranes, Das et al have shown that the human fibroblast PM contains three types of cholesterol pools, *i.e.* a pool accessible to the toxin, a SM-sequestered pool that binds to the toxin only when SM is abrogated and a residual pool that does not bind the toxin even after SM abrogation (Das et al., 2013). Whether these pools represent real domains remains to be determined. Likewise, in *S. cerevisiae*, two ergosterol pools, one enriched in sphingolipids and the other not, are involved in two different aspects of yeast mating, pheromone signaling and PM fusion, respectively (Jin et al., 2008).

Regarding lipid domain transbilayer distribution, a superposition of SM clusters in the outer PM leaflet and PIP_2 in the inner leaflet has been shown by super-resolution microscopy of LLC-PK1 cells (Abe et al., 2012) (Fig. 5d). By delivering fluorescent PIP_2 and F-actin specific probes using synthetic vesicles and real time live cell imaging, Chierico and coll. have shown that PIP_2 domain formation during the early stage of cell adhesion correlates with rafts (Chierico et al., 2014). Mayor and co-workers provided experimental and simulation data showing that nanoclustering of GPI-anchored proteins at the outer PM leaflet by dynamic cortical actin is made by the interdigitation and transbilayer coupling of long saturated acyl chains (Raghupathy et al., 2015).

6. Lipid domains – control

Biological membranes possess two characteristic, yet opposing, features. They present a fluid-like nature allowing for free movement of their constituents, while providing area for a variety of biological functions suggesting non-uniform distribution and formation of lipid/protein domains. A large variety of mechanisms, including energetic considerations (Section 6.1.), intrinsic membrane properties (Section 6.2.) and extrinsic factors (Section 6.3.), could contribute to control domains. We believe that these mechanisms can differentially control distinct lipid domains, as illustrated for RBCs at Fig. 6.

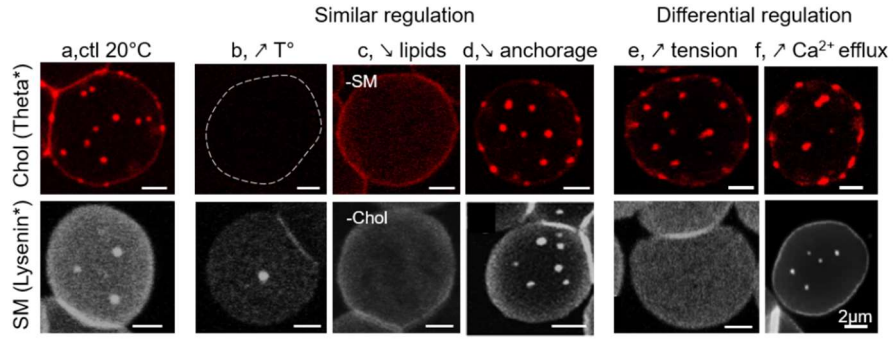

Figure 6. Regulation of submicrometric lipid domains in RBCs. Illustration for cholesterol (chol)- and SM-enriched domains (respectively labelled by Theta* & Lysenin*). (a) Control (ctl) RBCs at 20°C. (b-d) Similar regulation: (b) increased temperature (42°C), (c) specific lipid depletion (-SM or -Chol), (d) acute uncoupling of membrane:cytoskeleton anchorage at 4.1R complexes (PKC activation). (e,f) Differential regulation: (e) increased tension (increased spreading on coverslip), (f) increased Ca^{2+} efflux (Ca^{2+}-free medium containing EGTA). Adapted from (Carquin et al., 2015; Carquin et al., 2014) & Leonard et al, submitted.

6.1 Energetic considerations

Phase transition temperature (Section 6.1.1.) and line tension at phase boundary (Section 6.1.2.) are potential energetic sources for cell control of domain size.

(i) Phase transition temperature

Lipid immiscibility and Lo-Ld liquid phase separation, well-characterized on ternary mixture of polar lipids and cholesterol (Veatch and Keller, 2003), have been for a long time proposed to explain lipid domains. However, recent experiments on GPMVs expose liquid-phase separation at lower temperature (~15-25°C) than 37°C (Baumgart et al., 2007; Veatch et al., 2008). Since in the one-phase region micrometer-scale composition fluctuations occur and become increasingly large and long-lived as temperature is decreased to the transition, Veatch and coll. proposed that lipid rafts are the manifestation of transient compositional fluctuations and suggested that cells may exploit the low energy cost associated with (re)organizing components in membranes with critical composition (Veatch et al., 2008). By using the relatively long-range fluctuation-driven forces between membrane inclusions (called Casimir forces), Machta et al. proposed that cells may also take advantage of being close to the critical point to (re)organize the lateral segregation of membrane proteins (Machta et al., 2012).

In living cells, although no evidence of miscibility transition over a temperature range of 14-37°C was observed, GPMVs derived from these cells do instead exhibit such a transition, pointing out that phase transition is not driven in living cells by temperature in a range of 14-37°C. Il-Hyung therefore

suggested that living cells maintain either the T>T*m* or T<T*m* through the wide temperature range and highlighted the robustness of the cellular membrane to temperature change (Lee et al., 2015), an opposite view from the models of Veatch and Machta.

The discrepancy between Veatch/Machta and Il-Hyung models could arise from the fact that GPMVs, as compared to the mother-cell PM, have lost cytoskeleton anchorage and transmembrane asymmetry (Baumgart et al., 2007) and are no longer connected with cross-linking components or lipid recycling, all known to modulate liquid phase separation (see Sections 6.2. & 6.3.). Indeed, Il-Hyung have shown differential tension between living cell PMs and derived GPMVs, suggesting that cell membranes may be maintained in a different region of the phase diagram avoiding a temperature-driven phase transition (Lee et al., 2015). It is possible that interactions with cytoskeletal/membrane proteins or active cellular process dominate or even obliterate lipid miscibility effects.

Bagatolli and coworkers discussed the biological existence and significance of equilibrium thermodynamic phase and equilibrium critical points in biological membranes, which normally are in non-equilibrium conditions (Bagatolli et al., 2010a; Bagatolli and Mouritsen, 2013). They suggest that critical point phenomena are unlikely to be a major factor regulating biological phenomena since, for example, small mistuning near critical point could lead to drastic change in membrane structure and cell function. Another point of view is that biological system could exhibit a non-equilibrium critical behavior or a self-organized critical behavior (Adami, 1995). The self-organized critical system exposes a critical state which is robust to perturbations and needs no tuning as it evolves itself towards the critical state thought self-organization (Jensen, 1998). This idea is appealing for biological system regarding its robustness as compared to system near critical points.

(ii) Line tension at phase boundary

The line tension, *i.e.* the energy at domain interface, results from the different phase properties of the lipid domains and its surrounding, leading to thickness mismatch at domain boundary and unfavorable exposure of lipid hydrocarbon regions to water. Theoretical work exposed the central role of line tension for lipid domain lateral sorting (Heberle et al., 2013). Different observations on model membranes also support this view. First, lipid domains are circular and rapidly return to a circular shape after external perturbation (Samsonov et al., 2001) to minimize the boundary length, supporting the importance of line tension at the phase interface. Second, degrading cholesterol (a key regulator of differential thickness between lipid domains and surrounding membrane) in one monolayer induces irregular domain boundary followed by domain disappearance (Samsonov et al., 2001). Third, domain size increases with the extent of acyl chain unsaturation (Heberle et al., 2013), another regulator of differential thickness between lipid domains and surrounding membrane.

Fourth, domain size and the mismatch in bilayer thickness at phase boundary are directly correlated (Heberle et al., 2013). Fifth, with increasing temperature, GPMVs exhibit in their two-phase region a linear decrease of the line tension which approaches zero at the T*m* (Veatch et al., 2008). Experiments on living RBCs have confirmed some of these observations: (i) lipid domains are all circular (Carquin et al., 2015; Carquin et al., 2014); (ii) cholesterol or SM depletion induce irregular domain boundary (our unpublished data); and (iii) domain abundance and size are differently modulated by line-active agents (D'Auria et al., 2013a).

The energy cost of the line tension depends on the size of the height mismatch and the length of the boundary. Mechanisms minimizing hydrophobic exposure at domain boundary by reducing both factors were suggested to take place in the membrane. The first one involves elastic lipid deformation to decrease the step-like change in thickness at domain boundary (Kuzmin et al., 2005) while the second one favors domain coalescence to reduce domain boundary perimeter (Frolov et al., 2006). But, if the line tension at domain boundary is the only relevant energy consideration, any system with coexisting liquid domains would achieve equilibrium at one round domain. In fact, this is not the case since a stable distribution of lipid domain size can be observed in both model membranes and living cells. This suggests that other energy factors compete with the line tension, such as the entropic penalty for domain merge (Frolov et al., 2006). In addition, in living cells, the lipid composition is far more complex than in model membranes. Taking this in account, the step-like nature of lipid domain boundary found in a ternary mixture could be compensated in living cells by accumulation at domain boundary of (i) lipids of intermediate length, decreasing the abruptness of the boundary and the strength of the line tension (García-Sáez and Schwille, 2010), and (ii) proteins playing the role of line-active agents by accumulating at the interface (Simons and Vaz, 2004).

6.2 Intrinsic membrane properties

In this section, we will review the impact on lipid domains of membrane biophysical properties and their interplay with energetic considerations (see Section 6.1.). These include membrane lipid:lipid interactions (Section 6.2.1.), membrane curvature (Section 6.2.2.), transversal asymmetry (Section 6.2.3.), dipole potential (Section 6.2.4.) and membrane protein:lipid interactions (Section 6.2.5.).

(i) Membrane lipid:lipid interactions

Interactions between SM and cholesterol in the Lo phase are among the most favorable. SM/cholesterol co-enrichment is thus expected in cellular membranes, as proposed in the seminal definition of lipid rafts. Accordingly, cholesterol-enriched domains partially colocalize with SM-enriched domains at the living RBC PM and both lipid domains exhibit reciprocal dependence,

as revealed by specific cholesterol or SM membrane depletion (Carquin et al., 2015; Carquin et al., 2014). However, several other studies indicate the opposite. First, depletion of homogenously distributed cholesterol in mouse fibroblast PM does not influence the morphology of sphingolipid-enriched domains (Frisz et al., 2013b). Second, in yeast, sphingolipids do not accumulate in ergosterol-enriched domains (Grossmann et al., 2007) and sphingolipid-enriched domain structure and abundance do not depend on ergosterol metabolism (Aresta-Branco et al., 2011). Accordingly, stability of the proton-ATPase Pma1 at the yeast PM specifically requires sphingolipids but not sterols (Grossmann et al., 2007). All these observations suggest that sterol-sphingolipid interactions are not sufficient to explain the formation of lipid domains in cellular membranes. Besides SM/cholesterol, GSLs and ceramides, which present very particular physico-chemical properties, have been proposed to contribute to generate and/or maintain lipid domains (Castro et al., 2014; Ekyalongo et al., 2015; Sonnino et al., 2009; Sot et al., 2006) (see also Sections 5.2. & 5.4.).

(ii) Membrane curvature

Using simulation of complex asymmetric PM model containing seven lipid species including GM3 and PIP_2, Koldso and coll. have shown that the concave regions of the bilayer surface are enriched in GM3 (Koldso et al., 2014). The increase in GM1 concentration in POPC bilayers induces tighter lipid packing, driven mainly by inter-GM1 carbohydrate-carbohydrate interactions, leading to a greater preference for the positive curvature of GM1-containing membranes and larger cluster sizes of ordered-lipid clusters (Patel et al., 2016). These two studies suggest a relation between membrane curvature and lipid lateral sorting.

One step further, the observation of specific lipid sorting in vesicle and tubule budding from organelles involved in endocytosis (Mukherjee and Maxfield, 2000; Mukherjee et al., 1999) has suggested that membrane curvature could provide a mechanism for the spatial sorting of lipids. This hypothesis has been tested by experiments pulling membrane tubes out of GUVs, confirming a curvature-driven lipid sorting (Roux et al., 2005; Sorre et al., 2009). Mechanistically, it has been proposed that individual lipids are not effectively curvature-sorted according to their individual shape by membrane curvature differences of magnitudes found in intracellular membranes, but that cooperativity of lipid domains is needed to enable efficient curvature sorting in function of domain intrinsic curvature and bending stiffness (Raghuveer Parthasarathy et al., 2006; Tian and Baumgart, 2009). Besides domain bending stiffness and intrinsic curvature, a competition between domain bending rigidity and line tension at phase boundary is also proposed as driving force for lipid domain association to membrane curvature (Baumgart et al., 2003).

Thus, membrane curvature seems to provide a mechanism for lipid spatial sorting. It should be stressed that domain size and topography also imply on domain dimensionality that can switch from a flat to "dimpled" shape. This switch depends on the competition between (i) the 3D surface tension/mass ratio that favors small surface and then flat domain, and (ii) the 2D phase boundary line tension/mass ratio that prefers any domain morphology that reduces the boundary length (Simons and Vaz, 2004; Ursell et al., 2009). Ursell and coworkers used theoretical and experimental work to show that, when this competition results in a transition from a flat to dimpled domain shape, it leads to two dimpled domains that are able of repulsive elastic interaction, slowing domain merge and thus regulating domain size and topography (Ursell et al., 2009).

(iii) Membrane transversal asymmetry

As explained in Section 4.4., PM exhibits transversal asymmetry. Lipid mixtures that are typically found in the outer leaflet tend to phase-separate in Lo and Ld liquid phases when reconstituted in model membranes (Veatch and Keller, 2005). In contrast, lipid mixtures that represent the inner leaflet, do not undergo macroscopic phase separation and are in Ld state (Kiessling et al., 2006). In cells, whereas lipid domains have been more documented on the outer PM leaflet, they have nevertheless been identified at the inner leaflet of various cell types (Abe et al., 2012; Fujiwara et al., 2002; Nawaz et al., 2009), asking for a potential interleaflet coupling resulting in domain formation.

Theoretical works addressed physical mechanisms leading to fluid domain coupling across membranes. May focused on electrostatic coupling, cholesterol flip-flop and dynamic chain interdigitation as underlying mechanisms of interleaflet coupling, and argued that the latter likely provides the main contribution (May, 2009). Other potential mechanisms are the van der Waals interactions and composition curvature coupling (Leibler and Andelman, 1987). May also discussed the importance of a fine balance between interleaflet line tension at the bilayer midplane and intraleaflet line tension at domain interface within each leaflet as crucial energetic considerations for interleaflet coupling (May, 2009). As a first line of evidence for interleaflet coupling in lipid bilayers, Sackmann and coworkers imaged the deposition of a NBD-DMPE-labelled DMPC monolayer (Ld state) on a TR-DMPE-labelled-DMPE supported monolayer (So state). They evidenced the formation in the DMPC monolayer of crystalline domains which appear to be in perfect register with the So domains of the DMPE monolayer (Merkel et al., 1989).

Since asymmetric model membranes have long been difficult to obtain, experiments studying if and how one leaflet affects the structure and thermodynamic phase behavior of the apposed leaflet have generated controversial results. Recent preparation of asymmetric GUVs yielded significant insight and suggested that a Lo domain in one leaflet can induce a

Lo domain in the apposed leaflet (Collins and Keller, 2008; Kiessling et al., 2006). However, phase-state across leaflets of asymmetric bilayers appears to be highly sensitive to lipid composition in one leaflet (Collins and Keller, 2008). A recent elegant study, using fast Laurdan general polarization imaging on active planar supported bilayers and showing the formation of lipid domains upon lipase action, provides an example for the biological relevance of interleaflet coupling at non-equilibrium conditions (Brewer et al., 2017).

Three lines of evidence on living cells support the reciprocal interaction between inner and outer leaflet domains: (i) the superposition of outer SM and inner PIP_2 clusters (Abe et al., 2012) ; (ii) the colocalization of inner and outer leaflet proteins during signaling events (Kusumi et al., 2004); and (iii) the colocalization of inner leaflet-associated proteins with outer leaflet rafts (Gri et al., 2004; Pyenta et al., 2001).

(iv) Membrane dipole potential

Based on theoretical and experimental investigations on lipid monolayers to study the effect of domains of different dipole density, it has been shown that the size of domains results from balancing the line tension (which favors the formation of a large single circular domain) against the electrostatic cost of assembling the dipolar moments of the lipids (which prevent monolayers from reaching complete phase separation) (Lee and McConnell, 1993). Calculations were then extended to lipid bilayers. Hence, the work took in account ionic strength (Travesset, 2006), showing that, at high ionic strength, the effects of dipole are short-ranged and the system is dominated by line tension, leading to domain size increase. On living cells, an opposite effect of the transmembrane electric field on lipid domains is observed. The transmembrane voltage significantly increases the phase transition temperature in membranes squid axons (Inoue et al., 1973) and growing pollen tubes (Melamed-Harel and Reinhold, 1979) and abundance of SM-enriched domains is decreased in living yeast following membrane depolarization (Herman et al., 2015). Thus, it seems that depolarized membrane is more homogeneous than polarized membrane, but the mechanism underlying the induction of lipid domains by the transmembrane electric field is not clear yet (Malinsky et al., 2016).

(v) Membrane protein:lipid interactions

Since lipids diffuse fast in the membranes, the local synthesis of a given species is not sufficient to form lipid domains. Therefore, lipid diffusion must be confined by proteins to allow for domain formation and stabilization (Kusumi et al., 2004; Mayor and Rao, 2004; Rossy et al., 2014). Thus, lipid domains can be captured and stabilized by lipid:protein interactions thanks to lipid-anchored proteins, such as GPI-anchored proteins (Sharma et al., 2004), or transmembrane proteins. If the initial site for lipid:protein interaction is the boundary between the Lo domain and the adjacent Ld membrane, then

proteins could function as surfactants. For example, confocal microscopy and AFM have revealed the preferential *in vitro* localization of lipid-anchored N-Ras to Lo–Ld domain boundaries (Nicolini et al., 2006) and the reorganization of phase-separated membranes into irregular domains by the reduction of line tension at phase boundary due to the binding of a membrane-active peptide derived from the apoptotic protein Bax at the domain interface (García-Sáez et al., 2007b). Integral membrane proteins can also organize lipids, as the intramembrane protein needs to be solvated by the flexible disordered chains of phospholipids. Mouritsen's hydrophobic matching hypothesis proposes that integral membrane proteins perturb surrounding lipids so that bilayer thickness matches the length of the transmembrane domain (Jensen and Mouritsen, 2004). Consistently, recent work indicates that proteins might be the most important determinants of membrane thickness, at least in the exocytic pathway (Mitra et al., 2004). Larger more stable lipid domains can be formed by protein:protein interactions. As examples, one can cite the T cell receptor (TCR) and IgE receptor signaling platforms (Gaus et al., 2005; Larson et al., 2005).

6.3 Extrinsic factors

Besides membrane proteins (Section 6.2.5.) are those that shape the membrane such as cytoskeleton (Section 6.3.1.) and BAR domain proteins (Section 6.3.2.). Moreover, lipid domains can be influenced by electrostatic interactions with cations (Section 6.3.3.) and membrane/lipid turnover (Section 6.3.4.).

(i) Cytoskeleton

Proximity and direct interaction between the membrane and cytoskeleton *via* actin-binding proteins or complexes makes the cytoskeleton one of the most important extrinsic factor to influence PM lateral distribution. Kusumi and coll. suggested that the PM is compartmentalized into large areas containing smaller regions, resulting from an actin-based membrane cytoskeleton fence structure with anchored transmembrane proteins acting as pickets (Fujiwara et al., 2002; Kusumi et al., 2005).

However, membrane scaffolds can have strongly differential effects on lipid organization. Thus, Frisz and coll. demonstrated that actin depolymerization induces a randomization of ^{15}N-sphingolipids in fibroblasts, indicating that sphingolipid-enriched domains strongly depend on the actin-based cytoskeleton (Frisz et al., 2013b). Thanks to a genetically encoded fluorescent PS biosensor (GFP–LactC2) and a fluorescent PS analog together with single-particle tracking and fluorescence correlation spectroscopy, Grinstein and coll. revealed that a sizable fraction of PS with limited mobility exists in the PM and that cortical actin contributes to this confinement (Kay et al., 2012). More recently, Mayor and co-workers provided experimental and simulation data showing that nanoclustering of GPI-anchored proteins at the outer PM

leaflet by dynamic cortical actin is made by the interdigitation and transbilayer coupling of long saturated acyl chains and that cholesterol can stabilize Lo domains over a length scale that is larger than the size of the immobilized cluster (Raghupathy et al., 2015). In RBCs, observations are more contrasting since acute membrane:cytoskeleton uncoupling at 4.1R and ankyrin complexes differentially modulate the abundance of lipid submicrometric domains (Carquin et al., 2015). Effect of cytoskeleton on lipid phase separation in model membranes also led to contrasting results: (i) polymerization of dendritic actin network on the membrane of GUVs induces phase separation (Liu and Fletcher, 2006); (ii) actin fibers bound on supported lipid bilayer prevent lipid phase separation that occurs at low temperature (Honigmann et al., 2014); and (iii) the prokaryotic tubulin homolog FtsZ attached to GUVs suppresses large-scale phase separation below the phase transition temperature but preserves phase separation above this temperature (Arumugam et al., 2015).

Besides temperature (see Section 6.1.), two explanations can be provided for such differential effects. First, the properties of the anchoring type and pattern at the PM considerably vary between cell types and even within a same cell. Three types of membrane scaffold structures have been described so far and are well-summarized in (Honigmann and Pralle, 2016). First, the picket-and-fence model proposed by Kusumi and coll. (Kusumi et al., 2012a; Kusumi et al., 2012b; Kusumi et al., 2011) is based on actin fence formation and binding to transmembrane proteins and lipids *via* adaptor proteins. This model describes the PM organization into three domains of decreasing size and showing cooperative actions: (i) the membrane compartment (40-300nm in diameter), corresponding to the PM partitioning mediated by the interactions with the actin-based membrane cytoskeleton (fence) and the transmembrane proteins anchored to the membrane cytoskeleton fence (pickets); (ii) the raft domains (2-20nm) confined by the anchored transmembrane proteins; and (iii) the dynamic protein complex domains (3-10nm), including dimers/oligomers and greater complexes of membrane-associated and integral membrane proteins. Among the specialized soluble proteins that can bind membrane bilayers *via* lipid-binding domains, allowing for interaction between inner leaflet lipids and cortical actin and contributing to compartimentalize the PM, one can cite the ERM proteins (Janmey and Lindberg, 2004). The second model is based on the active actin fiber polymerizing binding to the membrane constituents that drives clustering through aster formation (Rao and Mayor, 2014; Sheetz et al., 2006). It is proposed that the living cell membrane is well-organized and that localization, clustering, transport and/or transformation of membrane molecules are allowed through the local engagement of the cortical actin machinery and need energy (Rao and Mayor, 2014). This model especially accounts for the transient clustering of molecules such as GPI-anchored proteins. Coupling of these proteins with the actin cytoskeleton involves long chain lipids which couple across the bilayer in the presence of

cholesterol (Raghupathy et al., 2015). Third, some cells such as RBCs and neurons exhibit regular spectrin/actin/ankyrin-based membrane scaffolds that provide mechanical robustness. For information on the RBC cytoskeleton, see Section 4.2. and (Lux, 2016).

Second, we have to keep in mind that the cytoskeleton does not provide a satisfactory explanation for all membrane-associated phenomena and there is no universal model of the PM lateral organization (Bernardino de la Serna et al., 2016). At least, cytoskeleton should be integrated in a more global view including membrane curvature, as recently proposed by (Honigmann et al., 2014). Based on computer simulations, super-resolution optical STED microscopy and FCS, it has been demonstrated that the cytoskeleton-based sorting mechanism persists to physiological temperatures (*i.e.* > Tm), while phase separation is prevented at low temperature. In the presence of curvature coupling, these two effects are enhanced (Honigmann et al., 2014). The idea behind is an extension of the picket-fence model, by including a coupling of the local membrane curvature to the membrane composition, in a way that the actin fibers cause the membrane to curve reinforcing the influence of the picket-fence (Honigmann et al., 2014).

(ii) Cross-binding proteins

Several observations indicate that peripheral protein binding may represent an additional regulator of lateral heterogeneity. First, cross-linking components like upon CTxB and Annexin V modulate phase transition temperatures in membrane models (Johnson et al., 2010). Second, GSL clustering induced by CTxB or Shiga toxin induce phase segregation in GUVs and GPMVs (Lingwood et al., 2008; Windschiegl et al., 2009). Third, besides their recognized roles in generating membrane protrusions or invaginations through the sculpting of PI-rich membranes, elegant studies have shown a role for BAR domain proteins in generating stable PIP_2 domains by limiting their lateral diffusion, before inducing membrane curvature (Picas et al., 2014; Zhao et al., 2013). These domains could play a role in various physiological processes including endocytosis, membrane protein trapping or storage of lipids in eisosomes (Zhao et al., 2013).

(iii) Electrostatic interactions of charged headgroups with cations

The inner PM leaflet is the most negatively charged membrane of all cell bilayers, attributed to its high PI and PS contents. Localized negative membrane charge achieved by cations represents an alternative mechanism for domain formation and/or stabilization. It is indeed well established that the lateral organization of PIP_2 can be modulated by Ca^{2+}, as shown in GUVs, lipid monolayers and bilayers (Carvalho et al., 2008; Levental et al., 2009a; Sarmento et al., 2014). PIP_2 heterogeneous distribution has been confirmed in the PM and depends on the interaction between PIP_2 and polybasic protein domains (such as MARCKS) that can be modulated by Ca^{2+} and calmodulin

(Laux et al., 2000; McLaughlin and Murray, 2005). Contrasting with the PIP_2 domain formation by cations, PS (which can also modulate membrane charge locally) domains seem to preferentially rely on the association with protein complexes immobilized by the cytoskeleton (Kay et al., 2012) than on anionic domains, suggesting that the formation of Ca^{2+} induced domains depend on the high charge density of the lipid (Levental et al., 2009a).

Such localized membrane charge can facilitate PM protein clustering to confined regions. For example, Ca^{2+} (but not Mg^{2+}) has been shown to promote the formation of syntaxin 1 (a SNARE protein) mesoscale domains through PIP_2 in PC12 cell sheets, indicating that this cation acts as a bridge that specifically and reversibly connect multiple syntaxin 1/PIP_2 complexes and suggesting a role for Ca^{2+} in PM reorganization during Ca^{2+}-regulated secretion (Milovanovic et al., 2016). Alternatively, localized membrane charge can induce conformational change of PM proteins (Shi et al., 2013), as shown during the activation of T cell receptor (TCR) upon antigen engagement. TCR interacts with acidic phospholipids through ionic interactions in quiescent T cells, resulting into deep membrane insertion of the tyrosine side chains. This renders TCR inaccessible to phosphorylation by the Src-kinase Lck. After antigen engagement of TCR, local Ca^{2+} concentration increases, leading to disruption of the ionic protein:lipid interaction, dissociation of tyrosines from the membrane and accessibility to Lck (Li et al., 2014; Shi et al., 2013).

In cells, a way to create localized membrane domains that differ in charge is through modification of local Ca^{2+}concentration by localized transient Ca^{2+} influx from membrane channels. Among these channels one can cite transient receptor potential ion channels that respond to mechanical stress induced by tension and trigger Ca^{2+} influx that interact with negatively-charged membrane lipids (Shi et al., 2013). For example, TRMP7 has been shown to drive the formation of Ca^{2+} domains during invadosome formation in neuroblastoma cells (Visser et al., 2013) and at the leading edge of migrating cells (Wei et al., 2009). It should be stressed that localized electrostatic interaction of charged lipid headgroups with cations could be linked to other mechanisms involved in membrane lipid lateral heterogeneity, such as actin dynamics (Wu et al., 2013). It remains to be determined if such localized membrane charge in the inner PM can have consequences on the organization of the outer PM leaflet (see Section 5.4.).

(iv) Membrane recycling and enzymatic activity

A key difference between biological and model membranes is that the former are not at thermodynamic equilibrium but subjected to active processes such as membrane recycling and lipid turnover. Lipid recycling can be due to permanent exchange of lipids with the surrounding medium (membrane reservoir) where lipids are locally inserted at a constant rate everywhere along the membrane and removed at a rate proportional to their local concentration

(Foret, 2005). Lipid recycling can also occur *via* vesicular lipid transport events that can either specifically target lipid domains or random areas of the membrane (Turner et al., 2005). For a review on this topic, please refer to (Schmid, 2016). In all living cells except RBCs, there is an active lipid recycling to and from the membrane that is proposed to limit lipid domain size (Fan et al., 2010). Lipid domains in mature RBCs are more large, stable and round than in other living cells (Carquin et al., 2015; Carquin et al., 2014), which could support the implication of active cellular processes in lipid domain destabilization in nucleated mammalian cells. In addition to lipid recycling, the molecular interactions that control phase behavior can also be dramatically affected by the activity of membrane lipases or kinases that generate phase-changing products (van Meer et al., 2008). A recent study on model membranes evidenced the formation of lipid domains upon lipase action (Brewer et al., 2017).

7. Lipid domains – function in (re)shaping

During the past years, increasing lines of evidence for the implication of rafts in immune signaling, host–pathogen interactions, cancer or vascular diseases has been reported on cells (ref). However, whether these lipid lateral heterogeneities could participate in cell shaping and reshaping (e.g. deformation and vesiculation) remains obscure. Here, we provide lines of evidence suggesting that domains could contribute to cell shaping, vesiculation and division.

7.1 Cell shaping

At short length scale, relationship between curvature and lipid molecular structure and lipid transbilayer sorting are well known (see Section 4.4.). At long length scales, different mechanisms may participate and whether lipid domains play a role in this process is still unresolved. However, the importance of cardiolipin-enriched domains in curvature maintenance in rod-shape bacteria gives evidence for the existence of such relationship. It was recently shown that cardiolipin localizes to the polar and septal regions of the inner membrane of *Escherichia coli* (Mileykovskaya and Dowhan, 2000), *Bacillus subtilis* (Kawai et al., 2004) and *Pseudomonas putida* (Bernal et al., 2007). Bacterial poles and septa are regions that have the largest curvature (Huang and Ramamurthi, 2010; Tocheva et al., 2010). As bacterial cardiolipin have a small ratio of head-to-tail surface areas (Hirschberg and Kennedy, 1972), it is thus tempting to invoke the negatively curved regions of the inner leaflet of bacterial membrane poles relative to the cylindrical midcell to explain cardiolipin localization. However, the relative affinity of a single nanometer-sized cardiolipin molecule for the very slightly curved poles is likely insufficient for stable polar localization in a micrometer-sized bacterium. An alternative explanation is that cardiolipin localization is purely

driven by lipid phase segregation. However, the observed rapid repartitioning of cardiolipin to the division site (Kawai et al., 2004; Mileykovskaya and Dowhan, 2000) would be strongly disfavored if cardiolipin is segregated in a single, large cluster at one or both poles. Instead, Wingreen and coll. proposed stable finite-sized cardiolipin clusters which can spontaneously and independently target the two cell poles as well as the nascent division site (Huang et al., 2006; Mukhopadhyay et al., 2008). Weibel and coll. found that a cardiolipin synthase mutant of the rod-shaped *Rhodobacter sphaeroides* produces ellipsoid-shaped cells in a reversible process, and that bacteria with impaired MreB expose the same shape changes (Lin et al., 2015). Huang and coll. recently demonstrated in *E. coli* that feedback between cell geometry and MreB cytoskeleton localization at the regions of negative curvature maintains rod-like shape by directing growth away from the poles and actively straightening locally curved cell regions (Ursell et al., 2014). In addition, cardiolipin has been shown to sense and transmit changes in inner membrane curvature to the bacterial phage shock protein (Psp) system (a cell envelope stress response system). Therefore, cardiolipin domains could be viewed as a membrane curvature sensor (due to its curvature-sorting properties) and as an indicator for membrane or cytoskeletal proteins that feedback on membrane curvature to maintain bacterial shape (due to its potential raft-like ability to segregate proteins).

7.2 Cell vesiculation

Convincing arguments for the implication of lipid domains in membrane vesiculation have been provided by simulation studies, membrane models and other cells. First, based on a two-component coarse-grained molecular dynamics RBC membrane model, Li and Lykotrafitis have revealed that the spontaneous curvature of the RBC membrane domains can cause the formation of nanovesicles and that lateral compression generates larger vesicles with heterogeneous composition, similar in size to the cytoskeleton corral (Li and Lykotrafitis, 2015). Second, using a combination of mechanical modeling and GUV experiments, Phillips et al showed that lipid domains can adopt a flat or dimpled morphology, depending on spontaneous curvature, boundary line tension of domains and domain size (Ursell et al., 2009). Third, Ld phases tend to spontaneously reside in curved membrane regions of GUVs whereas Lo phases are preferentially localized in flat regions (Baumgart et al., 2003). Fourth, in living keratinocytes labeled by the Ld marker DiIC18 and the Lo GM1 marker CTxB, submicrometric lipid domain separation together with spontaneous vesiculation of the Ld domains occur. Such vesiculation is still increased by cholesterol depletion, which further enhances Lo/Ld domain separation and detachment of the cortical cytoskeleton from the membrane (Vind-Kezunovic et al., 2008). Fifth, in activated neutrophils, cholesterol-enriched vesicles are released (Del Conde et al., 2005), suggesting that lipid domains might be the starting point of the vesiculation process. Sixth, rafts

are specifically selected and incorporated into the influenza virus envelope during the budding of enveloped viruses from the PM (Scheiffele et al., 1999). Finally, specific lipid sorting is observed in vesicle and tubule budding from organelles of the endocytic pathway (Mukherjee and Maxfield, 2000; Mukherjee et al., 1999).

7.3 Cell division

Prokaryotic membrane domains contribute to division and morphogenesis. Besides maintenance of membrane curvature and cell shape (see Section 7.1.), cardiolipin is also involved in curvature changes occurring during bacterial division. Based on polar localization of chemotaxis receptors in *E. coli* (Maddock and Shapiro, 1993) and septal localization of the division proteins MinCD and DivIVA in *B. subtilis* (Lutkenhaus, 2002; Mileykovskaya et al., 1998), it was proposed that cardiolipin domains could play a role in sorting proteins. Renner and Weibel developed a microtechnology-based technique to confirm the relationship between bacteria curvature, cardiolipin domain localization at the poles and the positioning of amphiphilic cytoplasmic proteins. Thus, in giant *E. coli* spheroplasts confined in polymer microchambers, they demonstrated that cardiolipin domains localize to regions of large negative curvature. By expressing YFP fused to the N-terminal domain of the cytoplasmic division protein MinD, they showed the dependence of negative membrane curvature on MinD localization in spheroplasts and its colocalization with cardiolipin domains (Renner and Weibel, 2011).

Membrane domains also participate to cell division in fungi. Elevated concentrations of sterols decorate developing membranes upon growth-induced elongation of the fungal cells *Candida albicans* and *Aspergillus nidulans* (Martin and Konopka, 2004; Takeshita et al., 2008) and septum or mating projection formation in the yeasts *Saccharomyces pombe* and *cerevisiae* (Bagnat and Simons, 2002; Wachtler et al., 2003). In fact, two sterol pools are required for two important aspects of mating in *S. cerevisiae*, pheromone signaling and PM fusion (Jin et al., 2008). Regarding the implication of sphingolipid-enriched domains, it has been shown in *S. cerevisiae* that: (i) the inhibition of sphingolipid synthesis induces the formation of multinuclear cells due to a defect in cytokinesis (Sun et al., 2000); and (ii) the organization in ordered domains at the mating projection depends on sphingolipids, as evidenced by microscopy with Laurdan (Proszynski et al., 2006). Lipid gradients in the inner PM leaflet have also been revealed: (i) PIP_2 is densely distributed in the shmoo tip of *S. cerevisiae* (Garrenton et al., 2010); (ii) the localized synthesis together with the restricted diffusion of PIP_2 in *C. albicans* result into a gradient from the tip of membrane protrusions to the neck (Vernay et al., 2012); and (iii) PE concentrates at polarized ends in budding yeast (Iwamoto et al., 2004).

In mammalian cells, cholesterol-containing domains concentrate at the cleavage furrow and possess a signaling pathway that contributes to cytokinesis (Ng et al., 2005). More recently, the transbilayer colocalization between the outer SM and the inner PIP_2 domains has been evidenced around the cleavage furrow and the midbody of HeLa cells by super-resolution fluorescence microscopy. This study highlights two key features of lipid domains. First, it shows the importance of SM domains in the regulation of cytokinesis, as revealed by PIP_2 domain dispersion, inhibition of the Rho GTPase RhoA recruitment to the cleavage furrow and regression of the cleavage furrow upon SMase treatment (Abe et al., 2012). Second, it indicates that PIP_2 in the inner leaflet also form and remain in domains. Several reasons can explain the restricted localization of PIP_2 around SM clusters: (i) SM, $PIP_5K\beta$ and PIP_2 interact, restricting the diffusion of PIP_2; (ii) the Rho GTPase positively regulates the activity of $PIP_5K\beta$, enhancing the formation of PIP_2 domains at the inner leaflet; and (iii) the mobility of PIP_2 is restricted by protein fences (Abe et al., 2012). Another possibility is that BAR domain proteins, besides their recognized role in membrane bending and curvature sensing, control the diffusion of PIP_2 through electrostatic interactions, thereby generating stable domains before inducing membrane deformation, as reported in (Zhao et al., 2013). Alternatively, PIP_2 domains could be stabilized by Ca^{2+} from the surrounding membrane. Whatever the mechanism, this study demonstrates the importance of outer SM domains to regulate inner PIP_2 clustering (Abe et al., 2012). PIP_2 accumulation in the cleavage furrow of dividing cells has been confirmed by others (Emoto et al., 2005; Field et al., 2005). In contrast, PE, which is normally restricted to the inner leaflet, is exposed to the outer leaflet of the cleavage furrow during cytokinesis, contributing to regulation of contractile ring disassembly (Emoto et al., 2005; Emoto and Umeda, 2000).

Altogether, while the existence of lipid domains is supported by several lines of evidence on different cell models, whether they could participate to cell (re)shaping remains to be demonstrated.

CHAPITRE 2

Justification of cell model, tools and methods & Aims and strategy of the study

Foreword

As highlighted in the Introduction Section (Chapter I), while the existence of lipid domains in cells is supported by increasing lines of evidence, **whether and how such lipid domains participate in cell reshaping, through their specific biophysical properties**, remain to be proven. Studying this question requires adequate cell models, tools and imaging methods. In the first section of the present chapter, I justify our choice of red blood cell (RBC) as a simple well-characterized cellular model to explore this question through its specific biconcave shape and drastic reshaping (*i.e.* deformation and vesiculation). In the second section, I describe the methods and tools used to investigate (i) RBC (re)shaping (section 2.1), (ii) lipid lateral heterogeneity at the outer plasma membrane (section 2.2.) and (iii) membrane biophysical properties (section 2.3.). In the third section, I summarize the aims and strategy of the study.

1. Justification of the cell model

According to us, the RBC constitutes a model of choice to investigate the potential role of lipid domains in cell function-associated (re)shaping, based on three main reasons. First, the mature RBC is the most simple and best-characterized human cell, whose only structural components, a PM linked to an underling cytoskeleton, account for all of its diverse functions (section 1.1.). Second, the RBC is a beautiful example of cell (re)shaping. Indeed, the specific biconcave shape allows RBC to undergo drastic deformation through the microvasculature to deliver oxygen to tissues. Such biconcavity is lost at the end of its life due to membrane vesiculation (section 1.2.). Third, RBC flat featureless membrane and absence of lipid trafficking (*i.e.* endocytosis) facilitate the study of lipid lateral heterogeneities. These two technical advantages were exploited by the CELL laboratory to evidence submicrometric lipid domains at the RBC PM (section 1.3.).

1.1 RBC as a simple well-characterized cell model

The RBC exposes unique function-associated features such as high elasticity (100-fold softer than a latex membrane of comparable thickness), rapid response to applied fluid stresses (time constants in the range of 100 milliseconds) and high strength (stronger than steel in terms of structural resistance) (Mohandas and Gallagher, 2008). All these unique characteristics derived from a simple composite structural organization, *i.e.* a PM composed of cholesterol, phospholipids and proteins, linked to a two-dimensional elastic network of skeletal proteins through transmembrane anchorage protein domains inserted in the lipid bilayer.

(i) Membrane lipids

The RBC lipid bilayer contains an exceptionally high level of cholesterol (Fig 1A). In the RBC PM, the cholesterol distributes both in the inner and in the outer membrane leaflets. In contrast, major phospholipids are asymmetrically distributed: phosphatidylcholine (PC) and sphingomyelin (SM) are mainly located in the outer leaflet while phosphatidylethanolamine (PE), phosphatidylserine (PS) and phosphoinositides (PI) are confined to the inner leaflet (Verkleij et al., 1973; Zwaal and Schroit, 1997) (Fig 1B).

A

Molar %	Polar lipids								Sterols[a]	Other
	PC	PE	PI	PS	PA	PG	CL	SLs[a]		
E. coli		82		traces		6	12			
S. cerevisiae	25	10	9	3	5		2	10-20 *MIPC*	30-40 *erg*	
Human RBCs	24	6	traces	3	traces			19 *SM*	48 *chol*	traces
Human platelets	18	20	1	12				16 *SM*	32 *chol*	
Fibroblast cell line (NIH 3T3)	43	16	8	6.5	1.5			12 *SM*	13 *chol*	
Chinese hamster ovary cells (CHO)	25	21	n.d.	7				12 *SM*	35 *chol*	
Schwann cell line (NF1T)	27	9	6	2				18 *SM*	38 *chol*	
Undifferentiated L6 myoblasts	24	9	2	6				16 *SM*	42 *chol*	
Human alveolar macrophages	30	21		21				7 *SM*	8 *chol*	13

B

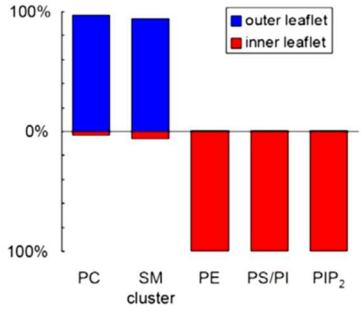

Figure 1. Human RBC lipid composition and transbilayer distribution. A. Lipid composition of the plasma membrane of RBCs in comparison to other cells. PC, phosphatidylcholine; PE, phosphatidylethanolamine; PI, phosphatidylinositol; PS, phosphatidylserine; PA, phosphatidic acid; PG, phosphatidylglycerol; CL, cardiolipin; SLs, sphingolipids; MIPC, mannosylinositol phosphorylceramide; SM, sphingomyelin; erg, ergosterol; chol, cholesterol. a, The most abundant lipid of these categories is indicated in italics. n.d., not detected. Adapted from (Carquin et al., 2016). B. **Asymmetric transbilayer lipid distribution at the human RBC plasma membrane**. PC and SM are almost exclusively located at the outer PM leaflet (98.1% and 98.5%, respectively), while PE, PS/PI and PIP_2 are exclusively distributed at the inner leaflet (99.8%, 99.3% and 99.7%, respectively). Figure from (Murate et al., 2015).

Different phospholipid transporters are involved in the maintenance of transversal asymmetry. For instance, flippases move phospholipids from the outer to the inner leaflet while floppases do the opposite. The steady-state asymmetry can be disrupted by the activation of scramblases which move phospholipids bi-directionally (Daleke, 2008; Sims and Wiedmer, 2001). The maintenance of asymmetric phospholipid distribution has several functional implications in RBCs. One can cite (i) the exposition of PS at their outer PM leaflet that is recognized by macrophages present into the reticuloendothelial system (especially the spleen), leading to RBC phagocytosis; and (ii) PS and phosphatidylinositol-4,5-bisphosphate (PIP_2) in the inner PM leaflet which regulate membrane mechanical properties through their interactions with skeletal proteins, such as spectrin and protein 4.1R (Manno et al., 2002; An et al., 2005, 2006).

(ii) Membrane proteins

Based on proteomic approaches, a comprehensive catalog of RBC proteins has been generated, with more than 300 proteins including 105 integral membrane proteins (Pasini et al., 2006). Many of them define the diverse blood group antigens while others are implicated in transport (*e.g.* water, gazes and ions), PM anchorage to the underlying cytoskeleton, adhesion (involved

in interactions of RBCs with other blood cells and endothelial cells), signaling and other still undefined activities (Mohandas and Gallagher, 2008).

The intracellular calcium (Ca^{2+}) concentration balance is a beautiful example of the interconnected work of RBC PM proteins to achieve optimal physiological output (Fig 2). Extremely low basal permeability of the human RBC membrane to Ca^{2+} and a powerful Ca^{2+} pump (PMCA) allows to maintain intracellular free Ca^{2+} levels between 30 and 60 nM, whereas blood plasma Ca^{2+} is approximately 1.8 mM. Ca^{2+} uptake by RBCs occurs through TRPC, $Ca_v2.1$, NMDA or Piezo-1 channels and has an impressive impact on multiple processes in RBC. It contributes to control RBC biophysical/morphological properties such as (i) membrane asymmetry through its action on scramblases (Woon et al., 1999; Stout et al., 1998), whose passive transport of lipids is Ca^{2+}-dependent (Morrot et al., 1989; Bitbol et al., 1987), (ii) volume decrease mediated by the Gardos channel, a Ca^{2+}-activated K^+ channel whose opening leads to hyperpolarisation and loss of K^+, Cl^- and water, resulting in cell shrinkage (Bogdanova et al., 2013), and (iii) membrane elasticity thought the Ca^{2+}-calmodulin complex and Ca^{2+}-dependent phosphorylation of the 4.1R protein by PKC, both playing a key role in the regulation of cytoskeletal stability. In addition, RBC intracellular Ca^{2+} concentration also controls physiological parameters such as RBC metabolic activity, redox state and cell clearance (Bogdanova et al., 2013).

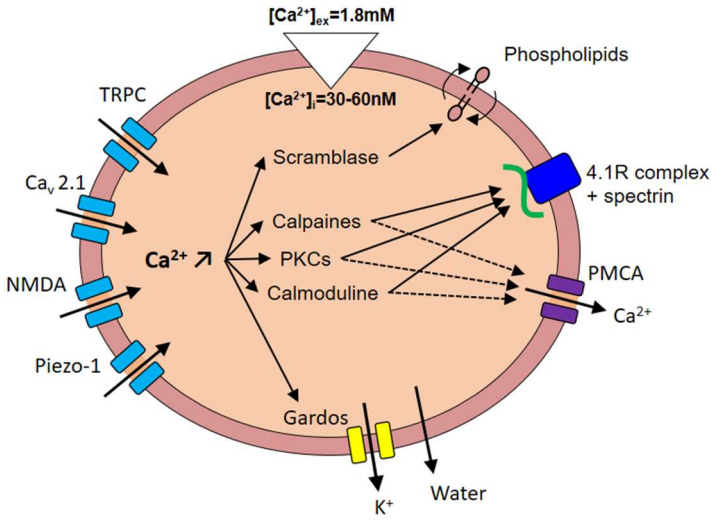

Figure 2. Calcium exchanges in RBC. RBC intracellular free Ca^{2+} level is maintained between 30-60 nM while blood plasma Ca^{2+} is approximately 1.8 mM. Ca^{2+} uptake is mediated by TRPC (transient receptor potential cation channel), $Ca_v2.1$ channel, NMDA receptor (*N*-methyl-D-aspartate) or Piezo-1 channel and Ca^{2+} efflux by the PMCA (plasma membrane Ca^{2+} ATPase). Intracellular Ca^{2+} concentration contributes to regulate (i) membrane asymmetry through its action on scramblases, (ii) volume decrease mediated by the Gardos channel which induces a loss of K^+, Cl^- and water, resulting in cell shrinkage, and (iii) cytoskeletal stability thought calcium-calmodulin complex and Ca^{2+} dependent phosphorylation of 4.1R protein by PKC.

(iii) Skeletal proteins

As mentioned in the previous paragraph, several RBC proteins play a central role in the anchorage of the PM to the underlying cytoskeleton. Such anchorage is particularly strong in RBCs, as compared to nucleated cells, contributing to the maintenance of RBC biconcavity, remarkable deformability and membrane cohesion (see below). The RBC two-dimensional network is mainly composed of α- and β-spectrin, actin, protein 4.1R, adducin, dematin, tropomyosin and tropomodulin (Mohandas and Gallagher, 2008). A unique structural feature of the long filamentous spectrin is its large number of triple-helical repeats of 106 amino acids, 20 in α-spectrin and 16 in β-spectrin. α- and β-spectrin form an antiparallel heterodimer through strong lateral interaction between repeats 19 and 20 near the C-terminus of α-spectrin and repeats 1 and 2 near the N-terminus of β-spectrin. The 36 triple-helical repeats of spectrin are structurally heterogeneous in terms of their thermal stability (Mohandas and Gallagher, 2008).

The RBC cytoskeleton network is attached to the bilayer at the end of the spectrin filaments (in green at Fig 3A) through the 4.1R protein-based complexes (in blue at Fig 3A) and at random points along a spectrin filament

length through the ankyrin-based complexes (in red at Fig 3A)[16,42-44]. Besides the 4.1R protein which links the cytoskeleton to the membrane, the 4.1R complex contains several integral membrane proteins such as the sialoglycoprotein glycophorin C (GPC) which contributes to the negative surface charge of the RBC membrane helping to prevent erythrocyte aggregation (Chasis and Mohandas, 1992), the anion transporter band-3 and the glucose transporter Glut1, *a.o.*(Mohandas and Gallagher, 2008). The 4.1R complex also contains the cytoskeleton protein F-actin and several peripheral proteins such as dematin, adducin and tropomodulin which play a role in the assembly and regulation of actin filaments (Mohandas and Gallagher, 2008) (Fig 3B, left). Besides ankyrin, the ankyrin-based complex contains several integral membrane proteins such as glycophorin A (GPA), the major contributor to the negative surface charge of RBC membrane (Chasis and Mohandas, 1992), the anion transporter Band 3(Mohandas and Gallagher, 2008), the water transporter aquaporin 1(Baines, 2010) and CD47 which is a marker-of-self and protects RBCs from phagocytosis by macrophages (Oldenborg et al., 2000). In addition, the ankyrin complex contains peripheral proteins such as the ATP-binding protein 4.2 which binds and regulates association of band 3 with Ankyrin (Mohandas and Gallagher, 2008) (Fig 3B, right).

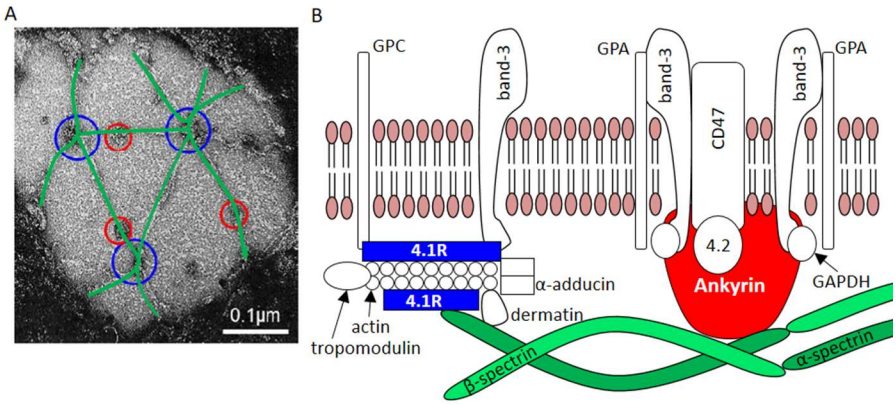

Figure 3. Organization of the two types of membrane:cytoskeleton anchorage complexes in RBC. A. Transmission electron microscopy image of the spectrin network attached at the RBC plasma membrane inner face. Spectrin tetramers (green) radiate from both 4.1R (blue) and ankyrin (red) anchorage complexes. Adapted from (Byers and Branton, 1985). **B. Schematic representation of the main proteins associated with the two complexes.** 4.1R (left) *vs* ankyrin (right) complexes. GPC, glycophorin C; GPA, glycophorin A; GAPDH, glyceraldehyde-3-phosphate dehydrogenase. Adapted from (Salomao et al., 2008).

The 4.1R complex participates to the "horizontal linkages", together with the spectrin dimer-dimer interaction. These "horizontal linkages" insure RBC membrane mechanical stability and prevent membrane fragmentation/break

up when the RBC is submitted to high deformation and shear stresses in the blood circulation. The ankyrin complex contributes to the "vertical linkages" which insure a strong cohesion between the cytoskeleton and the membrane, preventing membrane vesiculation and allowing for the maintenance of the membrane surface area.

1.2 RBC function-associated (re)shaping

The RBC is a beautiful example of function-associated (re)shaping. The RBC specific biconcave shape is needed to perform its primary function of delivering oxygen to the tissues by ensuring both optimal gas exchanges and RBC high deformability (Fig 4a). Indeed, the RBC must undergo drastic and reversible deformation while maintaining its integrity during its 120 days lifetime in the circulation. RBC high deformability is further tested for quality controlled by the spleen, where it undergoes drastic deformations (Fig 4b,c). Upon aging, RBC high deformability is lost by membrane vesiculation, leading to spleen entrapment and removal from circulation (Fig 4d).

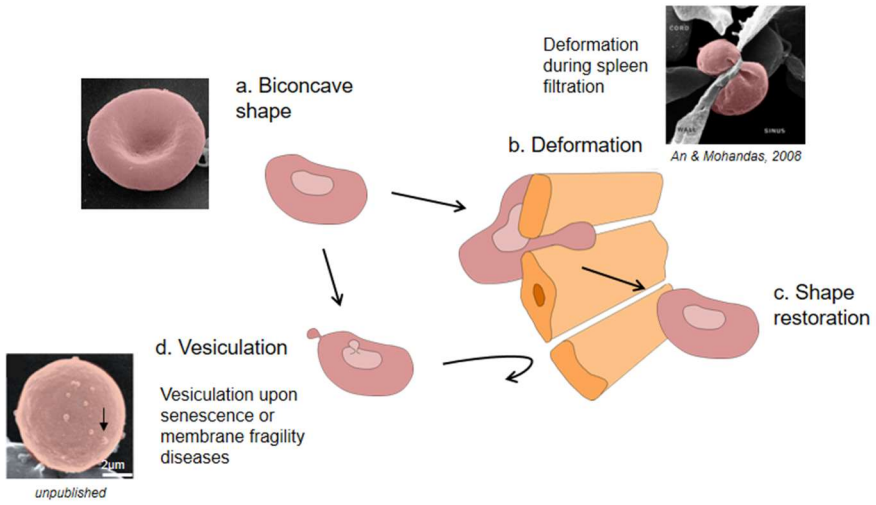

Figure 4. RBC function-associated (re)shaping. RBC exhibits a specific biconcave shape (a) allowing for its high deformability needed to deliver oxygen to the tissues through the capillaries and tested for quality control by the narrow pores of the spleen (b-c) but lost due to membrane vesiculation at the end of its lifetime or in membrane fragility diseases, leading to splenic entrapment and removal from circulation (d).

(i) RBC biconcavity

The maintenance of RBC specific biconcave shape is mainly attributed to its strong membrane:cytoskeleton anchorage and the dynamic remodeling of the coupling between the membrane and the spectrin network powered by ATP. This metabolically-driven dynamics, observed in the convex regions, is

thought to govern both non-equilibrium fluctuations and the biconcave shape in the RBC membrane (Park et al., 2010).

(ii) RBC deformation

Three RBC constitutive features have been identified as primary regulators of the RBC deformation: (i) its specific geometry, *i.e.* its high surface area to volume ratio (Fig 7a); (ii) its finely regulated cytoplasmic viscosity, determined by intracellular hemoglobin concentration; and (iii) its high membrane elasticity (Mohandas et al., 1983; Mohandas and Chasis, 1993; Mohandas and Evans, 1994).

RBC specific geometry - The normal human RBC exhibits a specific biconcave shape, with a ~90 fL volume and ~140 μm^2 surface area, which results in high area-to-volume ratio and leads to a ~40% surface excess as compared to a sphere of the same volume. This specific shape both ensures fast oxygen and carbon dioxide exchanges between haemoglobin molecules and the outside medium but also decreases the forces that have to be applied to deform the membrane as compared to a spherical shape (Canham, 1970). While a normal RBC can deform with linear extensions up to ~250%, its deformation involve no significant change in membrane surface area. Indeed, an increase of 3% to 4% in its surface area results in RBC lysis. Therefore, RBC Maintenance of RBC specific biconcave shape is generally attributed to the strong anchorage between the plasma membrane and the underlying cytoskeleton through vertical linkages that maintain the cohesion between the lipid bilayer and cytoskeleton, thereby preserving RBC from membrane vesiculation. An additional horizontal linkage by spectrin dimer-dimer interactions and spectrin-actin-protein 4.1R junctional complexes allow to preserve membrane mechanical stability by preventing deformation-induced membrane fragmentation when the cell encounters high fluid shear stresses in circulation.

RBC cytoplasmic viscosity and volume regulation - The ability of normal RBC to rapidly change its shape in response to fluid shear stresses also depends on its cytoplasmic viscosity, which is determined by intracellular hemoglobin concentration. By tight control of hemoglobin concentration within a narrow range, RBC minimizes the cytoplasmic viscous dissipation during deformation. While RBC regulates its mean cell hemoglobin concentration (MCHC) within a very narrow range (30-35 g/dL), its mean cell volume range can vary widely (20-200 fL). Hence, RBC ability to regulate its cytoplasmic viscosity within narrow limits critically dependent on its ability to control its volume. RBC cellular volume is tightly regulated by several ionic transports. The Na^+/K^+-ATPase and the Ca^{2+}-ATPase (also called PMCA) set up the major cation gradients across the RBC PM (Radosinska and Vrbjar, 2016; Maher and Kuchel, 2003). In addition, the RBC is endowed with a large variety of ion channels that are nowadays proposed to play a dynamic role

(reviewed in (Thomas et al., 2011)). Thus, upon shear stress in the circulation, a reversible increase in Ca^{2+} permeability occurs. Piezo1, a mechanosensitive non-selective cation channel, has been recently identified as the link between mechanical forces, Ca^{2+} influx and RBC volume homeostasis. This study clearly indicates a role for mechanotransduction in cell volume regulation *via* Ca^{2+} influx through Piezo1 and subsequent RBC dehydration *via* downstream activation of the Gardos channel (Cahalan et al., 2015), a Ca^{2+}-dependent K^+ efflux channel[22] (Fig 2).

RBC membrane elasticity - A unique feature of the normal RBC membrane is its high elasticity, which enables the cell to rapidly respond to applied fluid stresses in the circulation. While both theoretical and experimental evidence suggest a critical role for the spectrin-based skeletal network in determining membrane elasticity, the precise structural basis of the effect remains uncertain. The RBC two-dimensional spectrin-based membrane skeletal network is attached to the bilayer at the end of the spectrin filaments through the 4.1R protein-based complex. In response to externally imposed deformations, the attachment of the spectrin filament at its ends goes through a transient dissociation process. This process is triggered by Ca^{2+}-dependent phosphorylation of the 4.1R protein, allowing for a controlled reversible losing the cytoskeleton network and then RBC deformation (Betz et al., 2009; Park et al., 2010; Li et al., 2007; Gov, 2007a; Gov and Safran, 2005). In addition, an important structural feature of the long filamentous spectrin dimer is the succession of 36 spectrin repeats, 20 in α-spectrin and 16 in β-spectrin, which behave in part as independently folding units. Unfolding and refolding of distinct spectrin repeats make a major contribution to the elasticity of the normal red cell membrane (Mohandas and Gallagher, 2008). Besides the recognized role of the spectrin cytoskeleton in controlling RBC elasticity, it is possible that membrane lipid lateral heterogeneity also contributes to- or is modulated by- the high RBC membrane elasticity and deformability. This hypothesis is currently tested by another PhD student of the CELL unit (DDUV), Hélène Pollet.

(iii) Membrane vesiculation upon aging

Upon senescence *in vivo* RBCs undergo multiple changes. These include the decrease of activities of multiple enzymes, the gradual accumulation of oxidative damage, the loss of membrane by vesiculation, the redistribution of ions and alterations in cell volume, density and deformability. For comprehensive reviews on aging mechanisms in healthy human RBCs, please referred to (Lutz and Bogdanova, 2013; Antonelou et al., 2010). We will here focus on the release of vesicles that are generally classified into two groups, nanovesicles (~25nm size) and MVs (~60-300nm). In contrast to nanovesicles, MVs seem influenced by partial membrane:cytoskeleton uncoupling. Upon senescence, cytoskeleton stiffness and density both increase, leading to larger compressive forces on the cell membrane, that have

been hypothesized to be accommodated by increased membrane curvature and vesicle detachment from the membrane (Fricke and Sackmann, 1984; Gov and Safran, 2005; Edwards et al., 2005). It has been proposed that the loss of mid-point attachments of the spectrin filaments to the bilayer through the ankyrin complexes are involved in increasing stiffness of the cytoskeleton network, hence driving membrane vesiculation between the network nodes (Sens and Gov, 2007; Gov, 2007b). Membrane area loss by vesiculation leads to the loss of RBC specific biconcave shape and of high area to volume ratio. In contrast, only a little loss of hemoglobin is observed upon aging, resulting in progressive increase of cell density during the RBC 120-days life span. Loss of biconcave shape, decrease of surface to volume ratio and increase of intracellular viscosity altogether lead to decrease of RBC deformability. As RBC deformability is constantly tested for quality control when it squeezes through the very narrow pores of the spleen, its deformability loss leads to RBC splenic entrapment and removal from blood circulation (Mohandas and Gallagher, 2008). The removal of aged normal RBC through phagocytosis by macrophages occurs by recognition of clustered band 3 or PS exposure on their outer membrane leaflet (Low et al., 1985; Turrini et al., 1993). MVs have been proposed to contribute to RBC senescence by two opposite mechanisms. They may (i) prevent the elimination of the senescent but yet functional RBCs, by elimination of Band 3 neoantigen, denatured hemoglobin and oxidized proteins (Willekens et al., 2008); or instead (ii) promote removal of senescent RBCs from the circulation, by elimination of CD47(Stewart et al., 2005), PS exposure to the outer PM leaflet and increased intracellular Ca^{2+} concentration (Bogdanova et al., 2013).

1.3 Evidence for membrane lipid lateral heterogeneity

Besides their numerous advantages regarding model simplicity and drastic (re)shaping (see above), RBCs also offer a series of technical advantages. Among others, one can cite their featureless membrane and absence of lipid trafficking, which facilitate the interpretation of PM lateral heterogeneity by excluding artefacts due to membrane protrusions and/or endocytosis. This allowed the laboratory to (i) evidence round and well-defined submicrometric lipid domains at the PM of living RBCs and (ii) identify their control mechanisms.

(i) Evidence for submicrometric lipid domains

The organization of SM and chol, abundant lipids of the outer PM leaflet, was first studied by confocal vital imaging of RBCs spread on Poly-L-Lysine (PLL)-coated coverslips, upon either labeling with a fluorescent SM analog, BODIPY-SM, or decoration of endogenous SM and cholesterol by fluorescent Toxin* fragments called respectively Theta* and Lysenin* (see section 2.2 for the description of these lipid probes). This allowed to reveal SM- and chol-enriched domains that differ in abundance and distribution at the RBC surface

(Fig. 5) (D'auria et al., 2011; D'Auria et al., 2013b; Tyteca et al., 2010; D'Auria et al., 2013a; Carquin et al., 2014, 2015).

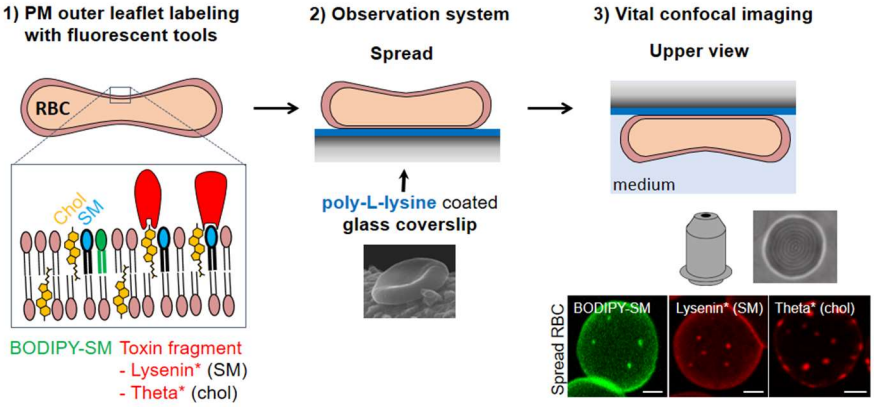

Figure 5. Vital confocal imaging procedure to evidence lipid submicrometric domains at the RBC PM. RBCs are labelled with fluorescent probes (fluorescent SM analog BODIPY-SM or decoration of endogenous sphingomyelin and cholesterol by fluorescent Toxin* fragments, Lysenin* and Theta*, respectively) spread on poly-L-lysine-coated coverslips and observed upside-down in their living state by confocal imaging.

To next identify whether these two domains partially coexist, double-labeling of spread RBCs were performed using BODIPY-SM and Theta* to decorate endogenous chol (Carquin et al., 2015). This study showed that almost all the domains labelled by BODIPY-SM are also decorated by Theta* while only one third of the Theta-labelled domains contain BODIPY-SM. This suggested that at least two populations of lipid domains coexist at the RBC surface, those mainly enriched in SM and chol *vs* another mainly enriched in chol (see Fig 6A).

(ii) Control of submicrometric lipid domains

Besides double-labeling experiments which revealed only partial colocalization between chol- and SM-enriched domains (see above & Fig 6A), Carquin and coll. also explored whether the two lipid domain populations could be differentially controlled by specific lipid depletion as well as by modulation of temperature, membrane:cytoskeleton anchorage and membrane tension. This revealed that chol- and SM-domains (i) show a similar dependence to temperature increase, with a peak of domain abundance at 20°C and domain maintenance at 37°C although to a lower extent; (ii) are similarly increased upon membrane:cytoskeleton uncoupling at 4.1R complexes; and (iii) exhibit a reciprocal dependence as revealed by disappearance of domains upon specific lipid depletion. In contrast, these two domains show a differential response to increased membrane tension (Fig 6B).

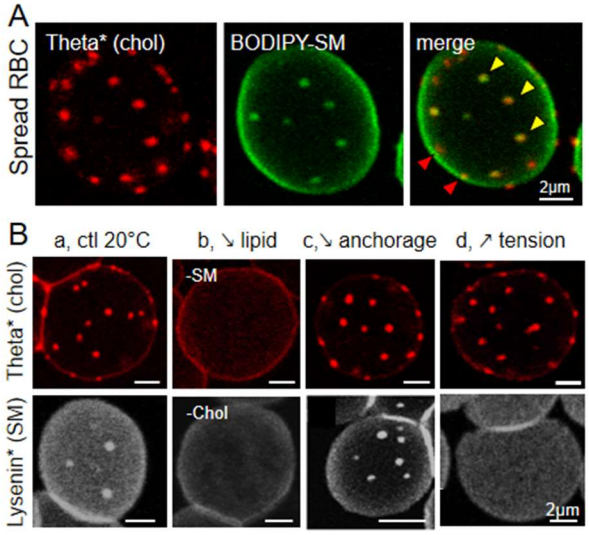

Figure 6. A. Spatial relation between chol- and SM-enriched submicrometric domains at the RBC plasma membrane. RBCs labelled by Theta* (endogenous cholesterol) then by exogenous BODIPY-SM. Two types of chol-enriched domains, enriched in either both cholesterol and SM (yellow arrowheads) or cholesterol mainly (red arrowheads), coexist. **B. Regulation of SM- and chol-enriched submicrometric domains.** (a) Control RBCs at 20°C. (b) Similar lipid domain abrogation upon specific lipid depletion. (c) Similar lipid domain increase upon acute uncoupling of membrane:cytoskeleton anchorage at 4.1R complexes (PKC activation). (d) Differential lipid domain modulation by increased tension (increased spreading on PLL-coated coverslips). Adapted from (Carquin et al., 2015, 2014).

Altogether, these data indicate the coexistence at the RBC outer PM leaflet of two types of domains, one enriched in SM/chol *vs* another enriched in chol. Whether these two types of domains could play a differential role in RBC shaping and reshaping is currently not known and has been explored in this Thesis.

2. Justification of tools and methods

To investigate whether and how lipid domains could contribute to RBC (re)shaping through their specific biophysical properties, we needed appropriate (i) methods and models to evaluate and modulate RBC biconcavity, deformation and vesiculation (section 2.1), and (ii) tools to visualize lipid domains (section 2.2) and monitor their biophysical properties (section 2.3).

2.1 Monitoring RBC (re)shaping

I describe in this Section the methods we used to observe RBC biconcave shape, induced deformation and vesiculation. Since lipid domain organization

(section 2.2) and biophysical properties (section 2.3) were investigated in these different RBC states, these systems must be compatible with vital imaging.

(i) Study of RBC biconcavity

To observe the RBC biconcave membrane, we used an observation system in which the RBCs are in suspension instead of spread onto poly-L-lysine. This "suspended" imaging system allows RBCs to lay down either on their flat side or their edges, and thus observation of RBCs in either upper or side view (Fig 7A). Side-viewed suspended RBCs allowed us to analyze membrane biconcavity. Membrane curvature was quantified by using the last version of the Shape Analysis by Fourier Descriptors computation plugging for ImageJ developed by Thomas Boudier. High and low curvature areas of the RBC biconcave membrane were defined respectively as the values above and below the average RBC biconcave membrane curvature (C_{mean} determined on several side-viewed suspended RBCs) (Fig 7 B).

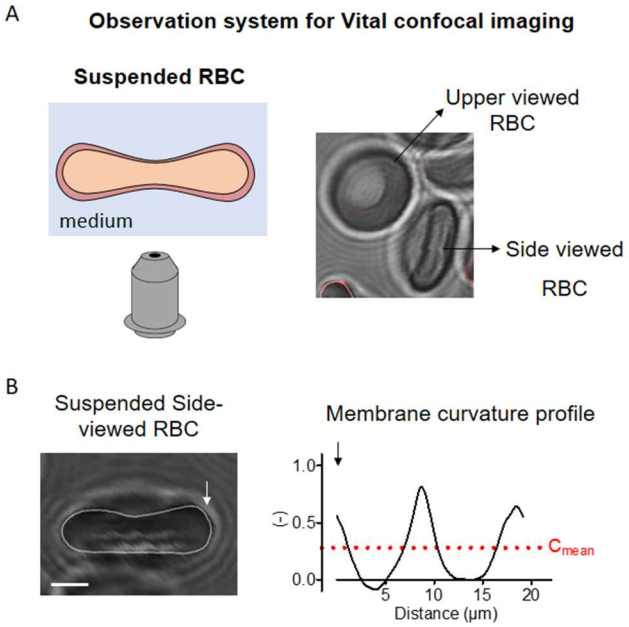

Figure 7. Imaging system to determine RBC biconcavity. RBCs are laid down in a microscopy chamber either on their flat side or their edges, allowing for observation in upper or side view. High and low curvature areas of the side-viewed suspended RBC biconcave membrane were defined respectively as the values above and below the average RBC biconcave membrane curvature (C_{mean}).

(ii) Study of RBC deformation

To measure changes in RBC deformability, we used the filtration method which examines the ability of a series of RBCs to pass through membrane

filters with defined pore diameters. The blood passes through holes in the membrane filter by using the force of gravity or by applying positive or negative pressure.

To then visualize the implication and the distribution of lipid domains upon RBC deformation, we analyzed two major parameters of RBC deformability: (i) membrane shape changes and (ii) volume modulation through Ca^{2+} exchanges.

To investigate RBC membrane shape changes, we analyzed (i) RBCs spread onto a PDMS chamber upon stretching (Fig 8A); and (ii) elliptocytes, as a model of affected RBC membrane shape. Hereditary elliptocytosis (HE, Fig 8B) is a clinically and genetically heterogeneous disorder, more common in malaria endemic regions. It is characterized by the presence of elliptically-shaped red cells on peripheral blood smear (Gallagher, 2004; Dhermy et al., 2007). Progressive transformation of RBC shape from discocyte to elliptocyte with time in the circulation is due to a mechanically unstable membrane resulting, in severe cases, to membrane fragmentation and reduced membrane surface area. Decreased membrane mechanical stability results from weakened horizontal linkages in membrane skeleton due defects in genes encoding for α-spectrin, β-spectrin or protein 4.1R (Mohandas and Gallagher, 2008). Shape changes generated in deformed RBC (elliptocyte or stretched healthy RBCs) were evaluated by determining changes in curvature as compared to healthy non deformed RBC. These changes were evaluated in the membrane edges of RBCs observed in upper view. Increased curvature areas created upon deformation were defined as the values being above the average maximum membrane curvature of healthy non deformed RBC. Decreased curvature areas created upon deformation were defined as the values being below the average minimum membrane curvature of healthy non deformed RBC.

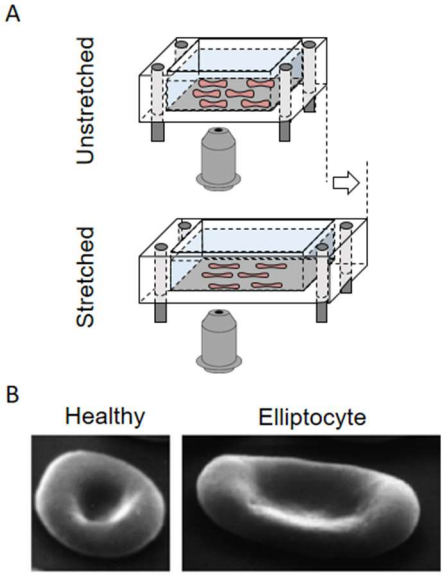

Figure 8. Investigation of RBC membrane shape changes. A. RBC stretching in PDMS chambers. RBCs spread on a PDMS chamber and then stretched to induce membrane deformation. **B Elliptocytes**, used as a model of affected RBC membrane shape.

RBC volume changes were evaluated by incubation in iso- to hypo-osmotic media (320 mOsm to 180 mOsm) and measurement of hemoglobin release. To study Ca^{2+} exchanges, RBCs were labelled with Fluo-4, a fluorescent indicator of intracellular Ca^{2+} concentration, and analyzed upon (i) spreading and stretching on a PDMS chamber, and (ii) incubation in either a Ca^{2+}-free medium supplemented with a Ca^{2+}-chelating agent (EGTA) or in a medium containing a Ca^{2+} ionophore (A23187), to stimulate Ca^{2+} exchanges.

(iii) Study of RBC vesiculation

Impairment of RBC elasticity and acceleration of the vesiculation process are observed upon RBC physiological aging, storage at 4°C and in RBC membrane fragility diseases, such as hereditary spherocytosis and elliptocytosis. A recent simulation study revealed that (i) vesicles released from spherocytotic and elliptocytotic RBC membranes are more diverse in size than those released from healthy RBCs; and (ii) vesicles released from the elliptocytotic, but not from the spherocytotic, membrane may contain fragments of the cytoskeleton (Li and Lykotrafitis, 2015). In this Thesis, we used spherocytes, elliptic RBCs and RBCs stored at 4°C to gain better insight in the potential implication of lipid domains in the RBC vesiculation process. To validate the use of stored RBCs at 4°C as an *in vitro* model to mimick RBC

aging, we asked whether they were positive for several *in vivo* aging markers such as external PM leaflet PS exposure or membrane surface loss.

RBCs from patients with hereditary spherocytosis were obtained from the Saint-Luc Hospital (UCL, Brussels) thanks to the great help and collaboration of Prof. Christiane Vermylen. Spherocytosis (HS) is a common inherited hemolytic anemia particularly common in Northern European countries. It is characterized by hemolysis with anemia, jaundice, splenomegaly, reticulocytosis and by the presence of spherocytes on peripheral blood smears (Eber and Lux, 2004; Gallagher and Ferriera, 1997). Change in RBC shape from discocytes to spherocytes results from a loss of membrane surface area that leads to impairment of deformability, spleen sequestration and removal from circulation. Mechanistically, membrane loss in HS results from decreased membrane cohesion due to reduced number of vertical linkages between the bilayer and skeleton due to defects in genes encoding for proteins of the ankyrin complex, such as band 3, ankyrin, protein 4.2 or spectrin (Mohandas and Gallagher, 2008). Accelerated RBC impaired functionality and viability upon storage at 4°C have been attributed to three interrelated mechanisms: altered metabolism, increased oxidative stress and membrane damage (Orlov and Karkouti, 2015).

2.2 Monitoring membrane lipid lateral heterogeneity

The constantly evolving view of lipid lateral heterogeneity has been influenced, in large part, by the development of new tools available for their investigation. Approaches based on detergent extraction, chol and sphingolipid depletion or model membranes made of simple lipid mixtures on one hand opened the debate about membrane lipid lateral distribution, and on the other hand exposed caveats, allowing only for indirect study of lipid domains. More recently, advances in the development of non-perturbing and specific labelling tools suitable for confocal microscopy allowed the visualization of lipid domains on diverse cell types, as described in the previous chapter.

The first suggestion for lateral heterogeneity of lipids and proteins in cell membrane was provided in the 70's from the observation of their **differential solubilisation by non-ionic detergents** under cold temperatures (Yu et al., 1973). Under such conditions, cellular membranes are separated into two fractions, detergent-soluble membranes and detergent-resistant membranes (DRMs). DRMs appeared to be specifically enriched in chol, sphingolipids, and glycosylphosphatidylinositol (GPI)-anchored proteins (Brown and Rose, 1992; Hanada et al., 1995; Schroeder et al., 1994). However, it quickly became clear that the protein composition of DRMs widely varies, depending on the choice of detergent, incubation temperature or detergent concentration (Schuck et al., 2003; Mayor and Maxfield, 1995). Therefore, although detergent extraction method opened the suggestion for lipid and protein lateral

heterogeneous distribution in membranes, it does not faithfully reflect the native composition and organization of membranes (Lichtenberg et al., 2005).

Besides the DRM approach, cell treatment with **specific compounds or enzymes impairing lipids** has been widely developed to investigate the potential physiological implication of lipid domains. Methyl-β-cyclodextrin (mβCD) is often used as a lipid domain-disrupting agent as it selectively and efficiently extracts chol from membranes (Mahammad and Parmryd, 2015). For example, removal of RBC PM chol by mβCD (15%) leads to the complete disappearance of chol-enriched domains (Fig 9A). However, it is important to consider that mβCD can also (i) increase membrane permeability to ions (Pottosin et al., 2007), (ii) be potentially cytotoxic (Mahammad et al., 2010) or (iii) preferentially deplete chol from Ld phases(Levental et al., 2016; Sanchez et al., 2011; Levental et al., 2009b). Drugs that target chol synthesis (*e.g.* statins (Hillyard et al., 2007)) or chol-modifying enzymes (*e.g.* chol oxidase(Ahn and Sampson, 2004)) could replace mβCD to disrupt rafts. However their specificity and effectiveness remain to be demonstrated. Sphingolipids are another central lipid in raft formation and various pharmacological treatments can interfere with their synthesis (*e.g.* fumonisin B1 (Merrill et al., 1993)) or stability (*e.g.* sphingomyelinase (Miller et al., 2015)). For example, sphingomyelinase has been used to remove RBC PM SM (15%), leading to the abrogation of SM-enriched domains (Fig 9B). However, it should be kept in mind that these treatments can affect the general sphingolipid metabolism and/or produce ceramides, which can in turn alter membrane properties in other ways.

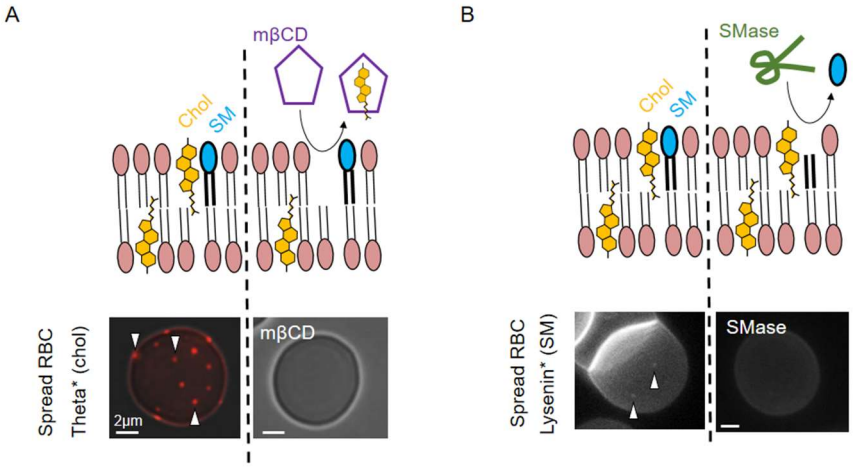

Figure 9. Pharmacological approaches used to induce the disappearance of cholesterol- and sphingomyelin-enriched domains. A. Removal of RBC plasma membrane cholesterol by mβCD leads to the complete disappearance of chol-enriched domains. **B. Removal of RBC plasma membrane sphingomyelin** induces the abrogation of SM-enriched domains. Adapted from (Carquin et al., 2015, 2014).

It is therefore more relevant **to directly visualize lipid domains** without any perturbation induced by the use of external compounds. However, non-perturbing, specific labelling of lipid domains in cells has been, and remains, one of the foremost challenges in the field. To ensure proper lipid domain visualisation, one has to work on living cells since fixation can lead to artefactual lipid redistribution. Vital imaging techniques such as high-resolution confocal or scanning probe microscopy are therefore recommended, instead of super-resolution or electron microscopy methods that generally require fixation. I will here describe the most validated probes compatible with confocal live cell imaging.

One of the simplest confocal live imaging approach is based on insertion of fluorescent probes in the PM. A few **intrinsically fluorescent lipid probes** are available, such as dehydroergosterol (DHE) who is structurally similar to chol. However, its poor photophysical characteristics have prevented its widespread application. As alternative are **fluorescent lipid analogs**. These are obtained by linking a fluorophore, mostly a small organic dyes such as 7-nitrobenz-2-oxa-1,3-diazol-4-yl (NBD) or 4,4-difluoro-5,7-dimethyl-4-bora-3a,4a-diaza-s-indacene (BODIPY), to the lipid fatty acyl chains or to its polar headgroup. For example, BODIPY-SM was used to target endogenous SM at the RBC PM, revealing submicrometric SM-enriched domains (Fig 10A). However, lipid analogues are structurally not equivalent to their endogenous counterpart. Moreover, although they are generally inserted at trace level in the plasma membrane, they can differentially partition in domains as compared to endogenous lipids (Wang and Silvius, 2000). This limitation can be minimized by the choice of a fluorophore which better preserves native phase partitioning, such as small and uncharged fluorophores like NBD or BODIPY (Sezgin et al., 2012b). Regarding fluorescent sterols, several probes are available (*e.g.* the 22- and 25-NBD-chol, BODIPY-chol analogues, fluorescent polyethyleneglycol (PEG) cholesteryl esters). However, to the best of our knowledge, none of these is currently satisfying.

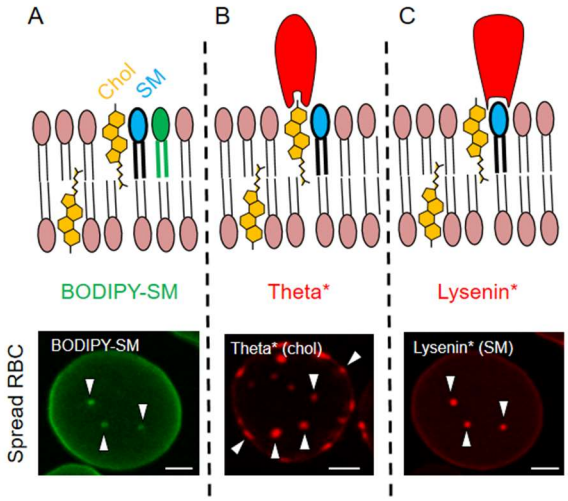

Figure 10. A. BODIPY-SM was used to target endogenous SM at the RBC PM, revealing submicrometric SM-enriched domains. **B.** To label membrane chol while avoiding cytotoxicity, truncated Theta limited to its C-terminal D4 domain (Theta-D4 or Theta*) has been fused with mCherry and allowed us to reveal chol-enriched domains at the RBC surface. **C.** Upon fusion with mCherry, Lysenin* was used to reveal SM-enriched domains at the RBC surface without toxicity. Adapted from(Carquin et al., 2015, 2014).

Since insertion of exogenous fluorescent lipids may not fully reflect endogenous lipid lateral heterogeneity, **labelling of endogenous lipids by intrinsically fluorescent small molecules** is generally preferred. Filipin, an intrinsically fluorescent molecule that forms a complex with chol and related sterols, has been widely used in the past. However, this molecule is quite toxic, precluding analyses on living cells. As alternative probes are **natural Toxins**. The most known are the chol-dependent cytolysins, the SM-specific toxins or the ganglioside GM1 and GM3-specific cholera toxin. The prototype of these Toxins is Cholera Toxin (secreted by the Gram-negative bacteria *Vibrio cholerae*), a multi-complex protein composed of two subunits: the toxic A subunit and the non-toxic pentameric B subunit (CTxB) which binds to GM1 ganglioside. Each monomer of the pentameric CTxB has one binding site, thus CTxB is able to bind up to five GM1. Theta Toxin (also named Perfringolysin O and produced by *Clostridium perfringens*) is one of the best-characterized chol-dependent cytolysins. Full Theta toxin is composed of four domains (D1-D4): D1 is the pore forming domain and D4 the minimal toxin fragment able to bind to chol with high affinity without causing lysis (Shimada et al., 2002; Waheed et al., 2001; Farrand et al., 2010; Nelson et al., 2008). To label membrane chol while avoiding cytotoxicity, truncated Theta limited to its C-terminal D4 domain (Theta-D4 or Theta*) has been fused with mCherry and

allowed us to reveal chol-enriched domains at the RBC surface without toxicity (Fig 10B) (Carquin et al., 2015). Lysenin (synthesized by the earthworm *Eisenia foetida*) is a pore forming toxin capable to bind to SM. Full Lysenin is composed of a pore forming domain in the N-terminus and the SM-binding site in the C-terminus, which is the minimal fragment responsible for specific SM binding without inducing oligomerization and pore formation (Ishitsuka et al., 2004; Ishitsuka and Kobayashi, 2004; Abe and Kobayashi, 2014; Kiyokawa et al., 2005; Kulma et al., 2010). As for Theta-D4 domain, non-Toxic Lysenin (NT-lysenin or Lysenin*) has been developed by keeping only the C-terminus domain of the full Lysenin to overcome limitations due to oligomerization and/or pore formation (Shogomori and Kobayashi, 2008; Skocaj et al., 2013; Abe and Kobayashi, 2014). Upon fusion with mCherry, Lysenin* was used to reveal SM-enriched domains at the RBC surface without toxicity (Fig 10C) (Carquin et al., 2014).

Despite absence of toxicity, Toxin fragments could nevertheless impair native membrane organization by inducing steric hindrance and/or clustering of their binding partner. Carquin and coll. recently demonstrated binding specificity of Lysenin* and Theta* using defined-composition liposomes, suggesting that steric hindrance of the probes does not prevent binding specificity (Carquin et al., 2014, 2015). In addition, double-labeling of the RBC PM shows that Lysenin* reveals the same lipid domains as insertion of BODIPY-SM (Fig 1a,b), whatever the order of labelling with the two probes, suggesting that Lysenin* does not trigger but rather reveals membrane organization (Carquin et al., 2014). The large probe size nevertheless affects lipid lateral diffusion, as evidenced by distinct fluorescence recovery after photobleaching (FRAP) of submicrometric domains at the RBC PM labeled by Lysenin* and BODIPY-SM (Carquin et al., 2014). A specific potential limitation of theta derivatives is that their binding to endogenous chol is triggered only upon a certain cholesterol concentration threshold (Ohno-Iwashita et al., 1992; Das et al., 2013). Lysenin binding depends on local distribution and density of SM (Ishitsuka and Kobayashi, 2004; Ishitsuka et al., 2004; Ohno-Iwashita et al., 2010). For more detail about fluorescent lipid probes advantages and drawbacks, please see (Carquin et al., 2016).

2.3 Monitoring membrane lipid fluidity and hydration

Lipid domain biophysical properties (*e.g.* lipid dynamics, hydration and order) are thought to be critical for the physiological functions of membranes. For example, it has been shown that the clustering of B cell receptors (BCRs) upon antigen binding induces the ordering of surrounding lipids, in turn helping BCR activation (Stone et al., 2017b). Therefore, monitoring lipid membrane biophysical properties, including fluidity and hydration, is essential to gain better insight in the mechanistic underlying lipid domain contribution to cellular function. Highly sensitive fluorescence techniques compatible with live cell imaging are available to study these biophysical properties. However,

when measured in cell membranes, lipid dynamics, hydration and order become less clearly defined and are often inter-related. Indeed, fluorescence anisotropy of diphenylhexatriene (DPH, Fig10) and trimethylammonium dihenylhexatriene (TMA-DPH, Fig10) respond to changes in both the microviscosity and order of the probe's surrounding environment; while the microviscosity alters the rate of probe movement, the order determines the range of possible motion. Furthermore, the degree of lipid packing can be quantified by polarity-sensitive membrane probes such as 6-lauryl-2-dimethylamino-napthalene (Laurdan, Fig10), as higher packing excludes polar water molecules from the otherwise nonpolar bilayer.

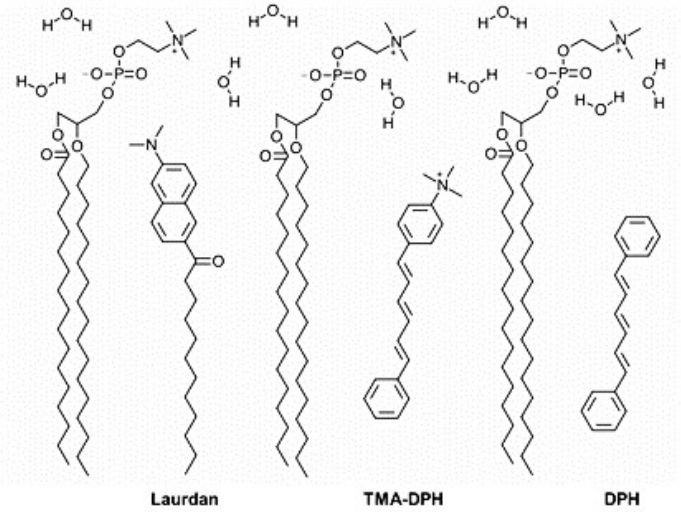

Figure 11. Fluorescent probes available to study lipid packing, membrane microviscosity and order. The degree of lipid packing can be quantified by polarity-sensitive membrane probes such as 6-lauryl-2-dimethylamino-napthalene (Laurdan). Fluorescence anisotropy of diphenylhexatriene (DPH) and trimethylammonium dihenylhexatriene (TMA-DPH) respond to changes in both the microviscosity and order of the probe's surrounding environment.

(i) Membrane fluidity

Membrane fluidity can be view as a combination of a dynamic (microviscosity) and static (structural order) components. Membrane fluidity can be approached by determining the rotational motion of fluorescent probes in the membrane. The probe movement is quantified by measuring the degree to which the probe fluorescence emission is depolarized following excitation by polarized light. The measured parameter is called the fluorescence anisotropy. The anisotropy (r) of the probe takes into account the ratio of the polarized components, *i.e.* the fluorescence intensity emitted by the probe and measured through an analyser placed parallelly (See I_{VV} in Fig 12) and perpendicularly to the excitation orientation (See I_{VH} in Fig 12). This ratio is

normalized to the total intensity emitted. Increased anisotropy therefore reflects a decrease in I_{VH}, meaning a decreased membrane fluidity leading to a decreased ability of the probe to rotate in the membrane and emit the light in another direction that the one it has been excited. Typical probes to study membrane fluidity are DPH and TMA-DPH (Barry R.Lentz, 1989).

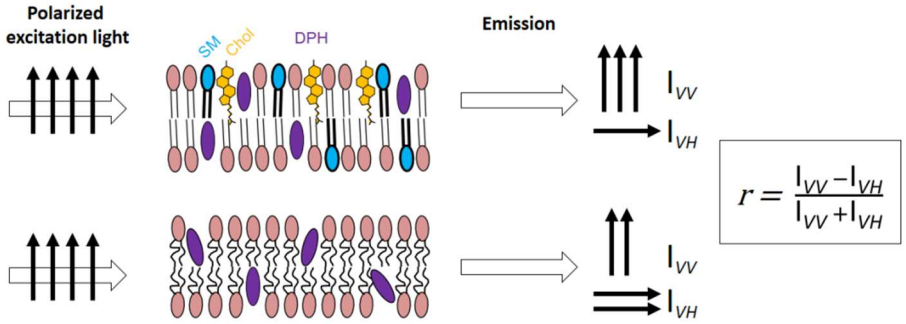

Figure 12. Determination of membrane fluidity by the use of DPH. The anisotropy (r) of the probe DPH takes into account the ratio of the polarized components, *i.e.* the fluorescence intensity emitted by the probe and measured through an analyser placed in parallel (I_{VV}) and perpendicularly to the excitation orientation (I_{VH}). This ratio is normalized to the total intensity emitted.

(ii) Membrane hydration

Membrane hydration, a parameter closely related to membrane fluidity and lipid phases is usually addressed by using fluorescent probes that expose shift in emission wavelength based on the polarity of their environments (Stott et al., 2008). Most polarity-sensitive probes exhibit an increase in charge separation when excited in polar solvents, resulting in larger dipole moment. It therefore exhibits more than one excited state: a locally excited state intrinsic to the fluorophore and an internal charge transfer (ITC) state created by the larger dipole moment. These transitions from locally excited state states in nonpolar solvents to ITC states in polar solvents shift the probe emission maxima. One of the most commonly used polarity-sensitive membrane probe is Laurdan. Laurdan exposes an emission spectra shift upon increasing environment polarity; from green wavelengths with an emission maximum centered at 490 nm to the blue wavelengths centered at 440 nm (Fig 13). Generalized Polarisation (GP) ratiometric analysis from the emission intensity at these two wavelengths can therefore be used to measure change in membrane polarity/hydration (Fig 13, where I_{440} and I_{490} are the fluorescence intensities at those wavelengths). Probing the degree of lipid packing provides an opportunity to visualize membrane domains and Laurdan has been intensively used to study/visualize higher-order lipid domains in model membranes and living cells.

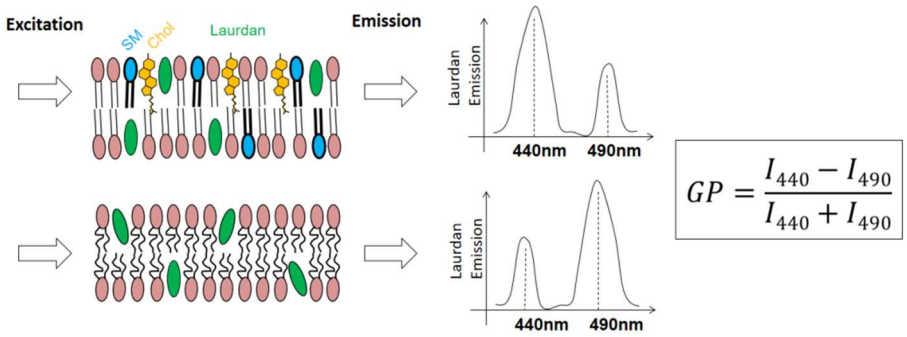

Figure 13. Determination of lipid order and membrane hydration by the use of Laurdan. Laurdan exposes an emission spectra shift upon increasing environment polarity; from green wavelengths with an emission maximum centered at 490 nm to blue wavelengths centered at 440 nm. Generalized Polarisation (GP) ratiometric analysis from the emission intensity at these two wavelengths can therefore be used to measure changes in membrane polarity/hydration (where I_{440} and I_{490} are the fluorescence intensities at those wavelengths).

3. Aims and strategy of the study

Altogether, **the RBC appears as a model of choice** to explore the importance of lipid domains in cell (re)shaping for the following reasons: (i) it is simple and well-characterized, (ii) it is subjected to deformation and vesiculation, (iii) it exhibits loss of deformation in membrane fragility diseases and upon physiological senescence, (iv) it has a flat featureless membrane facilitating the study of lipid lateral heterogeneities, and (v) it exhibits two types of domains, mainly enriched in chol or chol/SM. To **examine RBC deformation,** we used: (i) elliptocytes and deformed healthy RBCs in stretchable chambers compatible with fluorescent microscopy, to analyze lipid domains upon RBC deformation, and (ii) RBC filtration across filters with pores of controlled diameters, to quantify the abundance of deformable *vs* less deformable RBCs. To **analyze RBC vesiculation**, we used: (i) aged RBCs, obtained by incubation at 4°C during 2 weeks to accelerate the aging process, and (ii) spherocytes, as a model of less deformable RBCs. To **visualize lipid domains**, the fluorescent SM analog, BODIPY-SM, was inserted at trace level in the PM and fluorescent Toxin* fragments, Theta* and Lysenin*, were used to decorate endogenous chol and SM respectively (Carquin et al., 2014b, 2015b). These probes were selected based on their (i) previous extensive validation to study membrane lipid lateral heterogeneity (Carquin et al., 2014b, 2015b), (ii) compatibility with live confocal imaging (*i.e.* in the absence of fixation), (iii) ability to reveal lipid submicrometric domains at the RBC PM. To **investigate membrane lipid order**, RBCs were labelled with Laurdan, a well-validated fluorescent probe whose emission wavelength depends on its lipid order environment (Owen et al., 2011). Like BODIPY-

SM and Toxin* fragments, Laurdan is suitable for living imaging. Moreover, it can be combined with the Toxins* due to their distinct emission wavelength.

The first aim of my thesis was to investigate **whether and how the chol- and SM-enriched domains coexisting at the RBC PM contribute to RBC (re)shaping**. To this end, RBCs labelled with Theta* and Lysenin* were observed at resting state and upon reshaping. At resting state, chol- and SM-enriched domains were associated to distinct curvature areas of the RBC biconcave membrane, yet did not participate to the maintenance of this specific shape. Upon reshaping, chol-enriched domains gathered in increased curvature areas during deformation, while SM-enriched domains increased in abundance along with calcium efflux during shape and volume restoration. Upon RBC storage at 4 °C to mimic physiological aging, lipid domains appeared as specific vesiculation sites. Altogether, our data indicate that the two populations of lipid domains differentially contribute to RBC (re)shaping. This chapter was published in *Scientific Report* as an original research article entitled: "Contribution of plasma membrane lipid domains to red blood cell (re)shaping" **(Chapter 3.).**

The second aim of my thesis was to examine **whether the lipid domains and their surrounding membrane exhibit a differential lipid order that contributes to RBC (re)shaping or is modulated during this process.** To this end, RBCs were labelled with Laurdan and observed at resting state and upon (re)shaping, as above. We used the fluorescent hydration- and membrane packing-sensitive probe Laurdan to determine the Generalized Polarization (GP) values of lipid domains *vs* the surrounding membrane. We observed three domain populations differently enriched in cholesterol and sphingomyelin and exhibiting a diversity of lipid order states. Although all lipid domains were less ordered than the surrounding lipids in erythrocytes at resting state, they became more ordered than the bulk upon erythrocyte deformation (elliptocytes and stimulation of calcium exchanges) or membrane vesiculation (storage at 4°C). Upon aging and in membrane fragility diseases (spherocytosis), an increase in the difference of lipid order between domains and the surrounding lipids contributed to the initiation of domain vesiculation. The critical role of domain-bulk differential lipid order modulation for erythrocyte reshaping are discussed in relation with the pressure exerted by the cytoskeleton on the membrane. This chapter will be submitted very soon as an original research article **(Chapter 4.)**.

During my thesis, I also investigated the **mechanism of action of the saponin α-Hederin** on apoptosis of two cancerous cell lines, **through its interaction with membrane chol and its impact on membrane lipid order**. Our results indicate that lipid domains could be targeted by pharmacological components, opening the way for new types of treatments based on membrane biophysical properties. This paper was published as an original research article in *Planta Medica* **(Appendix)**.

In **Chapter 5**, after evaluation of the experimental strategy used, I summarize the major results reported in this Thesis and discuss them in the broader context of lipid domain biogenesis and diversity, modulation upon physiological changes and resulting functionality. I also discuss energetic considerations underlying lipid domain biogenesis, modulation and functionality. Based on these considerations, I propose a model for the implication of lipid domains in RBC reshaping in collaboration with the cytoskeleton and membrane proteins.

CHAPITRE 3

Contribution of plasma membrane lipid domains to red blood cell (re)shaping

Abstract

Although lipid domains have been evidenced in several living cell plasma membranes, their roles remain largely unclear. We here investigated whether they could contribute to function-associated cell (re)shaping. To address this question, we used erythrocytes as cellular model since they (i) exhibit a specific biconcave shape, allowing for reversible deformation in blood circulation, which is lost by membrane vesiculation upon aging; and (ii) display at their outer plasma membrane leaflet two types of submicrometric domains differently enriched in cholesterol and sphingomyelin. We here reveal the specific association of cholesterol- and sphingomyelin-enriched domains with distinct curvature areas of the erythrocyte biconcave membrane. Upon erythrocyte deformation, cholesterol-enriched domains gathered in high curvature areas. In contrast, sphingomyelin-enriched domains increased in abundance upon calcium efflux during shape restoration. Upon erythrocyte storage at 4°C (to mimick aging), lipid domains appeared as specific vesiculation sites. Our data indicate that lipid domains could contribute to erythrocyte function-associated (re)shaping.

1. Introduction

The acknowledgment of lipid heterogeneous lateral distribution in plasma membrane (PM) has changed our perception of their role, from simple cellular compartmentation structures to active participants in cellular functions (Pike, 2006). In the 90's, Simons and collaborators proposed that cholesterol (chol) and sphingolipids (SLs) can cluster into nanometric (10-200 nm), unstable (sec) assemblies, called the lipid rafts (Simons and Ikonen, 1997). From that time forward, the implication of lipid rafts in membrane sorting (Lingwood and Simons, 2010), signal transduction (Simons and Toomre, 2000) and membrane trafficking (Ikonen, 2001) has been highly discussed, but spatial and temporal features of such domains make direct demonstrations challenging to provide. Besides rafts, direct lines of evidence for larger (submicrometric) and more stable (min) domains, enriched or not in chol and SLs, were first reported in artificial membranes (Kahya et al., 2003; Bernardino de la Serna et al., 2004; Baumgart et al., 2007) then in fixed cells (Frisz et al., 2013b; Mizuno et al., 2011; Kiyokawa et al., 2005) and more recently in living cells, including red blood cells (RBCs) (Carquin et al., 2015; Sanchez et al., 2012; D'Auria et al., 2013b; Carquin et al., 2014; Tyteca et al., 2010).

RBC is the most simple and best characterized human cell, whose only structural components are a PM linked to an underlying cytoskeleton. Furthermore, RBC featureless membrane and absence of lipid trafficking facilitate the investigation of PM lateral heterogeneity. During the past years, we examined the organization of abundant lipids of the RBC outer PM leaflet, sphingomyelin (SM) and chol, by confocal vital imaging of RBCs spread onto poly-L-lysine (PLL)-coated coverslips (Carquin et al., 2015; Sanchez et al., 2012; D'Auria et al., 2013b; Carquin et al., 2014; Tyteca et al., 2010). We first inserted at the RBC surface BODIPY analogs of SM. Whereas this approach allowed us to evidence submicrometric domains (Supplementary Fig. 1Aa), it nevertheless presents the limitation that PM-inserted probes can differentially partition as compared to endogenous lipids, depending on membrane lipid composition and on the fluorophore (Sezgin et al., 2012b). Thus, to further explore relevance of fluorescent domains for endogenous lipids, we used mCherry-non-toxic parts of Toxins, *i.e.* the minimal fragment of the Lysenin Toxin responsible for specific SM binding (Kiyokawa et al., 2005) and the D4 Theta domain as the minimal Toxin fragment able to bind to chol with high affinity without causing lysis (Shimada et al., 2002). We verified that both Toxin fragments (hereafter referred as Lysenin* & Theta*) are specific, non-toxic, sensitive and quantitative probes of SM and chol accessible at the outer PM leaflet of living RBCs (Carquin et al., 2015), (Carquin et al., 2014). We then provided evidence for SM- and chol-enriched domains similar to those observed upon trace insertion of BODIPY-SM (Supplementary Fig. 1Ab,c).

Importantly, BODIPY-SM and Lysenin* perfectly colocalize (Supplementary Fig. 1Ba). SM- and chol-enriched domains (i) exhibit a peak of abundance at 20°C and are maintained at 37°C, although to a lower extent; (ii) are similarly increased upon membrane:cytoskeleton uncoupling at 4.1R complexes (Supplementary Fig. 1Cc,g); and (iii) show a reciprocal dependence as revealed by disappearance of domains upon specific lipid depletion (Supplementary Fig. 1Cb,f). In contrast, domains exhibit a differential response to increased membrane tension (Supplementary Fig. 1Cd,h) and are only partially spatially colocalized (Supplementary Fig. 1Bb). Altogether, these data indicate the coexistence of two types of domains, one enriched in SM/chol *vs* another enriched in chol mainly. However, despite evidence for PM submicrometric lipid domains, their specific functions remain largely unknown (Carquin et al., 2016).

PMs have evolved in a wide range of function-associated shapes and the mechanisms underlying membrane complex architecture shaping and remodelling in relation with cellular functions generate broad interest (McMahon and Boucrot, 2015; Zimmerberg and Kozlov, 2006). The RBC is one typical example of cells exhibiting specific (re)shaping in relation to their functions. Indeed, RBC exhibits a specific biconcave shape in circulation, which results in high area-to-volume ratio and leads to a ~40% surface excess as compared to a sphere of the same volume. This specific shape both ensures fast oxygen and carbon dioxide exchanges between the RBC interior and its environment but also decreases the forces that have to be applied to deform the membrane as compared to a spherical shape (Canham, 1970). Such deformability is required when RBC passes through the microvasculature to deliver oxygen to the tissues, and is further tested for quality control when it squeezes through the very narrow pores of the spleen sinusoids. At the end of its 120-day lifetime, biconcavity and deformability are lost due to local membrane vesiculation, leading to RBC splenic entrapment and removal from blood circulation (Mohandas and Gallagher, 2008). Whether and how submicrometric lipid domains contribute to RBC (re)shaping is currently not known. Maintenance of the specific RBC biconcave shape (Park et al., 2010), global membrane shape changes upon deformation (Kabaso et al., 2010) and local membrane vesiculation upon aging (Bosman et al., 2008) are generally attributed to the dynamic, strongly membrane-anchored cytoskeleton. RBC (re)shaping also implies tight volume regulation by ion exchanges. For instance, following RBC membrane mechanical stress, intracellular calcium (Ca^{2+}) concentration transiently increases, followed by the secondary activation of the Gardos channel leading to transient volume decrease (Dyrda et al., 2010; Bogdanova et al., 2013)·(Cahalan et al., 2015).

We here took benefit from the RBC wide range of function-related (re)shaping processes to investigate the potential role of submicrometric lipid domains in cell shape control. To this end, we probed by vital imaging the lateral

distribution of chol and SM (using either specific Toxin fragments or trace insertion of BODIPY-SM as previously (Carquin et al., 2015, 2014)) in relation with: (i) membrane biconcavity of resting RBC; (ii) membrane curvature changes and Ca^{2+} exchanges upon mechanical stretching of healthy RBCs or in elliptocytes, a RBC model of impaired shape (Mohandas and Gallagher, 2008); and (iii) membrane vesiculation upon RBC aging. Our results revealed that, although they were not essential to the maintenance of RBC biconcavity, chol- and SM-enriched domains specifically associated with high and low curvature areas of the biconcave RBC membrane. Upon reshaping, chol-enriched domains gathered in areas of increased curvature, as revealed in elliptocytes and healthy RBC stretching experiments. In contrast, SM-enriched domains increased in abundance along with Ca^{2+} efflux during subsequent shape and volume restoration. Finally, both domains were identified as preferential sites for membrane vesiculation. Our results revealed the contribution of lipid domains to erythrocyte function-associated (re)shaping.

2. Results

2.1 Distinct topological distribution of chol- and SM-enriched domains in both spread and suspended RBCs

We first analyzed lipid domain distribution on Theta* (*red*) or Lysenin* (*grey*)-labeled RBCs spread onto poly-L-lysine (PLL)-coated coverslips. We observed that the submicrometric domains respectively enriched in chol or SM were not randomly distributed (Fig. 1a, *spread upper view*); while chol-enriched domains were associated with both the center of the RBC membrane (*yellow arrowheads*) and the edges (*green arrowheads*), those enriched in SM were restricted to the center of the membrane (quantification at Fig. 1b, *spread*). Although RBC spreading is an easy system for lipid domain imaging (preventing RBC from moving during image acquisition and allowing to analyze the major domain population in one image due to RBC flattening), it was nevertheless crucial to ask about the influence of RBC spreading on intrinsic lipid domain topography.

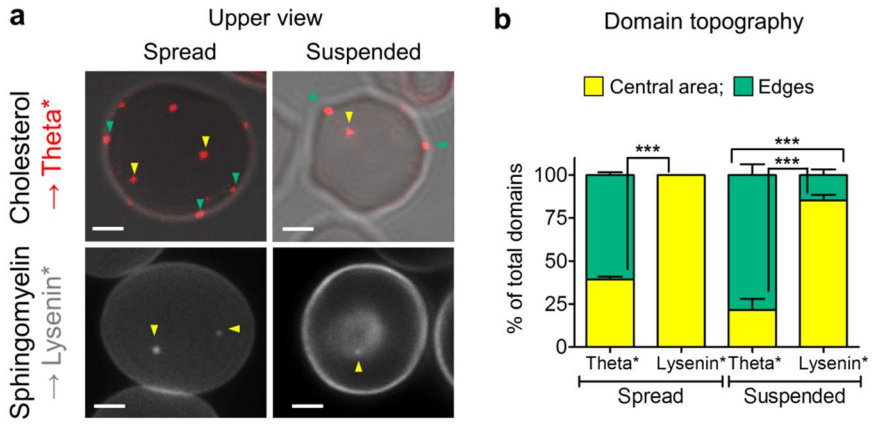

Figure 1. Distinct topological distribution of chol- and SM-enriched domains in both spread and suspended RBCs. Fresh healthy RBCs were labelled in suspension with Theta* *(red; chol)* or Lysenin* *(grey; SM)*, washed and then either spread onto poly-L-lysine (PLL)-coated coverslips *(spread)* or left in suspension *(suspended)* and directly visualized by vital confocal/fluorescence microscopy. (**a**) Representative imaging. *Yellow* and *green arrowheads* point to the central area and the edges of the RBC membrane, respectively. Representative of 3 experiments, *scale bars* 2 µm. (**b**) Quantification of domain association (number by hemi-RBC expressed as percentage of total domains) with the central area (*yellow*) and the edges (*green*) of the RBC membrane. Results are means ± SEM of 40-150 RBCs from three independent experiments. Statistical significance was tested with two-sample t-tests.

Therefore, we used an alternative imaging system in which RBCs were laid down in medium, giving rise to suspended, non-spread, RBCs (Fig. 1a, *suspended vs spread*). Suspended RBCs exposed similar domain abundance as compared to spread RBCs, as revealed by full projection (compare Supplementary Fig. 2a with Fig. 1a, *spread*). Importantly, the respective preferential association of chol- and SM-enriched domains with the edges (*green arrowheads*) and the center (*yellow arrowheads*) of the PM was confirmed in this observation system, despite the slightly higher proportion of both chol- and SM-enriched domains associated with the edges (Fig. 1a; quantification at Fig. 1b, *suspended*). We thus concluded to the preferential association of chol- and SM-enriched domains with the edges and the center of RBC membrane, respectively, as revealed in both spread and suspended systems.

2.2 Specific association of chol- and SM-enriched domains with high and low curvature areas of the biconcave RBC membrane, respectively

The distinct topological distribution of chol- and SM-enriched domains raised the hypothesis of their association with different membrane curvature areas, a

feature obviously distinguishing RBC membrane center and edges and resulting from its singular biconcave shape. To investigate this question we turned to RBC observation in side view. We first explored by scanning electron microscopy (SEM) the membrane curvature of spread RBCs in side view (Fig. 2a, *spread*) and calculated on a series of membrane curvature profiles the average membrane curvature value (Fig. 2a and b, C_{mean}). This value was defined as the threshold between low and high membrane curvature areas in side viewed spread RBCs. Using this value, we confirmed on side-viewed membrane curvature profiles that the edges were associated to high curvature areas (> C_{mean}, referred as *HC* in figures), while the center corresponded to low curvature area (< C_{mean}, referred as *LC* in figures). To further evaluate the impact of RBC spreading on side-viewed membrane curvature, we applied the same approach on suspended RBCs using vital confocal imaging. Indeed, this system allows RBCs to lay down either on their flat side or their edges, and thus observation in either upper or side view (Fig. 2a and b, *suspended*). The calculated threshold value and curvature profiles were very close to those of spread RBCs, suggesting that, in our hands, RBC spreading did not significantly impact biconcavity. Furthermore, like in spread RBCs, the edges were associated to high curvature areas (> C_{mean}), while the center of the RBC membrane corresponded to low curvature area (< C_{mean}).

To next examine whether chol- and SM-enriched domains could associate with distinct membrane curvature areas, we compared membrane curvature profiles with Theta* or Lysenin* intensity profiles on suspended RBCs observed in side view by vital imaging. Chol- and SM-enriched domains respectively associated with high (> C_{mean}) and low (< C_{mean}) curvature areas, as revealed by profile analysis (Fig. 2c and gallery of profiles in Supplementary Figs. 3 and 4), and exposed average curvature values respectively higher and lower than the one of the bulk membrane (membrane without domains) and C_{mean} (Fig. 2d). Furthermore, we asked if these domains were not only associated to, but also involved in, RBC specific biconcave curvature. We therefore abrogated both chol- and SM-enriched domains by treatment with methyl-ß-cyclodextrin (mßCD) as previously (Carquin et al., 2014, 2015), but did not observe any impact on RBC biconcavity (Supplementary Fig. 5).

Our results thus suggested that, while chol- and SM- enriched domains were associated to distinct membrane curvature areas of the biconcave RBC, they were not involved in the maintenance of this specific shape.

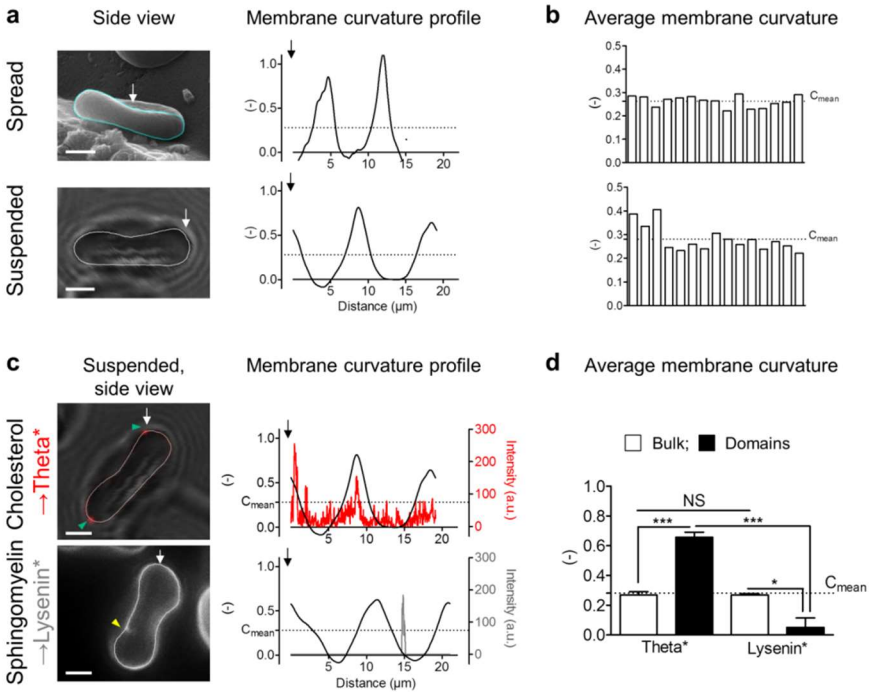

Figure 2. Specific association of chol- and SM-enriched domains with high and low curvature areas of the RBC biconcave membrane, respectively. Fresh healthy RBCs were labelled or not (a,b) as in Fig.1 (c,d), then either spread onto PLL-coated coverslips *(spread)* and observed by scanning electron microscopy (SEM), or left in suspension *(suspended)* and visualized by vital confocal/fluorescence microscopy. (**a**) Representative imaging of side viewed unlabelled RBCs *(left panels)* and membrane curvature profiles along paths indicated at *left* by *cyan or withe curved lines* (*right panels)*. Profiles are going counterclockwise from starting points indicated by *white arrows*. Representative of three independent experiments, s*cale bars* 2 µm. (**b**) Quantification of average side viewed membrane curvature. *Dashed lines* represent the average membrane curvature of 15 side viewed RBCs (0.26 for *spread* and 0.28 for *suspended RBCs*). (**c**) Representative imaging (*left panels, yellow* and *green arrowheads* point to the central area and the edges of the RBC membrane, respectively*)* and profiles comparing Theta* or Lysenin* intensity (*red* or *grey*) and membrane curvature (*black*; *right panels)*. Profiles along paths indicated in *left panel* by *white curved lines* on side viewed suspended RBCs (counterclockwise from starting point indicated by *white arrows*). *Dashed lines* represent the average membrane curvature calculated in (b). Representative imaging and profiles of three independent experiments, s*cale bars* 2 µm. (**d**) Quantification of average curvature values for bulk membrane (membrane without domains, *open bars*) and Theta*- or Lysenin*-enriched domains (*filled bars*), calculated on profiles from side viewed suspended RBCs. *Dashed lines* represent the average curvature value calculated in (b). Results are means ± SEM of 4-10 RBCs from three independent experiments. Statistical significance was tested with one-way ANOVA followed by Tukey's post-hoc test.

2.3 Preferential association of chol-enriched domains with increased curvature areas in the rim of elliptocytes

The different association of chol- and SM-enriched domains with distinct membrane curvature areas raised the question of their implication in membrane curvature changes required for RBC reshaping. As a model of affected membrane curvature, we used RBCs from a patient suffering from elliptocytosis, a genetic disease resulting from impaired RBC cytoskeleton and leading to RBC shape changes (Gallagher, 2005). Regarding membrane curvature, suspended elliptocytes exhibited no changes in side-viewed biconcave membrane (compare Supplementary Fig. 6a with Fig. 2c) but affected upper-viewed membrane edges/rim as compared to healthy RBCs (compare Supplementary Fig. 6b with Fig. 1a, right panel). To quantify these changes in elliptocyte rim, we therefore analysed membrane curvature of RBCs in upper view. We determined membrane curvature profiles on a series of upper-viewed healthy RBC membranes (Fig. 3a), and calculated the average minimum (Fig. 3b, HC_{min}) and maximum curvatures (HC_{max}) as threshold values to determine decreased *(*$< HC_{min}$) and increased *(*$> HC_{max}$) curvature areas in the rim of elliptocytes *vs* discoid healthy RBCs (Fig. 3c). Change in curvature associated with elliptocytosis was confirmed by the wider distribution of membrane curvature values in elliptocytes *vs* healthy RBCs (Fig. 3d).

We then used the HC_{max} value to explore whether membrane curvature increase was associated to changes in lipid domain distribution in the rim of elliptocytes *vs* healthy RBCs. Profile analyses (Fig. 3c) and resulting average membrane curvature values (Fig. 3e) indicated that chol-enriched domains were associated with increased curvature areas *(*$> HC_{max}$) of the elliptocyte rim. In contrast, no impact was observed on SM-enriched domain topography, still restricted to the center, and no specific SM enrichment was observed in areas of increased curvature of the rim (Supplementary Fig. 7). Thus, chol-, but not SM-, enriched domains specifically associated with increased curvature areas generated in the rim of elliptocytes.

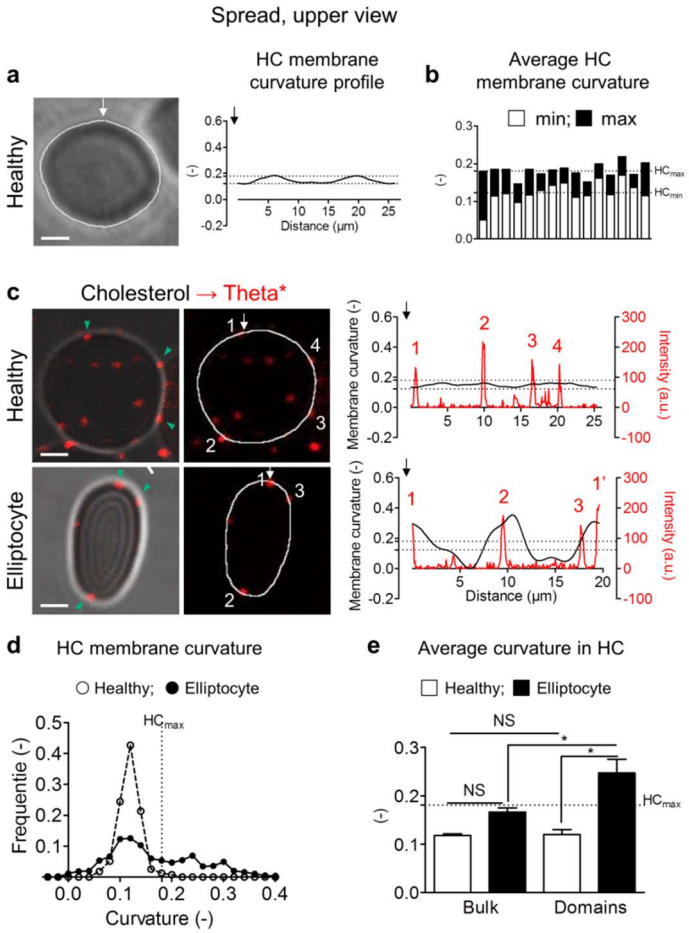

Figure 3. Preferential association of chol-enriched domains with increased curvature areas in the rim of elliptocytes. Fresh healthy and elliptocytotic RBCs were labelled (c-e) or not (a,b) with Theta*, spread and observed in upper view as in Fig. 1. (**a**) Representative phase contrast (*left panel)* and membrane curvature profile along path indicated in *left panel* by *white curved line* (*right panel)*. Profile is going counterclockwise from starting point indicated by *white arrow*. Representative of three independent experiments, s*cale bar* 2 µm. (**b**) Quantification of minimum and maximum membrane curvature values. *Dashed lines* represent the average minimum and maximum curvature values of 15 side viewed RBCs (0.12 for HC_{min} and 0.18 for HC_{max}). (**c**) Representative vital confocal imaging of Theta*-labelled RBCs (*left & central panels; green arrowheads* indicate domains in HC membrane areas) and relation between Theta* intensity (*red*) and membrane curvature (*black*) on profiles along paths indicated *in central panel* by *white curved lines* starting by *white arrows (right panel)*. Domains (*red numbers*) are labelled with *white numbers* in *central panel; dashed lines* represent HC_{min} and HC_{max} calculated in (b). Representative of four independent experiments, s*cale bars* 2 µm. (**d**,**e**) Quantification of curvature value distribution of HC membrane (**d**) and average curvature values of HC bulk and

domains (**e**) calculated on profiles of healthy RBCs (*open symbols and bars*) and elliptocytes (*black symbols and bars)*. Results are means ± SEM of 4-10 RBCs from two independent experiments. Statistical significance was tested with one-way ANOVA followed by Tukey's post-hoc test.

2.4 Specific recruitment of chol-enriched domains in increased curvature areas of the RBC rim upon stretching

As chol-enriched domains specifically associated with increased curvature areas created in the rim of elliptocytes, we asked whether these domains could participate in membrane curvature changes during RBC deformation by stretching. To do so, Theta*-labeled healthy RBCs were spread onto PLL-coated polydimethylsiloxane (PDMS) chambers and observed in their resting state (Fig. 4a, *unstretched*) or upon stretching (*stretched*). RBC stretching induced visible changes in membrane curvature of upper-viewed RBCs (Fig. 4b; quantification in Fig. 4c) and an increased association of chol-enriched domains with the cell edges (*green arrowheads* at Fig. 4b; quantification in Fig. 4d). Total occupation of the RBC surface by chol-enriched domains (Fig. 4e) and associated total Theta* intensity (Supplementary Fig. 8) were not modified upon stretching. This could indicate that domains were neither formed nor lost during stretching, suggesting that chol-enriched domain topographic changes are related to domain rearrangement. Furthermore, chol-enriched domains specifically gathered in areas of increased curvature of the membrane rim (white dashed boxes at Fig. 4b, $> HC_{max}$), which was confirmed by the increased average curvature of chol-enriched domains after stretching, above the bulk average curvature and HC_{max} (Fig. 4f & gallery of profiles in Supplementary Fig. 9). In contrast, no recruitment of SM-enriched domains in areas of modified curvature was observed (data not shown). Altogether, these results indicated the specific recruitment of chol-, but not SM-, enriched domains in areas of increased curvature of the membrane rim upon RBC deformation.

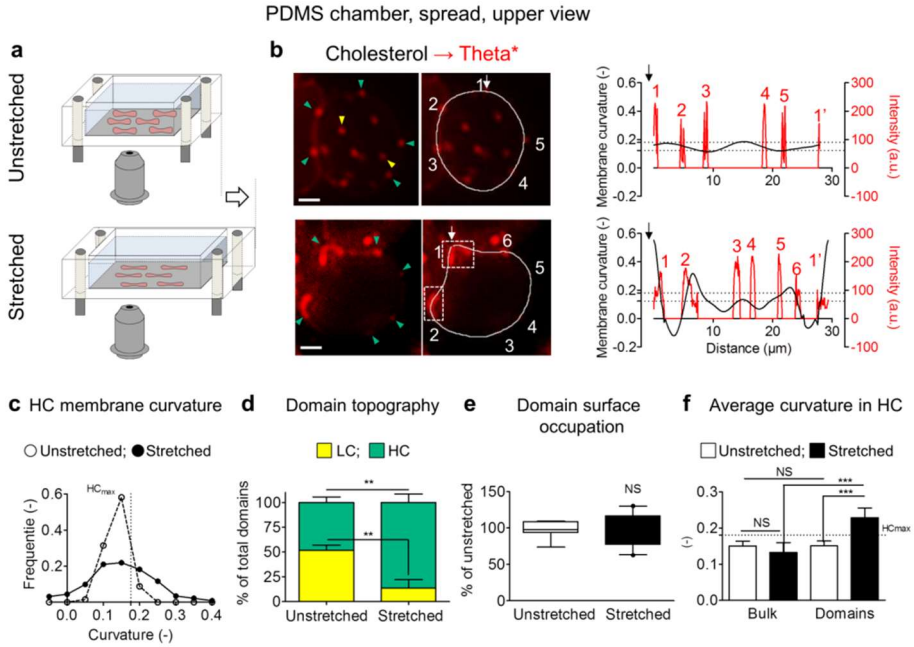

Figure 4. Recruitment of chol-enriched domains in increased curvature areas of the RBC rims upon stretching. Fresh healthy RBCs were labelled with Theta*, washed and spread onto PLL-coated polydimethylsiloxane (PDMS) chamber and directly visualized by vital fluorescence microscopy before (*unstretched*) and after stretching (*stretched*). (**a**) Schematic representation of the stretching system. (**b**) Representative imaging (*left & central panels*) and comparison of Theta* intensity (*red*) and membrane curvature (*black*) profiles (*right panel*). Y*ellow* and *green arrowheads* indicate LC and HC membrane areas, respectively. Profiles are done along paths indicated *in central panel* by *white curved lines* starting by *white arrows*; domains (*red numbers*) are labelled with *white numbers* in *central panel*; *dashed lines* represent HC_{min} and HC_{max}. Theta* domains associated with increased curvature (> HC_{max}) are boxed in *central panel*. Representative of two independent experiments, s*cale bars* 2 µm. (**c**) Quantification of curvature value distribution of HC membrane calculated on profiles of unstretched (*open symbols)* and stretched RBCs (*black symbols*). (**d**,**e**) Quantification of domain topography (d; number by hemi-RBC, expressed as percentage of total domains) and surface occupation (e; total domain area by hemi-RBC area, expressed as percentage of unstretched). (**f**) Quantification of average curvature values of HC bulk membrane and domains. Results are means ± SEM of 13-18 RBCs from two independent experiments. Statistical significance was tested with two-sample t-tests, except one-way ANOVA followed by Tukey's post-hoc test in f.

2.5 Loss of high curvature areas in elliptocytes and impairment of healthy RBC deformability upon chol-enriched domain abrogation

The next question was thus to ask whether chol-enriched domain abrogation could affect membrane curvature and RBC deformability. To investigate the importance of chol-enriched domains for membrane curvature changes, healthy RBCs and elliptocytes were treated as previously (Carquin et al., 2015, 2014) with mßCD to deplete chol and abrogate chol-enriched domains, as revealed by the suppression of Theta* labeling (Fig. 5a). This treatment decreased elliptocytotic, but not healthy, membrane curvature rim, without any detectable impact on the RBC perimeter (Fig. 5b).

To evaluate whether chol-enriched domains are involved in RBC deformability, we compared the consequences of combined chol- and SM-enriched domain depletion *vs* specific chol-enriched domain abrogation on RBC deformability tested upon RBC squeezing across tiny pores by filtration. To abrogate both chol- and SM-enriched domains, RBCs were treated with mßCD (Fig. 5c, *-Chol & -SM domains;* Supplementary Fig. 10A & B, central panels). To specifically deplete chol-enriched domains, we used mßCD followed by chol repletion (*mβCD →+Chol)*. This treatment allows to (i) fully replete membrane chol (Supplementary Fig. 10A, right panel); (ii) fully restore SM-enriched domains, as revealed by both Lysenin* and BODIPY-SM labelling (Fig. 5c, *-Chol domains;* Supplementary Fig. 10Bf,i, yellow arrowheads); and (iii) reform only a small part of chol-enriched domains, *i.e.* those that are localized in the center of the RBC (Supplementary Fig. 10Bc, yellow arrowheads) and co-enriched in chol and SM (data not shown).

Combined chol- and SM-enriched domain abrogation (*mβCD*) and specific chol-enriched domain depletion (*mβCD → +Chol*) similarly impaired RBC ability to pass across the filter pores (Fig. 5d). Reduced deformability was similar to that obtained with RBCs maintained for 2 weeks at 4°C to accelerate aging (*stored at 4°C*, see below for characterization of RBC modification upon storage), included in the experiment as an internal control for decreased deformability. Altogether, these results indicated that chol-enriched domain abrogation induced the loss of high curvature areas in the rim of elliptocytes and a decreased deformability in healthy RBCs.

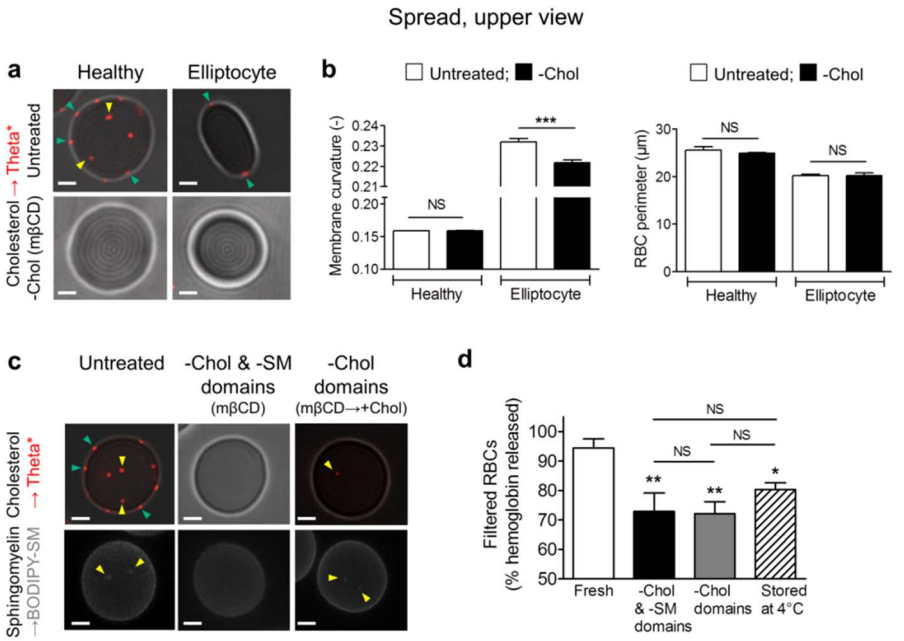

Figure 5. Loss of high curvature areas in elliptocytes and impairment of healthy RBC deformability upon chol-enriched domain abrogation. (**a**,**b**) Relation between lipid domains and RBC curvature. Fresh healthy and elliptocytotic RBCs were either left untreated (*untreated*) or incubated with methyl-ß-cyclodextrin (mßCD, *-Chol*), then labelled with Theta*, spread and observed as in Fig. 1. (**a**) Representative imaging of four independent experiments. Y*ellow* and *green arrowheads* indicate respectively LC and HC membrane areas, *scale bars* 2 µm. (**b**) Quantification of membrane average curvature and RBC perimeter of untreated (*open bars*) and treated (*black bars*) healthy and elliptocytotic RBCs. (**c**,**d**) Relation between lipid domains and RBC deformability. Fresh healthy RBCs were either left untreated *(untreated)* or incubated with mßCD (*-Chol & -SM domains*) or mßCD followed by chol repletion (*-Chol domains*), or maintained at 4°C during 2 weeks to accelerate aging (*Aged*). All preparations were then labelled with Theta* or BODIPY-SM, spread and observed as in Fig. 1. **(c)** Representative imaging of three independent experiments. Y*ellow* and *green arrowheads* indicate respectively LC and HC membrane areas, *scale bars* 2 µm. (**d**) RBC filtration. The amount of RBCs that passed through the filter was measured by haemoglobin release after complete RBC lysis and expressed as percentage of the amount of RBCs before filtration. Results are means ± SEM of 6-8 filtrations from 2-4 independent experiments. Statistical significance was tested with one-way ANOVA followed by Tukey's post-hoc test.

2.6 Transient increase of SM-enriched domains and calcium efflux upon RBC shape restoration

Although SM-enriched domains were not associated with membrane curvature changes, they transiently increased in abundance in the RBC center, starting about 5 min after stretching and lasting around 10 min (Fig. 6a and quantification in Fig. 6b, upper panel). We thus asked whether there could be a relation between SM domain abundance and transient Ca^{2+} exchanges, which are known to be involved in transient volume modulation upon RBC deformation (Dyrda et al., 2010). Ca^{2+} exchanges were determined by RBC labeling with Fluo-4, a fluorescent indicator of intracellular Ca^{2+} concentration ($[Ca^{2+}]_i$). A $[Ca^{2+}]_i$ increase was observed in the first 0 - 5 min after stretching, followed by a decrease during the next 15 min (Fig. 6a and quantification in Fig. 6b, lower panel).

The temporal concordance ([6 - 14 min]) between increase of SM-enriched domain abundance and stimulation of Ca^{2+} efflux suggested a combined stimulation of these two events upon shape/volume restoration. To assess this hypothesis, BODIPY-SM-labelled RBCs were observed in their resting state (Fig. 6c, *unstretched*), then returned to their initial shape (*destretched*) after a rapid stretching (during 1 min). Destretched RBCs exhibited within a 6 - 14 min time interval after stretching a simultaneous transient increase of SM-enriched domain abundance and Ca^{2+} efflux (Fig. 6c and quantification in Fig. 6d), showing again the stimulation of SM-enriched domains in shape restoration, along with Ca^{2+} efflux.

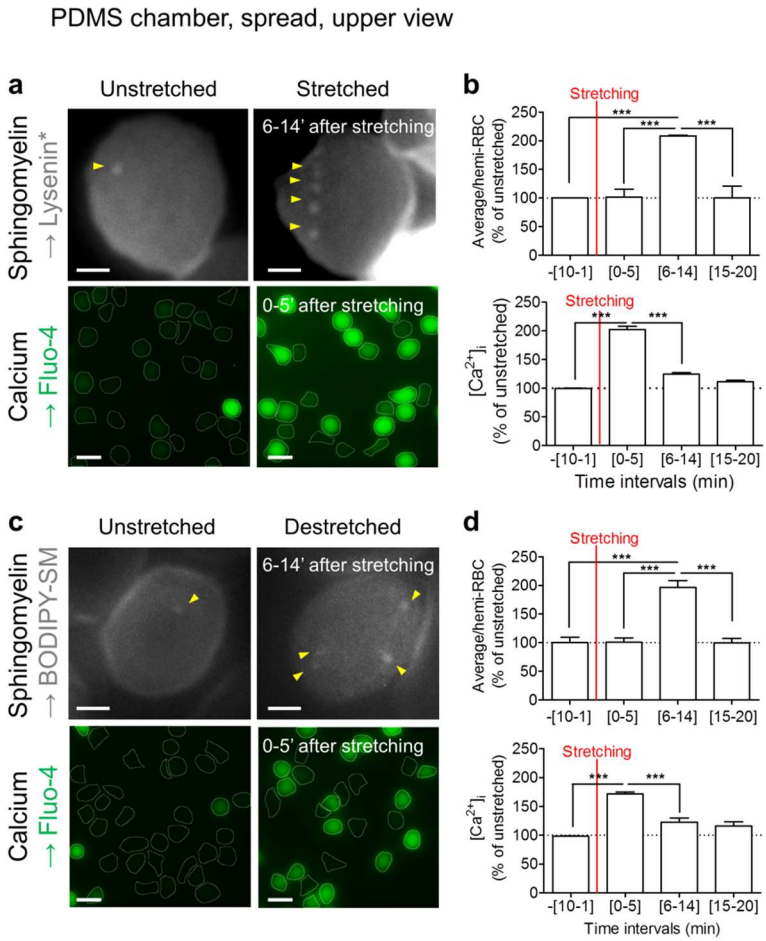

Figure 6. Transient increase of SM-enriched domains and calcium efflux during RBC shape restoration. Fresh healthy RBCs labelled for SM (Lysenin*/BODIPY-SM) or intracellular Ca^{2+} (Fluo-4) and spread onto PLL-coated PDMS chambers were visualized before stretching (*unstretched*) and either after stretching (*stretched*; a,b) or upon return to initial shape after a 1-min stretching (*destretched;* c,d). (**a,c**) Representative imaging. In *upper panels* (SM labelling), one representative RBC is shown; y*ellow arrowheads* point to domains in LC membrane area. *In lower panels* (Ca^{2+} labelling), several RBCs are shown. Representative imaging of 2-3 independent experiments, s*cale bars* 2 µm in *upper panels* and 10 µm in *lower panels*. (**b**,**d**) Quantification of domain abundance (number by hemi-RBC expressed as percentage of unstretched, *upper panels*) and Fluo-4 intensity (average intensity by hemi-RBC expressed as percentage of unstretched, *lower panels*). Results were grouped by time intervals around stretching time. Results are means ± SEM of 1459-1914 RBCs from 2-3 independent experiments. Statistical significance was tested with one-way ANOVA followed by Tukey's post-hoc test.

2.7 Specific increase of SM-enriched domains upon calcium efflux

We next investigated if SM-enriched domain stimulation and secondary Ca^{2+} efflux, observed during shape restoration, could be related. Ca^{2+} efflux was induced by RBC incubation in Ca^{2+}-free medium supplemented with EGTA, a Ca^{2+}-chelating agent (Fig. 7a and b, upper panels). An increased abundance of SM-enriched domains was observed in the RBC concavity (Fig. 7a and b, lower panels). This effect was reversible (data not shown), excluding toxicity. In contrast, the abundance of chol-enriched domains was not significantly increased (Supplementary Fig. 11).

To better mimic Ca^{2+} exchanges occurring during RBC deformation, RBCs were incubated with a very low concentration of the Ca^{2+} ionophore A23187 to induce $[Ca^{2+}]_i$ increase (*A23187*) without hemolysis (data not shown), then in A23187-free medium (*A23187 → DMEM*) to favor secondary Ca^{2+} efflux (Fig. 7c and d, upper panels, quantifications after 10 min in A23187-free medium). This experiment confirmed the increased abundance of SM-enriched domains in the RBC concavity upon Ca^{2+} secondary efflux (Fig. 7c and d, lower panels). Altogether, our results indicated that SM-, but not chol-, enriched domains were stimulated during Ca^{2+} efflux.

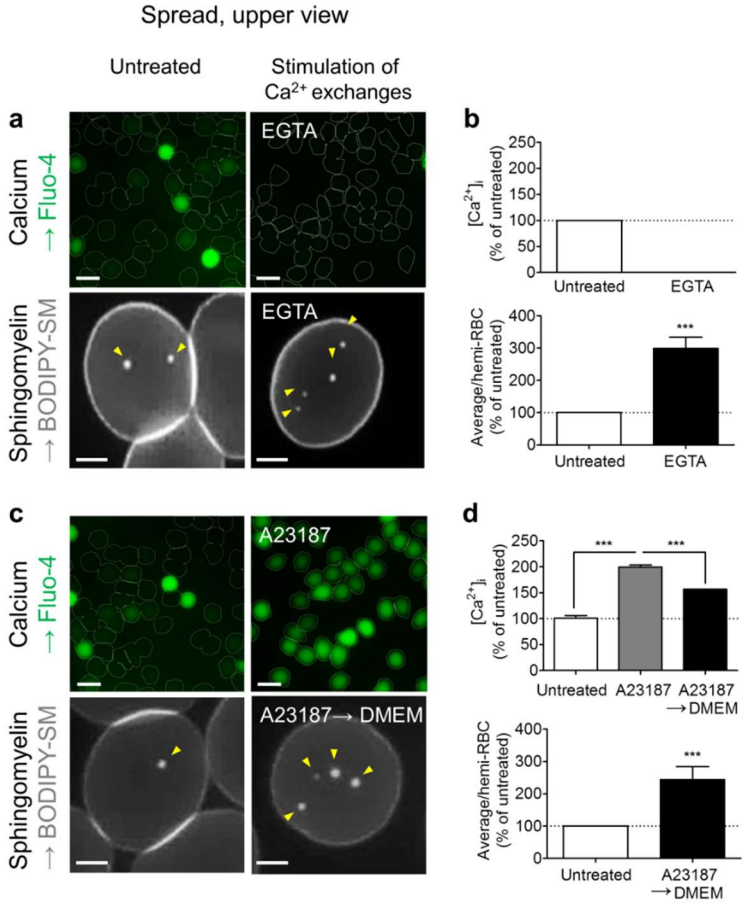

Figure 7. Increase of SM-enriched domains during calcium efflux. Fresh healthy RBCs were either left untreated (*open bars*) or stimulated for Ca^{2+} exchanges (*black & grey bars*), either by incubation with EGTA in Ca^{2+}-free medium (a,b) or by treatment with the Ca^{2+} ionophore A23187 followed or not by a reincubation in A23187-free medium (c,d). RBCs were then labelled with Fluo-4 or BODIPY-SM, washed and either spread onto PLL-coated coverslips and visualized by vital confocal/fluorescence microscopy (a,c and *lower panels* in b,d) or left in suspension and evaluated for Fluo-4 intensity by spectrophotometry (*upper panels* in b,d). (**a**,**c**) Representative imaging. In *lower panels*, on representative RBC; y*ellow arrowheads* indicate domains in LC membrane area. Representative imaging of 3-7 independent experiments, s*cale* 10 µm in *upper panel* and 2 µm in *lower panel*. (**b**,**d**) Quantification of Fluo-4 intensity (*upper panels*; average intensity by sample expressed as a percentage of untreated RBCs) and domain number (*lower panels*; average number by hemi-RBC expressed as a percentage of untreated RBCs). Results are means ± SEM of 11-12 samples (*upper panels*) and 82-1654 RBCs (*lower panels*) from 3-7 independent experiments. Statistical significance was tested with two-sample t-tests, except one-way ANOVA followed by Tukey's post-hoc test in *upper panel* in d.

2.8 Impairment of intracellular calcium concentration and volume increase ability upon SM-enriched domain abrogation

We finally asked whether Ca^{2+} efflux and volume increase, two processes occurring during shape restoration, could be impaired upon lipid domain abrogation. We therefore measured $[Ca^{2+}]_i$ in RBCs treated with increasing concentrations of sphingomyelinase, which converts SM into ceramide. Between 1 and 10 mU/ml, this treatment decreased the SM level from ~10 to 60 % and induced a concomitant increase of $[Ca^{2+}]_i$ (Fig. 8a), indicating the inverse relationship between SM membrane level and $[Ca^{2+}]_i$. Because sphingomyelinase is able to abrogate both SM- and chol-enriched domains (Carquin et al., 2015, 2014), we then evaluated $[Ca^{2+}]_i$ upon both chol- and SM-enriched domain abrogation (*-Chol & -SM domains*) and upon specific chol-enriched domain depletion (*-Chol domains*). Abrogation of both chol- and SM-enriched domains induced an increase of $[Ca^{2+}]_i$, which was significantly restored 10 min after SM-enriched domain repletion (Fig. 8b, *-Chol domains*).

Since RBC volume increase seems to be at the center of the relation between SM-enriched domains and Ca^{2+} efflux during RBC shape restoration, we then evaluated lipid domain abundance and hemoglobin release upon RBC incubation in media of decreasing osmolarity, a simple way to evaluate RBC ability to increase their volume (Mohandas et al., 1980). RBCs incubated in iso- to hypo-osmotic media (320 mOsm to 180 mOsm) increased SM-enriched domain abundance in the concavity of the cell (Fig. 8c), as a first line of evidence for the relation between volume increase and SM-enriched domain stimulation. We then evaluated the impact of chol- and SM-enriched domain abrogation (*-Chol & -SM domains*) and specific chol-enriched domain depletion (*-Chol domains*) on hemoglobin release by RBCs incubated in media of decreased osmolarity. As compared to untreated fresh RBCs, chol- and SM-enriched domain abrogation (*-Chol & -SM domains*) and RBC storage at 4°C, but not chol-enriched domain depletion only (*-Chol domains*), impaired resistance to hemolysis (Fig. 8d,e). Altogether these experiments confirmed the relation between SM-, but not chol-, enriched domains and the regulation of $[Ca^{2+}]_i$ and volume increase, two processes involved in RBC shape restoration after deformation.

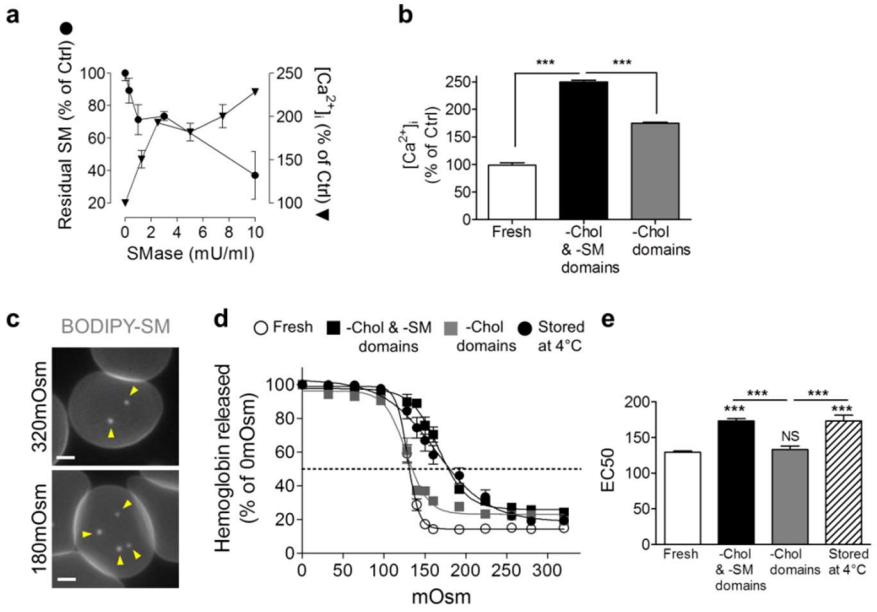

Figure 8. Impairment of intracellular calcium concentration and volume increase ability upon SM-enriched domain abrogation. (**a**) Fresh healthy RBCs were preincubated with Fluo-4, treated with the indicated concentrations of sphingomyelinase *(SMase)* to deplete endogenous SM and evaluated for SM residual content (*black circles*) and $[Ca^{2+}]_i$ (*black triangles*). Results are expressed as percentage of control *(0 mU/ml SMase)* and are means ± SEM from three independent experiments. (**b**) RBCs were preincubated with Fluo-4, treated to abrogate both chol and SM domains (*-Chol & -SM domains*) or chol domains (*-Chol domains*) only as described in Fig. 5 and then evaluated for $[Ca^{2+}]_i$. Results are expressed as percentage of untreated RBCs and are means ± SEM of 8 samples from two independent experiments. (**c**) RBCs were labelled with BODIPY-SM, washed, spread onto PLL-coated coverslips and visualized by fluorescence microscopy in media of indicated osmolarity. Representative imaging of 4 independent experiments, s*cale bars* 2 µm. (**d,e**) Fresh RBCs treated for domain abrogation (as in Fig. 5) or stored at 4°C were incubated in media of indicated osmolarity and evaluated for haemoglobin release (d, average haemoglobin absorbance by sample expressed as a percentage of 0 mOsm; e, EC50). Results are means ± SEM of 12-18 samples from 4-6 independent experiments. Statistical significance was tested with one-way ANOVA followed by Tukey's post-hoc test.

2.9 Specific vesiculation of chol- and SM-enriched domains upon aging

Upon senescence *in vivo,* RBCs undergo multiple changes including the loss of membrane by vesiculation and alterations in cell volume, density and deformability (Antonelou et al., 2010; Lutz and Bogdanova, 2013). Different experimental conditions have been developed in the literature to investigate the mechanisms underlying the RBC vesiculation process, including blood storage at 4°C. Several lines of evidence indicate that the changes to the RBC membrane during blood storage somehow mimick *in vivo* RBC senescence mechanisms (Kriebardis et al., 2008, 2007; Bogdanova et al., 2013). Accordingly, after 15 days of RBC storage at 4°C, we observed: (i) an increased susceptibility to vesiculation, as shown by scanning electron microscopy on unlabeled RBCs (Fig. 9b, lower panels & Supplementary Fig. 12Ab); (ii) a decreased membrane area (Fig. 9a, *upper and central panels*; quantification in c) and biconcavity (Fig. 9a, *lower panels*) together with an increase of RBC circularity (Supplementary Fig. 12B); (iii) a decreased deformability, as revealed by filtration through polycarbonate filters (Fig. 5); (iv) phosphatidylserine (PS) exposure to the outer PM leaflet, as revealed by Annexin V labeling (Supplementary Fig. 12Ad); (v) Band 3 aggregates, thanks to maleimide labelling (Supplementary Fig. 12Af); and (vi) an increased intracellular Ca^{2+} concentration (Supplementary Fig. 12C).

We then analyzed lipid domains in RBCs stored at 4°C to assess if they could be involved in membrane vesiculation upon aging. Stored RBCs lost both types of lipid domains (Fig. 9a, *upper and central panels*; quantification for chol-enriched domains in d). We believe that such loss was not due to Toxin* labelling, as vesiculation was also observed on unlabelled RBCs (Fig. 9b, *white arrowheads lower panels*), but resulted from specific domain vesiculation and not from random membrane loss (arrowheads at Fig. 9b, *white arrowheads at upper and lower panels*). Accordingly, the significant decrease of total domain occupation of the RBC surface in stored *vs* fresh RBCs suggested a higher sensitivity to vesiculation of domains *vs* surrounding membrane (bulk) (Fig. 9e).

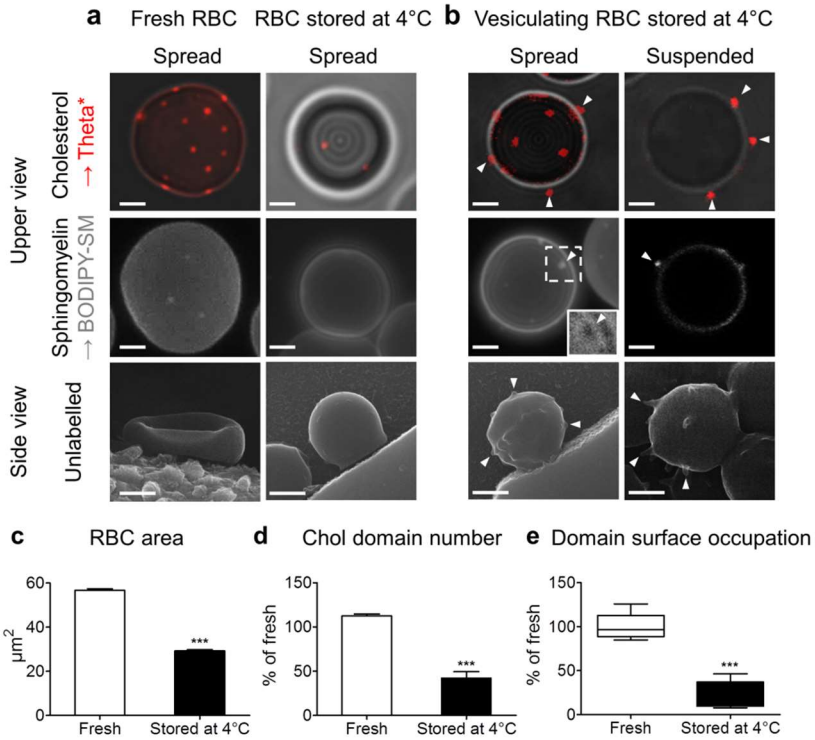

Figure 9. Specific vesiculation of chol- and SM-enriched domains upon storage at 4°C. Fresh and stored (15 days at 4°C) healthy RBCs were labelled (a and b, *upper and central panels*) or not (a and b, *lower panels*), left in suspension *(suspended)* or spread (*spread*) and observed by vital confocal/fluorescence microscopy (a and b, *upper and central panels*) or SEM (a and b, *lower panels*). (**a**,**b**) Representative imaging. *White arrowheads* point to membrane vesiculation (b). SM-enriched vesiculating domain in spread RBC is boxed and can be observed by specific transmission pattern (see 2x zoom in right lower corner of the image). Representative images of 2-3 independent experiments, *scale bars* 2 µm. (**c-e**) Quantification of RBC area (c; μm^2 by hemi-RBC), chol-enriched domain number (d; average by hemi-RBC expressed as percentage of fresh RBCs) and domain surface occupation (e; total domain area by hemi-RBC area, expressed as a percentage of fresh RBCs). Results are means ± SEM of 128-252 RBCs from two independent experiments. Statistical significance was tested with two-sample t-tests.

3. Discussion

Although PM lipid domains have been evidenced in several living cells, their functions remain largely unclear. We here investigated whether they could contribute to function-related cell (re)shaping processes, a central role of the PM. To assess this question, we used erythrocytes since they (i) exhibit a specific biconcave shape ; (ii) expose drastic reshaping upon both reversible deformation and membrane vesiculation upon aging; (iii) display at their outer PM submicrometric domains differentially enriched in chol and SM; and (iv) offer a featureless surface and no lipid trafficking which facilitate the study of these domains.

Deciphering the importance of lipid domains for cell (re)shaping requires specific, non-toxic, sensitive and quantitative tools compatible with live cell imaging. Hence, these probes should decorate and not induce domains. Since the small fluorescent SM analog (BODIPY-SM) and the large Toxin Lysenin* detect spatially undistinguishable domains at the RBC surface whatever the order of labelling, we suggested that mCherry-Toxin fragments do not trigger but rather reveal preexisting submicrometric domains (Carquin et al., 2015). RBC labeling with low-molecular weight fluorescent chol reporters, such as the polyene antibiotic filipin and dehydroergosterol, did not produce significant signal without obvious signs of RBC abnormal shape (our unpublished data), precluding comparison with Theta* for analysis of chol lateral heterogeneity. We however observed that sphingomyelinase treatment has no effect on total Theta* binding but fully abrogates submicrometric domains (Carquin et al., 2014), implying that chol-enriched domains critically depend on endogenous SM and further suggesting that, at least upon SM depletion, Theta* by itself is unable to trigger domain formation. We also excluded the possibility that SM-enriched domains track cell curvature due to Lysenin* binding. Indeed, the specific association of SM-enriched domains with RBC low curvature areas was similarly observed with the small probe BODIPY-SM. We were not able to test this possibility for chol-enriched domains due to the reasons mentioned above.

Using these two specific Toxin* fragments and/or BODIPY-SM, we first highlighted the preferential association of chol- and SM-enriched submicrometric domains with high and low membrane curvature areas of the RBC biconcave membrane, respectively (Fig. 10a). RBC biconcavity was not impacted by domain abrogation, suggesting that chol- and SM-enriched domains are not actively involved in RBC specific biconcave membrane shape. Instead, the specific association of lipid domains to distinct membrane curvature areas could suggest that lipid domain topography is controlled by the RBC membrane curvature. While no data are currently available on eukaryotic living cells, experiments on model membranes made of lipid mixtures indicate that a curvature-driven lipid domain sorting is possible, on

model membranes with preexisting phase separation or not (Parthasarathy et al., 2006; Roux et al., 2005; Tian and Baumgart, 2009). Mechanistically, lipid domains seem not effectively curvature-sorted according to the individual lipid shape, but instead by cooperative properties of lipid domains, such as domain intrinsic curvature or lipid domain order and correlated bending stiffness(Parthasarathy et al., 2006; Roux et al., 2005; Tian and Baumgart, 2009). Taking into account the high order of chol-enriched domains in model membranes, their association with high curvature areas is surprising. However, unfavorable properties like bending rigidity could be circumvented by domain-associated binding proteins that are curvature sorted (Arumugam and Bassereau, 2015) or the line tension at domain boundary (Baumgart et al., 2003). It should be nevertheless stressed that the absolute values of the RBC PM curvatures are very small as compared to domain size, when comparing with the mentioned experiments on model membranes (tubes pulled from GUVs or surfaces imposing curvature to lipid bilayers), questioning the possibility of such curvature-driven mechanism. Non-mutually exclusive additional mechanisms could be proposed, such as the cytoskeleton and transmembrane protein pinning (Arumugam and Bassereau, 2015) or interleaflet coupling.

After investigating the relation between PM lipid domains and RBC specific shape, we turned to analyze their potential implication in RBC reshaping during (i) deformation, (ii) shape restoration after deformation, and (iii) local membrane vesiculation upon aging. First, we observed the recruitment of chol-enriched domains in areas of increased membrane curvature created in the rim of elliptocytes and of healthy RBCs stretched on PDMS chambers (Fig. 10b). Hence, specific abrogation of chol-enriched domains both decreased RBC deformability and abrogated elliptocyte high curvature areas, suggesting that chol-enriched domains could contribute to RBC deformability as membrane bending modulator/stabilizer. Indeed, microfluidic deformation of GUVs shows the gathering and reorganization of lipid phases, which could be favorable due to the reduction of the line tension at domain boundary (Robinson et al.). However, RBCs are far from more complex than GUVs due to the presence of membrane proteins and cytoskeleton, which are known to be involved in membrane bending and RBC deformation. The potential contribution of those actors remains to be determined, in order to decipher whether lipid domains are primary actors in membrane deformation through the modulation/stabilization of membrane curvature or not.

Second, we highlighted the increase of SM-enriched domains in RBC concavity along with secondary Ca^{2+} efflux during shape restoration after deformation. It is tempting to propose that SM-enriched domains are involved in secondary Ca^{2+} efflux allowing for shape and volume restoration after deformation (Fig. 10c), based on the following lines of evidence: (i) the same specific increase of SM-enriched domain abundance was observed upon Ca^{2+}

efflux stimulation with either A23187 or EGTA treatments, (ii) $[Ca^{2+}]_i$ increase was observed upon SM- and chol-enriched domain abrogation, which was partially restored after specific SM-enriched domain repletion, (iii) RBC ability for volume increase in hypo-osmotic medium was impaired upon combined chol- and SM-enriched domain abrogation, but was recovered upon specific SM-enriched domain repletion, and (iv) upon RBC membrane mechanical deformation, a transient $[Ca^{2+}]_i$ increase is observed, followed by the secondary activation of the Gardos channel leading to a transient volume decrease (Dyrda et al., 2010). In this context, SM-enriched domains could potentially represent platforms for the sorting and/or activation of Ca^{2+} efflux membrane proteins, which is the oldest and most frequently hypothesised function for lipid domains.

Third, we revealed the specific loss of chol- and SM-enriched domains upon storage at 4°C (mimicking aging), suggesting that chol- and SM-enriched domains could represent sites for vesiculation upon aging and storage (Fig. 10d). Accordingly, chol-enriched domains have been proposed to be the sites for membrane fusion upon HIV infection (Yang et al., 2016). Theoretical works (Lipowsky, 1992) and biophysical experiments on model membranes (Yang et al., 2016; Baumgart et al., 2003) propose the line tension associated to domain boundary is responsible for specific lipid domain vesiculation. In this context lipid domains could be specific fragility sites for membrane vesiculation due to line tension at domain boundary.

To the best of our knowledge, this is the first comprehensive study reporting on living eukaryotic cells the implication of different lipid domains in cell reshaping processes (Fig. 10 a-d). From our data it is tempting to propose that PM lipid domains contribute to RBC reshaping as membrane bending modulator/stabilizer upon deformation, platforms allowing for Ca^{2+} efflux during the following volume and shape restoration and fragility sites for membrane vesiculation upon aging (Fig. 10a-d). However, several unanswered questions remain: are the domains primary actors or not; to what extent do these domains act on, or are recruited by, membrane proteins or the cytoskeleton; whether these mechanisms are relevant to conditions closer to RBC physiological environment (*e.g.* at 37°C and under application of a shear stress). While unveiling their functions is the first step for understanding lipid domains, it raises the issue of underlying mechanisms of action and energy considerations/driving forces. We hope our model, by providing two types of optically resolved lipid domains with distinct composition, topography and potential functions, could help progressing towards these questions.

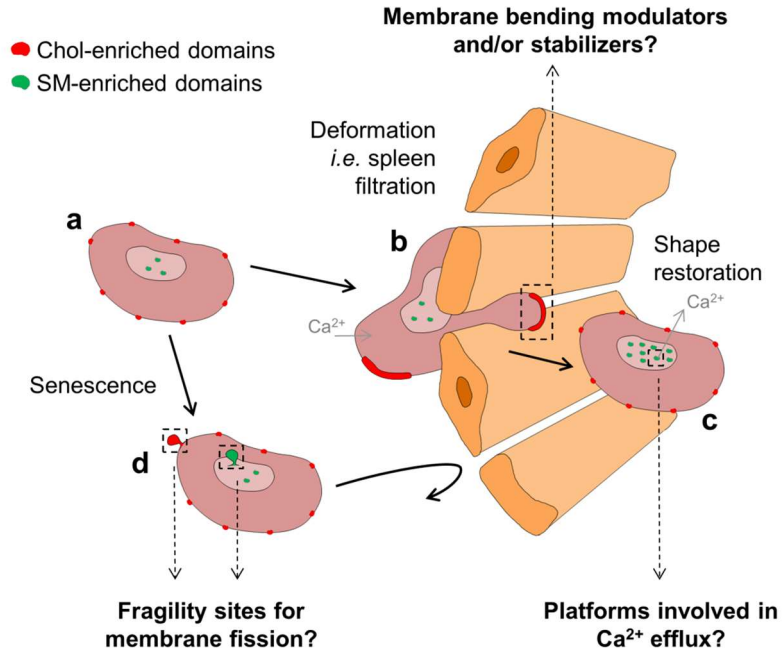

Figure 10. Model summarizing the relation between chol- and SM-enriched submicrometric domains and RBC (re)shaping and their hypothetical implication in these processes (dashed arrows). (a) In fresh healthy RBCs, chol- (*red*) and SM- (*green*) enriched submicrometric domains associate to distinct membrane areas with high and low curvature, respectively. (b,c) Upon deformation, chol-enriched domains are recruited to the edges and gather in increased curvature areas of the membrane. During shape and volume restoration after deformation, SM-enriched domains increase in abundance in the concavity of the RBC, along with Ca^{2+} efflux. (d) During RBC aging, both lipid domains appear as specific sites for membrane loss by vesiculation. From our data we suggest that PM lipid domains could contribute to RBC reshaping as membrane bending modulator/stabilizer upon deformation, platforms allowing for Ca^{2+} efflux during the following volume and shape restoration and fragility sites for membrane vesiculation upon aging but these hypotheses need further investigation.

4. Methods

4.1 Red blood cell isolation

This study was approved by the Medical Ethics Institutional Committee of the Université catholique de Louvain; each donor gave written informed consent. All methods were performed in accordance with the relevant guidelines and regulations. RBCs were freshly isolated from healthy volunteers (Ctrl) and one patient with hereditary elliptocytosis. Blood was collected by venopuncture into dry K^+/EDTA-coated tubes. For each experiment, blood was diluted 1:10 in Dulbecco's Modified Eagle Medium (DMEM containing 25 mM glucose, 25 mM HEPES and no phenol red, Invitrogen), then washed twice by centrifugation at 133 *g* for 2 min and resuspension. Washed RBCs were kept at 2* 10^7 cells/ml (washed RBCs:medium ratio of 1:11, *v:v*), then incubated or not with pharmacological agents and measured for Ca^{2+} or hemolysis or imaged by confocal/fluorescence or scanning electron microscopy (see below). Most experiments were carried out on fresh RBCs, except for storage at 4°C. For the later study, healthy RBCs were maintained during 2 weeks at 4°C into the K^+/EDTA-coated tubes.

4.2 Calcium modulation and measurement

Modulation of the $[Ca^{2+}]_i$ was performed on washed RBCs in suspension at room temperature (RT) under continuous agitation in (i) DMEM containing 0.3 µM of the Ca^{2+} ionophore A23187 (Sigma-Aldrich) for 10 min; (ii) A23187-containing DMEM for 10 min followed by reincubation in A23187-free medium for another 10 min; or (iii) Ca^{2+}-free homemade medium containing 1 mM Ca^{2+}-chelating agent ethylene glycol-bis(β-aminoethyl ether)-N,N,N',N'-tetraacetic acid (EGTA, Sigma-Aldrich) for 10 min. All RBCs were then pelleted at 133 *g* for 2 min, resuspended in the adequate medium and either used in suspension for $[Ca^{2+}]_i$ measurement or hemolysis tests or spread onto PLL-coated coverslips and observed by vital microscopy for lipid domains (see below) or Ca^{2+} determination. To evaluate $[Ca^{2+}]_i$, washed RBCs were preincubated in suspension at RT with 5 µM Fluo-4 (Invitrogen) in Ca^{2+}-free medium for 60 min under continuous agitation, pelleted at 133 *g* for 2 min and resuspended in Ca^{2+}-free medium, then treated with the above modulators and either measured for Ca^{2+} in 96-well plates (excitation 490 nm, emission 520 nm; SpectraCountTM, Packard BioScience Co.) or spread onto PLL-coated coverslips for intracellular Ca^{2+} signal (see below).

4.3 SM and chol content modulation and measurement

To modulate SM and/or chol contents, washed RBCs were preincubated in suspension at RT in DMEM containing 1 mg/ml bovine serum albumin (BSA; Sigma-Aldrich) supplemented with (i) 0.5 mM or 0.9 mM methyl-ß-cyclodextrin (mβCD; Sigma-Aldrich) for 30 min; (ii) 0–10 mU/ml Bacillus cereus sphingomyelinase (Sigma-Aldrich) for 10 min; or (iii) 0.9 mM mβCD, followed by repletion with 3.5 µg/ml mβCD:chol (Sigma-Aldrich) for 60 min. All RBCs were then pelleted at 133 g for 2 min, resuspended in DMEM and either used in suspension for hemolysis tests (see below) or Ca^{2+} (see above) or spread onto PLL-coated coverslips for vital imaging of lipid domains (see below). SM and chol contents were determined as previously described (D′auria et al., 2011; Carquin et al., 2014).

4.4 RBC labelling and vital fluorescence/confocal imaging

Washed RBCs were labeled with Toxin* fragments or BODIPY-SM. Lysenin* and Theta* were produced as previously described (Carquin et al., 2014, 2015), dissolved in 1 mg/ml DMEM-BSA and cleared of aggregates before each experiment by centrifugation at 20,000 *g* for 10 min. RBC labeling with Toxins* was performed in suspension (*i.e.* before immobilization) with either 1.25 µM Lysenin* or 0.55 µM Theta* in DMEM/BSA at 20°C for 25 min under continuous agitation, then pelleted at 133 *g* for 2 min and resuspended in DMEM. RBC labeling with BODIPY-SM (Invitrogen) was performed after RBC immobilization on coverslips at 0.75 µM at 20°C for 15 min. To immobilize RBCs for imaging we developed two complementary systems, spreading onto poly-L-lysine (PLL, 70–150 kDa; Sigma-Aldrich)-coated coverslips and suspended RBCs. For spread RBCs, coverslips were first coated with PLL:DMEM (1:1, *v:v*) at 37°C for 40 min, then washed with DMEM at 20°C for 5 min. Labelled RBCs were then plated onto the coated coverslips at 20°C for exactly 4 min, the suspension was removed and replaced by fresh medium, and attached RBCs were allowed to spread for another 4 min. The coverslip was placed upside down on a Lab-Tek chamber and then observed. For the "in suspension" system, labelled RBCs were dropped to settle down in µ-Slide $VI^{0.4}$ uncoated IBIDI chambers (IBIDI, Proxylab; 100 µl by channel). All preparations were examined at RT either with a Zeiss LSM510 confocal microscope using a plan-Apochromat 63X NA 1.4 oil immersion objective or with a Zeiss wide-field fluorescence microscope (Observer.Z1) using a plan-Apochromat 100X/1.4 oil Ph3 objective.

4.5 RBC (de)stretching on PDMS chambers

Deformation experiments were conducted by spreading Toxin*/BODIPY-SM- or Fluo-4-labelled RBCs on a 4 cm^2 PLL-coated polydimethylsiloxane (PDMS) stretchable chamber (B-Bridge, Gentaur). Washed RBC labelling with Toxin* or Fluo-4 was done in suspension before spreading whereas labelling with BODIPY-SM was performed after spreading on the PDMS chamber. Briefly, PDMS chamber was first coated with PLL:DMEM (1:1, *v:v*) at 37°C for 40 min, washed with DMEM at 20°C for 5 min and fixed to the stretching device (STREX, cell strain instrument, B-Bridge). Labelled RBCs were plated into the PDMS chamber for exactly 5 min, then the suspension was removed and replaced by fresh medium, and attached RBCs were allowed to spread for another 5 min. The PDMS chamber was then immediately observed at RT without stretching (unstretched) with a Zeiss wide-field fluorescence microscope (Observer.Z1) using a plan-Neofluar 63X/0.75 Ph2 objective. Stretching and destretching of the chamber were thereafter respectively performed by (i) axial stretching of the right side of the PDMS chamber from 7-17 % of the chamber length (stretching); and (ii) return to the initial state after a quick (1 min) axial stretching of the right side of the PDMS chamber from 7-17 % of the chamber length (destretching).

4.6 RBC separation by filtration

3 ml of washed RBCs, then 2 ml of DMEM for washing, were forced to pass through a polycarbonate filter with 1.2 µm-pores (ipPORE) by applying a pressure below 0.2 bar. RBCs that passed through the filter were quantified by achieving full hemolysis with 0.2 % Triton X-100. The quantity of recovered RBCs was expressed as percentage of total RBCs before filtration.

4.7 Measurement of hemoglobin release

Measurement of hemoglobin released in supernatants was used for evaluating innocuity of pharmacological treatments to RBCs and RBC resistance to hemolysis in media of decreased osmolarity. The latter was determined by incubation of washed RBCs in media of decreasing osmolality (from 320 to 0 mOsm, by dilution of DMEM with demineralized water) for 10 min at RT. Hemoglobin released in supernatants was then read at 560 nm in 96-well plates (SpectraCountTM, Packard BioScience Co.). For normalization, full hemolysis was achieved by 0.2 % Triton X-100.

4.8 Scanning electron microscopy

Washed RBCs were spread onto poly-L-lysine-coated nude grids and quickly washed three times with DMEM. Cells were then fixed by 1 % glutaraldehyde (Fluka-Sigma) and post-fixed with 1 % (w/v) osmium tetroxide in 0.1 M cacodylate buffer. Samples were washed three times in 0.1 M cacodylate

buffer, then in water, dryed overnight and dehydrated in graded ethanol series and critical-point dried (Leica EM CPD030, Vienna, Austria). A 10-nm gold film was sputter-coated (Leica EM MED020, Vienna, Austria) and specimens were observed in a CM12 electron microscope (Philips, Eindhoven, Netherlands) at 80kV with the use of the secondary electron detector as described (Tyteca et al., 2010).

4.9 Image analysis

Measurements of (i) RBC total projected area (referred to as hemi-RBC), circularity and membrane curvature; (ii) abundance and size of chol- and SM-enriched domains; and (iii) distribution of domains at the lateral PM were performed on high-resolution confocal or epifluorescence images. Except for domain abundance which was assessed by manual counting, all other analyses were done on ImageJ software. Briefly, domains and RBC projected contour were either detected on fluorescent channel images (or transmission images for RBC projected contour when no continuous labeling of the RBC membrane was observed), using analyzed particles plugging, or manually drawn if no detection was possible. These selections were then used for all the following analyses. Prior to contour selection, threshold of both fluorescent and transmission images were adjusted using default methods in ImageJ and were converted in binary images. Domain area, total RBC projected area and RBC membrane circularity were measured with the analyzed particles plugging. Domain occupation of RBC surface was calculated by expressing total domain area of each RBC as a percentage of the corresponding RBC area. Distribution of chol domains at the lateral PM was performed on untresholded fluorescent channel images and that of SM domains on untresholded fluorescent channel images after applying a mask allowing to keep only the domain intensity, both using ImageJ plot profile plugging. Membrane curvature was analyzed using the last version of the Shape Analysis by Fourier Descriptors computation plugging for ImageJ developed by Thomas Boudier. The average curvature associated to chol- and SM-enriched domains and surrounding bulk was obtained by combining results from intensity profiles and curvature profiles.

4.10 Statistical analysis

Values are presented as means ± SEM. Statistical significance was tested either with two-sample t-test or one-way ANOVA followed by Tukey's post-hoc test (NS, not significant; *, $p<0.05$; **, $p<0.01$ and ***, $p<0.001$).

5. Supplementary material

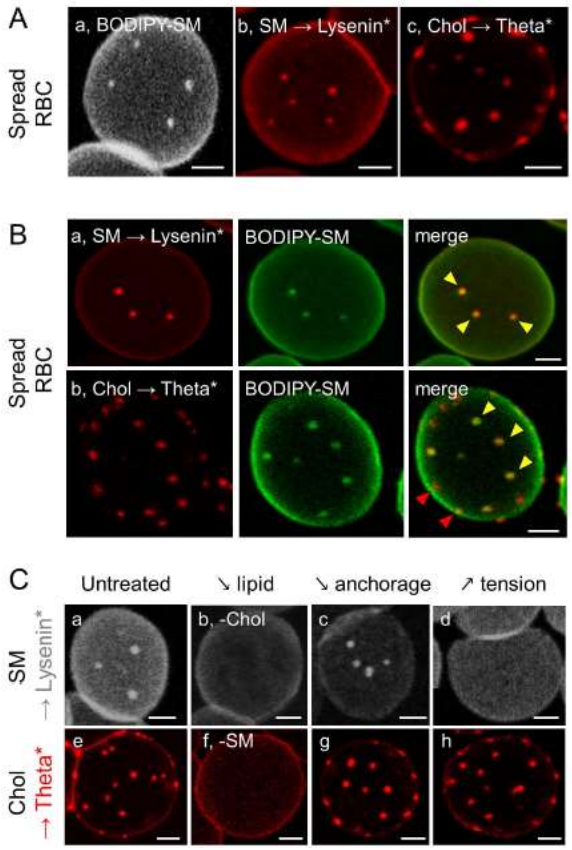

Figure S1. Evidence, spatial relation and regulation of SM- and chol-enriched submicrometric domains at the living RBC plasma membrane. (A) Evidence on spread RBCs. Trace PM insertion of BODIPY-SM (a) or labeling by fluorescent Toxin fragments of endogenous SM (Lysenin*; b) and chol (Theta*; c). RBCs were spread and then analysed by confocal vital imaging. **(B)** Spatial relation. RBCs were labelled by Lysenin* (a; endogenous SM) or Theta* (b; endogenous chol), then by exogenous BODIPY-SM. Whereas Lysenin* and BODIPY-SM perfectly co-localize (a), two types of chol-enriched domains, enriched in either both chol and SM (yellow arrowheads, b) or chol mainly (red arrowheads, b), coexist. **(C)** Regulation. RBCs were either left untreated (a,e; visualization at 20°C) or modulated for: (b,f) endogenous chol or SM content (c,g), membrane:cytoskeleton anchorage at 4.1R complexes (PKC activation), or (d,h) membrane tension (increased spreading on PLL-coated coverslips). All preparations were then labelled with either Lysenin* (a-d) or Theta* (e-h), spread and visualized as at A. Notice similar lipid domain abrogation upon specific lipid depletion (b,f) and similar lipid domain increase upon acute uncoupling of membrane:cytoskeleton anchorage (c,g) but differential lipid domain modulation by increased tension (d,h). *All scale bars* 2µm. Adapted from [42,43].

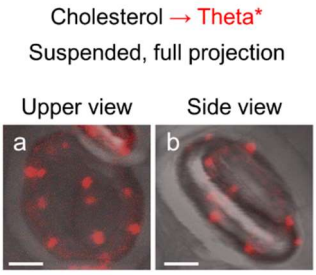

Figure S2 (extension of Fig. 1). Full projection of Theta*-labelled suspended RBCs, observed in upper or side view, reveals similar abundance of chol-enriched domains than spread RBCs. Fresh healthy RBCs were labelled with Theta*, washed, left in suspension in IBIDI chambers and directly visualized in their upper (**a**) or side view (**b**) by vital confocal microscopy. Z-stack images were reconstructed using ImageJ software. S*cale bars* 2 µm.

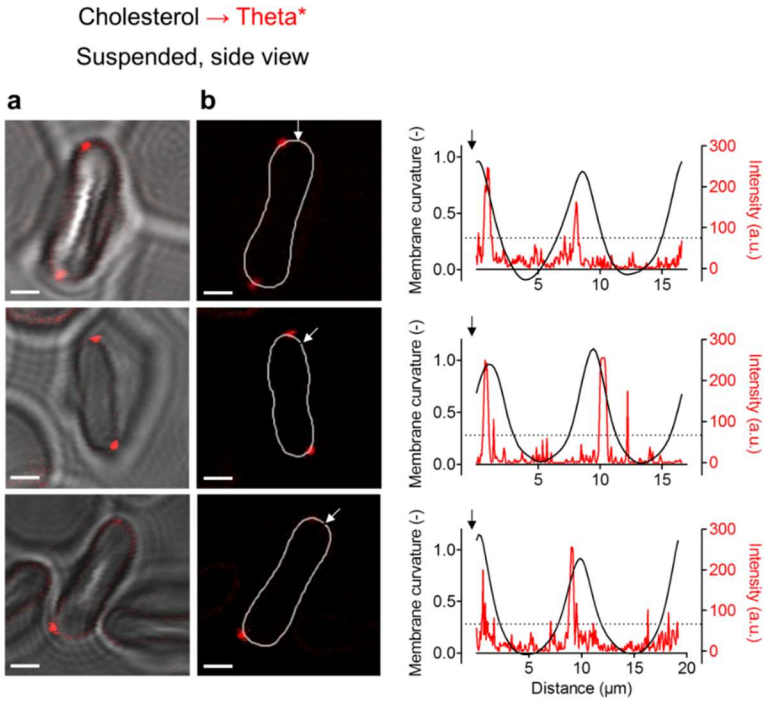

Figure S3 (extension of Fig. 2). Specific association of chol-enriched domains with high curvature areas of the RBC biconcave membrane: gallery of images and profiles. Fresh healthy RBCs were labelled with Theta*, then visualized in suspension by vital confocal microscopy. (**a**) Representative imaging, s*cale bars* 2 µm. (**b**) Profiles comparing Theta* intensity (*red*; *right panels*) and membrane curvature (*black)*. Profiles along paths indicated in *left panels* by *white curved lines* on side-viewed suspended RBCs (counterclockwise from starting point indicated by *white arrows*). *Dashed lines* represent the membrane curvature average value (C_{mean}). Representative imaging and profiles of 3 independent experiments.

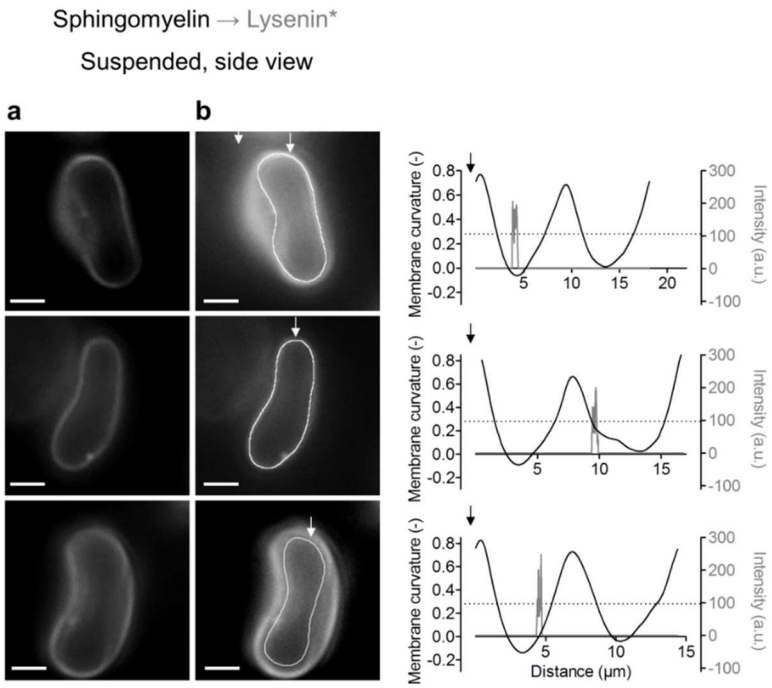

Figure S4 (extension of Fig. 2). Specific association of SM-enriched domains with low curvature areas of the RBC biconcave membrane: gallery of images and profiles. Fresh healthy RBCs were labelled with Lysenin*, then visualized in suspension by vital fluorescence microscopy. (**a**) Representative imaging, s*cale bars* 2 µm. (**b**) Profiles comparing Lysenin* intensity (*grey*; *right panels*) and membrane curvature (*black)*. Profiles along paths indicated in *left panel* by *white curved lines* on side-viewed suspended RBCs (counterclockwise from starting point indicated by *white arrows*). *Dashed lines* represent the membrane curvature average value (C_{mean}). Representative imaging and profiles of 3 independent experiments.

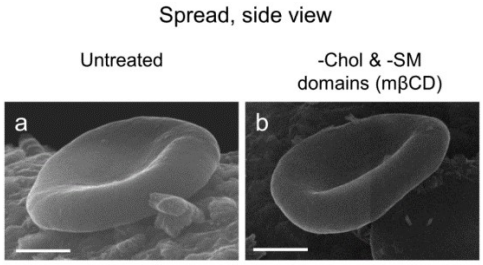

Figure S5 (extension of Fig. 2). Specific association of lipid domains with distinct curvature areas of the RBC biconcave membrane is not involved in the maintenance of this specific shape. Fresh healthy RBCs were either left untreated (a, *untreated*) or incubated with methyl-ß-cyclodextrin (mßCD, b, *-Chol & -SM domains*), then spread and observed in side view by SEM. S*cale bars* 2 µm.

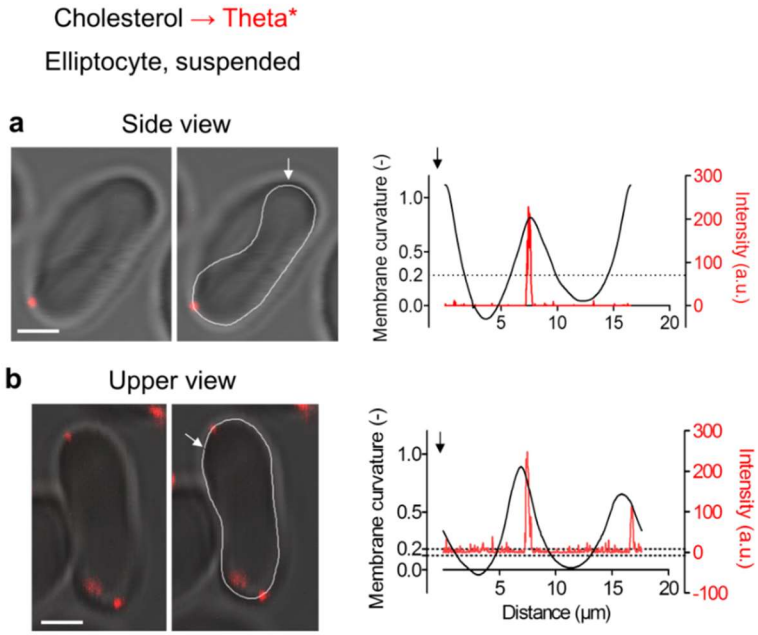

Figure S6 (extension of Fig. 3). Preserved biconcavity in elliptocyte and preferential association of chol-enriched domains with increased curvature areas in the rim of suspended elliptocytes. Fresh elliptocytotic RBCs were labelled in suspension with Theta* then visualized in suspension by vital confocal microscopy either in side view (a) or upper view (b). Representative imaging (*left and central panels)* and profiles comparing Theta* intensity (*red*, *right panels*) and membrane curvature (*black)*. Profiles along paths indicated in *central panel* by *white curved lines* on side- and upper-viewed RBCs in suspension (counterclockwise from starting point indicated by *white arrows*). *Dashed lines* represent either the mean average membrane curvature value (C_{mean}, a) or HC_{min} and HC_{max} (b). Representative imaging and profiles of three independent experiments, s*cale bars* 2 µm.

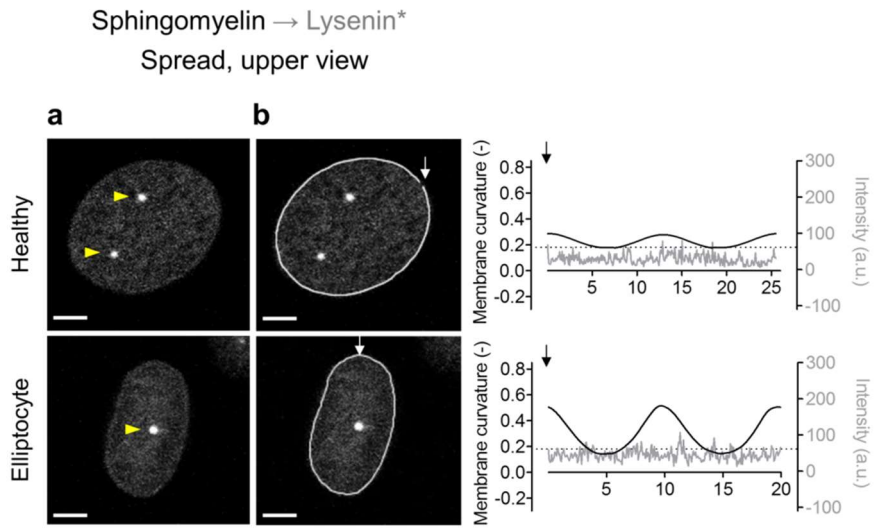

Figure S7 (extension of Fig. 3, 4 & 6). Absence of SM-enrichment in increased curvature areas of the rims of elliptocytes. Fresh healthy (*Healthy*) or elliptocytotic RBCs (*Elliptocyte*) were labelled in suspension with Lysenin*, spread onto PLL-coated coverslip and observed by vital confocal microscopy. (**a**) Representative imaging. Y*ellow arrowheads* indicate domains in LC membrane area, s*cale bars* 2 µm. (**b**) Profiles comparing Lysenin* intensity (*grey*, *right panels*) and membrane curvature (*black)*. Profiles along paths indicated in *left panel* by *white curved lines* (counterclockwise from starting point indicated by *white arrows*). *Dashed lines* represent HC_{max}. Representative imaging and profiles of 2 independent experiments.

CHAPITRE 4

Tuning of differential lipid order between submicrometric domains and surrounding membrane upon erythrocyte reshaping

Abstract

Transient nanometric cholesterol- and sphingolipid-enriched domains, called rafts, are characterized by higher lipid order as compared to surrounding lipids. Here, we asked whether the seminal concept of highly ordered rafts could be refined with the presence of lipid domains differently enriched in cholesterol and sphingomyelin. We also investigated how differences in lipid order between domains and surrounding membrane are regulated and whether changes in order differences could participate to erythrocyte deformation and vesiculation. We used the fluorescent hydration- and membrane packing-sensitive probe Laurdan to determine the Generalized Polarization (GP) values of lipid domains *vs* the surrounding membrane. We observed three domain populations differently enriched in cholesterol and sphingomyelin and exhibiting a diversity of lipid order states. Although all lipid domains were less ordered than the surrounding lipids in erythrocytes at resting state, they became more ordered than the bulk upon erythrocyte deformation (elliptocytes and stimulation of calcium exchanges) or membrane vesiculation (storage at 4°C). Upon aging and in membrane fragility diseases (spherocytosis), an increase in the difference of lipid order between domains and the surrounding lipids contributed to the initiation of domain vesiculation. The critical role of domain-bulk differential lipid order modulation for erythrocyte reshaping are discussed in relation with the pressure exerted by the cytoskeleton on the membrane.

1. Introduction

The differential lipid order between lipid domains and the surrounding bulk membrane is thought to be highly relevant for cell physiology (Owen et al., 2012; Stone et al., 2017b). Accordingly, a recent study highlighted that lipid order differences arising from domain formation participate in selective sorting of membrane proteins (Lorent et al., 2017). This concept was first suggested in the 90's by the lipid raft hypothesis, which proposed that sterols and sphingolipids (SLs), due to their favorable interaction, can self-aggregate into rafts of higher lipid order as compared to the surrounding bulk lipids, thereby mediating protein sorting and cellular functions. During the past years, evidences for such lipid membrane lateral heterogeneities have been provided in membrane and cell models of increasing complexity. First, sterol-containing biomimetic model membranes, including planar supported lipid layers and giant unilamellar vesicles (GUVs), expose the coexistence of two liquid phases, one enriched in cholesterol (chol) and SLs of high lipid order (L_o, "raft-like") and one enriched in unsaturated lipids of low lipid order (L_d, non "raft-like") (Dietrich et al., 2001; Jacobson et al., 2007). Second, giant plasma membrane vesicles (GPMVs) derived from living cells (Baumgart et al., 2007) reveal that L_o and L_d phases in natural plasma membranes (PM) can assume a wide range of lipid order states resulting from lipid order tuning upon active cellular processes (Sezgin et al., 2015). Third, cellular PMs exhibit regions of higher lipid order than the bulk lipids, either as small domains or larger areas depending on cellular processes (Gaus et al., 2005; Owen et al., 2010; Rentero et al., 2008; Stone et al., 2017b). As an additional level of complexity, several studies on cells reveal the existence of lipid domains with a wider diversity of lipid composition, such as only partial sterol and SL co-enrichment (Aresta-Branco et al., 2011; Carquin et al., 2015; Frisz et al., 2013a; Frisz et al., 2013b; Grossmann et al., 2007). Hence, segregation mechanisms distinct from favorable sterol-SL interactions are proposed, such as charge-mediated sequestration (van den Bogaart et al., 2011), integral membrane proteins (Gomez et al., 2010) or membrane:cytoskeleton anchorage (Bernardino de la Serna et al., 2016; Gomez-Llobregat et al., 2013; Kraft, 2013; Kusumi et al., 2011; Raghupathy et al., 2015; Sevcsik and Schütz, 2016).

Here, we investigate (i) whether lipid domains also exhibit a lipid order which is different from the bulk and (ii) whether and how the differential lipid order can be modulated by, and/or participate in, cellular function. We studied this question in red blood cells (RBCs), based on three main features. First, the RBC is the simplest human cell, with a PM linked to an underlying cytoskeleton as only structural components, reducing interference of intracellular membranes. Second, the RBC exhibits optically-resolved lipid domains, revealed by confocal imaging upon PM trace insertion of BODIPY-

lipid analogs or upon decoration of endogenous chol and sphingomyelin (SM) by mCherry-Toxin fragments (Theta and Lysenin, respectively) (Carquin et al., 2015; Carquin et al., 2014; D'Auria et al., 2013a; D'Auria et al., 2013b; D′auria et al., 2011; Tyteca et al., 2010). At least two types of lipid domains have been shown to coexist at the RBC PM, exhibiting differential lipid enrichment and topography: one mainly enriched in chol mainly (hereafter referred as chol-enriched domains) and mostly present at the highly curved edges of the RBC biconcave membrane, *vs* another co-enriched in SM and chol (hereafter referred as SM/Chol-enriched domains) and restricted to the membrane center of lower curvature (Supplementary Fig. 1 (Leonard et al., 2017b)). Third, chol- and SM/Chol-enriched domains are differently involved in RBC function-associated reshaping such as deformation and vesiculation (Leonard et al., 2017b). *In vivo*, RBC deformation is required when it passes through the microvasculature to deliver oxygen to the tissues and is further tested for quality control when it squeezes through the narrow splenic pores. At the end of its 120-day lifetime, RBC deformability is lost upon membrane vesiculation and is followed by RBC splenic entrapment and removal from blood circulation (Mohandas and Gallagher, 2008). By using abnormally-shaped elliptocytes and by stretching healthy RBCs, we revealed that chol-enriched domains gather in increased curvature areas of the RBC membrane edges upon deformation (Leonard et al., 2017b). In contrast, SM/Chol-enriched domain abundance increases in the central membrane area in relation with secondary calcium (Ca^{2+}) efflux, a process involved in the subsequent shape and volume restoration (Leonard et al., 2017b). Additionally, by mimicking RBC membrane vesiculation upon aging by storage at 4°C, we showed that both lipid domains represent specific sites for membrane vesiculation upon aging (Supplementary Fig. 2) (Leonard et al., 2017b).

These recently obtained data compelled us to investigate whether the varied lipid domains evidenced at the living RBC surface (Leonard et al., 2017b) could exhibit a different lipid order than the bulk, and whether these differences could be modulated by and/or participate in RBC reshaping. To this end, RBCs were labelled with Laurdan, a membrane fluorescent dye sensitive to lipid hydration and order (Kaiser et al., 2009; Owen et al., 2011), and examined at their resting state and upon *in vitro* reshaping, *i.e.* deformation and vesiculation (Leonard et al., 2017b). In resting RBCs, Laurdan imaging allowed to detect a third domain population, in addition to those enriched in chol mainly and those co-enriched in SM/Chol. These various lipid domain populations exhibited a diversity of lipid order states but were all less ordered than the bulk membrane. Upon RBC deformation (elliptocytes and stimulation of calcium exchanges) or membrane vesiculation (storage at 4°C), domains became more ordered than the bulk. In aging RBCs and in membrane fragility diseases (spherocytosis), an increase in bulk-domain lipid order difference was associated to the initiation of domain

vesiculation. Altogether, differences in lipid domain order in RBC membranes are modulated upon RBC reshaping and connected to vesiculation upon aging, suggesting the relevance of this specific lipid property for other lipid domains than lipid rafts.

2. Results

2.1 Laurdan labelling of living RBCs reveals submicrometric lipid domains

When RBCs were labelled with Laurdan and spread on poly-L-lysine (PLL)-coated coverslips (Fig. 1A, Spread RBC) as previously (Carquin et al., 2015; Carquin et al., 2014; D'Auria et al., 2013a; D'Auria et al., 2013b; D'auria et al., 2011; Leonard et al., 2017b; Tyteca et al., 2010), well-defined round submicrometric domains (Fig. 1A, arrowheads) and their surrounding membrane were revealed. We then explored whether these domains corresponded to the chol- and SM/Chol-enriched domains previously evidenced (Carquin et al., 2015; Carquin et al., 2014) by careful comparison of the behavior of the domains labelled by Laurdan with those revealed by the Toxin* fragments, Theta* and Lysenin*. To confirm our observations we then performed double labelling between Laurdan and the Toxin* fragments.

We first analyzed Laurdan-labelled domain behavior in conditions for which Theta*- and Lysenin*-labelled domains behave similarly, *i.e.* (i) presence in both spread and suspended RBCs (Leonard et al., 2017b), (ii) loss upon RBC storage at 4°C (Leonard et al., 2017b), (iii) decrease of abundance upon temperature increase from 20 to 37°C (Carquin et al., 2015; Carquin et al., 2014), and (iv) vanishing upon ~15 % chol depletion (0.25 mM mβCD, 30 min) and strong decrease upon ~20 % SM depletion (2 mU/ml SMase, 10 min) (Carquin et al., 2015; Carquin et al., 2014). Like Toxin*-labelled domains (Leonard et al., 2017b), those revealed by Laurdan were present in both spread and suspended RBCs (Fig. 1A, arrowheads) and multiple stack acquisition on suspended RBCs exposed similar domain abundance than spread RBCs (Supplementary Fig. 3 *vs* Fig. 1A,a). In addition, the vast majority of Laurdan-labelled domains were lost upon storage at 4°C (Fig. 1D,b *vs* a). In contrast to Toxin*-labelled domains, Laurdan-labelled domains exhibited a similar abundance between 20 and 37°C (Fig. 1B). In addition, upon ~15 % chol depletion by mβCD (0.25 mM mBCD, 30 min) and ~20 % SM depletion by SMase (2 mU/ml SMase, 10 min), Laurdan-labelled domains were only decreased by ~25 % and ~40 % respectively (Fig. 1C). Such differential effect of environmental conditions on Laurdan- and Toxin*-labelled domains could not be due to alteration of Toxin* binding as verified before by preserved I^{125}-Theta* and -Lysenin* binding to RBCs upon treatments and by similar decrease of BODIPY-SM- and Lysenin*-labelled domains upon mβCD

treatment. All these results therefore suggested that Laurdan- and Toxin*-labelled domains only partially corresponded.

To gain better insight in this discrepancy, Laurdan-labelled domain behavior was then examined in conditions for which Theta*- and Lysenin*-labelled domains behave differently, *i.e.* (i) different abundance (Theta* >> Lysenin*) (Carquin et al., 2015; Carquin et al., 2014), (ii) preferential topographic association with the center of low curvature (Lysenin*) *vs* the highly curved edges (Theta*) of the RBC membrane (Leonard et al., 2017b), (iii) specific vanishing upon increased RBC spreading state (Lysenin*) (Carquin et al., 2015; Carquin et al., 2014), (iv) specific recruitment in highly curved edges of elliptocytes (Theta*), a model of deformed RBC (Leonard et al., 2017b), and (v) specific increased abundance with Ca^{2+} efflux stimulation (Lysenin*) (Leonard et al., 2017b). First, Laurdan-labelled domains (~3 domains/hemi-RBC) exhibited an intermediate abundance between those labelled by Lysenin* and Theta* (Carquin et al., 2015; Carquin et al., 2014). Second, they were present both in high curvature (HC) and low curvature (LC) regions (Fig. 1Aa,c), although less abundant than Theta*-labeled domains in HC (compare Fig. 1A *spread* with Supplementary Fig. 1A) (Leonard et al., 2017b). Third, Laurdan-labelled domains were moderately affected by increased spreading (Fig. 1A,b *vs* a), as Theta*-labelled domains but in contrast to those labelled by Lysenin* (Carquin et al., 2015; Carquin et al., 2014). Fourth, they were revealed in increased curvature areas of the elliptocyte edges (Fig. 1D,c), as Theta*-labelled domains (Leonard et al., 2017b). Fifth, Laurdan-labelled domains were increased in abundance along with Ca^{2+} efflux (Fig. 1D,d), as those revealed by Lysenin* (Leonard et al., 2017b). Altogether, these observations indicated that Laurdan-labelled domains at least partially corresponded to those we previously revealed by Lysenin* and Theta*, although only a part of the Theta*-labelled domain population in HC was labelled by Laurdan.

To further check for this observation, RBCs were double-labelled with Laurdan and Toxins*. As expected, Theta*-labelled domains were partly revealed by Laurdan in HC (Fig. 1Ea,a'; purple *vs* red arrowheads) whereas majority of Theta*- and Lysenin*-labelled domains were revealed by Laurdan in LC (Fig. 1Ea,b; purple arrowheads). Moreover, Laurdan revealed an additional, less abundant, domain population not decorated by Theta* or Lysenin* in LC (blue arrowhead at a & b). This additional population labelled by Laurdan could explain the discrepancy of response to environmental conditions (temperature increase and chol and SM content decrease) as compared to Toxin*-labelled domains. Altogether these data indicated that Laurdan revealed part of the Theta*-labelled domains in HC, the majority of Theta* and Lysenin*-labelled domains in LC and an additional population not decorated by Theta* or Lysenin* in LC.

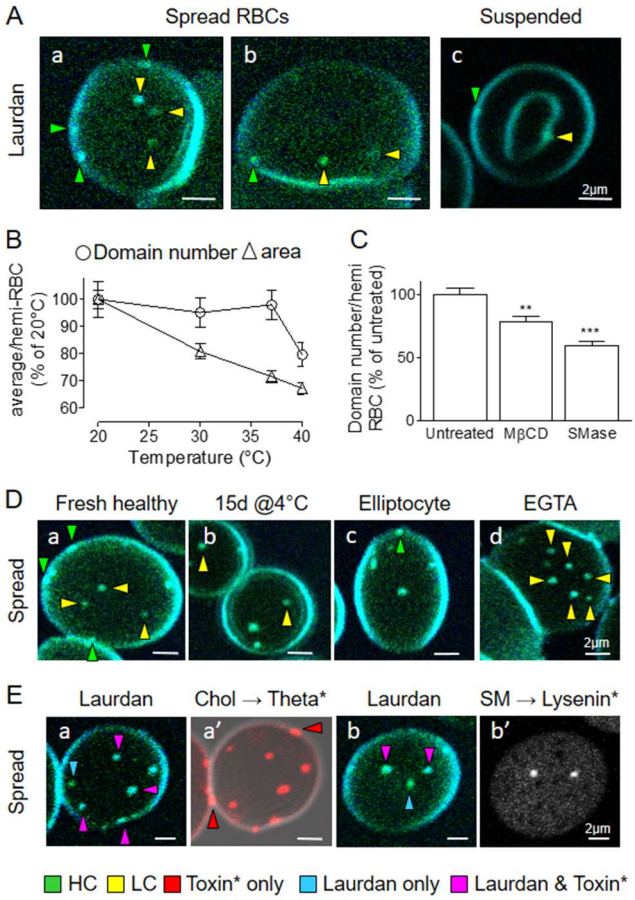

Figure 1. Labelling of living (*i.e.* non-fixed) RBCs with Laurdan reveals submicrometric domains that largely correspond to those evidenced by the Toxins*. Healthy or elliptocytotic (*elliptocyte*, D,c) RBCs, either fresh or maintained at 4°C during 15 days (*15d @ 4°C*, D,b), were left untreated or treated with EGTA in Ca^{2+}-free medium (*EGTA*, D,d), labelled with Laurdan alone or Laurdan followed by Toxins* (Theta*, *red → chol* or Lysenin*, *grey → SM*, E), spread onto PLL-coated coverslips *(spread)* or left in suspension *(suspended*, A*)* and observed by vital multiphoton (Laurdan) or multiphoton/confocal (Laurdan+Toxins*) microscopy at 20°C. (**A**) Representative imaging. Y*ellow* and *green arrowheads* point respectively to the central area (*low curvature, LC*) and the edges (*high curvature, HC*) of the RBC membrane. a and b represent different stages of spreading. (**B**) Quantification of domain number and area (both expressed as percentage of 20°C) in function of temperature. (**C**) Quantification of domain abundance (average by hemi-RBC expressed as percentage of *untreated*) upon chol (*MβCD*) or SM depletion (*SMase*). (**D**) Representative imaging. *Yellow* and *green arrowheads* point respectively to *LC* and *HC* domains. (**E**) Representative imaging. *Red, blue and purple arrowheads* point respectively to domains revealed by Toxin* only, Laurdan only or both Laurdan and Toxins*. Images are representative from 2–4 independent experiments. Results in B

and C are means ± SEM of 211–488 RBCs from 2–4 independent experiments. Statistical significance was tested with one-way ANOVA followed by Tukey's post-hoc test.

2.2 In RBCs at resting state, submicrometric lipid domains exhibit a lower order than the bulk membrane

We then examined the lipid order of submicrometric lipid domains on spread RBCs at 20°C, while keeping in mind the two differences mentioned above between Laurdan and Toxin* labeling. The GP values extracted from the Laurdan imaging were significantly lower (*i.e.* lower lipid order) for the domains than the bulk (Fig. 2A, untreated). At first glance, this observation was surprising since Laurdan experiments on model membranes show higher lipid order for chol- and SM-enriched phases (Dietrich et al., 2001; Jacobson et al., 2007). We therefore excluded potential artefacts related to Laurdan physicochemical properties or preferential partitioning. The strong photoselection of Laurdan molecules, particularly when located within the more ordered phases (Fidorra et al., 2009), was strongly reduced by using a Nomarski prism (see Material and methods Section). We also precluded a preferential partitioning of Laurdan in labelled domains in L_d-phase, as seen for C-Laurdan in GUVs (our unpublished data) or in *N*-palmitoyl-enriched-D-*erythro*-sphingosine-enriched domains (Pinto et al., 2013).

We then asked whether the lower lipid order of domains as compared to the surrounding bulk could be dependent on the RBC membrane composition, temperature, RBC spreading or membrane curvature. Chol or SM depletion using mβCD and SMase (in the same range of concentrations as above) decreased lipid order of the domains while preserving the bulk (Fig. 2A & B), in agreement with the ordering effect of chol and SM enrichment on living cells. The lower GP value for the domains than the bulk was further confirmed in suspended RBCs (Fig. 2C) and at temperature ranging from 20 to 40°C with a maximal delta GP bulk-domains ($\Delta GP_{bulk\text{-}domains}$) in the 30-37°C range (Fig. 2D), suggesting physiological relevance. Regarding topography, both lipid domains and bulk membrane exhibited higher order in the highly curved edges (HC) than the center of low curvature (LC) of the RBC membrane, in spread as well as suspended RBCs (Fig. 2E & F). However, a slight impact of RBC spreading on lipid order was observed, mainly for the domains in HC.

Altogether, these data indicated a differential lipid order between the domains and the bulk, as revealed in the $\Delta GP_{bulk\text{-}domains}$ (Fig. 2D-F, grey symbols and columns and right axes), lipid domains exposing a lower lipid order than the bulk in both spread and suspended RBCs, HC and LC areas and in a large temperature range. Whereas bulk and domain lipid order exposed similar trends in their responses to temperature and membrane curvature, lipid domain order was more dependent than the bulk on PM chol and SM contents. Several hypotheses related to differential membrane curvature and interaction with the

cytoskeleton are proposed in the Discussion to explain the lower lipid order of domains *vs* the bulk membrane.

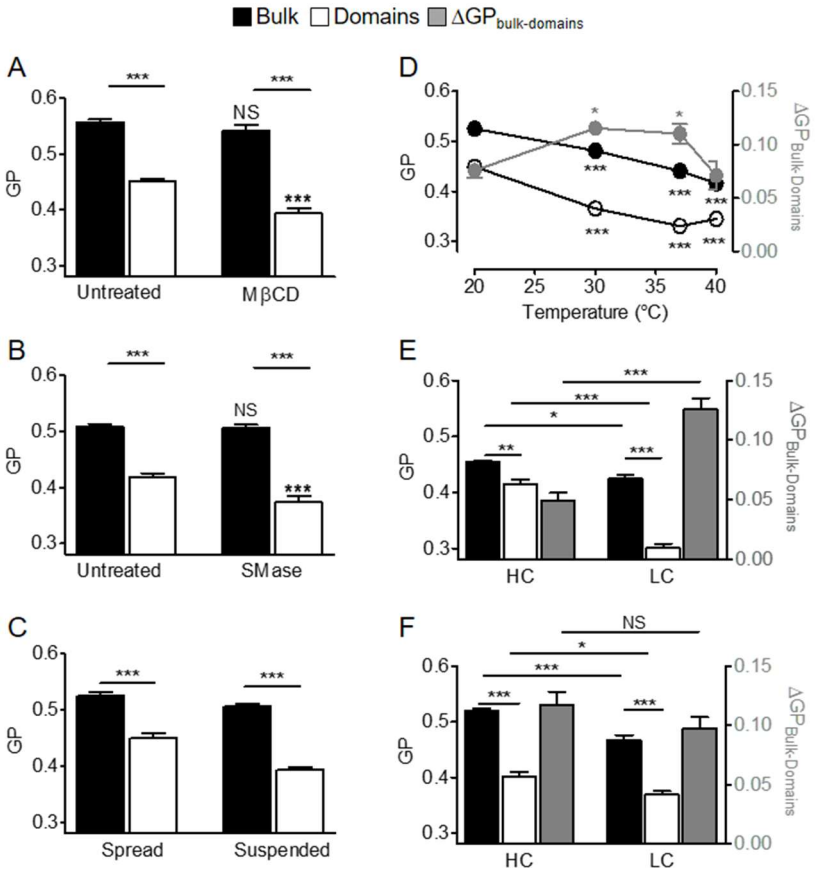

Figure 2. Lipid domains exhibit a lower order than the bulk membrane. Healthy RBCs, either left untreated or treated with MβCD or SMase (A, B), were labelled with Laurdan, spread onto PLL-coated coverslips or left in suspension *(suspended*, C*)* and observed by vital multiphoton microscopy at 20°C (except in D). Bulk (*black columns and bullets, left axis*) and domain (*open columns and bullets, left axis*) GP values were then determined and expressed as difference in GP values between bulk and domains ($\Delta GP_{bulk\text{-}domains}$, *grey bullets and columns, right axis, D-F*) or not (A-C). (**A**, **B**) RBCs depleted in chol (A, *MβCD*) or SM (B, *SMase*) and spread; (**C**) RBCs either spread *(spread)* or left in suspension *(suspended)*; (**D**) Spread RBCs analyzed in the 20-40°C temperature range; (**E**, **F**) RBCs either spread (E) or suspended (F) and compared for the central area (*low curvature, LC*) and the edges (*high curvature, HC*) of the membrane. Results are means ± SEM of 175–352 RBCs from 2–3 independent experiments. Statistical significance was tested with one-way ANOVA followed by Tukey's post-hoc test *(open and black columns)* or two-sample t-tests (*grey columns*). Statistical test mentioned above a bar reveals comparison to the control condition (*i.e.* fresh, untreated, healthy RBCs at 20°C), while statistical test above a connecting line indicates comparison inside a group.

2.3 Three types of submicrometric lipid domains with distinct order, composition and topography coexist at the RBC plasma membrane

Based on our suggestion for the coexistence of three Laurdan-labelled domain populations (those chol-enriched in HC, those SM/Chol-co-enriched in LC and those not enriched in these lipids in LC) and since lipid domains in HC showed higher order than those in LC, we asked whether the three domain populations could exhibit distinct lipid order. To this aim, we analyzed the GP distribution of the domains using GP density histograms (Fig. 3A) and GP images (Fig. 3B) both obtained from Laurdan images. In terms of lipid order, while the HC area of the membrane seemed to reveal one domain population (major P1 *vs* P2 contribution in Fig. 3A left; P'1, green arrowheads in Fig. 3B), two populations appeared to coexist in LC (P1 and P2 contribution in Fig. 3A right; P'1 and P'2, yellow arrowheads in Fig. 3B). However, the HC population had a very close GP value to the more ordered population in LC (compare P1 in Fig. 3A left *vs* right, and P'1 in Fig. 3B green *vs* yellow arrowheads). These results suggested the presence of at least two distinct populations in terms of lipid order, a more ordered population associated to both HC and LC (P1 in GP density distribution and P'1 in HSB images) and a less ordered population observed in LC (P2 in GP density distribution and P'2 in HSB images).

We then asked for the identity between these two domain populations, revealed by Laurdan domain GP distribution and imaging, and the three domain populations previously unveiled based on chol and SM enrichment and topography. We first evaluated the impact of partial chol or SM depletion on the domain GP distribution, in the conditions for which we previously showed a decrease of the global domain GP value and a higher abrogation of the chol- and SM-enriched domain populations than on the one not enriched in these lipids. These treatments did not, or only slightly, changed P1 and P2 mean GP values (Fig. 3C) but decreased the contribution of P1 *vs* P2 to the global domain GP distribution (Fig. 3C, orange filled columns and right axes). This suggested that the more ordered P1 population could be mostly influenced by chol- and SM/Chol-enriched domains while the less ordered P2 population could represent those not enriched in these lipids. This hypothesis was confirmed by analysis of lipid order in RBCs co-labeled with Laurdan and Toxins* which indicated that Laurdan-labelled domains colocalized either with Theta* or Lysenin* exposed a close GP value, significantly higher than those only labelled by Laurdan (Fig. 3D). Furthermore, it should be noticed that the P1 population was considerably more abundant than the P2 one as revealed by P1 weight (Fig. 3C, untreated). Accordingly, the chol- and SM/Chol-enriched domains were more abundant than those not enriched in these lipids.

All these observations suggested the coexistence at the PM of living RBCs of at least three domain populations in terms of lipid composition, topography and lipid order. The population associated with the edges and enriched in chol mainly showed a GP value close to the one of the population restricted to the cell center and enriched in both chol and SM. In contrast, the domain population restricted to the center of the cell but enriched neither in chol nor SM exhibited a lower GP value than the two other domain populations.

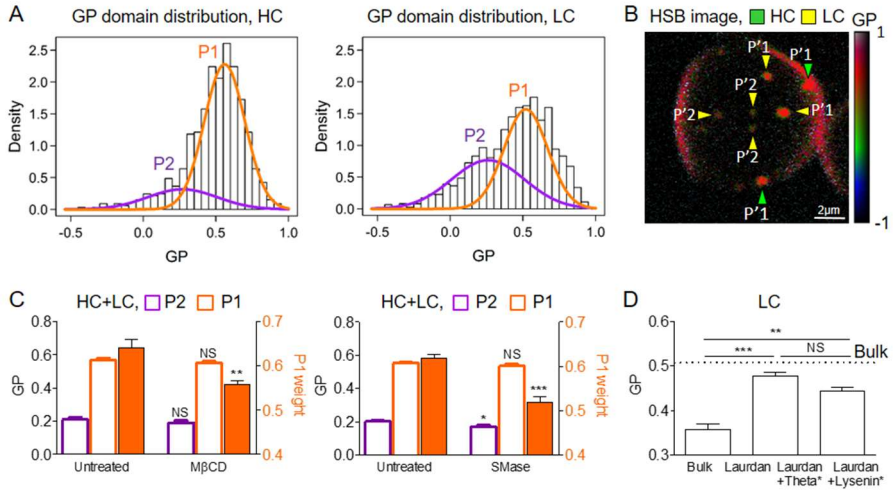

Figure 3. Three types of lipid domains with distinct lipid order and topography coexist. Fresh healthy RBCs, either left untreated or treated with MβCD or SMase (C), were labelled with Laurdan alone (A-C) or Laurdan followed by Toxins* (D; Theta*→ *chol* or Lysenin*→ *SM*), spread onto PLL-coated coverslips and observed by vital multiphoton (Laurdan alone) or multiphoton/confocal (Laurdan+Toxins*) microscopy at 20°C. (**A**) GP domain distribution in *HC* (*left panel*) and *LC* (*right panel*) calculated from one Laurdan image (35 RBCs). Notice one major GP domain population in *HC* (*P1*) and two in *LC* (*P1* and *P2*). (**B**) Representative HSB imaging of one Laurdan-labelled RBC. *Yellow* and *green arrowheads* point respectively to the central area (*low curvature, LC*) and the edges (*high curvature, HC*) of the RBC membrane. Notice one GP domain population in *HC* (*P'1*) and two in *LC* (*P'1* and *P'2*). (**C**) Quantification based on representative data presented at A: GP values of *P1* (*white columns boxed in orange, left axis*) and *P2* (*white columns boxed in purple*) and of the proportion of *P1* as compared to *P2* (*orange columns and left axis)* in untreated RBCs or upon chol or SM depletion. (**D**) Quantification of GP values for LC domains (*open columns*) labelled with Laurdan only (*Laurdan*) or Laurdan and Toxins* (*Laurdan+Theta**, *Laurdan+Lysenin**). GP distributions (calculated from 35 RBCs) and the GP image are representative of 6 independent experiments. Results are means ± SEM of 142–352 RBCs from 2–3 independent experiments (C-D). Statistical significance was tested with one-way ANOVA followed by Tukey's post-hoc test or two-sample t-tests (*orange columns*). Asterisk directly above a bar indicates a mean significantly different from its counterpart in the control condition, while the

significance level above a connecting line indicates a difference between two means observed inside a group.

2.4 Upon RBC deformation and vesiculation, lipid domain order increases to a similar or higher level than the bulk, leading to a $\Delta GP_{bulk\text{-}domains}$ decrease

We previously exposed the implication of chol- and SM/Chol-enriched domains in RBC deformation and vesiculation (Leonard et al., 2017b): (i) chol-enriched domains are recruited in increased curvature areas of the membrane edges upon deformation, (ii) SM/Chol-enriched domains are increased in abundance in low curvature areas, allowing for Ca^{2+} efflux during the following shape and volume restoration, and (iii) both lipid domains are specific sites for membrane vesiculation upon aging (Leonard et al., 2017b). As shown in Fig. 1D, Laurdan-labelled domains were similarly reorganized during these processes. Because the differential lipid order between lipid domains and the surrounding membrane is thought to be relevant for cell physiology through its impact on membrane protein sorting (Owen et al., 2012; Stone et al., 2017b), we therefore asked whether lipid domain order and differential bulk-domain order ($\Delta GP_{bulk\text{-}domains}$) are modulated during RBC reshaping.

To study lipid domain order in HC upon RBC deformation, we used as previously elliptocytes as a model of affected RBC shape (Leonard et al., 2017b). We first verified by RBC double-labeling with Laurdan and Theta* that Laurdan-labelled domains in HC of elliptocyte membrane corresponded to those enriched in chol, as previously observed (Leonard et al., 2017b) (Supplementary Fig. 4A). We then compared healthy RBCs and elliptocytes for their bulk and domain lipid order in HC (Fig. 4A, green arrowheads in left). We observed in elliptocytes an increase of the bulk order (Fig. 4A, black columns in right panel) along with an even stronger increase of domain lipid order (Fig. 4A, open columns) that reached higher GP value than the one of the bulk, leading to a decreased $\Delta GP_{bulk\text{-}domains}$ (Fig. 4A, grey columns and right axis). The GP density histogram of elliptocyte HC domains revealed only one domain population, as for healthy RBCs (Supplementary Fig. 4B), suggesting that the global domain order change was not due to the formation of a new domain population with higher order but instead to the order increase of the preexisting one. Altogether, these data indicated that lipid domains in HC can reach a higher order than the bulk. In the Discussion, we propose a possible explanation for the increase of lipid domain order in elliptocytotic RBC, based on horizontal cytoskeleton link impairment responsible for progressive shape transformation from discocyte to elliptocyte with time in the circulation (Mohandas and Gallagher, 2008).

We then stimulated Ca^{2+} efflux through RBC incubation with a Ca^{2+}-chelating agent (*i.e.* EGTA) in a Ca^{2+}-free medium (Leonard et al., 2017b) to induce SM/Chol-enriched domain abundance increase in LC during shape and volume restoration after deformation (Leonard et al., 2017a). This approach, which increased Laurdan-labelled domain abundance in LC as observed before with Lysenin* or BODIPY-SM (Leonard et al., 2017a) (Supplementary Fig. 4C), slightly increased the lipid order of LC domains while preserving the bulk lipid order, resulting into a decreased $\Delta GP_{bulk\text{-}domains}$ (Fig. 4B). More precisely, we observed an increased proportion of the more ordered P1 population (Supplementary Fig. 4D), without significant changes in P1 and P2 lipid order. This indicates that the increase of LC domain order by Ca^{2+} efflux stimulation could result from an increased abundance of the more ordered P1 population, as an additional line of evidence for the coexistence of two domain populations in LC and for the correspondence of SM/Chol-enriched domains and P1 populations.

Finally, we took benefit from the possibility to induce lipid domain local vesiculation by RBC storage at 4°C (Leonard et al., 2017b) to ask whether lipid domain order is modulated upon their vesiculation. Vesiculating chol-enriched domains, evidenced by double-labelling with Laurdan and Theta* (Fig. 4C, left panel, white arrows), exposed an increased lipid order, that became higher than the bulk and led to a decreased $\Delta GP_{bulk\text{-}domains}$ (Fig. 4C, right panel). Similar GP values were obtained for vesicles in aged RBCs labelled with Laurdan only (Supplementary Fig. 4E). Thus, lipid domains exposed an increased lipid order upon local membrane vesiculation.

Altogether, these data indicated that the lipid order of lipid domains, lower than the one of the bulk in resting RBCs, was increased upon RBC deformation and vesiculation to higher GP values than the bulk, leading to a decreased order difference between the domains and the bulk.

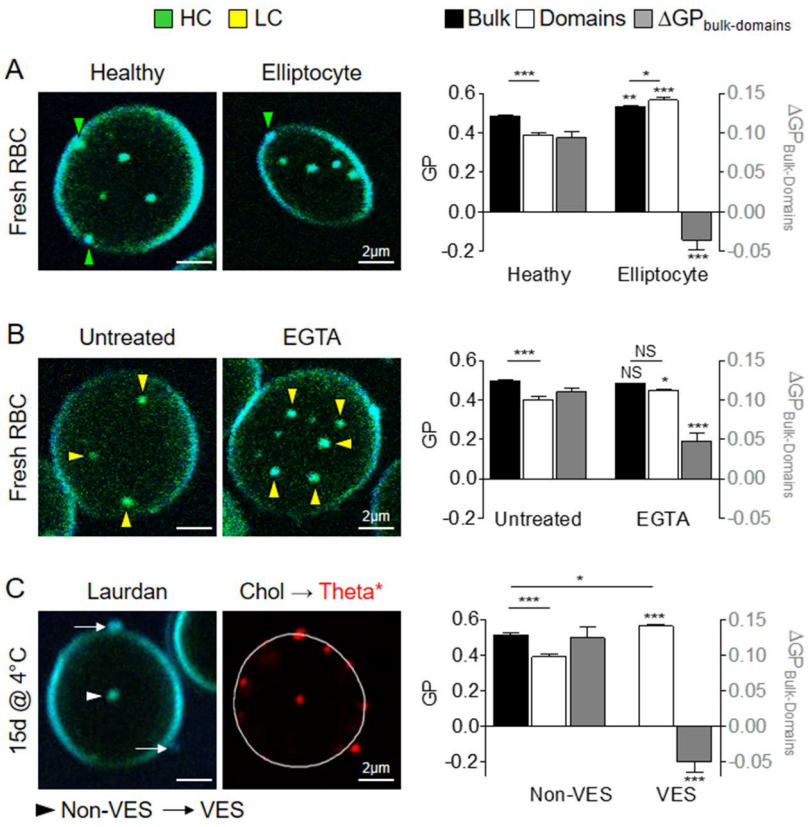

Figure 4. Lipid domain order increases upon RBC deformation and vesiculation, leading to a decrease of the bulk-domain differential order. Healthy or elliptocytotic (A) RBCs, either fresh or maintained at 4°C during 15 days (15d @ 4°C, C), were left untreated or treated with EGTA in Ca^{2+}-free medium (*EGTA*, B), labelled with Laurdan alone (A, B) or Laurdan followed by Theta* (C), spread and observed by vital microscopy at 20°C. Left panels, representative vital imaging. *Yellow* and *green arrowheads* point respectively to *LC* and *HC domains*, while *white arrowhead* and *arrows* point to non-vesiculating (*Non-VES*) and vesiculating (*VES*) Laurdan-labelled chol-enriched domains in aged RBCs. Right panels, quantification of the GP values of the bulk (*black columns, left axis*) and domains (*open columns, left axis*) and difference in bulk and domain GP values ($\Delta GP_{bulk\text{-}domains}$, *grey columns, right axis*) in *HC* (*A)* or *LC* (*B)* and *Non-VES* and *VES* (*C)*. Images are representative from 2–4 independent experiments. Results are means ± SEM of 281–412 RBCs from 2–4 independent experiments. Statistical significance was tested with one-way ANOVA followed by Tukey's post-hoc test (*black and open columns*) or with two-sample t-tests (*grey columns*). Asterisk directly above a bar indicates a mean significantly different from its counterpart in the control condition, while the significance level above a connecting line indicates a difference between two means observed inside a group.

2.5 Upon RBC storage at 4°C, bulk lipid order increases, leading to a $\Delta GP_{bulk\text{-}domains}$ increase and domain vesiculation

Upon RBC aging, cytoskeleton stiffness and density increase, possibly due to the loss of mid-point attachments of the spectrin filaments to the bilayer through the ankyrin complexes (Sens and Gov, 2007). These changes lead to larger compressive forces on the cell membrane and have been hypothesized to be accommodated by increased membrane curvature and vesicle detachment from the membrane (Edwards et al., 2005; Fricke and Sackmann, 1984; Gov and Safran, 2005). Additionally, theoretical works and experiments on model membranes propose that lipid order disparity between L_o and L_d phases, and the related unfavorable line tension at domain boundary, drives specific domain budding and following fission (Baumgart et al., 2003; García-Sáez et al., 2007b; Jülicher and Lipowsky, 1993). We therefore asked whether the increased cytoskeleton compression applied to the membrane could contribute, along with changes in lipid order disparity, to the initiation of lipid domain vesiculation in RBCs upon aging, by respectively measuring the GP_{bulk} and the $\Delta GP_{bulk\text{-}domains}$ in RBCs upon storage at 4°C to mimick RBC aging.

RBCs upon storage at 4°C were first characterized for their surface area and circularity as well as for their lipid domain abundance (Fig. 5A-C). Two stages of aging were defined: Aged#1, with moderate surface area loss, slight circularity increase and no significant domain loss, and Aged#2, with high membrane loss, high circularity and large domain loss. Aged#1 could therefore correspond to aged RBCs before domain vesiculation, while Aged#2 could represent aged RBCs after major domain vesiculation. Unlike vesiculating domains (see Fig. 4C), domain lipid order was not modified upon aging before domain vesiculation (Fig. 5D, open columns and left axis, Aged#1 and Aged#2). In contrast, bulk lipid order was first increased at Aged#1 and thereafter decreased at Aged#2 (Fig. 5D, black columns and left axis). This led to an increased $\Delta GP_{bulk\text{-}domains}$ at Aged#1 stage, *i.e.* prior major domain vesiculation, followed by a decreased $\Delta GP_{bulk\text{-}domains}$ back to its initial value at Aged#2, *i.e.* after major domain vesiculation (Fig. 5D, grey columns and right axis).

Altogether, these data indicated that GP_{bulk} was increased upon aging, leading to an increased $\Delta GP_{bulk\text{-}domains}$ (Aged#1), together with the initiation of domain vesiculation (Aged#2).

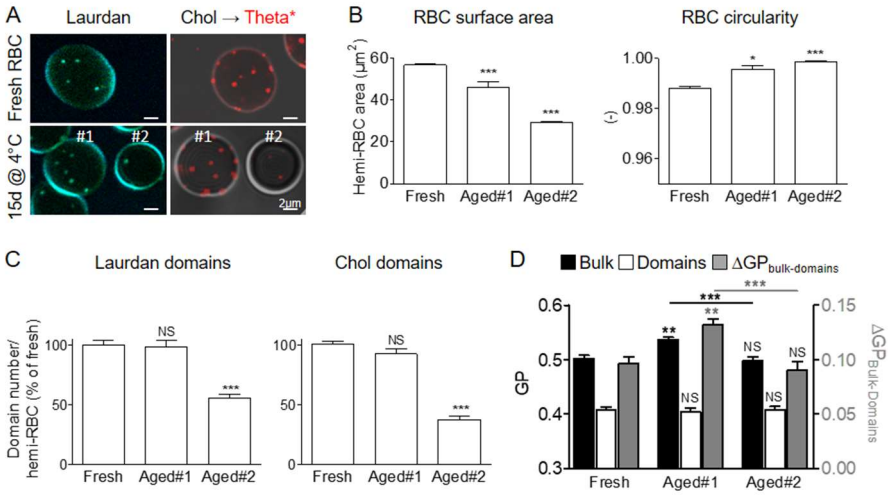

Figure 5. Bulk membrane order increases upon aging, leading to an increase of the bulk-domain differential order and to domain vesiculation. Healthy RBCs, fresh or maintained during 15 days at 4°C (*15d @ 4°C*), were labelled with Laurdan or Theta* (*chol*), spread and observed by vital multiphoton or confocal microscopy at 20°C. *#1* and *#2* label respectively the first and second stage of aging in terms of RBC surface area and circularity (B) and domain number (C). (**A**) Representative vital imaging. Images of Theta* labeling were superposed to RBCs in transmission to highlight cell periphery. (**B**) Quantification of RBC area (µm^2 by hemi-RBC) and circularity. **(C)** Quantification of Laurdan- and Theta*-labeled domain abundance (average by hemi-RBC expressed as percentage of fresh RBCs). **(D)** Quantification of bulk (*black columns, left axis*) and domain GP values (*open columns, left axis*) and difference in GP values between bulk and domains ($\Delta GP_{bulk\text{-}domains}$, *grey columns, right axis*) for fresh RBCs and RBCs at their two stages of aging during the 15 days at 4°C. Images are representative from 2 independent experiments. Results are means ± SEM of 37–231 RBCs from 2 independent experiments. Statistical significance was tested with one-way ANOVA followed by Tukey's post-hoc test (*black and open columns*) or with two-sample t-tests (*grey columns*). Asterisk directly above a bar indicates a mean significantly different from its counterpart in the control condition (*i.e.* fresh RBCs), while the significance level above a connecting line indicates a difference between two means observed inside a group.

2.6 Both $\Delta GP_{bulk\text{-}domains}$ and domain vesiculation are increased in spherocytosis but instead decreased in elliptocytosis

We then further investigated the potential link between the increased cytoskeleton compression applied to the membrane (reflected by the GP_{bulk} increase), the increased lipid order disparity (reflected by the $\Delta GP_{bulk\text{-}domains}$ increase) and the initiation of domain vesiculation, using RBCs from a patient with spherocytosis, the most common hereditary RBC membrane disorder caused by defects in proteins that vertically connect the membrane to the

cytoskeleton, *i.e.* the ankyrin complexes (Eber and Lux, 2004). Indeed, as upon healthy RBC aging, such a defect induces impairment of membrane:cytoskeleton cohesion and increases the pressure exerted by the cytoskeleton on the membrane, leading to membrane destabilization, the release of vesicles and the decrease of the RBC surface area-to-volume ratio and deformability (Perrotta et al., 2008). In terms of lipid order, the increased membrane pressure should give rise to more compressed and ordered lipids, as observed for healthy RBC aging. As expected, fresh spherocytes exposed a higher increase of lipid order in the bulk (Fig. 6B, black columns and left axis) than in the lipid domains (Fig. 6B, open columns and left axis), leading to an increased $\Delta GP_{bulk\text{-}domains}$ (Fig. 6B, grey columns and right axis). These changes were similar to those observed in healthy Aged#1 RBCs (Supplementary Fig. 5B). Upon storage at 4°C for 7 days, spherocytes showed a decrease of both Laurdan-labelled and chol-enriched domains (Fig. 6A; quantification in Fig. 6C for Laurdan-labelled domains and in Supplementary Fig. 5A for chol-enriched domains). Such decrease could result from the budding of chol-enriched vesicles from the membrane during this time interval, reducing thereby the pressure exerted by the cytoskeleton on the membrane, as reflected in the decrease of the GP_{bulk} (Supplementary Fig. 5B) and the $\Delta GP_{bulk\text{-}domains}$ back to their initial values (Fig. 6D). All these changes were similar to those found in healthy Aged#2 RBCs after 15 days of storage.

Based on the relation between the increased cytoskeleton compression applied to the membrane, the increased lipid order disparity and the initiation of domain vesiculation observed in both healthy RBC aging and spherocytosis, we then examined lipid order upon lower cytoskeleton pressure expected to rather produce a lower rate of vesicles. This was achieved by analyzing upon aging RBCs from patients with elliptocytosis, a disease due to disruptions of horizontal cytoskeleton interactions, resulting into alteration of spectrin tetramer self-association and decreased deformability (Diez-Silva et al., 2010). As already shown at Fig. 4A, fresh elliptocytes exhibited a higher increased lipid order in the domains (Fig. 6B, open columns and left axis) than in the bulk (Fig. 6B, black columns and left axis), leading to a decreased $\Delta GP_{bulk\text{-}domains}$ (Fig. 6B, grey columns and right axis). Moreover, as hypothesized, elliptocytes exhibited no domain loss in the 0-15 days storage (Fig. 6A; quantification in Fig. 6C for Laurdan-labelled domains and in Supplementary Fig. 5A for chol-enriched domains) and the lower $\Delta GP_{bulk\text{-}domains}$ in fresh elliptocytes as compared to Aged#1 healthy RBCs or spherocytes was accordingly maintained all along the storage.

Altogether, these data indicated that, in comparison to healthy RBCs, fresh spherocytes, which exhibited higher pressure applied by the cytoskeleton on the membrane, exposed higher $\Delta GP_{bulk\text{-}domains}$ together with an accelerated initiation of domain vesiculation upon aging. The opposite was observed for elliptocytes, which exhibited lower pressure applied by the cytoskeleton on

the membrane and exposed lower $\Delta GP_{bulk\text{-}domains}$ and reduced domain vesiculation upon aging. This suggests that the cytoskeleton pressure mainly contributes to control the $\Delta GP_{bulk\text{-}domains}$ and to drive RBC vesiculation.

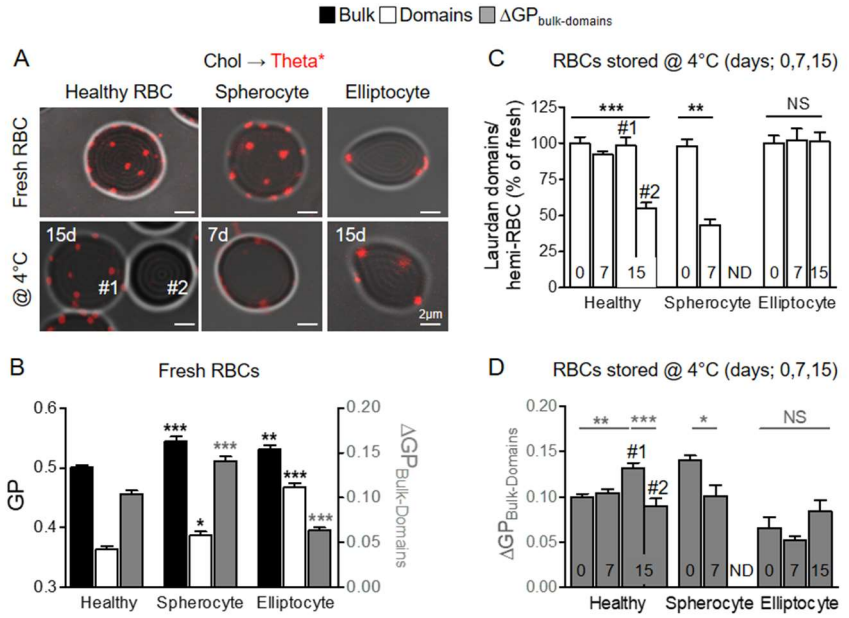

Figure 6. Spherocytes and elliptocytes respectively exhibit higher and lower bulk-domain differential order than healthy RBCs, resulting into accelerated and reduced domain vesiculation upon aging. Healthy RBCs, spherocytes or elliptocytes, either fresh or maintained for the indicated times at 4°C, were labelled with Laurdan (B-D) or Theta* (A, *chol*), spread and observed by vital multiphoton or confocal microscopy at 20°C. *#1* and *#2* label respectively the first and second stage of aging, as defined at Fig. 5. (**A**) Representative vital imaging of chol-enriched domains upon aging. (**B**) Quantification of bulk (*black columns, left axis*) and domain GP values (*open columns, left axis*) and difference in GP values between bulk and domains ($\Delta GP_{bulk\text{-}domains}$, *grey columns, right axis*) for fresh healthy RBCs, spherocytes and elliptocytes. (**C**, **D**) Quantification of Laurdan-labeled domain number (C; average by hemi-RBC expressed as percentage of fresh RBCs) and $\Delta GP_{bulk\text{-}domains}$ (D) for healthy RBCs, spherocytes and elliptocytes maintained for the indicated times at 4°C (*numbers* in *open* and *grey columns*). Images are representative of 2 independent experiments. Results are means ± SEM of 66–231 RBCs from 2 independent experiments. Statistical significance was tested with one-way ANOVA followed by Tukey's post-hoc test. Asterisk directly above a bar indicates a mean significantly different from its counterpart in the control condition while the significance level above a connecting line indicates a difference between two means observed inside a group.

3. Discussion

The differential lipid order between lipid rafts and the surrounding bulk membrane is thought to be highly relevant for cell physiology. Based on our recent demonstration of submicrometric domains enriched in chol or SM/Chol at the living RBC surface (Carquin et al., 2015; Carquin et al., 2014) and their contribution to RBC deformation and vesiculation upon aging (Leonard et al., 2017b), we here asked whether the seminal concept of high ordering of lipid rafts could also be relevant for submicrometric lipid domains. We also explored whether the differential lipid order between submicrometric domains and the surrounding membrane can be modulated by, and/or participate in, cell functions such as RBC reshaping.

Upon Laurdan labeling of the RBC PM, submicrometric domains were revealed, as previously reported by Sanchez and coll. at the rabbit RBC surface (Sanchez et al., 2012). Thanks to RBC double-labelling with Laurdan and Toxin* fragments, three domain populations were revealed by Laurdan at the resting RBC PM: (i) a part of Theta*-labelled domains in HC; (ii) the vast majority of Theta*- and Lysenin*-labelled domains in LC; and (iii) an additional population in LC, not labelled by the Toxins*. By analysis of the GP distribution on GP histogram density plots and GP images, two very distinct populations were evidenced in terms of lipid order: (i) one more ordered, more abundant and present in both HC and LC, and (ii) another less ordered, less abundant and associated to LC. Based on membrane chol and SM content decrease using pharmacological agents and co-labelling of Laurdan with the Toxins*, we suggested that the first population corresponded to chol-enriched domains in HC and to SM/Chol co-enriched domains in LC, while the second one corresponded to domains not enriched in these lipids and labeled by Laurdan alone in LC.

Two characteristics of lipid domains allowed to distinct them from the bulk upon Laurdan labeling, *i.e.* their higher fluorescence intensity and their lower GP values at resting state. One potential hypothesis to explain the higher fluorescence intensity of Laurdan-labelled domains than the bulk relates to the high curvature that the domains could adopt (Ursell et al., 2009). Highly curved membranes are able to accumulate lipids or stains with high intrinsic curvature (Heinrich et al., 2010). Since Laurdan structurally resembles to lysolipids, known for their positive intrinsic curvature because of their single lipid tail, it could accumulate in highly curved domains, explaining the increase of their fluorescence intensity. Regarding GP values of lipid domains *vs* the bulk membrane, the range we showed in living resting RBCs was smaller than the one evidenced in sterol-containing biomimetic GUVs (Dietrich et al., 2001; Jacobson et al., 2007), but close to that observed on the more natural GPMVs (ΔGP from 0.05 to ~0.15 in RBCs and from ~0.07 to ~0.1 in GPMVs *vs* ~0.8 in GUVs) (Sezgin et al., 2015). This was not

surprising since biological membranes likely maintain rather small order differences, as this configuration could allow cells to modulate them with relatively little energy input. More amazing was that the different lipid domain populations in fresh healthy RBCs at resting state exhibited lower order than the bulk, whatever the temperature, RBC spreading state and membrane curvature. Although in agreement with the major coverage of the membrane by an ordered phase in rabbit RBCs (Sanchez et al., 2012), apical membranes of polarized epithelial cells (Meder et al., 2006), CHO cells (Sanchez et al., 2012) and HeLa cells (Owen et al., 2012), our observation did not fit with the higher lipid order of rafts as compared to the surrounding bulk lipids. Several non-exclusive explanations can be provided to explain the lower GP values of Laurdan-labelled domains than the bulk. The first one relates to the higher curvature that the domains could adopt (Ursell et al., 2009), hence a highly positive curvature would allow for more water penetration at the exoplasmic interfacial part of the membrane, resulting in a red-shift of the laurdan emission spectra and a decrease of its GP (Parasassi et al., 1994). Second, a reduced GP in the domains as compared to the bulk could result from a partial loss of membrane asymmetry in those spots. This hypothesis is unlikely since fresh RBCs were not labelled with Annexin V, a fluorescent probe for outer leaflet phosphatidylserine, indicating preservation of lipid asymmetry in fresh RBCs at resting state (unpublished data). Third, a differential enrichment in membrane proteins between the bulk and the domains could contribute to regulate their distinct lipid order. Indeed, transmembrane proteins have been shown to restrict lipid lateral mobility in the RBC membrane (Golan et al., 1984). This is also suggested by our results since lipid domain and bulk lipid order increased during their local vesiculation, yet RBC vesicles are highly enriched in proteins (D'Alessandro et al., 2010) and RBC bulk lipid order decreases after vesiculation (Aged#2).

Although lipid domains all exhibited a lower GP value than the bulk at RBC resting state, it should be noticed that only a part of the Theta*-labelled domain population in high curvature areas was labelled by Laurdan, either due to a too close fluorescence intensity or GP value between these domains and their surrounding bulk environment. We can therefore not exclude the possibility that the chol-enriched domain population not revealed by Laurdan and associated with RBC high curvature exhibits a higher order than the bulk. Furthermore, while our GP imaging did not reveal significant differences between the chol-enriched domain population in high curvature and the SM/chol-enriched domains in low curvature, it is possible that they in fact expose different lipid order. Accordingly, high spatial resolution atomic force microscopy of the RBC membrane allowed us to reveal lipid domains correlated with both local minima and maxima areas in the Young's modulus maps (Dumitru et al, submitted). This suggests that the RBC membrane is made of lipid domains exhibiting differential local mechanical properties,

which could depend on the specific lipid domain composition and on their differential association to membrane and cytoskeletal proteins.

Since the differential bulk-domain lipid order was systematically modulated in RBC aging, in spherocytosis and in elliptocytosis, the cytoskeleton density and its membrane anchorage should play a key role in controlling bulk membrane lipid order and the differential lipid order between the domains and the bulk. We propose that bulk membrane, but not lipid domains, exhibits high connectivity to the cytoskeleton, in turn causing higher lipid order through the spectrin filaments and/or the membrane:cytoskeleton anchorage complexes. Three lines of evidence support this hypothesis. First, upon RBC labeling of CD47 to identify ankyrin-based complexes in healthy RBCs, we have previously shown that antibody-induced CD47 patches and lipid domains (revealed upon insertion of BODIPY-lipids) are not colocalized but are in close proximity (D'Auria et al., 2013b), suggesting the preferential membrane:cytoskeleton interaction outside of the domains. Second, we here evidenced an increase of the bulk lipid order in spherocytosis. If the GP value serves as a sensor for the compressive pressure applied by the cytoskeleton on the membrane, higher the bulk order is, higher the compression due to the cytoskeleton should be. This is exactly what we observed in RBCs of this patient, which exhibit an increased spectrin network density (unpublished; confocal and transmission electron microscopy). It remains to determine how interactions with anchorage complexes are also affected in these spherocytotic RBCs, but theoretical studies by Gov and coll. show that the loss of the spectrin:membrane anchorage stiffens the cytoskeleton (Gov, 2007b; Lai et al., 2015). These spherocytotic RBCs also have a higher content in intracellular calcium, known to increase the connectivity of the RBC cytoskeleton (Liu et al., 2005), supporting increased connectivity to the cytoskeleton and resulting higher membrane compression. Third, lipid order of the bulk membrane was also increased in aged RBCs, which exhibit higher calcium content but reduced ATP level (unpublished). Since both features are known to give rise to more fully connected spectrin network and higher compression, this represents an additional line of evidence for the increased lipid order of the bulk membrane due to higher connectivity to the cytoskeleton.

The increased lipid order of the bulk membrane observed upon RBC aging and in spherocytosis could result into membrane vesiculation allowing for membrane compression reduction. Indeed, it has been hypothesized several years ago that upon RBC aging the larger compressive forces on the cell membrane due to cytoskeleton stiffness and density increase could be accommodated by increased membrane curvature and vesicle detachment from the membrane (Edwards et al., 2005; Fricke and Sackmann, 1984; Gov and Safran, 2005). Accordingly, based on a two-component coarse-grained molecular dynamics RBC membrane model, Li and Lykotrafitis have revealed

that lateral compression generates large vesicles with heterogeneous composition, similar in size to the cytoskeleton corral (Li and Lykotrafitis, 2015). The lower vesiculation we observed here in elliptocytosis is also in agreement with the role of the cytoskeleton, since a lower compression is expected to occur in elliptocytotic RBCs. Besides the cytoskeleton pressure, our data suggest that the biophysical properties of the lipid domain that will become a vesicle, *i.e.* differential order between bulk and domains, also represent a key feature in driving the budding vesicle. This is supported by the following lines of evidence (i) vesiculation of chol- and SM-enriched domains is evident after 15 days of storage at 4°C (Leonard et al., 2017b); (ii) healthy RBCs showed a $\Delta GP_{bulk\text{-}domains}$ increase upon aging (Aged#1), resulting from bulk order increase and preceding domain vesiculation (Aged#2); (iii) fresh spherocytes exposed an increased $\Delta GP_{bulk\text{-}domains}$, along with accelerated domain vesiculation upon aging, as compared to healthy RBCs; (iv) fresh and aged elliptocytes exposed a lower $\Delta GP_{bulk\text{-}domains}$, along with a reduced domain vesiculation upon aging, as compared to healthy RBCs; and (v) both aged healthy RBCs and spherocytes did not vesiculate anymore when $\Delta GP_{bulk\text{-}domains}$ decreased back to its initial value in fresh healthy RBCs. We propose that this increase in the bulk-domain differential lipid order could increase line tension at domain boundary, thereby acting as triggering event for domain vesiculation. Indeed, the line tension at L_o/L_d boundary increases quadratically with thickness difference between the phases (Akimov et al., 2007; García-Sáez et al., 2007b; Kuzmin et al., 2005). Whether L_o/L_d lipid order difference could also reflect the line tension is unknown, yet is supported by C-Laurdan experiments on GPMVs exposing a strong linear correlation between $\Delta GP_{Lo/Ld}$ and T_{mix} (Levental and Veatch, 2016), the line tension being proportional to T_{mix} (García-Sáez et al., 2007b) (however not in a simple way for complex membrane systems (Bleecker et al., 2016; Heberle et al., 2013)). Additionally, theoretical works suggest that the reduction of the domain-bulk interface length, hence the line tension energy associated at the boundaries between coexisting fluid (L_o/L_d) domains, is the driving force for domain budding and fission (Lipowsky, 1992). If so, the compressive force and the line tension can act together to complete the bud growth and detachment in a "synergistic" model where the cytoskeleton pressure on the membrane plays a major role and is coupled to the lipid order properties of the nascent budding vesicle: cytoskeleton compression causes the initial bud to form from a lipid domain exhibiting a differential local curvature, lipid composition and lipid order compared to the surrounding membrane. This model is in agreement with theoretical studies speculating that the forces applied to the membrane by the cytoskeleton combined with lipid composition segregation can drive vesiculation (Sens and Gov, 2007).

In elliptocytosis, a model of RBC reshaping, lipid order associated to the chol-enriched domains increased to higher level than the bulk. Since lipids are

unlikely to contribute alone to membrane curvature (Zimmerberg and Kozlov, 2006), changes in lipid order could reflect lipid interaction with membrane bending proteins (Zhao et al., 2013) or cytoskeleton proteins (Arumugam and Bassereau, 2015). In favor of the latter hypothesis, the weaker cytoskeleton network due to impairment of horizontal links in elliptocytosis exerts a weaker compression on the membrane. The domains may therefore be less curved and present higher order as compared to healthy RBCs. We still need to explore whether lipid domain order changes can influence and/or can be influenced by protein sorting.

Overall, this study demonstrates that the lipid order of submicrometric domains differs from the one of the bulk and can be modulated by, and is involved in, physiological processes such as RBC reshaping. Furthermore, we propose that the differential lipid order between the domains and the bulk can be tuned by cells, through cytoskeleton compression applied to the membrane to use the line tension energy at domain boundary as a control mechanism of lipid domain participation in vesiculation. Besides lipid order, it would be appealing to evaluate other biophysical properties that are known to participate to the line tension energy (*e.g.* domain bending rigidity, intrinsic curvature or thickness) and alternative control mechanisms than membrane:cytoskeleton anchorage (*e.g.* membrane bending proteins and charge-mediated sequestration). Altogether, this study brings news concepts regarding the complexity and tunability of membrane lipid heterogeneities and their participation to cellular functions.

4. Material and methods

4.1 Red blood cell isolation and washing

This study was approved by the Medical Ethics Institutional Committee of the Université catholique de Louvain and experiments were performed according to relevant guidelines. RBCs were freshly isolated from four healthy volunteers, one splenectomized patient with spherocytosis and one patient with hereditary elliptocytosis; each donor gave written informed consent. Blood was collected by venopuncture into dry K^+/EDTA-coated tubes and, prior experiments, diluted at 1:10 in Dulbecco's Modified Eagle Medium (DMEM containing 25 mM glucose, 25 mM HEPES and no phenol red, Invitrogen) and then washed twice by centrifugation (133 *g* for 2 min) and resuspension, as previously described (Carquin et al., 2015; Carquin et al., 2014; D'Auria et al., 2013a; D'Auria et al., 2013b; Leonard et al., 2017b; Tyteca et al., 2010). Incubation with pharmacological agents, labelling and confocal microscopy (see below) were performed at a dilution of 2 * 10^7 RBCs/ml in DMEM. All experiments were carried out on fresh RBCs, except for aging experiments for which RBCs were maintained at 4 °C during 1 to 15 days into the K^+/EDTA-coated tubes.

4.2 SM and chol depletion

Modulation of PM SM and chol contents were performed as previously described (Carquin et al., 2015; Carquin et al., 2014; Leonard et al., 2017b). Briefly, washed and diluted RBCs were preincubated at RT in suspension under continuous agitation with 2 or mU/ml *Bacillus cereus* sphingomyelinase (SMase; Sigma-Aldrich) for 10 min or with 0.25 mM methyl-ß cyclodextrin (mβCD; Sigma-Aldrich) for 30 min, all in DMEM containing 1 mg/ml bovine serum albumin (BSA; Sigma-Aldrich). All RBCs were then pelleted at 133 g for 2 min, resuspended in DMEM and analyzed by vital imaging for lipid domains (see below).

4.3 Intracellular calcium depletion

Decrease of $[Ca^{2+}]_i$ was performed as described in (Leonard et al., 2017b). Briefly, washed and diluted RBCs were preincubated at room temperature (RT) in suspension under continuous agitation in Ca^{2+}-free homemade medium containing 1 mM Ca^{2+}-chelating agent ethylene glycol-bis(β-aminoethyl ether)-N,N,N',N'-tetraacetic acid (EGTA, Sigma-Aldrich) for 10 min, then analyzed by vital imaging for lipid domains (see below).

*4.4 Living RBC labelling with Laurdan and/or Toxins**

A stock solution of Laurdan was prepared in DMSO and conserved as described in (Owen et al., 2011). After production, Lysenin* and Theta* maintained at -80°C in in 20 mM NaCl supplemented with 25 mM HEPES (pH 7.2) and 5 % glycerol at 80°C. Both types of probes were extemporaneously diluted in DMEM containing 1 mg/ml BSA (DMEM/BSA). Washed and diluted RBCs were labeled at RT in suspension under continuous agitation with: (i) 2.5 µM Laurdan for 60 min; or (ii) 1.25 µM Lysenin* or 0.55 µM Theta* for 25 min, as previously described (Carquin et al., 2015; Carquin et al., 2014; Leonard et al., 2017b). Labelled RBCs were then pelleted at 133 *g* for 2 min and resuspended in DMEM. For RBC double-labeling with Laurdan and Toxins*, RBCs were first labeled with 2.5 µM Laurdan for 40 min, then pelleted at 133 *g* for 2 min and resuspended with 2.5 µM Laurdan and either 1.25 µM Lysenin* or 0.55 µM Theta* for 25 min, then pelleted at 133 *g* for 2 min and resuspended in DMEM.

4.5 RBC immobilization and vital confocal/multiphoton imaging

After labeling in suspension, RBCs were either spread or maintained in suspension as previously described (Carquin et al., 2015; Carquin et al., 2014; Leonard et al., 2017b). Briefly, for spread RBCs, coverslips were first coated with poly-L-lysine (PLL, 70–150 kDa; Sigma-Aldrich) by incubation with PLL:DMEM (1:1, *v:v*) at 37 °C for 40 min, then washed with DMEM. PLL-coated coverslips were then incubated with labelled RBCs at 20 °C for exactly

4 min. Suspension was then removed and replaced by DMEM and attached RBCs were allowed to spread for another 4 min. The coverslip was finally placed upside down on a Lab-Tek chamber filled with DMEM and observed. For suspended RBCs, labelled RBCs were dropped to settle down in µ-Slide VI0.4 uncoated IBIDI chambers (IBIDI, Proxylab; 100 µl by channel). All preparations were examined at 20°C (except when otherwise stated) with a Zeiss LSM510 confocal/multiphoton microscope using a plan-Apochromat 63X NA 1.4 oil immersion objective, using a Nomarski prism to avoid the photoselection effect. Toxin*-labelled RBCs were acquired as previously in confocal mode (Carquin et al., 2015; Carquin et al., 2014; Leonard et al., 2017b), while Laurdan-labelled RBCs were acquired separately at 440 nm and 490 nm in multiphoton mode. Laurdan and Toxin*-colabelled RBCs were visualized first in the multiphoton mode for the Laurdan, then in the confocal mode for the Toxin*.

4.6 Determination of RBC area and circularity and domain topography and abundance

RBC total projected area (referred to as hemi-RBC) and circularity as well as abundance and topography of Laurdan- and chol-enriched domains were determined on high-resolution confocal images (or transmission images when no continuous membrane labeling was observed for the bulk). Domain abundance and topography were assessed by manual counting. Total RBC projected area and RBC membrane circularity were measured from ROI selections of the membrane with the analyzed particles plugging. Membrane ROI selections were obtained by thresholding fluorescent images using default methods in Image J followed by binarisation, then RBC membrane projected contours were detected using analyzed particles plugging. When no detection was possible, domain and bulk projected contours were drawn manually on fluorescent images. These selections were then used for all the following analyses.

4.7 Determination of lipid order

Domain and membrane ROIs were obtained from the two fluorescent channels (440 and 490 nm) of Laurdan images. Domain ROI selections were obtained as for the membrane (see above) but detected using analyzed particles plugging with distinct size and circularity features than for the membrane. To separate the Laurdan signal associated to the domains and the bulk, domains and bulk masks were used. Domain masks were obtained from domain ROI while bulk masks were deduced using membrane ROI subtracted from domain ROI. From these masks, three types of quantification were performed on the domains and the bulk independently. First, the two-dimensional (2D) GP map, where GP for each pixel was calculated from a ratio of the two fluorescence channels, was created using MATLAB (The MathWorks, Natick, MA).

Briefly, each image was binned (2 × 2) and thresholded, then the GP image was calculated for each pixel using the GP equation as described in (Owen et al., 2011) and the G_{fact} was measured as recommended in (Owen et al., 2011). The GP of the domains and bulk membrane were calculated by averaging pixels from a large representative area (35 RBCs). The determination of domains localized or not with the Toxins*, and the following separation of the domain masks, was done manually by comparing Laurdan and Theta* images. Second, the two domain populations exposing different lipid order (P1 and P2) were studied from GP histogram density plot. The mixture distribution of the GP histogram density plot, the GP values of P1 and P2 (the maximum of each mixture component), and the mixture weight were calculated from the two-dimensional (2D) GP map in MATLAB using the pdf_normmixture function. Third, HSB images (the GP image normalized by the intensity image), allowing for the visualization of the two domain populations exposing different lipid order (P'1 and P'2), were obtained using a plugging developed in (Owen et al., 2011).

4.8 Statistical analysis

Values are presented as means ± SEM. Statistical significance was tested either with two-sample t-test or one-way ANOVA followed by Tukey's post-hoc test (NS, not significant; * $p < 0.05$; ** $p < 0.01$ and *** $p < 0.001$). Statistical test mentioned above a bar indicates comparison *vs* the control condition (i.e. fresh, untreated, healthy RBCs at 20°C), while the significance test above a connecting line indicates a difference inside a group (*e.g.* control, treated, aged, spherocyte or elliptocyte).

Acknowledgments

We thank Drs. A. Miyawaki, M. Abe and T. Kobayashi (Riken Brain Science Institute, Saitama, Japan & University of Strasbourg, France) as well as H. Mizuno (KU Leuven, Belgium) for generously supplying the Dronpa-NT-Lysenin and Dronpa-theta-D4 plasmids. We also thank J. Maron (UCL) for technical support. We also kindly thank Joseph Lorent for reviewing the article. This work was supported by grants from UCL (FSR and Actions de Recherche Concertées, ARC), F.R.S-FNRS and the Salus Sanguinis foundation.

5. Supplementary Figures

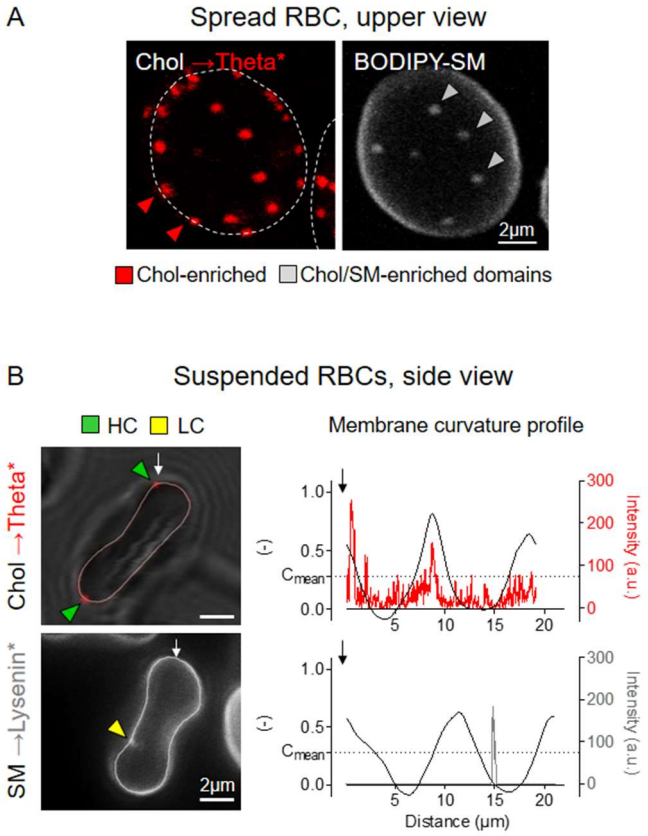

Supplementary Figure 1. At least two populations of submicrometric lipid domains, differing by composition and curvature association, coexist at the PM of living RBCs. Fresh healthy RBCs labelled with Theta* (A, *red → chol*) then by BODIPY SM (A, *green → SM*) or with Toxins* only (B; Theta*, *red → chol* or Lysenin*, *grey → SM*), spread onto PLL-coated coverslips *(A, spread)* or left in suspension *(B, suspended)* and observed by vital confocal or fluorescence microscopy. (**A**) Adapted from (Carquin et al., 2015). *Red* and *grey arrowheads* respectively point to chol-enriched domains and SM/Chol-enriched domains. (**B**) Adapted from (Leonard et al., 2017b). Left, *green* and *yellow arrowheads* respectively point to the highly curved (*HC*) edges and the central area of low curvature (*LC*) of the RBC membrane. Right, profiles comparing Theta* or Lysenin* intensity (*red* or *grey*) and membrane curvature (*black*; *right panels)* along paths indicated in *left panel* by *white curved lines* on side-viewed suspended RBCs (counterclockwise from starting point indicated by *white arrows*). *Dashed lines* (C_{mean}) represent the average membrane curvature of the RBC biconcave membrane observed on side view (left).

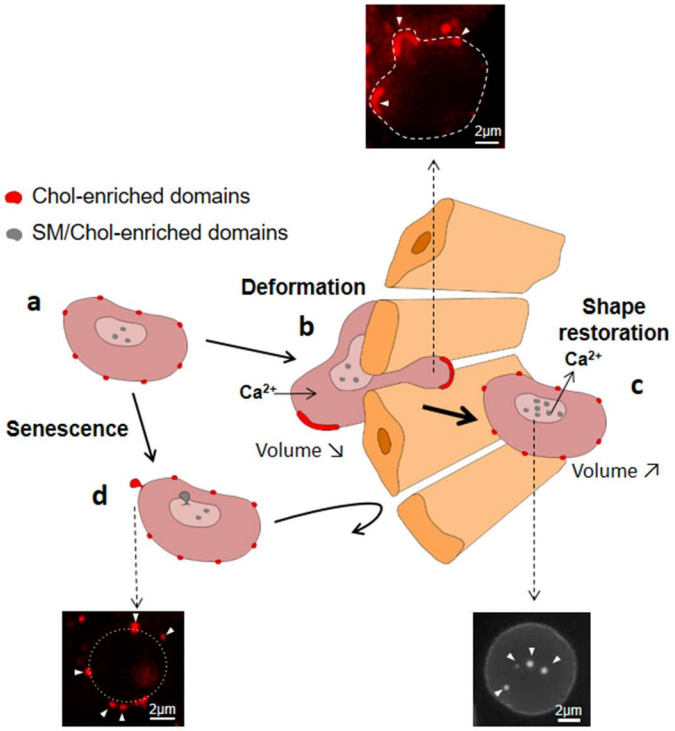

Supplementary Figure 2. Model for the implication of submicrometric lipid domains in RBC deformation and vesiculation. Adapted from (Leonard et al., 2017b). (**a**) In fresh healthy RBCs, chol- (*red*) and SM/Chol- (*grey*) enriched submicrometric domains associate to distinct membrane areas with high and low curvature, respectively. (**b,c**) Upon deformation, chol-enriched domains gather in increased curvature areas of the membrane edges. During shape and volume restoration after deformation, SM/Chol-enriched domains increase in abundance in the concavity of the RBC, along with Ca^{2+} efflux. (**d**) During RBC aging, both lipid domains appear as specific sites for membrane loss by vesiculation.

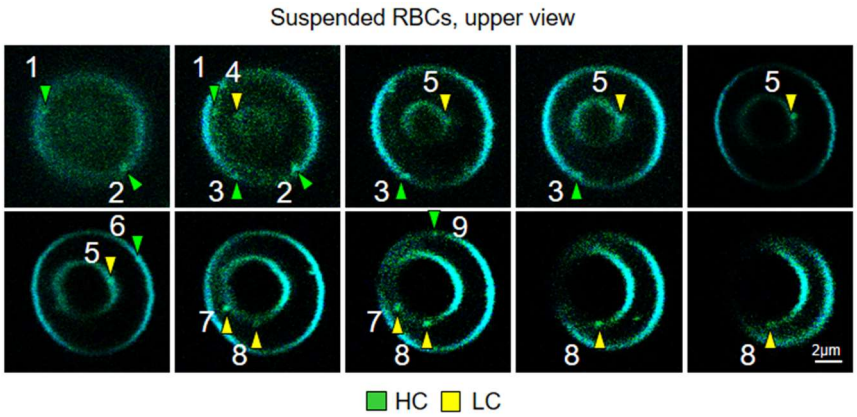

Supplementary Figure 3. Laurdan-labelling exhibits a similar amount of domains on RBCs in suspension. Healthy fresh RBCs were labelled with Laurdan and left in suspension for observation by vital multiphoton microscopy at 20°C. Representative vital imaging. Several stack images were taken for one RBC. *Yellow* and *green arrowheads* respectively point to *LC* and *HC domains* and are associated with *a number* which refers to the domains observed per image.

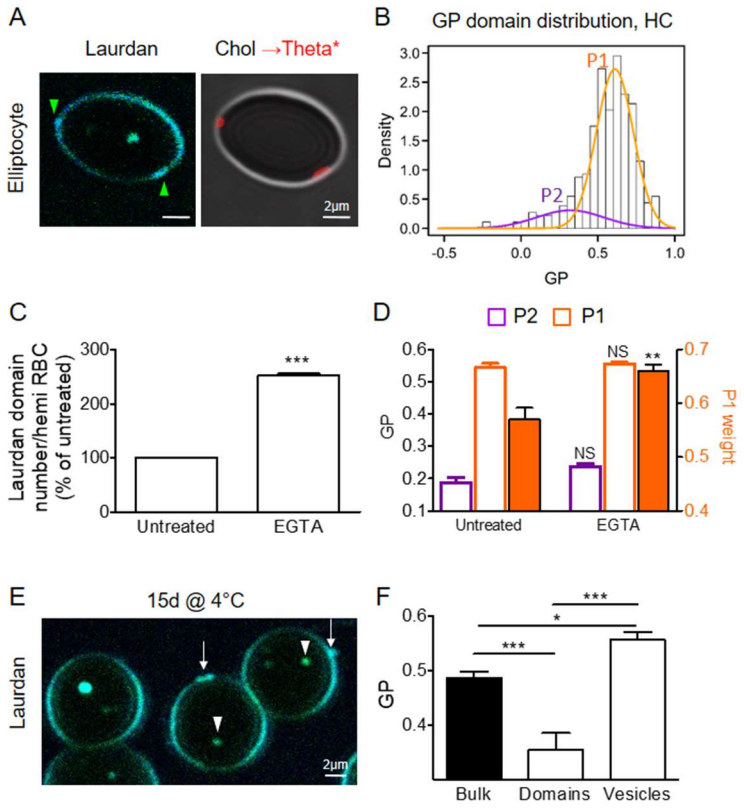

Supplementary Figure 4. Upon RBC deformation and vesiculation, Laurdan-labelled domains show a modulation of their abundance and curvature association similar to those revealed by Toxins* and an increase of their lipid order. Healthy or elliptocytotic (A, B) RBCs, either fresh or maintained at 4°C during 15 days (E, F), were left untreated or treated with EGTA in Ca^{2+}-free medium (*EGTA*, C, D), labelled with Laurdan (C-F) or Laurdan followed by Theta* (A, B), spread and observed by vital multiphoton/confocal microscopy at 20°C. (**A**) Representative imaging; *green arrowheads* point to the highly curved edges of the RBC biconcave membrane (HC). (**B**) GP value distribution (expressed as proportion of total values) of HC domains in elliptocytes. One major GP domain population (*P1*) can be observed. (**C**) Quantification of Laurdan-labelled domain number (average by hemi-RBC expressed as percentage of *untreated*) for RBCs left untreated (*untreated*) or stimulated for Ca^{2+} efflux (*EGTA*). (**D**) Quantification of the GP values of *P1* (*white columns boxed in orange, left axis*), *P2* (*white columns boxed in purple, left axis*) and of the proportion of *P1* as compared to *P2* (*orange columns, right axis)* for RBCs left untreated (*untreated*) or stimulated for Ca^{2+} efflux (*EGTA*). (**E**) Representative vital imaging; *white arrowheads* and *arrows* point to domains and vesicles in aged RBCs, respectively. (**F**) Quantification of the GP values of the bulk (*black column*) and domains or vesicles (*open columns*) in aged RBCs. Images are representative from 2–4 independent experiments. Results are means ± SEM of 140–412 RBCs from 2–4 independent experiments. Statistical significance was tested with one-way ANOVA

followed by Tukey's post-hoc test (*open and black columns*) or with two-sample t-tests (*orange columns*).

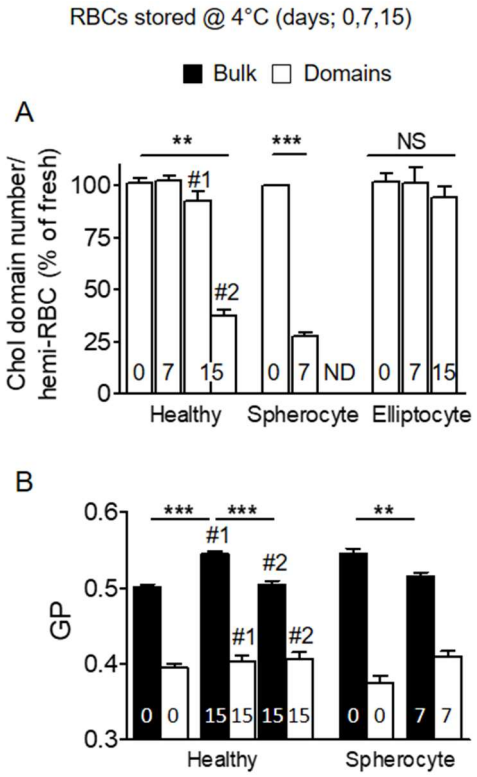

Supplementary Figure 5. In comparison to healthy RBCs, spherocytes, but not elliptocytes, expose accelerated domain vesiculation and bulk GP variations upon aging. Healthy, spherocytotic or elliptocytotic RBCs, either fresh or maintained for the indicated times at 4°C, were labelled with Theta* (A) or Laurdan (B), spread and observed by vital microscopy at 20°C. Quantification of Theta*-labeled domain number (A; average by hemi-RBC expressed as percentage of fresh RBCs) and GP values of the bulk (B; *black columns*) and domains (*open columns*) for healthy RBCs, spherocytes and elliptocytes maintained for the indicated times at 4°C (*numbers* in *columns*). Results are means ± SEM of 70–231 RBCs from 2 independent experiments. Statistical significance was tested with one-way ANOVA followed by Tukey's post-hoc test.

CHAPITRE 5

General discussion, perspectives and conclusion

Foreword

In this chapter, after highlighting strengths and weaknesses of the cell model, lipid tools and experimental conditions (Section 1), I summarize the major results obtained in this Thesis (Section 2). I then discuss the key findings in the broader context of membrane organization and function as follows: (i) membrane lipid domain biogenesis and resulting diversity (Section 3), (ii) lipid domain modulation upon physiological changes (Section 4), and (iii) their resulting functionalization (Section 5). In Section 6, I discuss energetic contributions involved in these processes.

1. Overview of strengths and weaknesses of the cell model, lipid tools and experimental conditions

1.1 Cell model

The simplicity and advanced characterization of the RBC, its flat featureless membrane and the lack of endocytosis make it an ideal cellular model to study lipid membrane organization. Furthermore, the presence of a transbilayer lipid asymmetry, a cytoskeleton anchorage and optically-resolved lipid domains in physiological conditions (living RBCs in suspension at 37°C in the absence of treatment) are definitively an asset as compared to GPMVs (Baumgart et al., 2007; Sezgin et al., 2012a; Levental and Levental, 2015), which is one of the most relevant and simplest model currently available to study lipid domains.

However, while GPMVs can be made from almost any specific cells, RBC is a very singular cell in relation to its specific function-associated (re)shaping ability. This should be kept in mind when using observations made on RBCs to draw general conclusions about cell membrane organization and function. As previously detailed, RBC specific function leads to singular characteristics such as a highly curved biconcave membrane, a fine intracellular ion concentration modulation and a strong cytoskeleton anchorage (Bogdanova et al., 2013; Mohandas and Gallagher, 2008). These characteristics could impact lipid domains, resulting into singular lipid domain function. Since drastic function-associated shaping and reshaping can be observed in other cells (see Chapter 1), *e.g.* epithelial cells and cancerous metastatic cells, it would be appealing to investigate whether and how lipid domains could also be involved in the (re)shaping processes of these particular cells.

RBC singularity as cell model exposes another limitation, *i.e.* the impossibility to express probes targeting the inner leaflet due its lack of nucleus. The study of membrane proteins is then limited to the ones that can be targeted at their external leaflet and no solid data are available on the inner leaflet lateral heterogeneities. In the future, microinjections or electroporations (Takao and Kamimura, 2010) of probes inside the cell could be used to overcome this problem.

1.2 Lipid labeling tools

Fluorescent Toxin* fragments, Theta* and Lysenin, were used to decorate endogenous chol and SM and the fluorescent probe Laurdan was inserted in the PM to investigate lipid order. These tools were selected as they are compatible with vital confocal imaging and since their excitation and emission spectra are sufficiently distinct to allow for double-labelling. These properties represent a real asset since most of the studies exploring lipid lateral heterogeneity and order are done on fixed cells and independently.

Carquin and coll. previously verified that both Toxin* fragments are specific, non-toxic, sensitive and quantitative probes of SM and chol and reveal lipid domains rather than inducing them (Carquin et al., 2014, 2015). Nevertheless, potential artifacts still need to be evaluated due to the Toxin* large sizes. First, since Toxin* binding restricts lipid lateral diffusion by 3-fold (Carquin et al., 2014, 2015), it could impact lipid domains response to on-stage deformation and shape restoration. Second, Toxin* binding could affect lipid domain order. Third, Toxin* binding could impose a specific curvature to the domains, affecting domain sorting along the biconcave membrane or during deformation. These concerns were disproven throughout the study by careful comparison of (i) lipid domain response to external modulations, (ii) membrane lipid order and (iii) curvature upon labeling with BODIPY-SM *vs* Toxin* and/or with Laurdan *vs* Laurdan/Toxin*.

Although high-resolution confocal microscopy is a powerful technics to study lipid compositional diversity, it is limited by potential artifacts and toxicity resulting from the use of fluorescent probes. To overcome this problem, we could develop technics such as high-resolution secondary ion mass spectrometry (Frisz et al., 2013a; Kraft, 2016; Frisz et al., 2013b) (SIMS) or atomic force microscopy (AFM) by grafting to the AFM probe the minimal Toxin* fragment recognizing a specific lipid. Indeed, such biospecific AFM mapping allowed the mapping of receptor sites on animal cells (Grandbois et al., 2000; Roduit et al., 2008; Kim et al., 2006). Furthermore, these technics expose higher spatial resolution than optic microscopy.

Laurdan also exhibits some drawbacks: (i) lipid order resolution is restricted by the GP imaging, (ii) Laurdan reveals only information about the hydration of the lipids (*i.e.* lipid order), and (iii) Laurdan slots in the upper part of the membrane leaflets, therefore mainly probing the order of lipid heads and not tails. Our study with Laurdan should then be completed using fluorescent probes revealing lipid fluidity by insertion closer to the lipid tails, such as diphenylhexatriene (Deleu et al., 2013; Demchenko et al., 2009) (DPH), fluorescence correlation spectroscopy (Bacia et al., 2004) (FCS) to study lipid diffusion and AFM(Sullan et al., 2009; Bremmell et al., 2006) to study membrane elasticity and thickness with high resolution.

1.3 Experimental conditions

To study lipid domains, D'Auria, Carquin and coll. used RBCs spread on poly-L-lysine (PLL)-coated coverslips and observed the coverslips in labTek chambers compatible with confocal or fluorescence imaging. Several parameters were tested, such as temperature of labelling and analysis, spreading extent, etc. During my thesis, I labelled RBCs at 20°C with the lipid probes, as chol- and SM-enriched domains expose a higher abundance at this temperature than at 37°C (Carquin et al., 2015, 2014). Moreover, I started to work on spread RBCs, a system allowing to observe an entire domain

population in one image due to RBC immobilization and flattening. However, since spreading could affect RBC biconcave shape or lipid organization, I then extended the study to RBC in suspension in IBIDI chambers. The comparison of membrane curvature of side and upper view of spread *vs* suspended RBCs showed little impact of spreading on RBC shape. Further comparisons of lipid domains of spread *vs* suspended RBCs revealed no drastic impact on domain size, shape and number. However, lipid domain topography was slightly impacted upon spreading, leading to a slightly higher domain association with the RBC center (observed with all the probes I used, *i.e.* Theta*, Lysenin*, BODIPY-SM and Laurdan). Several non-tested and non-exclusive hypotheses could explain this phenomenon, such as a differently impacted membrane curvature or lateral tension in the RBC center and edges, cytoskeleton rearrangement or interaction of membrane components with underlying PLL at the site of contact (*i.e.* the center of the cell) upon spreading. As our experimental conditions slightly impacted lipid domain abundance and topography, our observations should be confirmed in suspension at physiological temperature. In addition, experiments on model membranes highlight that shear stress, which is a key parameter in RBC physiological environment, impacts lipid domain organization(Robinson et al., [CSL STYLE ERROR: reference with no printed form.]; Sturzenegger et al., 2016). The next step will be therefore to follow, by microfluidics, the dynamics of lipid domain implication in resting state to deformation back to shape restoration of one RBC in suspension at physiological temperature upon application of a shear stress.

2. Summary of the key findings

Carquin et al previously exposed two types of lipid domains coexisting at the PM of living RBCs (Carquin et al., 2015, 2014): one mainly enriched in chol (referred to chol domains) and the other enriched in both SM and chol (referred to SM/chol domains). In the first part of this Thesis (Chapter 3), we investigated the potential implication of these lipid domains in RBC (re)shaping, a very specific function of the RBC PM. Our results reveal that, although lipid domains were not essential to the maintenance of the RBC biconcavity, chol- and SM-enriched domains specifically associated with high and low curvature areas of the RBC biconcave membrane respectively. Upon reshaping, chol-enriched domains gathered in areas of increased curvature, as revealed in elliptocytes and healthy stretched RBCs. In contrast, SM-enriched domains increased in abundance along with Ca^{2+} efflux during subsequent shape and volume restoration. Finally, both domains were identified as specific sites for membrane vesiculation. Altogether, our results revealed the contribution of lipid domains to RBC function-associated reshaping.

Since specific lipid domain order is thought to be at the center of their function in cells (Simons and Ikonen, 1997), we examined in the second part of the

Thesis (Chapter 4) whether lipid domains could expose differential lipid order than the surrounding membrane (bulk) and if such a difference could be involved in RBC physiopathology. We revealed that lipid domains in RBC at resting state were less ordered than the bulk and that a third domain population enriched neither in chol nor in SM exhibited a lower lipid order than the two domain populations enriched in these lipids. Upon implication of lipid domains in function-associated RBC reshaping, lipid domains order decreased, leading to a $\Delta GP_{bulk\text{-}domains}$ decrease. In contrast, prior to domain vesiculation upon RBC aging or in membrane fragility disease (*i.e.* spherocytosis), $\Delta GP_{bulk\text{-}domains}$ increased due to lipid bulk order decrease and was followed by domain vesiculation. Altogether, our results suggest that RBCs could modulate $\Delta GP_{bulk\text{-}domains}$ to functionalize lipid domains.

3. Lipid domain biogenesis and resulting diversity of characteristics

Considering the wide range of domain features (*e.g.* composition, order and topography) that lipid-lipid interactions can generate in model membranes with only a few different lipids, it is no surprise to unveil such a diversity of lipid domains amongst living cell membranes (see Chapter 1 section 5). Besides lipid-lipid interactions, domain biogenesis in living cell can result from a multitude of contributions such as cytoskeleton anchorage pinning, interleaflet coupling, lipid recycling or membrane curvature sorting (see Chapter 1 section 6), that vary amongst cells insuring their functional singularity. Our observations suggest the coexistence at the PM of living RBCs of at least three domain populations in terms of lipid composition, lipid order and topography. The population located at the edges is enriched in chol mainly, while the second domain population restricted to the center of the RBC is enriched in both chol and SM, both populations exhibiting a close lipid order. The third domain population, also restricted to the center of the cell, is neither enriched in chol nor in SM and exhibits significantly lower lipid order than the two other domain populations. Here, we discuss potential mechanisms by which cells could generate such diversity of lipid domain characteristics. The functional specificity resulting from this diversity will be discussed afterwards (Sections 3 and 4).

3.1 Lipid domain composition

Lipid-lipid interactions govern lipid preferential associations and subsequent spatial distribution in model membranes (Almeida, 2009). Phase separation in biomimetic model membranes made of ternary mixture such as POPC/SM/chol are driven by three pairs of binary interactions: unfavourable interaction between the POPC and SM, favourable interaction between chol and SM and unfavourable interaction of chol with the disordered POPC (Reigada et al., 2008; Frazier et al., 2007). This translates in the coexistence

of two phases; a chol- and SM-enriched phase ("raft-like") with a POPC-enriched phase ("non-raft-like"). However, only partial SM and chol co-enrichment was observed on several cell types (Aresta-Branco et al., 2011; Grossmann et al., 2007; Frisz et al., 2013a). Accordingly, we observed only partial colocalization and codependence between chol- and SM-enriched domains in RBCs. Additionally, Laurdan labelling revealed a third lipid domain population enriched neither in chol nor in SM. Based on co-labelling experiments currently performed in the laboratory between the Toxins* (Theta* or Lysenin*) and BODIPY-GM1 on living RBCs, one can suggest that the third domain population is enriched in GM1 (unpublished data). In model membranes, quaternary mixtures made of POPC/SM/chol/GM1 reveal that GM1 gangliosides strongly associate with each other and that chol preferentially associate with GM1 rather than SM (Gu et al., 2017). This translates in the coexistence of three phases: GM1 aggregates enriched in chol and weakly separated clusters formed with SM and chol, surrounded by a phase made of POPC. Louise Conrard, another PhD student of the group, performed careful mapping of the chol-enriched domains and those enriched in polar lipids such as SM, PC and GM1, and characterized the dependence of the latter domains to chol. These experiments revealed large colocalization and dependence of SM-, PC- and GM1-enriched domains to chol PM content, suggesting that the lipid-lipid interactions occurring in simple model membranes made of quaternary lipid mixture are not sufficient to explain observations made on living cells. Alternatively, it is possible that the third population labelled with Laurdan reflects inner leaflet heterogeneity (Yeung et al., 2008; Hammond et al., 2012) (*e.g.* PS, PE or PI-enriched domains). Indeed, in contrast to the Toxins* which decorate the outer PM leaflet only, Laurdan can rapidly flip-flop between the two leaflets (Dinic et al., 2011).

Moreover, besides lipid-lipid interactions, proteins and cytoskeleton anchorage could also participate to domain biogenesis through protein-lipid interactions (*e.g.* charge-mediated sequestration or specific binding to recognition sequences) or lipid diffusion restriction by cytoskeleton anchorage (picket and fence hypothesis). Accordingly, we previously observed on living RBCs distinct protein-lipid domain associations and domain abundance restriction by cytoskeleton anchorage (D'Auria et al., 2013b). Numerous additional factors could also participate to lipid domain biogenesis in cells, such as membrane potential or interleaflet coupling.

3.2 Lipid domain order

Along with their diversity of composition, lipid domains expose distinct lipid order in model membranes. For instance, the phase enriched in chol and SM is more ordered in comparison to the one enriched in POPC in the POPC/Chol/SM ternary mixture, while the domains enriched in GM1 and chol are less ordered *vs* those enriched in chol and SM in the POPC/SM/Chol/GM1 quaternary mixture (Gu et al., 2017). These observations are consistent with

the lipid order of the domain populations in RBC: those enriched in chol and SM/chol are more ordered than the third population that could be enriched in GM1 (our unpublished data). This suggests that lipid-lipid interactions could govern lipid domain order in RBC at resting state.

However, phase lipid order observed in model membranes is not consistent with the higher lipid order of the bulk as compared to the domains in living RBCs at resting state. This suggests that lipid-lipid interactions could not govern, by themselves only, lipid order in RBC at resting state. In Chapter 4, we propose that the bulk lipid order is also controlled by the combined contribution of membrane proteins (*e.g.* due to hydrophobic mismatch between the protein hydrophobic core and lipid bilayer) and cytoskeleton density and/or anchorage, that can impact membrane lipid order in different ways. Indeed, it has been exposed that while transient dissociation of the spectrin filament at its ends (4.1R complex) induces reversible loss of the cytoskeleton network hence decreased compression applied to the membrane, the loss of mid-point attachments of the spectrin filaments to the bilayer (ankyrin complex) increases cytoskeleton network stiffness hence compression applied to the membrane (Sens and Gov, 2007; Gov, 2007b). Accordingly, we observed an increase of the bulk lipid order in RBCs from a patient with spherocytosis exhibiting a deficiency in ankyrin complex proteins. Moreover, our unpublished data in confocal and transmission electron microscopy indicate that RBCs of this patient exhibit an increased spectrin network density as compared to other spherocytotic patients, along with higher bulk lipid order increase. This suggest that higher the spectrin density is, higher the bulk order is. The possibility that membrane proteins could also partially account for the higher bulk than domain lipid order is supported by three lines of evidence: (i) proteins rather than chol modulate the average bilayer thickness in cells (Mitra et al., 2004), (ii) membrane proteins restrict lipid lateral mobility at the RBC membrane (Golan et al., 1984), and (iii) RBC bulk lipid order decreases after vesiculation, yet these vesicles are highly enriched in proteins (D'Alessandro et al., 2010). Alternatively, as discussed in Chapter 4, it is possible that the lower lipid order of lipid domains as compared to the bulk membrane, observed by Laurdan labelling, is related their dimensionality, *i.e.* curved shape (dimpling of domains) (Ursell et al., 2009).

3.3 Lipid domain topography

Additionally, lipid domains reveal a topographical segregation at the RBC PM: those enriched in chol mainly are located at the edges while the two other populations are restricted to the center of the cell. In Chapter 3, we discussed the potential curvature sorting of lipid domains at the RBC biconcave PM. Such lipid- and lipid domain-sorting mechanism is often proposed in theoretical works and works on model membranes (Roux et al., 2005; Parthasarathy et al., 2006; Tian and Baumgart, 2009) and in some living

bacteria, but has never been explored on RBC. As discussed in the Chapter 3, individual lipid shape cannot explain such sorting, which is confirmed by the restriction of domains enriched GM1 (an inverted cone-shaped lipid) in the RBC PM center of low curvature. Instead, cooperative domain properties like curvature, lipid order and correlated bending stiffness could participate to such curvature mediated sorting. However, experiments on model membranes suggested that domain bending stiffness does not regulate their association to membrane curvature, both L_o and L_d phases being able to associate with high and low curvature areas (Baumgart et al., 2003). Accordingly, we observed no relation between lipid domain order and membrane curvature association, the more ordered domain populations (chol and SM/chol enriched) being both associated with the edges and the center of RBCs. Domain curvature sorting then results either from intrinsic domain curvature, which can be determined by the molecular structure of sterol in model membranes (Bacia et al., 2005), or from its association with binding proteins that are curvature sorted (Arumugam and Bassereau, 2015). However, the absolute curvature values of the RBC PM are very small as compared to the domain size, questioning the possibility of lipid domain sorting according to their intrinsic curvature. Furthermore, while the PM edge shape change from discoid to ellipsoid in elliptocyte impacts chol-enriched domain topography, modulation of the PM cell center shape from concave to spherical in spherocytes does not impact SM/chol-enriched domain sorting. While chol-enriched domains could be curvature sorted, other sorting mechanisms should be investigated for SM/chol-enriched domains, such as interactions with specific proteins, cytoskeleton anchorage, interleaflet coupling or charge-mediated interaction.

To conclude

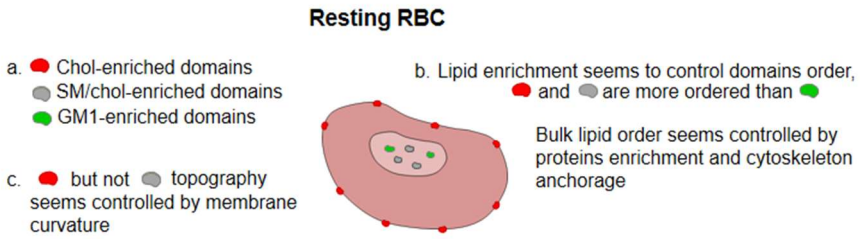

Lipid domain biogenesis in living RBCs cannot only result from simple lipid-lipid interactions centered on chol, as observed in biomimetic model membranes. Lipid domains with differential composition, order and topography could rather result from the additional contribution of membrane curvature, lipid-protein interactions and cytoskeleton anchorage. Other contributions, not investigated here, such as membrane potential or interleaflet coupling could also participate to domain biogenesis and diversity of characteristics. An even more complex lipid domain composition, order and topography could exist at the RBC PM outer and inner leaflets. This will need further investigation.

4. Lipid domain distinct modulation by environmental changes

Like in any other cell, the RBC PM is impacted by environmental changes (*e.g.* imposed shear stress and variations in membrane tension or mechanical cell shape and volume modulation). For this particular cell, physiological variations are highly related to its deformation ability, which is essential to its function and is constantly subjected to test in the blood circulation. In response to changes imposed to the RBC PM, chol- and SM/chol-enriched domains do not exhibit identical behaviors: while chol-enriched domain topography is modulated upon membrane shape change, SM/chol-enriched domain abundance is impacted by cytoskeleton anchorage loosening and local elevation in Ca^{2+} concentration. In this section, we discuss how the distinct characteristics of chol- and SM/chol-enriched domains could explain these different responses to physiological variations.

4.1 Chol-enriched domains and RBC shape modulation

As discussed in the previous section, chol-, but not SM/chol-, enriched domain topography is modulated upon membrane shape changes. This could be attributed to domain cooperative properties resulting in curvature-induced sorting. However, contribution of chol-enriched domains for membrane bending was suggested by the loss of ellipsoid membrane edges back to their discoid shape upon depletion of chol-enriched domains. Implication of chol-enriched domains in RBC PM shape change could result from individual and specific chol properties such as its equimolar presence in both leaflets combined to its ability to rapidly flip-flop and its tendency to intercalate between other lipids. Micropipette experiments, inducing pressure-based RBC membrane deformation from discoid to echinocyte shape, exposed that RBC PM shape change can rely on the bilayer couple hypothesis (Artmann et al., 1997). This mechanism is based on the recruitment of individual lipids from one leaflet to the other, which participate in membrane bending due to resulting differences in outer to inner leaflet area (Sheetz and Singer, 1974; Singer and Oster, 1992). Using healthy discoid RBCs, we were able to generate echinocytes by excess of both Theta* or Lysenin* binding but only chol- and not SM-enriched domains were observed at the top of the protrusions (unpublished data). This suggests that chol could be preferentially recruited from the inner to the outer leaflet to induce PM shape changes based on the bilayer couple hypothesis. Chol-enriched domains could then participate to membrane bending based on the combined bilayer hypothesis and specific chol properties. It should be noted that the contribution of chol-enriched domains to PM shape changes could also result from their specific association to proteins involved in membrane bending.

4.2 SM/chol-enriched domains and cytoskeleton anchorage loss and/or transient calcium concentration increase

In contrast, at the center of the cell, SM/chol-enriched domains exposed an increased abundance upon pathological (hereditary spherocytosis to uncouple membrane:cytoskeleton at ankyrin complexes) or pharmacological (activation of PKC to uncouple membrane:cytoskeleton at 4.1R complexes) cytoskeleton anchorage loosening (D'Auria et al., 2013b), pharmacological $[Ca^{2+}]_i$ increase (Leonard et al., 2017b), volume increase (incubation in hypotonic medium) or ATP depletion (unpublished data). Interestingly, all these approaches lead to two major RBC modifications: (i) a loss of membrane:cytoskeleton anchorage, and (ii) a local increase in $[Ca^{2+}]_i$. Indeed, both membrane:cytoskeleton anchorage loss and increase in $[Ca^{2+}]_i$ are characteristics features of spherocytosis. Upon RBC deformation, reversible cytoskeleton loosening is triggered by both Ca^{2+} and ATP, through the Ca^{2+}-dependent phosphorylation of the 4.1R protein by PKC (Gauthier et al., 2011). Additionally, RBC volume is increased by $[Ca^{2+}]_i$ increase, resulting in secondary activation of the Gardos channel (Dyrda et al., 2010) and loss of the cytoskeleton anchorage (Bogdanova et al., 2013). This suggests a restriction of SM/chol-enriched domains in LC, but not of chol-enriched domains in HC, by spectrin network density and/or membrane:cytoskeleton anchorage. Accordingly, we observed higher spectrin network density in LC than in HC, but this needs to be quantified (unpublished data). An opposite effect is often attributed to the membrane:cytoskeleton anchorage, *i.e.* domains are rather favored by cytoskeleton confinement of membrane components (picket-and-fence model (Kusumi et al., 2005)). The potential mechanism behind cytoskeleton anchorage restriction of SM/chol-enriched domains in LC should therefore be further investigated. As a non-mutually exclusive hypothesis, the increase of SM/chol-enriched domain abundance could result from the local transient increase in $[Ca^{2+}]_i$. Indeed, in both model membranes (Wang et al., 2012) and cells (Jin and Pralle, 2016), it has been shown that a local Ca^{2+} increase is able to induce by electrostatic interactions the clustering of PIP_2 in the inner leaflet. This could in turn induce the transbilayer clustering of SM in superposition in the outer leaflet (Abe et al., 2012), as revealed by super-resolution microscopy in LLC-PK1 cells (Abe et al., 2012).

To conclude

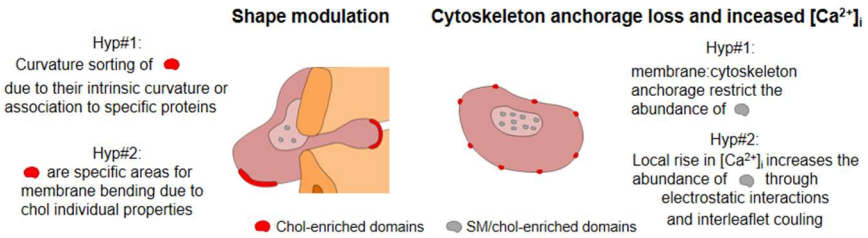

Chol- and SM/chol-enriched domains exhibit different responses to external changes due to their specific features such as composition, order and topography. Membrane shape changes, membrane:cytoskeleton anchorage loss and modulation of $[Ca^{2+}]_i$ could then act as switch to individually regulate lipid domains. Furthermore, other factors could also participate in the distinct modulation of lipid domains and other domains, such as those enriched in GM1, could also be individually modulated.

5. Lipid domain distinct modulation resulting in specific functionalization

From the differential modulation of lipid domains upon physiological changes can result a specific functionalization in living cells. For example, during the cell growth of rod-shaped bacteria, wall curvature is affected, impacting cardiolipin (CL) domain topography which in turn feedbacks to cytoskeleton-controlled cell growth (Huang et al., 2006; Mukhopadhyay et al., 2008; Renner and Weibel, 2011; Mileykovskaya and Dowhan, 2000; Lin et al., 2015). Another example is the clustering of B cell receptors (BCRs), upon antigen binding to BCRs, which induces ordering of surrounding lipids and in turn helps BCR activation (Stone et al., 2017b). In RBC, the diversity of lipid domain characteristics and responses to physiological changes could translate in their functional specificity and their distinct topography in the spatial segregation of these functions. Indeed, the physiological modulations discussed in the previous section are involved in RBC deformation. In response to mechanical stress, local transient increase in Ca^{2+} levels occurs in the vicinity of the RBC PM (Dyrda et al., 2010). This most likely serves as a signal to mediate rapid reversible Ca^{2+}- and/or ATP-dependent cytoskeletal loosening (Gauthier et al., 2011) and Ca^{2+}-dependent volume decrease allowing for variation in membrane plasticity and cell shape. When the mechanical stress is relieved, initial $[Ca^{2+}]_i$, cytoskeleton anchorage and RBC volume and shape are restored. As described in Chapter 3, upon mechanical deformation of RBC spread on a PDMS chamber, we observed the gathering of chol-enriched domains in increased curvature areas of the membrane edges, followed by the stimulation of SM/chol-enriched domains along with secondary Ca^{2+} efflux during shape restoration. In the present Section we discuss how the domains could participate to RBC deformation processes.

5.1 Chol-enriched domains and RBC deformability

Chol-enriched domains could contribute to membrane bending modulation and/or stabilisation either (i) through the specific individual chol properties combined with the bilayer couple hypothesis, or (ii) through the domain cooperative properties and association with proteins involved in membrane bending. In addition, chol-enriched domains could participate to the stimulation of mechanosensitive pumps involved in Ca^{2+} entry into the cell upon deformation, such as Cav2.1 and TRPC channels (Beech et al., 2009; Balijepalli et al., 2006; Linetti et al., 2010) or Piezo1(Cahalan et al., 2015) The combined association of mechanosensitive pumps involved in Ca^{2+} entry with chol-enriched domains and recruitment of chol-enriched domains in membrane bending areas could lead to the activation of these mechanosensitive pumps upon mechanical stress. As membrane bending and Ca^{2+} entry are both essential to RBC deformability, these two mechanisms suggest the implication of chol-enriched domains in RBC deformation.

Accordingly, we observed the same deformability loss of RBCs upon depletion of chol-enriched domains only or upon depletion of both chol- and SM/chol-enriched domains and upon loss of chol-enriched domains upon RBC aging. Unpublished data of the laboratory indicate that microvesicles isolated from RBCs upon aging are indeed enriched in cholesterol as compared to the RBC membrane from which they originate.

5.2 SM/chol-enriched domains and RBC deformation reversibility

Controlled reversible loosening of cytoskeletal network, triggered by mechanical deformations and Ca^{2+} uptake when RBCs are passing through capillaries is an advantage. On the contrary, uncontrolled irreversible impairment of cytoskeletal density and/or anchorage in RBCs of patients with haemolytic anemia, in which Ca^{2+} is permanently upregulated, compromises mechanical stability of the RBC membrane (Manno et al., 2005). Reversibility of cytoskeleton loosening upon deformation is therefore essential to the cell integrity. Indeed, the local increase in Ca^{2+} levels occurring in the vicinity of the PM in response to mechanical stress is transient and $[Ca^{2+}]_i$ is restored when the stress is relieved. In RBC, Ca^{2+} efflux arises only from one pump, the PMCA, whose functionality is drastically depending on its lipid environment (Pignataro et al., 2015; Dodes Traian et al., 2012). Sorting and activation of membrane proteins is the most often cited and studied function of lipid domains. It could arise from several mechanisms such as hydrophobic mismatch, charge-mediated interactions or specific binding of lipids to recognition sequences in proteins. We propose that SM/chol-enriched domains are essential to secondary Ca^{2+} efflux by acting on PMCA activation. This is supported by the decreased ability of RBC to induce secondary Ca^{2+} efflux and correlated volume increase upon the depletion of chol- and SM/chol-enriched domains, both ability being restored upon SM/chol-enriched domain repletion. Since RBC deformation in the dynamic circulation flow and rapid passage through the spleen tiny pores expose short temporal features in terms of shape, volume and cytoskeleton anchorage variations, the reversibility of deformation probably needs to occur almost instantaneously. We thus propose that, in response to mechanical stress, local $[Ca^{2+}]_i$ increases in the PM vicinity, inducing cytoskeleton anchorage loosening and rapidly leading to SM/chol-enriched domain abundance increase (either due to membrane:cytoskeleton anchorage loss or local $[Ca^{2+}]_i$ increases) and secondary Ca^{2+} efflux by PMCA activation to ensure immediate retroactive cytoskeleton loosening reversibility essential to the cell stability. Accordingly, we observed an increased abundance of SM/chol-enriched domains and the correlated Ca^{2+} efflux rapidly after stretching, with or without PDMS chamber destretching.

To conclude

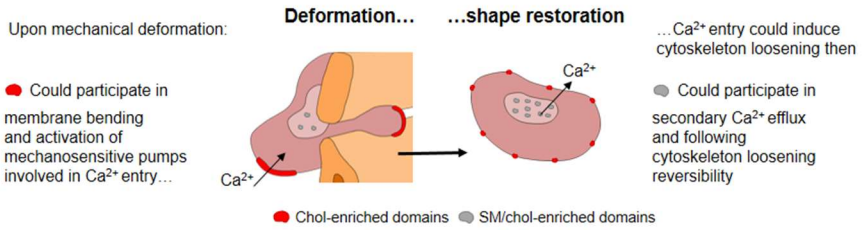

The involvement of chol-enriched domains in RBC deformability and of SM/chol-enriched domains in an immediate retroactive reversibility suggests the essential role of these domains for this cell submitted to constant dynamic flow and rapid deformation. We still need to confirm the specific implication of chol- and SM/chol-enriched domains in cytoskeletal loosening and loosening reversibility, through respectively Ca^{2+} uptake and secondary efflux. This could be done by using elliptocytes and spherocytes, which respectively expose impaired chol-enriched domain distribution and SM/chol-enriched domain abundance due to affected horizontal and vertical cytoskeleton links. Accordingly, increased $[Ca^{2+}]_i$ is generally observed in spherocytotic RBCs (Johnsson et al., 1978; Shimoda et al., 1984). This will help to elucidate the molecular mechanism behind their impaired deformability, which is still poorly understood although they are the most common RBC membrane disorders and therefore no powerful diagnostic or treatment are currently available(Barcellini et al., 2011).

6. Lipid domain biogenesis, modulation and functionality: an energetic point of view

To insure their function, proteins find energy in different ways such as ATP hydrolysis or taking advantage of electrochemical gradients. It is obvious that lipid domains make use of protein energetic input. However, model membranes made of lipid mixtures expose that phase separations can store energy at their boundary, which is called the line tension energy. In model membranes, line tension participates in phase separation stability (Levental et al., 2016), domain size (Heberle et al., 2013; Samsonov et al., 2001), membrane component partitioning between phases (Sezgin et al., 2015), specific domain budding (Jülicher and Lipowsky, 1993; Baumgart et al., 2003; García-Sáez et al., 2007b), fusion at domain boundary (Yang et al., 2016) or domain reorganization upon deformation (Robinson, 2013). Here, we asked

whether the line tension energy at domain boundary could participate in domain biogenesis, modulation and functionality. In a simplistic model, the boundary energy of an isolated domain in a membrane is given by $E=\gamma L_{domain}$, where γ is the line tension and L_{domain} the circumference of the domain (Kuzmin et al., 2005). Supposing that $|\Delta GP_{bulk\text{-}domains}|$ is correlated to the line tension (see Chapter 4), The energy associated to the line tension at domains boundary could result from two factors, the difference of lipid order between the domains and the bulk ($\Delta GP_{bulk\text{-}domains}$) and the domain boundary length ($L_{domains}$).

6.1 Line tension and domain biogenesis

We first focused on the potential role of the line tension energy in domain biogenesis. At first glance, it is striking to observe that despite their characteristic differences (composition, order and topography), lipid domains of the RBC PM at resting state all share a similar size and a well-defined circular shape. This circular shape suggests the minimization of domain boundary due to unfavorable line tension. The contribution of line tension to lipid domain shape is confirmed by the recovery of chol-enriched circular shape after the relieve of the mechanical stress upon which it was lost (unpublished data). Furthermore, elliptocytes exhibit chol-enriched domains of lower circularity (unpublished data) along with lower $\Delta GP_{bulk\text{-}domains}$ as compared to healthy RBCs. If $\Delta GP_{bulk\text{-}domains}$ is contributive to the line tension energy, as proposed in Chapter 4, this could be another line of evidence for the control of domain shape by the line tension. If only the line tension is taken into account, lipid domains would evolved towards one single domains, however domain merging is balanced by an entropy cost (Frolov et al., 2006). The similar size of the different domain populations could suggest that line tension also strongly contributes to domain size (*i.e.* the number of optically resolved domains). This is supported by the modulation of domain number upon incubation of RBCs with diverse line active agents (D'Auria et al., 2013a). As observed in model membrane taking only lipid-lipid interactions into account, these observations suggest the energetic contribution of the line tension at domain boundary to domain shape and size/number in the more complex context of living cells.

6.2 Line tension and domain modulation and functionalization

While line tension seems central in domain biogenesis, it could also be involved in domain modulation and functionalization. As proposed in Chapter 4, the cell might modulate membrane biophysical properties impacting the line tension at domain boundary, such as $\Delta GP_{bulk\text{-}domains}$, to functionalize domains. While this hypothesis has been detailled for lipid domain vesiculation in Chapter 4, it could also be relevant for lipid domain contribution to RBC reshaping. Indeed, upon microfluidic deformation of GUVs, domains merge

to decrease the line tension energy at domain boundary (Robinson, 2013), in response to increased line tension due to increased lateral tension (Akimov et al., 2007). Accordingly, we previously observed the gathering of chol-enriched domains in increased curvature areas upon RBC deformation and in elliptocytes. Sending lipid domains towards either (i) reversible reorganization upon deformation due to increased membrane compression applied by external forces to the membrane, or (ii) irreversible vesiculation upon aging due to increased compression applied by the cytoskeleton to the membrane, could be controlled by the difference in the strength and/or reversibility/time scale of the stress imposed. Indeed, a more drastic and long lasting increase in line tension at domain boundary could occur upon aging, while a prompt compression is applied upon deformation. It should be noticed that evaluation of $\Delta GP_{bulk\text{-}domains}$ contribution to the line tension energy is needed. Furthermore, other differences in domain-bulk characteristics than lipid order could participate in the line tension (*e.g.* bending rigidity, intrinsic curvature or thickness). Finally, other control mechanisms than membrane compression imposed by external mechanical stress or cytoskeleton stiffness could be used by the cell and play in concert to functionalize lipid domains by modulation of the line tension energy at domains boundary (*e.g*. electrostatic interaction or interleaflet coupling).

To conclude

In conclusion, we propose that cells could functionalize lipid domains by modulation of biophysical properties affecting the line tension energy at domains boundary (e.g. $\Delta GP_{bulk\text{-}domains}$). Sending lipid domains towards either reversible reorganization upon deformation or irreversible vesiculation upon aging could be controlled by the difference in the strength and/or reversibility/time scale of the compression imposed to the membrane, hence the impact on the line tension at domains boundary. Additionally to the mechanisms proposed here, various biophysical properties (*e.g.* bending rigidity, intrinsic curvature or thickness) could be used by the cell to modulate the line tension energy at domains boundary though a diversity of control factors (e.g. electrostatic interaction or interleaflet coupling).

7. **Final conclusion**

Altogether, the collective body of information gathered during this Thesis clearly exposes the contribution of PM lipid domains in RBC reshaping. However, lipids alone cannot govern such process. We instead suggest that lipid domains and their biophysical properties contribute with the cytoskeleton and membrane/peripheral proteins to allow for cell reshaping. Although the exact nature of such tight interconnection still requires investigation, our results pave the way towards a better understanding of (i) these incredibly complex cellular processes, and (ii) the diversity of organization, modulation and function of lipid domains in membranes.

References

Abe, M., A. Makino, F. Hullin-Matsuda, K. Kamijo, Y. Ohno-Iwashita, K. Hanada, H. Mizuno, A. Miyawaki, and T. Kobayashi. 2012. A role for sphingomyelin-rich lipid domains in the accumulation of phosphatidylinositol-4,5-bisphosphate to the cleavage furrow during cytokinesis. Mol Cell Biol. 32:1396-1407.

Abe, M., and T. Kobayashi. 2014. Imaging local sphingomyelin-rich domains in the plasma membrane using specific probes and advanced microscopy. Biochim. Biophys. Acta. 1841:720–6.

Adami, C. 1995. Self-organized criticality in living systems. Physics Letters A. 2013:29-32.

Agbani, E.O., M.T. van den Bosch, E. Brown, C.M. Williams, N.J. Mattheij, J.M. Cosemans, P.W. Collins, J.W. Heemskerk, I. Hers, and A.W. Poole. 2015. Coordinated membrane ballooning and procoagulant spreading in human platelets. Circulation. 132:1414-1424.

Aggarwal, S., L. Yurlova, and M. Simons. 2011. Central nervous system myelin: structure, synthesis and assembly. Trends Cell Biol. 21:585-593.

Ahn, K., and N.S. Sampson. 2004. Cholesterol oxidase senses subtle changes in lipid bilayer structure . Biochemistry. 43:827–836.

Ailte, I., A.B. Lingelem, S. Kavaliauskiene, J. Bergan, A.S. Kvalvaag, A.G. Myrann, T. Skotland, and K. Sandvig. 2016. Addition of lysophospholipids with large head groups to cells inhibits Shiga toxin binding. Sci. Rep. 6:30336.

Akimov, S.A., P.I. Kuzmin, J. Zimmerberg, and F.S. Cohen. 2007. Lateral tension increases the line tension between two domains in a lipid bilayer membrane. Physical Review E. 75:011919-011919.

Almeida, P.F.F. 2009. Thermodynamics of lipid interactions in complex bilayers. Biochim. Biophys. Acta - Biomembr. 1788:72–85.

Alsteens, D., H. Trabelsi, P. Soumillion, and Y.F. Dufrene. 2013. Multiparametric atomic force microscopy imaging of single bacteriophages extruding from living bacteria. Nat. Commun. 4:2926.

An, X., G. Debnath, X. Guo, S. Liu, S.E. Lux, A. Baines, W. Gratzer, and N. Mohandas. 2005. Identification and Functional Characterization of Protein 4.1R and Actin-Binding Sites in Erythrocyte β Spectrin: Regulation of the Interactions by Phosphatidylinositol-4,5-bisphosphate †. Biochemistry. 44:10681–10688.

An, X., X. Zhang, G. Debnath, A.J. Baines, and N. Mohandas. 2006. Phosphatidylinositol-4,5-biphosphate (PIP2) differentially regulates the interaction of human erythrocyte protein 4.1 (4.1R) with membrane proteins. Biochemistry. 45:5725-5732.

Andreae, L.C., and J. Burrone. 2015. Spontaneous neurotransmitter release shapes dendritic arbors via long-range activation of NMDA receptors. Cell Rep. pii: S2211-1247(15)00057-1.

Antonelou, M.H., A.G. Kriebardis, and I.S. Papassideri. 2010. Aging and death signalling in mature red cells: from basic science to transfusion practice. Blood Transfus. 8 Suppl 3:s39-47.

Arashiki, N., M. Saito, I. Koshino, K. Kamata, J. Hale, N. Mohandas, S. Manno, and Y. Takakuwa. 2016. An Unrecognized Function of Cholesterol: Regulating the Mechanism Controlling Membrane Phospholipid Asymmetry. Biochemistry. 55:3504-3513.

Aresta-Branco, F., A.M. Cordeiro, H.S. Marinho, L. Cyrne, F. Antunes, and R.F. de Almeida. 2011. Gel domains in the plasma membrane of Saccharomyces cerevisiae: highly

ordered, ergosterol-free, and sphingolipid-enriched lipid rafts. J Biol Chem. 286:5043-5054.

Artmann, G.M., K.L. Sung, T. Horn, D. Whittemore, G. Norwich, and S. Chien. 1997. Micropipette aspiration of human erythrocytes induces echinocytes via membrane phospholipid translocation. Biophys. J. 72:1434–1441.

Arumugam, S., and P. Bassereau. 2015. Membrane nanodomains: contribution of curvature and interaction with proteins and cytoskeleton. Essays Biochem. 57:109–119.

Arumugam, S., E.P. Petrov, and P. Schwille. 2015. Cytoskeletal pinning controls phase separation in multicomponent lipid membranes. Biophys J. 108:1104-1113.

Aspenstrom, P. 2014. BAR domain proteins regulate Rho GTPase signaling. Small GTPases. 5:7.

Bach, J.N., and M. Bramkamp. 2013. Flotillins functionally organize the bacterial membrane. Mol Microbiol. 88:1205-1217.

Bacia, K., D. Scherfeld, N. Kahya, and P. Schwille. 2004. Fluorescence correlation spectroscopy relates rafts in model and native membranes. Biophys. J. 87:1034–1043.

Bacia, K., P. Schwille, and T. Kurzchalia. 2005. Sterol structure determines the separation of phases and the curvature of the liquid-ordered phase in model membranes. Proc. Natl. Acad. Sci. 102:3272–3277.

Bagatolli, L.A. 2006. To see or not to see: Lateral organization of biological membranes and fluorescence microscopy. Biochimica et Biophysica Acta (BBA) - Biomembranes. 1758:1541-1556.

Bagatolli, L.A., and O.G. Mouritsen. 2013. Is the fluid mosaic (and the accompanying raft hypothesis) a suitable model to describe fundamental features of biological membranes? What may be missing? Front Plant Sci. 4:457.

Bagatolli, L.A., J.H. Ipsen, A.C. Simonsen, and O.G. Mouritsen. 2010a. An outlook on organization of lipids in membranes: searching for a realistic connection with the organization of biological membranes. Prog. Lipid Res. 49:378-389.

Bagatolli, L.A., J.H. Ipsen, A.C. Simonsen, and O.G. Mouritsen. 2010b. An outlook on organization of lipids in membranes: searching for a realistic connection with the organization of biological membranes. Prog Lipid Res. 49:378-389.

Bagnat, M., and K. Simons. 2002. Cell surface polarization during yeast mating. Proc Natl Acad Sci U S A. 99:14183-14188.

Baines, A.J. 2010. The spectrin–ankyrin–4.1–adducin membrane skeleton: adapting eukaryotic cells to the demands of animal life. Protoplasma. 244:99–131.

Bali, R., L. Savino, D.A. Ramirez, N.M. Tsvetkova, L. Bagatolli, F. Tablin, J.H. Crowe, and C. Leidy. 2009. Macroscopic domain formation during cooling in the platelet plasma membrane: an issue of low cholesterol content. Biochim Biophys Acta. 1788:1229-1237.

Balijepalli, R.C., J.D. Foell, D.D. Hall, J.W. Hell, and T.J. Kamp. 2006. Localization of cardiac L-type Ca2+ channels to a caveolar macromolecular signaling complex is required for beta2-adrenergic regulation. Proc. Natl. Acad. Sci. 103:7500–7505.

Bao, N., G.C. Kodippili, K.M. Giger, V.M. Fowler, P.S. Low, and C. Lu. 2011. Single-cell electrical lysis of erythrocytes detects deficiencies in the cytoskeletal protein network. Lab on a chip. 11:3053-3056.

Barcellini, W., P. Bianchi, E. Fermo, F.G. Imperiali, A.P. Marcello, C. Vercellati, A. Zaninoni, and A. Zanella. 2011. Hereditary red cell membrane defects: diagnostic and clinical aspects. Blood Transfus. 9:274–277.

Barry R.Lentz. 1989. Membrane “fluidity” as detected by diphenylhexatriene probes. Chem. Phys. Lipids. 50:171–190.

Baumgart, T., A.T. Hammond, P. Sengupta, S.T. Hess, D.A. Holowka, B.A. Baird, and W.W. Webb. 2007a. Large-scale fluid/fluid phase separation of proteins and lipids in giant plasma membrane vesicles. Proc Natl Acad Sci U S A. 104:3165-3170.

Baumgart, T., S.T. Hess, and W.W. Webb. 2003. Imaging coexisting fluid domains in biomembrane models coupling curvature and line tension. Nature. 425:821-824.

Baumgartner, W., P. Hinterdorfer, W. Ness, A. Raab, D. Vestweber, H. Schindler, and D. Drenckhahn. 2000. Cadherin interaction probed by atomic force microscopy. Proc. Natl. Acad. Sci. U. S. A. 97:4005-4010.

Beech, D.J., Y.M. Bahnasi, A.M. Dedman, and E. Al-Shawaf. 2009. TRPC channel lipid specificity and mechanisms of lipid regulation. Cell Calcium. 45:583–8.

Bernal, P., J. Muñoz-Rojas, A. Hurtado, J.L. Ramos, and A. Segura. 2007. A Pseudomonas putida cardiolipin synthesis mutant exhibits increased sensitivity to drugs related to transport functionality. Environmental Microbiology. 9:1135-1145.

Bernardino de la Serna, J., G. Oradd, L.A. Bagatolli, A.C. Simonsen, D. Marsh, G. Lindblom, and J. Perez-Gil. 2009. Segregated phases in pulmonary surfactant membranes do not show coexistence of lipid populations with differentiated dynamic properties. Biophys J. 97:1381-1389.

Bernardino de la Serna, J., G.J. Schutz, C. Eggeling, and M. Cebecauer. 2016. There Is No Simple Model of the Plasma Membrane Organization. Front Cell Dev Biol. 4:106.

Bernardino de la Serna, J., J. Perez-Gil, A.C. Simonsen, and L.A. Bagatolli. 2004. Cholesterol rules: direct observation of the coexistence of two fluid phases in native pulmonary surfactant membranes at physiological temperatures. J Biol Chem. 279:40715-40722.

Betz, T., M. Lenz, J.F. Joanny, and C. Sykes. 2009. ATP-dependent mechanics of red blood cells. Proc Natl Acad Sci U S A. 106:15320-15325.

Bigay, J., and B. Antonny. 2012. Curvature, lipid packing, and electrostatics of membrane organelles: defining cellular territories in determining specificity. Dev. Cell. 23:886-895.

Bitbol, M., P. Fellmann, A. Zachowski, and P.F. Devaux. 1987. Ion regulation of phosphatidylserine and phosphatidylethanolamine outside-inside translocation in human erythrocytes. Biochim. Biophys. Acta. 904:268–82.

Bleecker, J.V., P.A. Cox, R.N. Foster, J.P. Litz, M.C. Blosser, D.G. Castner, and S.L. Keller. 2016. Thickness mismatch of coexisting liquid phases in noncanonical lipid bilayers. The Journal of Physical Chemistry B. 120:2761-2770.

Bogdanova, A., A. Makhro, J. Wang, P. Lipp, and L. Kaestner. 2013. Calcium in Red Blood Cells—A Perilous Balance. Int. J. Mol. Sci. 14:9848–9872.

Boggs, J.M., and H. Wang. 2004. Co-clustering of galactosylceramide and membrane proteins in oligodendrocyte membranes on interaction with polyvalent carbohydrate and prevention by an intact cytoskeleton. Journal of neuroscience research. 76:342-355.

Boggs, J.M., W. Gao, J. Zhao, H.J. Park, Y. Liu, and A. Basu. 2010. Participation of galactosylceramide and sulfatide in glycosynapses between oligodendrocyte or myelin membranes. FEBS Lett. 584:1771-1778.

Bosman, G.J.C.G.M., J.M. Werre, F.L.A. Willekens, and V.M.J. Novotný. 2008. Erythrocyte ageing in vivo and in vitro : structural aspects and implications for transfusion. Transfus. Med. 18:335–347.

Bouwstra, J.A., P.L. Honeywell-Nguyen, G.S. Gooris, and M. Ponec. 2003. Structure of the skin barrier and its modulation by vesicular formulations. Prog Lipid Res. 42:1-36.

Bramkamp, M., and D. Lopez. 2015. Exploring the existence of lipid rafts in bacteria. Microbiology and Molecular Biology Reviews. 79:81-100.

Bremmell, K.E., A. Evans, and C.A. Prestidge. 2006. Deformation and nano-rheology of red blood cells: An AFM investigation. Colloids and Surfaces B: Biointerfaces. 50:43-48.

Bretscher, A., D. Chambers, R.A. Nguyen, .and D. Reczek. 2000. ERM-merlin and EBP50 protein families in plasma membrane organization and function. Annual Review of Cell and Developmental Biology. 16:113-143.

Bretscher, M.S. 1972. Phosphatidyl-ethanolamine: differential labelling in intact cells and cell ghosts of human erythrocytes by a membrane-impermeable reagent. J Mol Biol. 71:523-528.

Brewer, J., H.S. Thoke, R.P. Stock, and L.A. Bagatolli. 2017. Enzymatic studies on planar supported membranes using a widefield fluorescence LAURDAN Generalized Polarization imaging approach. Biochim Biophys Acta. 1859:888-895.

Brown, D.A., and E. London. 1998. Functions of lipid rafts in biological membranes. Annu. Rev. Cell Dev. Biol. 14:111-136.

Butt, H.-J., B. Cappella, and M. Kappl. 2005. Force measurements with the atomic force microscope: Technique, interpretation and applications. Surf. Sci. Rep. 59:1-152.

Byers, T.J., and D. Branton. 1985. Visualization of the protein associations in the erythrocyte membrane skeleton. Proc. Natl. Acad. Sci. U. S. A. 82:6153–7.

Cahalan, S.M., V. Lukacs, S.S. Ranade, S. Chien, M. Bandell, A. Patapoutian, J. Rinehart, P. Gallagher, H. Allayee, X. Li, A. Radhakrishnan, S. Tan, K. Voss, C. Weichenberger, C. Albers, A. Al-Hussani, F. Asselbergs, M. Ciullo, F. Danjou, C. Dina, T. Esko, D. Evans, L. Franke, M. Gögele, J. Hartiala, M. Hersch, H. Holm, J. Hottenga, S. Kanoni, M. Kleber, V. Lagou, C. Langenberg, L. Lopez, L. Lyytikäinen, O. Melander, F. Murgia, I. Nolte, P. O'Reilly, S. Padmanabhan, A. Parsa, N. Pirastu, E. Porcu, L. Portas, I. Prokopenko, J. Ried, S. Shin, C. Tang, A. Teumer, M. Traglia, S. Ulivi, H. Westra, J. Yang, J. Zhao, F. Anni, A. Abdellaoui, A. Attwood, B. Balkau, S. Bandinelli, F. Bastardot, B. Benyamin, B. Boehm, W. Cookson, D. Das, P. de Bakker, R. de Boer, E. de Geus, M. de Moor, M. Dimitriou, F. Domingues, A. Döring, G. Engström, G. Eyjolfsson, L. Ferrucci, K. Fischer, R. Galanello, S. Garner, B. Genser, Q. Gibson, G. Girotto, D. Gudbjartsson, S. Harris, A. Hartikainen, C. Hastie, B. Hedblad, T. Illig, J. Jolley, M. Kähönen, I. Kema, J. Kemp, L. Liang, H. Lloyd-Jones, R. Loos, S. Meacham, S. Medland, C. Meisinger, Y. Memari, E. Mihailov, K. Miller, et al. 2015. Piezo1 links mechanical forces to red blood cell volume. Elife. 4:1908–1915.

Cahalan, S.M., V. Lukacs, S.S. Ranade, S. Chien, M. Bandell, and A. Patapoutian. 2015. Piezo1 links mechanical forces to red blood cell volume. Elife. 4.

Cai, M., W. Zhao, X. Shang, J. Jiang, H. Ji, Z. Tang, and H. Wang. 2012. Direct evidence of lipid rafts by in situ atomic force microscopy. Small. 8:1243-1250.

Canham, P.B. 1970. The minimum energy of bending as a possible explanation of the biconcave shape of the human red blood cell. J. Theor. Biol. 26:61–81.

Carquin, M., H. Pollet, M. Veiga-da-Cunha, A. Cominelli, P. Van Der Smissen, F. N'Kuli, H. Emonard, P. Henriet, H. Mizuno, P.J. Courtoy, and D. Tyteca. 2014. Endogenous sphingomyelin segregates into submicrometric domains in the living erythrocyte membrane. J Lipid Res. 55:1331-1342.

Carquin, M., L. Conrard, H. Pollet, P. Van Der Smissen, A. Cominelli, M. Veiga-da-Cunha, P.J. Courtoy, and D. Tyteca. 2015. Cholesterol segregates into submicrometric domains at the living erythrocyte membrane: evidence and regulation. Cell Mol Life Sci. 72:4633-4651.

Carquin, M., L. D'Auria, H. Pollet, E.R. Bongarzone, and D. Tyteca. 2016. Recent progress on lipid lateral heterogeneity in plasma membranes: From rafts to submicrometric domains. Prog Lipid Res. 62:1-24.

Carvalho, K., L. Ramos, C. Roy, and C. Picart. 2008. Giant unilamellar vesicles containing phosphatidylinositol(4,5)bisphosphate: characterization and functionality. Biophys J. 95:4348-4360.

Castro, B.M., M. Prieto, and L.C. Silva. 2014. Ceramide: a simple sphingolipid with unique biophysical properties. Prog Lipid Res. 54:53-67.

Chasis, J.A., and N. Mohandas. 1992. Red blood cell glycophorins. Blood. 80:1869–79.

Chernomordik, L.V., and M.M. Kozlov. 2008. Mechanics of membrane fusion. Nat. Struct. Mol. Biol. 15:675-683.

Chiantia, S., and E. London. 2012. Acyl chain length and saturation modulate interleaflet coupling in asymmetric bilayers: effects on dynamics and structural order. Biophys. J. 103:2311-2319.

Chierico, L., A.S. Joseph, A.L. Lewis, and G. Battaglia. 2014. Live cell imaging of membrane/cytoskeleton interactions and membrane topology. Sci Rep. 4:6056.

Chivukula, V.K., B.L. Krog, J.T. Nauseef, M.D. Henry, and S.C. Vigmostad. 2015. Alterations in cancer cell mechanical properties after fluid shear stress exposure: a micropipette aspiration study. Cell health and cytoskeleton. 7:25-35.

Clarke, R.J. 1997. Effect of lipid structure on the dipole potential of phosphatidylcholine bilayers. Biochimica et Biophysica Acta (BBA) - Biomembranes. 1327:269-278.

Collins, M.D., and S.L. Keller. 2008. Tuning lipid mixtures to induce or suppress domain formation across leaflets of unsupported asymmetric bilayers. Proceedings of the National Academy of Sciences. 105:124-128.

Cullis, P.R., and B. De Kruijff. 1979. Lipid polymorphism and the functional roles of lipids in biological membranes. Biochimica et Biophysica Acta (BBA) - Reviews on Biomembranes. 559:399-420.

D'Alessandro, A., G. Liumbruno, G. Grazzini, and L. Zolla. 2010. Red blood cell storage: the story so far. Blood Transfus. 8:82–8. doi:10.2450/2009.0122-09.

D'Auria, L., M. Deleu, S. Dufour, M.-P. Mingeot-Leclercq, and D. Tyteca. 2013a. Surfactins modulate the lateral organization of fluorescent membrane polar lipids: A new tool to study drug:membrane interaction and assessment of the role of cholesterol and drug acyl chain length. Biochim. Biophys. Acta - Biomembr. 1828:2064–2073.

D'Auria, L., M. Fenaux, P. Aleksandrowicz, P. Van Der Smissen, C. Chantrain, C. Vermylen, M. Vikkula, P.J. Courtoy, and D. Tyteca. 2013b. Micrometric segregation of fluorescent membrane lipids: relevance for endogenous lipids and biogenesis in erythrocytes. J. Lipid Res. 54:1066–76.

D′Auria, L., P. Van Der Smissen, F. Bruyneel, P.J. Courtoy, and D. Tyteca. 2011. Segregation of Fluorescent Membrane Lipids into Distinct Micrometric Domains: Evidence for Phase Compartmentation of Natural Lipids? PLoS One. 6:e17021. doi:10.1371/journal.pone.0017021.

Daleke, D.L. 2008. Regulation of phospholipid asymmetry in the erythrocyte membrane. Curr. Opin. Hematol. 15:191-195.

D'Alessandro, A., G. Liumbruno, G. Grazzini, and L. Zolla. 2010. Red blood cell storage: the story so far. Blood transfusion, 8:82-88.

Danilchik, M.V., E.E. Brown, and K. Riegert. 2006. Intrinsic chiral properties of the Xenopus egg cortex: an early indicator of left-right asymmetry? Development. 133:4517-4526.

Das, A., J.L. Goldstein, D.D. Anderson, M.S. Brown, and A. Radhakrishnan. 2013. Use of mutant 125I-perfringolysin O to probe transport and organization of cholesterol in membranes of animal cells. Proc Natl Acad Sci U S A. 110:10580-10585.

Decker, L., and C. ffrench-Constant. 2004. Lipid rafts and integrin activation regulate oligodendrocyte survival. J Neurosci. 24:3816-3825.

Del Conde, I., C.N. Shrimpton, P. Thiagarajan, and J.A. Lopez. 2005. Tissue-factor-bearing microvesicles arise from lipid rafts and fuse with activated platelets to initiate coagulation. Blood. 106:1604-1611.

Deleu, M., J. Lorent, L. Lins, R. Brasseur, N. Braun, K. El Kirat, T. Nylander, Y.F. Dufrêne, and M.-P. Mingeot-Leclercq. 2013. Effects of surfactin on membrane models displaying lipid phase separation. Biochim. Biophys. Acta - Biomembr. 1828:801–815.

Demchenko, A.P., Y. Mély, G. Duportail, and A.S. Klymchenko. 2009. Monitoring biophysical properties of lipid membranes by environment-sensitive fluorescent probes. Biophys. J. 96:3461–70.

Deplaine, G., I. Safeukui, F. Jeddi, F. Lacoste, V. Brousse, S. Perrot, S. Biligui, M. Guillotte, C. Guitton, S. Dokmak, B. Aussilhou, A. Sauvanet, D. Cazals Hatem, F. Paye, M. Thellier, D. Mazier, G. Milon, N. Mohandas, O. Mercereau-Puijalon, P.H. David, and P.A. Buffet. 2011. The sensing of poorly deformable red blood cells by the human spleen can be mimicked in vitro. Blood. 117:e88-95.

Dhermy, D., J. Schrével, and M.-C. Lecomte. 2007. Spectrin-based skeleton in red blood cells and malaria. Curr. Opin. Hematol. 14:198–202.

Dietrich, C., L.A. Bagatolli, Z.N. Volovyk, N.L. Thompson, M. Levi, K. Jacobson, and E. Gratton. 2001. Lipid Rafts Reconstituted in Model Membranes. Biophysical Journal. 80:1417-1428.

Diez-Silva, M., M. Dao, J. Han, C.T. Lim, and S. Suresh. 2010. Shape and Biomechanical Characteristics of Human Red Blood Cells in Health and Disease. MRS Bull. 35:382-388.

Dinic, J., A. Riehl, J. Adler, and I. Parmryd. 2015. The T cell receptor resides in ordered plasma membrane nanodomains that aggregate upon patching of the receptor. Sci Rep. 5:10082.

Dinic, J., H. Biverståhl, L. Mäler, and I. Parmryd. 2011. Laurdan and di-4-ANEPPDHQ do not respond to membrane-inserted peptides and are good probes for lipid packing. Biochim. Biophys. Acta - Biomembr. 1808:298–306.

Dodes Traian, M.M., D.I. Cattoni, V. Levi, and F.L. González Flecha. 2012. A Two-Stage Model for Lipid Modulation of the Activity of Integral Membrane Proteins. PLoS One. 7:e39255.

Donovan, C., and M. Bramkamp. 2009. Characterization and subcellular localization of a bacterial flotillin homologue. Microbiology. 155:1786-1799.

Doughty, D.M., M. Dieterle, A.L. Sessions, W.W. Fischer, and D.K. Newman. 2014. Probing the subcellular localization of hopanoid lipids in bacteria using NanoSIMS. PLOS ONE. 9:e84455.

Downing, D.T. 1992. Lipid and protein structures in the permeability barrier of mammalian epidermis. J Lipid Res. 33:301-313.

Drin, G., and B. Antonny. 2010. Amphipathic helices and membrane curvature. FEBS Letters. 584:1840-1847.

Dufrêne, Y.F., D. Martinez-Martin, I. Medalsy, D. Alsteens, and D.J. Muller. 2013. Multiparametric imaging of biological systems by force-distance curve-based AFM. Nat. Methods. 10:847-854.

Dyrda, A., U. Cytlak, A. Ciuraszkiewicz, A. Lipinska, A. Cueff, G. Bouyer, S. Egée, P. Bennekou, V.L. Lew, and S.L.Y. Thomas. 2010. Local Membrane Deformations Activate Ca2+-Dependent K+ and Anionic Currents in Intact Human Red Blood Cells. PLoS One. 5:e9447.

Eber, S., and S.E. Lux. 2004. Hereditary spherocytosis--defects in proteins that connect the membrane skeleton to the lipid bilayer. Semin. Hematol. 41:118–141.

Edwards, C.L., M.T. Scales, C. Loughlin, G.G. Bennett, S. Harris-Peterson, L.M. De Castro, E. Whitworth, M. Abrams, M. Feliu, S. Johnson, M. Wood, O. Harrison, and A. Killough. 2005. A brief review of the pathophysiology, associated pain, and psychosocial issues in sickle cell disease. Int. J. Behav. Med. 12:171–179.

Ehrlich, M., W. Boll, A. van Oijen, R. Hariharan, K. Chandran, M.L. Nibert, and T. Kirchhausen. Endocytosis by random initiation and stabilization of clathrin-coated pits. Cell. 118:591-605.

Ekyalongo, R.C., H. Nakayama, K. Kina, N. Kaga, and K. Iwabuchi. 2015. Organization and functions of glycolipid-enriched microdomains in phagocytes. Biochim Biophys Acta. 1851:90-97.

Elani, Y., S. Purushothaman, P.J. Booth, J.M. Seddon, N.J. Brooks, R.V. Law, and O. Ces. 2015. Measurements of the effect of membrane asymmetry on the mechanical properties of lipid bilayers. Chem. Commun. (Camb.). 51:6976-6979.

Emoto, K., and M. Umeda. 2000. An essential role for a membrane lipid in cytokinesis. Regulation of contractile ring disassembly by redistribution of phosphatidylethanolamine. J Cell Biol. 149:1215-1224.

Emoto, K., H. Inadome, Y. Kanaho, S. Narumiya, and M. Umeda. 2005. Local change in phospholipid composition at the cleavage furrow is essential for completion of cytokinesis. J Biol Chem. 280:37901-37907.

Ernst, R., C.S. Ejsing, and B. Antonny. 2016. Homeoviscous adaptation and the regulation of membrane lipids. J. Mol. Biol. 428:4776-4791.

Fan, J., M. Sammalkorpi, and M. Haataja. 2010. Formation and regulation of lipid microdomains in cell membranes: Theory, modeling, and speculation. FEBS Letters. 584:1678-1684.

Fanning, A.S., C.M. Van Itallie, and J.M. Anderson. 2012. Zonula occludens-1 and -2 regulate apical cell structure and the zonula adherens cytoskeleton in polarized epithelia. Mol Biol Cell. 23:577-590.

Farrand, A.J., S. LaChapelle, E.M. Hotze, A.E. Johnson, and R.K. Tweten. 2010. Only two amino acids are essential for cytolytic toxin recognition of cholesterol at the membrane surface. Proc. Natl. Acad. Sci. 107:4341–4346.

Feeser, E.A., and E.M. Ostap. 2010. Myo1e Binds Anionic Phospholipids with high affinity. Biophysical Journal. 98:561a.

Fidorra, M., L. Duelund, C. Leidy, A.C. Simonsen, and L.A. Bagatolli. 2006. Absence of fluid-ordered/fluid-disordered phase coexistence in ceramide/POPC mixtures containing cholesterol. Biophysical journal. 90:4437-4451.

Fidorra, M., T. Heimburg, and L.A. Bagatolli. 2009. Direct visualization of the lateral structure of porcine brain cerebrosides/POPC mixtures in presence and absence of cholesterol. Biophys J. 97:142-154.

Field, S.J., N. Madson, M.L. Kerr, K.A. Galbraith, C.E. Kennedy, M. Tahiliani, A. Wilkins, and L.C. Cantley. 2005. PtdIns(4,5)P2 functions at the cleavage furrow during cytokinesis. Curr Biol. 15:1407-1412.

Foret, L.. 2005. A simple mechanism of raft formation in two-component fluid membranes. Europhysics Letters (EPL). 71:508-514.

Frazier, M.L., J.R. Wright, A. Pokorny, and P.F.F. Almeida. 2007. Investigation of Domain Formation in Sphingomyelin/Cholesterol/POPC Mixtures by Fluorescence Resonance Energy Transfer and Monte Carlo Simulations. Biophys. J. 92:2422–2433.

Fricke, K., and E. Sackmann. 1984. Variation of frequency spectrum of the erythrocyte flickering caused by aging, osmolarity, temperature and pathological changes. Biochim. Biophys. Acta. 803:145–52.

Frisz, J.F., H.A. Klitzing, K. Lou, I.D. Hutcheon, P.K. Weber, J. Zimmerberg, and M.L. Kraft. 2013a. Sphingolipid domains in the plasma membranes of fibroblasts are not enriched with cholesterol. J Biol Chem. 288:16855-16861.

Frisz, J.F., K. Lou, H.A. Klitzing, W.P. Hanafin, V. Lizunov, R.L. Wilson, K.J. Carpenter, R. Kim, I.D. Hutcheon, J. Zimmerberg, P.K. Weber, and M.L. Kraft. 2013b. Direct chemical evidence for sphingolipid domains in the plasma membranes of fibroblasts. Proc Natl Acad Sci U S A. 110:E613-622.

Frolov, V.A.J., Y.A. Chizmadzhev, F.S. Cohen, and J. Zimmerberg. 2006. "Entropic traps" in the kinetics of phase separation in multicomponent membranes stabilize nanodomains. Biophysical journal. 91:189-205.

Frost, A., V.M. Unger, and P. De Camilli. 2009. The BAR domain superfamily: membrane-molding macromolecules. Cell. 137:191-196.

Fujita, A., J. Cheng, and T. Fujimoto. 2009. Segregation of GM1 and GM3 clusters in the cell membrane depends on the intact actin cytoskeleton. Biochimica et biophysica acta. 1791:388-396.

Fujiwara, T., K. Ritchie, H. Murakoshi, K. Jacobson, and A. Kusumi. 2002. Phospholipids undergo hop diffusion in compartmentalized cell membrane. J Cell Biol. 157:1071-1081.

Fukami, K., K. Furuhashi, M. Inagaki, T. Endo, S. Hatano, and T. Takenawa. 1992. Requirement of phosphatidylinositol 4,5-bisphosphate for [alpha]-actinin function. Nature. 359:150-152.

Fukami, K., N. Sawada, T. Endo, and T. Takenawa. 1996. Identification of a Phosphatidylinositol 4,5-Bisphosphate-binding Site in Chicken Skeletal Muscle α-Actinin. Journal of Biological Chemistry. 271:2646-2650.

Gallagher, P.G. 2004. Hereditary elliptocytosis: spectrin and protein 4.1R. Semin. Hematol. 41:142–64.

Gallagher, P.G. 2005. Red Cell Membrane Disorders. Hematology. 2005:13–18.

Gallagher, P.G., and J.D. Ferriera. 1997. Molecular basis of erythrocyte membrane disorders. Curr. Opin. Hematol. 4:128–35.

García-Sáez, A.J., and P. Schwille. 2010. Stability of lipid domains. FEBS Letters. 584:1653-1658.

García-Sáez, A.J., S. Chiantia, and P. Schwille. 2007a. Effect of line tension on the lateral organization of lipid membranes. Journal of Biological Chemistry. 282:33537-33544.

García-Sáez, A.J., S. Chiantia, J. Salgado, and P. Schwille. 2007b. Pore formation by a Bax-derived peptide: effect on the line tension of the membrane probed by AFM. Biophysical journal. 93:103-112.

Garrenton, L.S., C.J. Stefan, M.A. McMurray, S.D. Emr, and J. Thorner. 2010. Pheromone-induced anisotropy in yeast plasma membrane phosphatidylinositol-4,5-bisphosphate distribution is required for MAPK signaling. Proceedings of the National Academy of Sciences of the United States of America. 107:11805-11810.

Gaus, K., E. Chklovskaia, B. Fazekas de St. Groth, W. Jessup, and T. Harder. 2005. Condensation of the plasma membrane at the site of T lymphocyte activation. The Journal of Cell Biology. 171:121-131.

Gauthier, E., X. Guo, N. Mohandas, and X. An. 2011. Phosphorylation-dependent perturbations of the 4.1R-associated multiprotein complex of the erythrocyte Membrane. Biochemistry. 50:4561–4567.

Gawrisch, K., D. Ruston, J. Zimmerberg, V.A. Parsegian, R.P. Rand, and N. Fuller. 1992. Membrane dipole potentials, hydration forces, and the ordering of water at membrane surfaces. Biophysical journal. 61:1213-1223.

Gerber, C., and H.P. Lang. 2006. How the doors to the nanoworld were opened. Nature Nanotechnology. 1:3-5.

Gimona, M., K. Djinovic-Carugo, W.J. Kranewitter, and S.J. Winder. 2002. Functional plasticity of CH domains. FEBS Letters. 513:98-106.

Girard, P., J. Pécréaux, G. Lenoir, P. Falson, J.-L. Rigaud, and P. Bassereau. 2004. A New Method for the Reconstitution of Membrane Proteins into Giant Unilamellar Vesicles. Biophysical Journal. 87:419-429.

Golan, D.E., M.R. Alecio, W.R. Veatch, and R.R. Rando. 1984. Lateral mobility of phospholipid and cholesterol in the human erythrocyte membrane: effects of protein-lipid interactions. Biochemistry. 23:332-339.

Golebiewska, U., M. Nyako, W. Woturski, I. Zaitseva, and S. McLaughlin. 2008. Diffusion coefficient of fluorescent phosphatidylinositol 4,5-bisphosphate in the plasma membrane of cells. Mol Biol Cell. 19:1663-1669.

Gomez, J., F. Sagues, and R. Reigada. 2010. Effect of integral proteins in the phase stability of a lipid bilayer: application to raft formation in cell membranes. J Chem Phys. 132:135104.

Gomez-Llobregat, J., J. Buceta, and R. Reigada. 2013. Interplay of cytoskeletal activity and lipid phase stability in dynamic protein recruitment and clustering. Sci Rep. 3:2608.

Gomez-Mouton, C., J.L. Abad, E. Mira, R.A. Lacalle, E. Gallardo, S. Jimenez-Baranda, I. Illa, A. Bernad, S. Manes, and A.C. Martinez. 2001. Segregation of leading-edge and uropod components into specific lipid rafts during T cell polarization. Proc Natl Acad Sci U S A. 98:9642-9647.

Goni, F.M. 2014. The basic structure and dynamics of cell membranes: an update of the Singer-Nicolson model. Biochim. Biophys. Acta. 1838:1467-1476.

Goodman, S.R., O. Daescu, D.G. Kakhniashvili, and M. Zivanic. 2013. The proteomics and interactomics of human erythrocytes. Exp Biol Med (Maywood). 238:509-518.

Gossett, D.R., H.T. Tse, S.A. Lee, Y. Ying, A.G. Lindgren, O.O. Yang, J. Rao, A.T. Clark, and D. Di Carlo. 2012. Hydrodynamic stretching of single cells for large population mechanical phenotyping. Proc Natl Acad Sci U S A. 109:7630-7635.

Gousset, K., W.F. Wolkers, N.M. Tsvetkova, A.E. Oliver, C.L. Field, N.J. Walker, J.H. Crowe, and F. Tablin. 2002. Evidence for a physiological role for membrane rafts in human platelets. J Cell Physiol. 190:117-128.

Gov, N.S. 2007a. Active elastic network: Cytoskeleton of the red blood cell. Phys. Rev. E. 75:11921.

Gov, N.S. 2007b. Less is more: removing membrane attachments stiffens the RBC cytoskeleton. New J. Phys. 9:429–429.

Gov, N.S., and S.A. Safran. 2005. Red blood cell membrane fluctuations and shape controlled by ATP-induced cytoskeletal defects. Biophys J. 88:1859-1874.

Grandbois, M., W. Dettmann, M. Benoit, and H.E. Gaub. 2000. Affinity imaging of red blood cells using an atomic force microscope. J. Histochem. Cytochem. 48:719-724.

Grassme, H., V. Jendrossek, A. Riehle, G. von Kurthy, J. Berger, H. Schwarz, M. Weller, R. Kolesnick, and E. Gulbins. 2003. Host defense against Pseudomonas aeruginosa requires ceramide-rich membrane rafts. Nature medicine. 9:322-330.

Gri, G., B. Molon, S. Manes, T. Pozzan, and A. Viola. 2004. The inner side of T cell lipid rafts. Immunology Letters. 94:247-252.

Grossmann, G., M. Opekarova, J. Malinsky, I. Weig-Meckl, and W. Tanner. 2007. Membrane potential governs lateral segregation of plasma membrane proteins and lipids in yeast. EMBO J. 26:1-8.

Gu, R.-X., H.I. Ingólfsson, A.H. de Vries, S.J. Marrink, and D.P. Tieleman. 2017. Ganglioside-lipid and ganglioside-protein interactions revealed by coarse-grained and atomistic molecular dynamics simulations. J. Phys. Chem. B. 121:3262–3275. doi:10.1021/acs.jpcb.6b07142.

Guck, J., S. Schinkinger, B. Lincoln, F. Wottawah, S. Ebert, M. Romeyke, D. Lenz, H.M. Erickson, R. Ananthakrishnan, D. Mitchell, J. Kas, S. Ulvick, and C. Bilby. 2005. Optical deformability as an inherent cell marker for testing malignant transformation and metastatic competence. Biophys J. 88:3689-3698.

Guiney, E.L., A.R. Goldman, J.E. Elias, and M.S. Cyert. 2015. Calcineurin regulates the yeast synaptojanin Inp53/Sjl3 during membrane stress. Molecular Biology of the Cell. 26:769-785.

Gupta, A., and L. Pulliam. 2014. Exosomes as mediators of neuroinflammation. J Neuroinflammation. 11:68.

Haldar, S., Ravi K. Kanaparthi, A. Samanta, and A. Chattopadhyay. 2012. Differential effect of cholesterol and its biosynthetic precursors on membrane dipole potential. Biophysical Journal. 102:1561-1569.

Hammond, A.T., F.A. Heberle, T. Baumgart, D. Holowka, B. Baird, and G.W. Feigenson. 2005. Crosslinking a lipid raft component triggers liquid ordered-liquid disordered phase separation in model plasma membranes. Proceedings of the National Academy of Sciences. 102:6320-6325.

Hammond, G.R. V., M.J. Fischer, K.E. Anderson, J. Holdich, A. Koteci, T. Balla, and R.F. Irvine. 2012. PI4P and PI(4,5)P2 are essential but independent lipid determinants of membrane identity. Science. 337:727–730.

Hanada, K., M. Nishijima, Y. Akamatsu, and R.E. Pagano. 1995. Both sphingolipids and cholesterol participate in the detergent insolubility of alkaline phosphatase, a glycosylphosphatidylinositol-anchored protein, in mammalian membranes. J. Biol. Chem. 270:6254–60.

Hansen, G.H., L.L. Niels-Christiansen, L. Immerdal, B.T. Nystrom, and E.M. Danielsen. 2007. Intestinal alkaline phosphatase: selective endocytosis from the enterocyte brush border during fat absorption. Am J Physiol Gastrointest Liver Physiol. 293:G1325-1332.

Hao, M., S. Mukherjee, and F.R. Maxfield. 2001. Cholesterol depletion induces large scale domain segregation in living cell membranes. Proc Natl Acad Sci U S A. 98:13072-13077.

Heberle, F.A., R.S. Petruzielo, J. Pan, P. Drazba, N. Kučerka, R.F. Standaert, G.W. Feigenson, and J. Katsaras. 2013. Bilayer Thickness Mismatch Controls Domain Size in Model Membranes. Journal of the American Chemical Society. 135:6853-6859.

Heemskerk, J.W., W.M. Vuist, M.A. Feijge, C.P. Reutelingsperger, and T. Lindhout. 1997. Collagen but not fibrinogen surfaces induce bleb formation, exposure of phosphatidylserine, and procoagulant activity of adherent platelets: evidence for regulation by protein tyrosine kinase-dependent Ca2+ responses. Blood. 90:2615-2625.

Heinrich, M., A. Tian, C. Esposito, and T. Baumgart. 2010. Dynamic sorting of lipids and proteins in membrane tubes with a moving phase boundary. Proceedings of the National Academy of Sciences of the United States of America. 107:7208-7213.

Henon, S., G. Lenormand, A. Richert, and F. Gallet. 1999. A new determination of the shear modulus of the human erythrocyte membrane using optical tweezers. Biophys J. 76:1145-1151.

Herman, P., J. Vecer, M. Opekarova, P. Vesela, I. Jancikova, J. Zahumensky, and J. Malinsky. 2015. Depolarization affects the lateral microdomain structure of yeast plasma membrane. FEBS Journal. 282:419-434.

Heu, C., A. Berquand, C. Elie-Caille, and L. Nicod. 2012. Glyphosate-induced stiffening of HaCaT keratinocytes, a peak force tapping study on living cells. J. Struct. Biol. 178:1-7.

Hillyard, D.Z., C.D. Nutt, J. Thomson, K.J. McDonald, R.K. Wan, A.J.M. Cameron, P.B. Mark, and A.G. Jardine. 2007. Statins inhibit NK cell cytotoxicity by membrane raft depletion rather than inhibition of isoprenylation. Atherosclerosis. 191:319–25.

Hinshaw, J.E., and S.L. Schmid. 1995. Dynamin self-assembles into rings suggesting a mechanism for coated vesicle budding. Nature. 374:190-192.

Hirschberg, C.B., and E.P. Kennedy. 1972. Mechanism of the enzymatic synthesis of cardiolipin in Escherichia coli. Proceedings of the National Academy of Sciences of the United States of America. 69:648-651.

Hochmuth, R.M. 2000. Micropipette aspiration of living cells. Journal of biomechanics. 33:15-22.

Holdbrook, D.A., R.G. Huber, T.J. Piggot, P.J. Bond, and S. Khalid. 2016. Dynamics of Crowded Vesicles: Local and Global Responses to Membrane Composition. PLoS. One. 11:e0156963.

Holthuis, J.C., and A.K. Menon. 2014. Lipid landscapes and pipelines in membrane homeostasis. Nature. 510:48-57.

Honigmann, A., and A. Pralle. 2016. Compartmentalization of the Cell Membrane. J Mol Biol. 428:4739-4748.

Honigmann, A., S. Sadeghi, J. Keller, S.W. Hell, C. Eggeling, and R. Vink. 2014. A lipid bound actin meshwork organizes liquid phase separation in model membranes. eLife. 3:e01671.

Hosseini, S.M., and J.J. Feng. 2012. How malaria parasites reduce the deformability of infected red blood cells. Biophys J. 103:1-10.

Hou, H.W., Q.S. Li, G.Y. Lee, A.P. Kumar, C.N. Ong, and C.T. Lim. 2009. Deformability study of breast cancer cells using microfluidics. Biomedical microdevices. 11:557-564.

Huang, K.C., and K.S. Ramamurthi. 2010. Macromolecules that prefer their membranes curvy. Molecular Microbiology. 76:822-832.

Huang, K.C., R. Mukhopadhyay, and N.S. Wingreen. 2006. A curvature-mediated mechanism for localization of lipids to bacterial poles. PLoS Comput. Biol. 2:e151.

Huang, Z., and E. London. 2016. Cholesterol lipids and cholesterol-containing lipid rafts in bacteria. Chem. Phys. Lipids. 199:11-16.

Huijbregts, R.P., A.I. de Kroon, and B. de Kruijff. 2000. Topology and transport of membrane lipids in bacteria. Biochim. Biophys. Acta. 1469:43-61.

Hurley, J.H., and P.I. Hanson. 2010. Membrane budding and scission by the ESCRT machinery: it's all in the neck. Nat Rev Mol Cell Biol. 11:556-566.

Ikenouchi, J., M. Suzuki, K. Umeda, K. Ikeda, R. Taguchi, T. Kobayashi, S.B. Sato, T. Kobayashi, D.B. Stolz, and M. Umeda. 2012. Lipid polarity is maintained in absence of tight junctions. J Biol Chem. 287:9525-9533.

Ikonen, E. 2001. Roles of lipid rafts in membrane transport. Curr. Opin. Cell Biol. 13:470–477.

Inoue, I., Y. Kobatake, and I. Tasaki. 1973. Excitability, instability and phase transitions in squid axon membrane under internal perfusion with dilute salt solutions. Biochimica et Biophysica Acta (BBA) - Biomembranes. 307:471-477.

Ishitsuka, R., A. Yamaji-Hasegawa, A. Makino, Y. Hirabayashi, and T. Kobayashi. 2004. A Lipid-Specific Toxin Reveals Heterogeneity of Sphingomyelin-Containing Membranes. Biophys. J. 86:296–307.

Ishitsuka, R., and T. Kobayashi. 2004. Lysenin: A new tool for investigating membrane lipid organization. Anat. Sci. Int. 79:184–190.

Iwamoto, K., S. Kobayashi, R. Fukuda, M. Umeda, T. Kobayashi, and A. Ohta. 2004. Local exposure of phosphatidylethanolamine on the yeast plasma membrane is implicated in cell polarity. Genes Cells. 9:891-903.

Jackman, N., A. Ishii, and R. Bansal. 2009. Oligodendrocyte development and myelin biogenesis: parsing out the roles of glycosphingolipids. Physiology (Bethesda). 24:290-297.

Jacobson, K., O.G. Mouritsen, and R.G.W. Anderson. 2007. Lipid rafts: at a crossroad between cell biology and physics. Nature Cell Biology. 9:7-14.

Janmey, P.A., and P.K. Kinnunen. 2006. Biophysical properties of lipids and dynamic membranes. Trends Cell Biol. 16:538-546.

Janmey, P.A., and U. Lindberg. 2004. Cytoskeletal regulation: Rich in lipids. Nature Reviews Molecular Cell Biology. 5:658-666.

Jensen, H. 1998. Self-organized criticality: emergent complex behavior in physical and biological systems. Cambridge lecture notes inPhysics.

Jensen, M.Ø., and O.G. Mouritsen. 2004. Lipids do influence protein function—the hydrophobic matching hypothesis revisited. Biochimica et Biophysica Acta (BBA) - Biomembranes. 1666:205-226.

Jin, H., J.M. McCaffery, and E. Grote. 2008. Ergosterol promotes pheromone signaling and plasma membrane fusion in mating yeast. The Journal of cell biology. 180:813-826.

Jin, W., and A. Pralle. 2016. Transient Effect of Calcium Influx on PIP2 Clusters in the Inner Plasma Membrane Leaflet of Intact Cells. In Biophysical Journal. BPS. 204a.

Johnson, S.A., B.M. Stinson, M.S. Go, L.M. Carmona, J.I. Reminick, X. Fang, and T. Baumgart. 2010. Temperature-dependent phase behavior and protein partitioning in giant plasma membrane vesicles. Biochimica et Biophysica Acta (BBA) - Biomembranes. 1798:1427-1435.

Johnsson, R., S. Santaholma, and N.E. Saris. 1978. Calcium transport and adenosine triphosphatase activities of erythrocyte membranes in congenital spherocytosis. Scand. J. Clin. Lab. Invest. 38:121–125.

Jülicher, and Lipowsky. 1993. Domain-induced budding of vesicles. Physical review letters. 70:2964-2967.

Kabaso, D., R. Shlomovitz, T. Auth, V.L. Lew, and N.S. Gov. 2010. Curling and local shape changes of red blood cell membranes driven by cytoskeletal reorganization. Biophys. J. 99:808–816.

Kabeche, R., M. Madrid, J. Cansado, and J.B. Moseley. 2015. Eisosomes Regulate Phosphatidylinositol 4,5-Bisphosphate (PI(4,5)P2) Cortical Clusters and Mitogen-

activated Protein (MAP) Kinase Signaling upon Osmotic Stress. Journal of Biological Chemistry. 290:25960-25973.

Kahya, N., D. Scherfeld, K. Bacia, B. Poolman, and P. Schwille. 2003. Probing lipid mobility of raft-exhibiting model membranes by fluorescence correlation spectroscopy. J Biol Chem. 278:28109-28115.

Kaiser, H.J., D. Lingwood, I. Levental, J.L. Sampaio, L. Kalvodova, L. Rajendran, and K. Simons. 2009. Order of lipid phases in model and plasma membranes. Proc Natl Acad Sci U S A. 106:16645-16650.

Kawai, F., M. Shoda, R. Harashima, Y. Sadaie, H. Hara, and K. Matsumoto. 2004. Cardiolipin domains in Bacillus subtilis marburg membranes. Journal of bacteriology. 186:1475-1483.

Kay, J.G., M. Koivusalo, X. Ma, T. Wohland, and S. Grinstein. 2012. Phosphatidylserine dynamics in cellular membranes. Mol Biol Cell. 23:2198-2212.

Kiessling, V., J.M. Crane, and L.K. Tamm. 2006. Transbilayer Effects of Raft-Like Lipid Domains in Asymmetric Planar Bilayers Measured by Single Molecule Tracking. Biophysical Journal. 91:3313-3326.

Kim, H., H. Arakawa, N. Hatae, Y. Sugimoto, O. Matsumoto, T. Osada, A. Ichikawa, and A. Ikai. 2006. Quantification of the number of EP3 receptors on a living CHO cell surface by the AFM. Ultramicroscopy. 106:652-662.

Kiyokawa, E., T. Baba, N. Otsuka, A. Makino, S. Ohno, and T. Kobayashi. 2005. Spatial and functional heterogeneity of sphingolipid-rich membrane domains. J Biol Chem. 280:24072-24084.

Klose, C., C.S. Ejsing, A.J. Garcia-Saez, H.J. Kaiser, J.L. Sampaio, M.A. Surma, A. Shevchenko, P. Schwille, and K. Simons. 2010. Yeast lipids can phase-separate into micrometer-scale membrane domains. J Biol Chem. 285:30224-30232.

Koldso, H., D. Shorthouse, J. Helie, and M.S. Sansom. 2014. Lipid clustering correlates with membrane curvature as revealed by molecular simulations of complex lipid bilayers. PLoS Comput Biol. 10:e1003911.

Köster, D.V., and S. Mayor. 2016. Cortical actin and the plasma membrane: inextricably intertwined. Current Opinion in Cell Biology. 38:81-89.

Koynova, R., and M. Caffrey. 1998. Phases and phase transitions of the phosphatidylcholines. Biochim. Biophys. Acta. 1376:91-145.

Kraft, M.L. 2013. Plasma membrane organization and function: moving past lipid rafts. Molecular Biology of the Cell. 24:2765-2768.

Kraft, M.L. 2016. Sphingolipid organization in the plasma membrane and the mechanisms that influence it. Front. cell Dev. Biol. 4:154.

Kriebardis, A.G., M.H. Antonelou, K.E. Stamoulis, E. Economou-Petersen, L.H. Margaritis, and I.S. Papassideri. 2007. Storage-dependent remodeling of the red blood cell membrane is associated with increased immunoglobulin G binding, lipid raft rearrangement, and caspase activation. Transfusion. 47:1212–1220.

Kriebardis, A.G., M.H. Antonelou, K.E. Stamoulis, E. Economou-Petersen, L.H. Margaritis, and I.S. Papassideri. 2008. RBC-derived vesicles during storage: ultrastructure, protein composition, oxidation, and signaling components. Transfusion. 48:1943–1953.

Kulma, M., M. Hereć, W. Grudziński, G. Anderluh, W.I. Gruszecki, K. Kwiatkowska, and A. Sobota. 2010. Sphingomyelin-rich domains are sites of lysenin oligomerization: Implications for raft studies. Biochim. Biophys. Acta - Biomembr. 1798:471–481.

Kusumi, A., C. Nakada, K. Ritchie, K. Murase, K. Suzuki, H. Murakoshi, R.S. Kasai, J. Kondo, and T. Fujiwara. 2005. Paradigm shift of the plasma membrane concept from the two-

dimensional continuum fluid to the partitioned fluid: high-speed single-molecule tracking of membrane molecules. Annu Rev Biophys Biomol Struct. 34:351-378.

Kusumi, A., I. Koyama-Honda, and K. Suzuki. 2004. Molecular Dynamics and Interactions for Creation of Stimulation-Induced Stabilized Rafts from Small Unstable Steady-State Rafts. Traffic. 5:213-230.

Kusumi, A., K.G. Suzuki, R.S. Kasai, K. Ritchie, and T.K. Fujiwara. 2011. Hierarchical mesoscale domain organization of the plasma membrane. Trends Biochem Sci. 36:604-615.

Kusumi, A., T.K. Fujiwara, N. Morone, K.J. Yoshida, R. Chadda, M. Xie, R.S. Kasai, and K.G. Suzuki. 2012b. Membrane mechanisms for signal transduction: the coupling of the meso-scale raft domains to membrane-skeleton-induced compartments and dynamic protein complexes. Seminars in cell & developmental biology. 23:126-144.

Kusumi, A., T.K. Fujiwara, R. Chadda, M. Xie, T.A. Tsunoyama, Z. Kalay, R.S. Kasai, and K.G. Suzuki. 2012a. Dynamic organizing principles of the plasma membrane that regulate signal transduction: commemorating the fortieth anniversary of singer and nicolson's fluid-mosaic model. Annu Rev Cell Dev Biol. 28:215-250.

Kuzmin, P.I., S.A. Akimov, Y.A. Chizmadzhev, J. Zimmerberg, and F.S. Cohen. 2005. Line tension and interaction energies of membrane rafts calculated from lipid splay and tilt. Biophysical journal. 88:1120-1133.

Lai, L., X. Xu, Chwee T. Lim, and J. Cao. 2015. Stiffening of Red Blood Cells Induced by Cytoskeleton Disorders: A Joint Theory-Experiment Study. Biophysical Journal. 109:2287-2294.

Larson, D.R., J.A. Gosse, D.A. Holowka, B.A. Baird, and W.W. Webb. 2005. Temporally resolved interactions between antigen-stimulated IgE receptors and Lyn kinase on living cells. The Journal of cell biology. 171:527-536.

Laux, T., K. Fukami, M. Thelen, T. Golub, D. Frey, and P. Caroni. 2000. GAP43, MARCKS, and CAP23 modulate PI(4,5)P(2) at plasmalemmal rafts, and regulate cell cortex actin dynamics through a common mechanism. J Cell Biol. 149:1455-1472.

Lee, I.-H., S. Saha, A. Polley, H. Huang, S. Mayor, M. Rao, and J.T. Groves. 2015. Live Cell Plasma Membranes Do Not Exhibit a Miscibility Phase Transition over a Wide Range of Temperatures. The Journal of Physical Chemistry B. 119:4450-4459.

Lee, K.Y.C., and H.M. McConnell. 1993. Quantized symmetry of liquid monolayer domains. The Journal of Physical Chemistry. 97:9532-9539.

Lee, L.M., and A.P. Liu. 2015. A microfluidic pipette array for mechanophenotyping of cancer cells and mechanical gating of mechanosensitive channels. Lab on a chip. 15:264-273.

Lee, W.G., H. Bang, H. Yun, J. Lee, J. Park, J.K. Kim, S. Chung, K. Cho, C. Chung, D.C. Han, and J.K. Chang. 2007. On-chip erythrocyte deformability test under optical pressure. Lab on a chip. 7:516-519.

Leibler, S., and D. Andelman. 1987. Ordered and curved meso-structures in membranes and amphiphilic films. Journal de Physique. 48:2013-2018.

Leonard, C., D. Alsteens, A. Dumitru, M. Mingeot-Leclercq, and D. Tyteca. 2017a. Lipid domains and membrane (re)shaping : from biophysics to biology. In The role of the physical properties of membranes in influencing biological phenomena. Vol. In press. J. Ruysschaert and R. Epand, editors. Springer series in biophysics.

Leonard, C., L. Conrard, M. Guthmann, H. Pollet, M. Carquin, C. Vermylen, P. Gailly, P. Van Der Smissen, M.P. Mingeot-Leclercq, and D. Tyteca. 2017b. Contribution of plasma membrane lipid domains to red blood cell (re)shaping. Scientific Reports. 7:4264-4264.

Levental, I., and S.L. Veatch. 2016. The Continuing Mystery of Lipid Rafts. Journal of Molecular Biology. 428:4749-4764.

Levental, I., D.A. Christian, Y.H. Wang, J.J. Madara, D.E. Discher, and P.A. Janmey. 2009a. Calcium-dependent lateral organization in phosphatidylinositol 4,5-bisphosphate (PIP2)- and cholesterol-containing monolayers. Biochemistry. 48:8241-8248.

Levental, I., F.J. Byfield, P. Chowdhury, F. Gai, T. Baumgart, and P.A. Janmey. 2009b. Cholesterol-dependent phase separation in cell-derived giant plasma-membrane vesicles. Biochem. J. 424:163–167.

Levental, I., M. Grzybek, and K. Simons. 2011. Raft domains of variable properties and compositions in plasma membrane vesicles. Proceedings of the National Academy of Sciences. 108:11411-11416.

Levental, K., J. Lorent, X. Lin, A. Skinkle, M. Surma, E. Stockenbojer, A. Gorfe, and I. Levental. 2016. Polyunsaturated Lipids Regulate Membrane Domain Stability by Tuning Membrane Order. Biophys. J. 110:1800–1810.

Levental, K.R., and I. Levental. 2015. Giant Plasma Membrane Vesicles: Models for Understanding Membrane Organization. In Current topics in membranes. 25–57.

Lhermusier, T., H. Chap, and B. Payrastre. 2011. Platelet membrane phospholipid asymmetry: from the characterization of a scramblase activity to the identification of an essential protein mutated in Scott syndrome. J. Thromb. Haemost. 9:1883-1891.

Li, H., and G. Lykotrafitis. 2015. Vesiculation of healthy and defective red blood cells. Phys Rev E Stat Nonlin Soft Matter Phys. 92:012715.

Li, J., G. Lykotrafitis, M. Dao, and S. Suresh. 2007. Cytoskeletal dynamics of human erythrocyte. Proc. Natl. Acad. Sci. U. S. A. 104:4937–42.

Li, L., X. Shi, X. Guo, H. Li, and C. Xu. 2014. Ionic protein-lipid interaction at the plasma membrane: what can the charge do? Trends in biochemical sciences. 39:130-140.

Lichtenberg, D., F.M. Goñi, and H. Heerklotz. 2005. Detergent-resistant membranes should not be identified with membrane rafts. Trends Biochem. Sci. 30:430–436.

Lin, M., and Y. Rikihisa. 2003. Ehrlichia chaffeensis and Anaplasma phagocytophilum lack genes for lipid A biosynthesis and incorporate cholesterol for their survival. Infect. Immun. 71:5324-5331.

Lin, Q., and E. London. 2015. Ordered raft domains induced by outer leaflet sphingomyelin in cholesterol-rich asymmetric vesicles. Biophys. J. 108:2212-2222.

Lin, T.-Y., T.M.A. Santos, W.S. Kontur, T.J. Donohue, and D.B. Weibel. 2015. A Cardiolipin-Deficient Mutant of Rhodobacter sphaeroides Has an Altered Cell Shape and Is Impaired in Biofilm Formation. Journal of bacteriology. 197:3446-3455.

Linetti, A., A. Fratangeli, E. Taverna, P. Valnegri, M. Francolini, V. Cappello, M. Matteoli, M. Passafaro, and P. Rosa. 2010. Cholesterol reduction impairs exocytosis of synaptic vesicles. J. Cell Sci. 123:595–605. doi:10.1242/jcs.060681.

Lingwood, D., and K. Simons. 2010. Lipid rafts as a membrane-organizing principle. Science. 327:46-50.

Lingwood, D., J. Ries, P. Schwille, and K. Simons. 2008. Plasma membranes are poised for activation of raft phase coalescence at physiological temperature. Proc Natl Acad Sci U S A. 105:10005-10010.

Lipowsky, R. 1992. Budding of membranes induced by intramembrane domains. J. Phys. II. 2:1825–1840. doi:10.1051/jp2:1992238.

Liu, A.P., and D.A. Fletcher. 2006. Actin polymerization serves as a membrane domain switch in model lipid bilayers. Biophys J. 91:4064-4070.

Liu, F., H. Mizukami, S. Sarnaik, and A. Ostafin. 2005. Calcium-dependent human erythrocyte cytoskeleton stability analysis through atomic force microscopy. Journal of structural biology. 150:200-210.

Liu, S.L., R. Sheng, J.H. Jung, L. Wang, E. Stec, M.J. O'Connor, S. Song, R.K. Bikkavilli, R.A. Winn, D. Lee, K. Baek, K. Ueda, I. Levitan, K.P. Kim, and W. Cho. 2016a. Orthogonal lipid sensors identify transbilayer asymmetry of plasma membrane cholesterol. Nat. Chem. Biol.

Liu, X., S. Shu, N. Billington, C.D. Williamson, S. Yu, H. Brzeska, J.G. Donaldson, J.R. Sellers, and E.D. Korn. 2016b. Mammalian Nonmuscle Myosin II Binds to Anionic Phospholipids with Concomitant Dissociation of the Regulatory Light Chain. Journal of Biological Chemistry. 291:24828-24837.

Lopez, D. 2015. Molecular composition of functional microdomains in bacterial membranes. Chem. Phys. Lipids. 192:3-11.

López, D., and R. Kolter. 2010. Functional microdomains in bacterial membranes. Genes & Development. 24:1893-1902.

Lopez-Lara, I.M., and O. Geiger. 2016. Bacterial lipid diversity. Biochim. Biophys. Acta.

Lorent, J.H., B. Diaz-Rohrer, X. Lin, K. Spring, A.A. Gorfe, K.R. Levental, and I. Levental. 2017. Structural determinants and functional consequences of protein affinity for membrane rafts. Nature communications. 8:1219-1219.

Low, P.S., S.M. Waugh, K. Zinke, and D. Drenckhahn. 1985. The role of hemoglobin denaturation and band 3 clustering in red blood cell aging. Science. 227:531–3.

Lutkenhaus, J. 2002. Dynamic proteins in bacteria. Current opinion in microbiology. 5:548-552.

Lutz, H.U., and A. Bogdanova. 2013. Mechanisms tagging senescent red blood cells for clearance in healthy humans. Front. Physiol. 4:387.

Lux, S.E.t. 2016. Anatomy of the red cell membrane skeleton: unanswered questions. Blood. 127:187-199.

Machta, B.B., S.L. Veatch, and J.P. Sethna. 2012. Critical Casimir Forces in Cellular Membranes. Physical Review Letters. 109:138101-138101.

MacKinnon, R. 2003. Potassium channels. FEBS Letters. 555:62-65.

Maddock, J.R., and L. Shapiro. 1993. Polar location of the chemoreceptor complex in the Escherichia coli cell. Science. 259:1717-1723.

Maekawa, M., and G.D. Fairn. 2014. Molecular probes to visualize the location, organization and dynamics of lipids. J Cell Sci. 127:4801-4812.

Maekawa, M., Y. Yang, and G.D. Fairn. 2016. Perfringolysin O Theta Toxin as a Tool to Monitor the Distribution and Inhomogeneity of Cholesterol in Cellular Membranes. Toxins (Basel). 8.

Mahammad, S., and I. Parmryd. 2015. Cholesterol Depletion Using Methyl-β-cyclodextrin. In Methods in molecular biology (Clifton, N.J.). 91–102.

Mahammad, S., J. Dinic, J. Adler, and I. Parmryd. 2010. Limited cholesterol depletion causes aggregation of plasma membrane lipid rafts inducing T cell activation. Biochim. Biophys. Acta - Mol. Cell Biol. Lipids. 1801:625–634. doi:10.1016/j.bbalip.2010.02.003.

Maher, A.D., and P.W. Kuchel. 2003. The Gárdos channel: a review of the Ca2+-activated K+ channel in human erythrocytes. Int. J. Biochem. Cell Biol. 35:1182–97.

Makino, A., M. Abe, M. Murate, T. Inaba, N. Yilmaz, F. Hullin-Matsuda, T. Kishimoto, N.L. Schieber, T. Taguchi, H. Arai, G. Anderluh, R.G. Parton, and T. Kobayashi. 2015. Visualization of the heterogeneous membrane distribution of sphingomyelin associated with cytokinesis, cell polarity, and sphingolipidosis. FASEB J. 29:477-493.

Malinska, K., J. Malinsky, M. Opekarova, and W. Tanner. 2003. Visualization of protein compartmentation within the plasma membrane of living yeast cells. Mol Biol Cell. 14:4427-4436.

Malinsky, J., W. Tanner, and M. Opekarova. 2016. Transmembrane voltage: Potential to induce lateral microdomains. Biochimica et Biophysica Acta (BBA) - Molecular and Cell Biology of Lipids. 1861:806-811.

Manno, S., Y. Takakuwa, and N. Mohandas. 2002. Identification of a functional role for lipid asymmetry in biological membranes: Phosphatidylserine-skeletal protein interactions modulate membrane stability. Proc. Natl. Acad. Sci. U. S. A. 99:1943–8.

Manno, S., Y. Takakuwa, and N. Mohandas. 2005. Modulation of erythrocyte membrane mechanical function by protein 4.1 phosphorylation. J Biol Chem. 280:7581-7587.

Manno, S., Y. Takakuwa, K. Nagao, and N. Mohandas. 1995. Modulation of erythrocyte membrane mechanical function by beta-spectrin phosphorylation and dephosphorylation. J Biol Chem. 270:5659-5665.

Martin, S.W., and J.B. Konopka. 2004. Lipid raft polarization contributes to hyphal growth in Candida albicans. Eukaryot Cell. 3:675-684.

May, S. 2009. Trans-monolayer coupling of fluid domains in lipid bilayers. Soft Matter. 5:3148-3148.

Mayor, S., and F.R. Maxfield. 1995. Insolubility and redistribution of GPI-anchored proteins at the cell surface after detergent treatment. Mol. Biol. Cell. 6:929–44.

Mayor, S., and M. Rao. 2004. Rafts: Scale-Dependent, Active Lipid Organization at the Cell Surface. Traffic. 5:231-240.

McConnell, H.M., and M. Vrljic. 2003. Liquid-liquid immiscibility in membranes. Annu. Rev. Biophys. Biomol. Struct. 32:469-492.

McIntosh, T.J., A.D. Magid, and S.A. Simon. 1989. Repulsive interactions between uncharged bilayers. Hydration and fluctuation pressures for monoglycerides. Biophysical journal. 55:897-904.

McKenna, J.M.D., and E.M. Ostap. 2009. Kinetics of the Interaction of myo1c with Phosphoinositides. Journal of Biological Chemistry. 284:28650-28659.

McLaughlin, S., and D. Murray. 2005. Plasma membrane phosphoinositide organization by protein electrostatics. Nature. 438:605-611.

McMahon, H.T., and E. Boucrot. 2011. Molecular mechanism and physiological functions of clathrin-mediated endocytosis. Nat Rev Mol Cell Biol. 12:517-533.

McMahon, H.T., and E. Boucrot. 2015. Membrane curvature at a glance. J. Cell Sci. 128:1065-1070.

McMahon, H.T., and J.L. Gallop. 2005. Membrane curvature and mechanisms of dynamic cell membrane remodelling. Nature. 438:590-596.

Meder, D., M.J. Moreno, P. Verkade, W.L. Vaz, and K. Simons. 2006. Phase coexistence and connectivity in the apical membrane of polarized epithelial cells. Proc Natl Acad Sci U S A. 103:329-334.

Melamed-Harel, H., and L. Reinhold. 1979. Hysteresis in the responses of membrane potential, membrane resistance, and growth rate to cyclic temperature change. Plant physiology. 63:1089-1094.

Merkel, R., E. Sackmann, and E. Evans. 1989. Molecular friction and epitactic coupling between monolayers in supported bilayers. Journal de Physique. 50:1535-1555.

Merrill, A.H., G. van Echten, E. Wang, and K. Sandhoff. 1993. Fumonisin B1 inhibits sphingosine (sphinganine) N-acyltransferase and de novo sphingolipid biosynthesis in cultured neurons in situ. J. Biol. Chem. 268:27299–306.

Mileykovskaya, E., and W. Dowhan. 2000. Visualization of phospholipid domains in Escherichia coli by using the cardiolipin-specific fluorescent dye 10-N-nonyl acridine orange. J. Bacteriol. 182:1172–5.

Mileykovskaya, E., Q. Sun, W. Margolin, and W. Dowhan. 1998. Localization and function of early cell division proteins in filamentous Escherichia coli cells lacking phosphatidylethanolamine. Journal of bacteriology. 180:4252-4257.

Miller, H., T. Castro-Gomes, M. Corrotte, C. Tam, T.K. Maugel, N.W. Andrews, and W. Song. 2015. Lipid raft-dependent plasma membrane repair interferes with the activation of B lymphocytes. J. Cell Biol. 211:1193–205. doi:10.1083/jcb.201505030.

Milovanovic, D., M. Platen, M. Junius, U. Diederichsen, I.A. Schaap, A. Honigmann, R. Jahn, and G. van den Bogaart. 2016. Calcium promotes the formation of syntaxin 1 mesoscale domains through phosphatidylinositol 4,5-bisphosphate. J Biol Chem. 291:7868-7876.

Mim, C., and V.M. Unger. 2012. Membrane curvature and its generation by BAR proteins. Trends in Biochemical Sciences. 37:526-533.

Mitra, K., I. Ubarretxena-Belandia, T. Taguchi, G. Warren, and D.M. Engelman. 2004. Modulation of the bilayer thickness of exocytic pathway membranes by membrane proteins rather than cholesterol. Proc. Natl. Acad. Sci. U. S. A. 101:4083–8.

Mizuno, H., M. Abe, P. Dedecker, A. Makino, S. Rocha, Y. Ohno-Iwashita, J. Hofkens, T. Kobayashi, and A. Miyawaki. 2011. Fluorescent probes for superresolution imaging of lipid domains on the plasma membrane. Chem Sci. 2:1548-1553.

Mohandas, N., and E. Evans. 1994. Mechanical Properties of the Red Cell Membrane in Relation to Molecular Structure and Genetic Defects. Annu. Rev. Biophys. Biomol. Struct. 23:787–818.

Mohandas, N., and J.A. Chasis. 1993. Red blood cell deformability, membrane material properties and shape: regulation by transmembrane, skeletal and cytosolic proteins and lipids. Semin. Hematol. 30:171–92.

Mohandas, N., and P.G. Gallagher. 2008. Red cell membrane: past, present, and future. Blood. 112:3939–3948.

Mohandas, N., J.A. Chasis, and S.B. Shohet. 1983. The influence of membrane skeleton on red cell deformability, membrane material properties, and shape. Semin. Hematol. 20:225–42.

Mohandas, N., M.R. Clark, M.S. Jacobs, and S.B. Shohet. 1980. Analysis of factors regulating erythrocyte deformability. J. Clin. Invest. 66:563–573.

Montes, L.R., D.J. Lopez, J. Sot, L.A. Bagatolli, M.J. Stonehouse, M.L. Vasil, B.X. Wu, Y.A. Hannun, F.M. Goni, and A. Alonso. 2008. Ceramide-enriched membrane domains in red blood cells and the mechanism of sphingomyelinase-induced hot-cold hemolysis. Biochemistry. 47:11222-11230.

Morrot, G., P. Herve, A. Zachowski, P. Fellmann, and P.F. Devaux. 1989. Aminophospholipid translocase of human erythrocytes: phospholipid substrate specificity and effect of cholesterol. Biochemistry. 28:3456–3462.

Mukherjee, S., and F.R. Maxfield. 2000. Role of membrane organization and membrane domains in endocytic lipid trafficking. Traffic (Copenhagen, Denmark). 1:203-211.

Mukherjee, S., T.T. Soe, and F.R. Maxfield. 1999. Endocytic sorting of lipid analogues differing solely in the chemistry of their hydrophobic tails. J Cell Biol. 144:1271-1284.

Mukhopadhyay, R., K.C. Huang, and N.S. Wingreen. 2008. Lipid localization in bacterial cells through curvature-mediated microphase separation. Biophys. J. 95:1034-1049.

Mukhopadhyay, R., K.C. Huang, and N.S. Wingreen. 2008. Lipid localization in bacterial cells through curvature-mediated microphase separation. Biophys. J. 95:1034–49. doi:10.1529/biophysj.107.126920.

Müller, D.J., J. Helenius, D. Alsteens, and Y.F. Dufrêne. 2009. Force probing surfaces of living cells to molecular resolution. Nat. Chem. Biol. 5:383-390.

Muralidharan-Chari, V., J.W. Clancy, A. Sedgwick, and C. D'Souza-Schorey. 2010. Microvesicles: mediators of extracellular communication during cancer progression. J Cell Sci. 123:1603-1611.

Murate, M., and T. Kobayashi. 2015. Revisiting transbilayer distribution of lipids in the plasma membrane. Chem Phys Lipids.

Murate, M., M. Abe, K. Kasahara, K. Iwabuchi, M. Umeda, and T. Kobayashi. 2015. Transbilayer distribution of lipids at nano scale. J Cell Sci. 128:1627-1638.

Nawaz, S., A. Kippert, A.S. Saab, H.B. Werner, T. Lang, K.-A. Nave, and M. Simons. 2009. Phosphatidylinositol 4,5-bisphosphate-dependent interaction of myelin basic protein with the plasma membrane in oligodendroglial cells and its rapid perturbation by elevated calcium. Journal of Neuroscience. 29.

Nelson, L.D., A.E. Johnson, and E. London. 2008. How Interaction of Perfringolysin O with Membranes Is Controlled by Sterol Structure, Lipid Structure, and Physiological Low pH. J. Biol. Chem. 283:4632–4642.

Ng, M.M., F. Chang, and D.R. Burgess. 2005. Movement of membrane domains and requirement of membrane signaling molecules for cytokinesis. Dev Cell. 9:781-790.

Nicolini, C., J. Baranski, S. Schlummer, J. Palomo, M. Lumbierres-Burgues, M. Kahms, J. Kuhlmann, S. Sanchez, E. Gratton, H. Waldmann, and R. Winter. 2006. Visualizing association of N-Ras in lipid microdomains: influence of domain structure and interfacial adsorption. Journal of the American Chemical Society. 128:192-201.

Nicolson, G.L. 2014. The Fluid-Mosaic Model of Membrane Structure: still relevant to understanding the structure, function and dynamics of biological membranes after more than 40 years. Biochim. Biophys. Acta. 1838:1451-1466.

Ohno-Iwashita, Y., M. Iwamoto, S. Ando, and S. Iwashita. 1992. Effect of lipidic factors on membrane cholesterol topology--mode of binding of theta-toxin to cholesterol in liposomes. Biochim. Biophys. Acta. 1109:81–90.

Ohno-Iwashita, Y., Y. Shimada, M. Hayashi, M. Iwamoto, S. Iwashita, and M. Inomata. 2010. Cholesterol-Binding Toxins and Anti-cholesterol Antibodies as Structural Probes for Cholesterol Localization. In Sub-cellular biochemistry. 597–621.

Oldenborg, P.A., A. Zheleznyak, Y.F. Fang, C.F. Lagenaur, H.D. Gresham, and F.P. Lindberg. 2000. Role of CD47 as a marker of self on red blood cells. Science. 288:2051–4.

Orlov, D., and K. Karkouti. 2015. The pathophysiology and consequences of red blood cell storage. Anaesthesia. 70:29-e12.

Orsini, F., A. Cremona, P. Arosio, P.A. Corsetto, G. Montorfano, A. Lascialfari, and A.M. Rizzo. 2012. Atomic force microscopy imaging of lipid rafts of human breast cancer cells. Biochim Biophys Acta. 1818:2943-2949.

Osumi, M. 1998. The ultrastructure of yeast: cell wall structure and formation. Micron. 29:207-233.

Owen, D.M., C. Rentero, A. Magenau, A. Abu-Siniyeh, and K. Gaus. 2011. Quantitative imaging of membrane lipid order in cells and organisms. Nature protocols. 7:24-35.

Owen, D.M., D.J. Williamson, A. Magenau, and K. Gaus. 2012. Sub-resolution lipid domains exist in the plasma membrane and regulate protein diffusion and distribution. Nature communications. 3.

Owen, D.M., S. Oddos, S. Kumar, D.M. Davis, M.A.A. Neil, P.M.W. French, M.L. Dustin, A.I. Magee, and M. Cebecauer. 2010. High plasma membrane lipid order imaged at the immunological synapse periphery in live T cells. Molecular Membrane Biology. 27:178-189.

Ozgen, H., W. Schrimpf, J. Hendrix, J.C. de Jonge, D.C. Lamb, D. Hoekstra, N. Kahya, and W. Baron. 2014. The lateral membrane organization and dynamics of myelin proteins PLP and MBP are dictated by distinct galactolipids and the extracellular matrix. PloS one. 9:e101834.

Paparelli, L., N. Corthout, B. Pavie, D.L. Wakefield, R. Sannerud, T. Jovanovic-Talisman, W. Annaert, and S. Munck. 2016. Inhomogeneity based characterization of distribution patterns on the plasma membrane. PLoS computational biology. 12:e1005095.

Parasassi, T., M. Di Stefano, M. Loiero, G. Ravagnan, and E. Gratton. 1994. Cholesterol modifies water concentration and dynamics in phospholipid bilayers: a fluorescence study using Laurdan probe. Biophysical journal. 66:763-768.

Park, Y., C.A. Best, T. Auth, N.S. Gov, S.A. Safran, G. Popescu, S. Suresh, and M.S. Feld. 2010. Metabolic remodeling of the human red blood cell membrane. Proc Natl Acad Sci U S A. 107:1289-1294.

Parsons, J.B., and C.O. Rock. 2013. Bacterial lipids: metabolism and membrane homeostasis. Prog. Lipid Res. 52:249-276.

Parthasarathy, R., C. Yu, and J.T. Groves. 2006. Curvature-Modulated Phase Separation in Lipid Bilayer Membranes. Langmuir. 22:5095–5099.

Parton, R.G., and M.A. del Pozo. 2013. Caveolae as plasma membrane sensors, protectors and organizers. Nat Rev Mol Cell Biol. 14:98-112.

Pasini, E.M., M. Kirkegaard, P. Mortensen, H.U. Lutz, A.W. Thomas, and M. Mann. 2006. In-depth analysis of the membrane and cytosolic proteome of red blood cells. Blood. 108:791–801. doi:10.1182/blood-2005-11-007799.

Pataraia, S., Y. Liu, R. Lipowsky, and R. Dimova. 2014. Effect of cytochrome c on the phase behavior of charged multicomponent lipid membranes. Biochim Biophys Acta. 1838:2036-2045.

Patel, D.S., S. Park, E.L. Wu, M.S. Yeom, G. Widmalm, J.B. Klauda, and W. Im. 2016. Influence of Ganglioside GM1 Concentration on Lipid Clustering and Membrane Properties and Curvature. Biophys J. 111:1987-1999.

Paunola, E., P.K. Mattila, and P. Lappalainen. 2002. WH2 domain: a small, versatile adapter for actin monomers. FEBS Letters. 513:92-97.

Perkins, R.G., and R.E. Scott. 1978. Plasma membrane phospholipid, cholesterol and fatty acyl composition of differentiated and undifferentiated L6 myoblasts. Lipids. 13:334-337.

Perrotta, S., P.G. Gallagher, and N. Mohandas. 2008. Hereditary spherocytosis. Lancet. 372:1411-1426.

Peter, B.J., H.M. Kent, I.G. Mills, Y. Vallis, P.J.G. Butler, P.R. Evans, and H.T. McMahon. 2004. BAR Domains as Sensors of Membrane Curvature: The Amphiphysin BAR Structure. Science. 303:495-499.

Picas, L., F. Rico, M. Deforet, and S. Scheuring. 2013. Structural and mechanical heterogeneity of the erythrocyte membrane reveals hallmarks of membrane stability. ACS nano. 7:1054-1063.

Picas, L., J. Viaud, K. Schauer, S. Vanni, K. Hnia, V. Fraisier, A. Roux, P. Bassereau, F. Gaits-Iacovoni, B. Payrastre, J. Laporte, J.B. Manneville, and B. Goud. 2014. BIN1/M-Amphiphysin2 induces clustering of phosphoinositides to recruit its downstream partner dynamin. Nature communications. 5:5647.

Pierini, L.M., R.J. Eddy, M. Fuortes, S. Seveau, C. Casulo, and F.R. Maxfield. 2003. Membrane lipid organization is critical for human neutrophil polarization. J Biol Chem. 278:10831-10841.

Pignataro, M.F., M.M. Dodes-Traian, F.L. González-Flecha, M. Sica, I.C. Mangialavori, and J.P.F.C. Rossi. 2015. Modulation of Plasma Membrane Ca 2+ -ATPase by Neutral Phospholipids. J. Biol. Chem. 290:6179–6190. doi:10.1074/jbc.M114.585828.

Pike, L.J. 2006. Rafts defined: a report on the Keystone Symposium on Lipid Rafts and Cell Function. J Lipid Res. 47:1597-1598.

Pinto, S.N., F. Fernandes, A. Fedorov, A.H. Futerman, L.C. Silva, and M. Prieto. 2013. A combined fluorescence spectroscopy, confocal and 2-photon microscopy approach to re-evaluate the properties of sphingolipid domains. Biochim Biophys Acta. 1828:2099-2110.

Plasencia, I., L. Norlen, and L.A. Bagatolli. 2007. Direct visualization of lipid domains in human skin stratum corneum's lipid membranes: effect of pH and temperature. Biophys J. 93:3142-3155.

Pomorski, T.G., and A.K. Menon. 2016. Lipid somersaults: Uncovering the mechanisms of protein-mediated lipid flipping. Prog. Lipid Res. 64:69-84.

Pottosin, I.I., G. Valencia-Cruz, E. Bonales-Alatorre, S.N. Shabala, and O.R. Dobrovinskaya. 2007. Methyl-β-cyclodextrin reversibly alters the gating of lipid rafts-associated Kv1.3 channels in Jurkat T lymphocytes. Pflügers Arch. - Eur. J. Physiol. 454:235–244.

Proszynski, T.J., R. Klemm, M. Bagnat, K. Gaus, and K. Simons. 2006. Plasma membrane polarization during mating in yeast cells. The Journal of cell biology. 173:861-866.

Puth, K., H.F. Hofbauer, J.P. Saenz, and R. Ernst. 2015. Homeostatic control of biological membranes by dedicated lipid and membrane packing sensors. Biol. Chem. 396:1043-1058.

Pyenta, P.S., D. Holowka, and B. Baird. 2001. Cross-correlation analysis of inner-leaflet-anchored green fluorescent protein co-redistributed with IgE receptors and outer leaflet lipid raft components. Biophysical journal. 80:2120-2132.

Radosinska, J., and N. Vrbjar. 2016. The role of red blood cell deformability and Na,K-ATPase function in selected risk factors of cardiovascular diseases in humans: focus on hypertension, diabetes mellitus and hypercholesterolemia. Physiol. Res. 65 Suppl 1:S43-54.

Raghupathy, R., A.A. Anilkumar, A. Polley, P.P. Singh, M. Yadav, C. Johnson, S. Suryawanshi, V. Saikam, S.D. Sawant, A. Panda, Z. Guo, R.A. Vishwakarma, M. Rao, and S. Mayor. 2015. Transbilayer lipid interactions mediate nanoclustering of lipid-anchored proteins. Cell. 161:581-594.

Raghuveer Parthasarathy, a. Cheng-han Yu, and Jay T. Groves*. 2006. Curvature-modulated phase separation in lipid bilayer membranes. Langmuir, 22 :5095–5099

Raiborg, C., and H. Stenmark. 2009. The ESCRT machinery in endosomal sorting of ubiquitylated membrane proteins. Nature. 458:445-452.

Rand, R.P., and A.C. Burton. 1964. Mechanical properties of the red cell membrane. I. membrane stiffness and intracellular pressure. Biophys J. 4:115-135.

Rao, M., and S. Mayor. 2014. Active organization of membrane constituents in living cells. Curr Opin Cell Biol. 29:126-132.

Rao, Y., and V. Haucke. 2011. Membrane shaping by the Bin/amphiphysin/Rvs (BAR) domain protein superfamily. Cellular and Molecular Life Sciences. 68:3983-3993.

Reid, H.L., A.J. Barnes, P.J. Lock, J.A. Dormandy, and T.L. Dormandy. 1976. A simple method for measuring erythrocyte deformability. J Clin Pathol. 29:855-858.

Reigada, R., J. Buceta, J. Gómez, F. Sagués, and K. Lindenberg. 2008. Phase separation in three-component lipid membranes: From Monte Carlo simulations to Ginzburg-Landau equations. J. Chem. Phys. 128:25102. doi:10.1063/1.2817333.

Remmerbach, T.W., F. Wottawah, J. Dietrich, B. Lincoln, C. Wittekind, and J. Guck. 2009. Oral cancer diagnosis by mechanical phenotyping. Cancer Res. 69:1728-1732.

Renner, L.D., and D.B. Weibel. 2011. Cardiolipin microdomains localize to negatively curved regions of Escherichia coli membranes. Proc Natl Acad Sci U S A. 108:6264-6269.

Rentero, C., T. Zech, C.M. Quinn, K. Engelhardt, D. Williamson, T. Grewal, W. Jessup, T. Harder, and K. Gaus. 2008. Functional Implications of Plasma Membrane Condensation for T Cell Activation. PLoS ONE. 3:e2262-e2262.

Robinson, T. 2013. Reorganization of lipid domains in model membranes under deformation. 17th International Conference on Miniaturized Systems for Chemistry and Life Sciences.

Robinson, T., D. Hess, P. Kuhn, and P.S. Dittrich. 2012. Investigating the effects of membrane tension and shear stress on lipid domains in model membranes. 16th International Conference on Miniaturized Systems for Chemistry and Life Sciences .

Roduit, C., F.G. van der Goot, P. Los Rios, A. Yersin, P. Steiner, G. Dietler, S. Catsicas, F. Lafont, and S. Kasas. 2008. Elastic membrane heterogeneity of living cells revealed by stiff nanoscale membrane domains. Biophys. J. 94:1521-1532.

Rosenbluth, M.J., W.A. Lam, and D.A. Fletcher. 2008. Analyzing cell mechanics in hematologic diseases with microfluidic biophysical flow cytometry. Lab on a chip. 8:1062-1070.

Rossy, J., Y. Ma, and K. Gaus. 2014. The organisation of the cell membrane: do proteins rule lipids? Curr Opin Chem Biol. 20:54-59.

Roux, A., D. Cuvelier, P. Nassoy, J. Prost, P. Bassereau, and B. Goud. 2005. Role of curvature and phase transition in lipid sorting and fission of membrane tubules. The EMBO Journal. 24:1537-1545.

Saenz, J.P., E. Sezgin, P. Schwille, and K. Simons. 2012. Functional convergence of hopanoids and sterols in membrane ordering. Proc. Natl. Acad. Sci. U. S. A. 109:14236-14240.

Saleh, H.S., U. Merkel, K.J. Geißler, T. Sperka, A. Sechi, C. Breithaupt, and H. Morrison. 2009. Properties of an ezrin mutant defective in F-actin binding. Journal of Molecular Biology. 385:1015-1031.

Salomao, M., X. Zhang, Y. Yang, S. Lee, J.H. Hartwig, J.A. Chasis, N. Mohandas, and X. An. 2008. Protein 4.1R-dependent multiprotein complex: New insights into the structural organization of the red blood cell membrane. Proc. Natl. Acad. Sci. 105:8026–8031.

Samsonov, A. V., I. Mihalyov, and F.S. Cohen. 2001. Characterization of cholesterol-sphingomyelin domains and their dynamics in bilayer Membranes. Biophys. J. 81:1486–1500.

Sanchez, S.A., G. Gunther, M.A. Tricerri, and E. Gratton. 2011. Methyl-β-Cyclodextrins Preferentially Remove Cholesterol from the Liquid Disordered Phase in Giant Unilamellar Vesicles. J. Membr. Biol. 241:1–10.

Sanchez, S.A., M.A. Tricerri, and E. Gratton. 2012. Laurdan generalized polarization fluctuations measures membrane packing micro-heterogeneity in vivo. Proc Natl Acad Sci U S A. 109:7314-7319.

Sarmento, M.J., A. Coutinho, A. Fedorov, M. Prieto, and F. Fernandes. 2014. Ca(2+) induces PI(4,5)P2 clusters on lipid bilayers at physiological PI(4,5)P2 and Ca(2+) concentrations. Biochim Biophys Acta. 1838:822-830.

Schamberger, J., and R.J. Clarke. 2002. Hydrophobic ion hydration and the magnitude of the dipole potential. Biophysical journal. 82:3081-3088.

Scheiffele, P., A. Rietveld, T. Wilk, and K. Simons. 1999. Influenza viruses select ordered lipid domains during budding from the plasma membrane. The Journal of biological chemistry. 274:2038-2044.

Schmid, F. 2016. Physical mechanisms of micro- and nanodomain formation in multicomponent lipid membranes. Biochim Biophys Acta.

Schroeder, R., E. London, and D. Brown. 1994. Interactions between saturated acyl chains confer detergent resistance on lipids and glycosylphosphatidylinositol (GPI)-anchored proteins: GPI-anchored proteins in liposomes and cells show similar behavior. Proc. Natl. Acad. Sci. U. S. A. 91:12130–4.

Schuck, S., M. Honsho, K. Ekroos, A. Shevchenko, and K. Simons. 2003. Resistance of cell membranes to different detergents. Proc. Natl. Acad. Sci. U. S. A. 100:5795–800. doi:10.1073/pnas.0631579100.

Sens, P., and N. Gov. 2007. Force balance and membrane shedding at the red-blood-cell surface. Phys. Rev. Lett. 98:18102. doi:10.1103/PhysRevLett.98.018102.

Sevcsik, E., and G.J. Schütz. 2016. With or without rafts? Alternative views on cell membranes. BioEssays. 38:129-139.

Sevcsik, E., M. Brameshuber, M. Folser, J. Weghuber, A. Honigmann, and G.J. Schutz. 2015. GPI-anchored proteins do not reside in ordered domains in the live cell plasma membrane. Nature communications. 6:6969.

Sezgin, E., H.-J. Kaiser, T. Baumgart, P. Schwille, K. Simons, and I. Levental. 2012b. Elucidating membrane structure and protein behavior using giant plasma membrane vesicles. Nat. Protoc. 7:1042–1051.

Sezgin, E., I. Levental, M. Grzybek, G. Schwarzmann, V. Mueller, A. Honigmann, V.N. Belov, C. Eggeling, Ü. Coskun, K. Simons, and P. Schwille. 2012b. Partitioning, diffusion, and ligand binding of raft lipid analogs in model and cellular plasma membranes. Biochim. Biophys. Acta - Biomembr. 1818:1777–1784.

Sezgin, E., T. Gutmann, T. Buhl, R. Dirkx, M. Grzybek, Ü. Coskun, M. Solimena, K. Simons, I. Levental, and P. Schwille. 2015. Adaptive lipid packing and bioactivity in membrane domains. PloS one. 10:e0123930-e0123930.

Sharma, P., R. Varma, R.C. Sarasij, Ira, K. Gousset, G. Krishnamoorthy, M. Rao, and S. Mayor. 2004. Nanoscale organization of multiple GPI-anchored proteins in living cell membranes. Cell. 116:577-589.

Sheetz, M.P., and S.J. Singer. 1974. Biological membranes as bilayer couples. A molecular mechanism of drug-erythrocyte interactions. Proceedings of the National Academy of Sciences of the United States of America. 71:4457-4461.

Sheetz, M.P., and S.J. Singer. 1974. Biological membranes as bilayer couples. A molecular mechanism of drug-erythrocyte interactions. Proc. Natl. Acad. Sci. U. S. A. 71:4457–61.

Sheetz, M.P., J.E. Sable, and H.G. Dobereiner. 2006. Continuous membrane-cytoskeleton adhesion requires continuous accommodation to lipid and cytoskeleton dynamics. Annu Rev Biophys Biomol Struct. 35:417-434.

Shen, B., Y. Fang, N. Wu, and S.J. Gould. 2011. Biogenesis of the posterior pole is mediated by the exosome/microvesicle protein-sorting pathway. J Biol Chem. 286:44162-44176.

Shi, X., Y. Bi, W. Yang, X. Guo, Y. Jiang, C. Wan, L. Li, Y. Bai, J. Guo, Y. Wang, X. Chen, B. Wu, H. Sun, W. Liu, J. Wang, and C. Xu. 2013. Ca2+ regulates T-cell receptor activation by modulating the charge property of lipids. Nature. 493:111-115.

Shibata, Y., J. Hu, M.M. Kozlov, and T.A. Rapoport. 2009. Mechanisms Shaping the Membranes of Cellular Organelles. Annual Review of Cell and Developmental Biology. 25:329-354.

Shimada, Y., M. Maruya, S. Iwashita, and Y. Ohno-Iwashita. 2002. The C-terminal domain of perfringolysin O is an essential cholesterol-binding unit targeting to cholesterol-rich microdomains. Eur. J. Biochem. 269:6195–203.

Shimoda, M., K. Miyashima, and Y. Yawata. 1984. Increased calcium uptake in the red cells of unsplenectomized patients with hereditary spherocytosis: significant contribution of reticulocytosis. Clin. Chim. Acta. 142:183–192.

Shogomori, H., and T. Kobayashi. 2008. Lysenin: A sphingomyelin specific pore-forming toxin. Biochim. Biophys. Acta - Gen. Subj. 1780:612–618.

Simons, K., and D. Toomre. 2000. Lipid rafts and signal transduction. Nat. Rev. Mol. Cell Biol. 1:31–39. doi:10.1038/35036052.

Simons, K., and E. Ikonen. 1997. Functional rafts in cell membranes. Nature. 387:569-572.

Simons, K., and W.L.C. Vaz. 2004. Model systems, lipid rafts, and cell membranes. Annual Review of Biophysics and Biomolecular Structure. 33:269-295.

Sims, P.J., and T. Wiedmer. 2001. Unraveling the mysteries of phospholipid scrambling. Thromb. Haemost. 86:266–75.

Singer, S.J., and G.F. Oster. 1992. The bilayer couple hypothesis. Trends Cell Biol. 2:69-70–1.

Singer, S.J., and G.L. Nicolson. 1972. The fluid mosaic model of the structure of cell membranes. Science. 175:720-731.

Singleton, K., N. Parvaze, K.R. Dama, K.S. Chen, P. Jennings, B. Purtic, M.D. Sjaastad, C. Gilpin, M.M. Davis, and C. Wulfing. 2006. A large T cell invagination with CD2 enrichment resets receptor engagement in the immunological synapse. J Immunol. 177:4402-4413.

Sit, S.T., and E. Manser. 2011. Rho GTPases and their role in organizing the actin cytoskeleton. Journal of cell science. 124:679-683.

Skocaj, M., B. Bakrac, I. Krizaj, P. Macek, G. Anderluh, and K. Sepcic. 2013. The sensing of membrane microdomains based on pore-forming toxins. Current medicinal chemistry. 20:491-501.

Slotte, J.P. 2013. Biological functions of sphingomyelins. Prog. Lipid Res. 52:424-437.

Sodt, A.J., R.M. Venable, E. Lyman, and R.W. Pastor. 2016. Nonadditive Compositional Curvature Energetics of Lipid Bilayers. Phys. Rev. Lett. 117:138104.

Sonnino, S., A. Prinetti, H. Nakayama, M. Yangida, H. Ogawa, and K. Iwabuchi. 2009. Role of very long fatty acid-containing glycosphingolipids in membrane organization and cell signaling: the model of lactosylceramide in neutrophils. Glycoconj J. 26:615-621.

Sorre, B., A. Callan-Jones, J.B. Manneville, P. Nassoy, J.F. Joanny, J. Prost, B. Goud, and P. Bassereau. 2009. Curvature-driven lipid sorting needs proximity to a demixing point and is aided by proteins. Proceedings of the National Academy of Sciences. 106:5622-5626.

Sot, J., L.A. Bagatolli, F.M. Goni, and A. Alonso. 2006. Detergent-resistant, ceramide-enriched domains in sphingomyelin/ceramide bilayers. Biophys J. 90:903-914.

Spira, F., N.S. Mueller, G. Beck, P. von Olshausen, J. Beig, and R. Wedlich-Soldner. 2012. Patchwork organization of the yeast plasma membrane into numerous coexisting domains. Nat Cell Biol. 14:890-890.

Stachowiak, J.C., E.M. Schmid, C.J. Ryan, H.S. Ann, D.Y. Sasaki, M.B. Sherman, P.L. Geissler, D.A. Fletcher, and C.C. Hayden. 2012. Membrane bending by protein–protein crowding. Nat Cell Biol. 14:944-949.

Stancevic, B., and R. Kolesnick. 2010. Ceramide-rich platforms in transmembrane signaling. FEBS Lett. 584:1728-1740.

Starke-Peterkovic, T., and R.J. Clarke. 2009. Effect of headgroup on the dipole potential of phospholipid vesicles. European Biophysics Journal. 39:103-110.

Starke-Peterkovic, T., N. Turner, M.F. Vitha, M.P. Waller, D.E. Hibbs, and R.J. Clarke. 2006. Cholesterol effect on the dipole potential of lipid membranes. Biophysical journal. 90:4060-4070.

Stewart, A., S. Urbaniak, M. Turner, and H. Bessos. 2005. The application of a new quantitative assay for the monitoring of integrin-associated protein CD47 on red blood cells during storage and comparison with the expression of CD47 and phosphatidylserine with flow cytometry. Transfusion. 45:1496–1503.

Stone, M.B., S.A. Shelby, and S.L. Veatch. 2017a. Super-Resolution Microscopy: Shedding Light on the Cellular Plasma Membrane. Chem Rev. Chem. Rev., 117 :7457–7477

Stone, M.B., S.A. Shelby, M.F. Núñez, K. Wisser, and S.L. Veatch. 2017b. Protein sorting by lipid phase-like domains supports emergent signaling function in B lymphocyte plasma membranes. Elife. 6.

Stott, B.M., M.P. Vu, C.O. McLemore, M.S. Lund, E. Gibbons, T.J. Brueseke, H.A. Wilson-Ashworth, and J.D. Bell. 2008. Use of fluorescence to determine the effects of cholesterol on lipid behavior in sphingomyelin liposomes and erythrocyte membranes. J. Lipid Res. 49:1202–15.

Stout, J.G., Q. Zhou, T. Wiedmer, and P.J. Sims. 1998. Change in Conformation of Plasma Membrane Phospholipid Scramblase Induced by Occupancy of Its Ca 2+ Binding Site. Biochemistry. 37:14860–14866.

Sturzenegger, F., T. Robinson, D. Hess, and P.S. Dittrich. 2016. Membranes under shear stress: visualization of non-equilibrium domain patterns and domain fusion in a microfluidic device. Soft Matter. 12:5072–6. doi:10.1039/c6sm00049e.

Sullan, R.M.A., J.K. Li, and S. Zou. 2009. Direct Correlation of Structures and Nanomechanical Properties of Multicomponent Lipid Bilayers. Langmuir. 25:7471-7477.

Sun, Y., R. Taniguchi, D. Tanoue, T. Yamaji, H. Takematsu, K. Mori, T. Fujita, T. Kawasaki, and Y. Kozutsumi. 2000. Sli2 (Ypk1), a homologue of mammalian protein kinase SGK, is a downstream kinase in the sphingolipid-mediated signaling pathway of yeast. Mol Cell Biol. 20:4411-4419.

Szabo, G. 1974. Dual mechanism for the action of cholesterol on membrane permeability. Nature. 252:47-49.

Takao, D., and S. Kamimura. 2010. Single-Cell Electroporation of Fluorescent Probes into Sea Urchin Sperm Cells and Subsequent FRAP Analysis. Zoolog. Sci. 27:279–284.

Takatori, S., R. Mesman, and T. Fujimoto. 2014. Microscopic methods to observe the distribution of lipids in the cellular membrane. Biochemistry. 53:639-653.

Takeshita, N., Y. Higashitsuji, S. Konzack, and R. Fischer. 2008. Apical sterol-rich membranes are essential for localizing cell end markers that determine growth directionality in the filamentous fungus Aspergillus nidulans. Mol Biol Cell. 19:339-351.

Thie, M., R. Rospel, W. Dettmann, M. Benoit, M. Ludwig, H.E. Gaub, and H.W. Denker. 1998. Interactions between trophoblast and uterine epithelium: monitoring of adhesive forces. Human reproduction (Oxford, England). 13:3211-3219.

Thomas, J.A., and F.R. Rana. 2007. The influence of environmental conditions, lipid composition, and phase behavior on the origin of cell membranes. Orig. Life Evol. Biosph. 37:267-285.

Tian, A., and T. Baumgart. 2009. Sorting of lipids and proteins in membrane curvature gradients. Biophysical journal. 96:2676-2688.

Tocheva, E.I., Z. Li, and G.J. Jensen. 2010. Electron cryotomography. Cold Spring Harbor perspectives in biology. 2:a003442-a003442.

Toulmay, A., and W.A. Prinz. 2013. Direct imaging reveals stable, micrometer-scale lipid domains that segregate proteins in live cells. J Cell Biol. 202:35-44.

Travesset, A. 2006. Effect of dipolar moments in domain sizes of lipid bilayers and monolayers. The Journal of Chemical Physics. 125:084905-084905.

Turner, M.S., P. Sens, and N.D. Socci. 2005. Nonequilibrium raftlike membrane domains under continuous recycling. Phys. Rev. Lett. 95:168301.

Turrini, F., F. Mannu, P. Arese, J. Yuan, and P.S. Low. 1993. Characterization of the autologous antibodies that opsonize erythrocytes with clustered integral membrane proteins. Blood. 81:3146–52.

Turturici, G., R. Tinnirello, G. Sconzo, and F. Geraci. 2014. Extracellular membrane vesicles as a mechanism of cell-to-cell communication: advantages and disadvantages. American journal of physiology. Cell physiology. 306:C621-633.

Tyteca, D., L. D'Auria, P. Van Der Smissen, T. Medts, S. Carpentier, J.C. Monbaliu, P. de Diesbach, and P.J. Courtoy. 2010. Three unrelated sphingomyelin analogs spontaneously cluster into plasma membrane micrometric domains. Biochim. Biophys. Acta - Biomembr. 1798:909–927.

Tyteca, D., L. D'Auria, P. Van Der Smissen, T. Medts, S. Carpentier, J.C. Monbaliu, P. de Diesbach, and P.J. Courtoy. 2010. Three unrelated sphingomyelin analogs spontaneously cluster into plasma membrane micrometric domains. Biochim. Biophys. Acta - Biomembr. 1798:909–927.

Umeda, K., J. Ikenouchi, S. Katahira-Tayama, K. Furuse, H. Sasaki, M. Nakayama, T. Matsui, S. Tsukita, M. Furuse, and S. Tsukita. 2006. ZO-1 and ZO-2 independently determine where claudins are polymerized in tight-junction strand formation. Cell. 126:741-754.

Unwin, N. 2005. Refined Structure of the Nicotinic Acetylcholine Receptor at 4 Å Resolution. Journal of Molecular Biology. 346:967-989.

Ursell, T.S., J. Nguyen, R.D. Monds, A. Colavin, G. Billings, N. Ouzounov, Z. Gitai, J.W. Shaevitz, and K.C. Huang. 2014. Rod-like bacterial shape is maintained by feedback between cell curvature and cytoskeletal localization. Proceedings of the National Academy of Sciences of the United States of America. 111:E1025-1034.

Ursell, T.S., W.S. Klug, and R. Phillips. 2009. Morphology and interaction between lipid domains. Proc Natl Acad Sci U S A. 106:13301-13306.

Ursell, T.S., W.S. Klug, and R. Phillips. 2009. Morphology and interaction between lipid domains. Proc. Natl. Acad. Sci. U. S. A. 106:13301–6.

van den Bogaart, G., K. Meyenberg, H.J. Risselada, H. Amin, K.I. Willig, B.E. Hubrich, M. Dier, S.W. Hell, H. Grubmüller, U. Diederichsen, and R. Jahn. 2011. Membrane protein sequestering by ionic protein–lipid interactions. Nature. 479:552-555.

van Meer, G., D.R. Voelker, and G.W. Feigenson. 2008. Membrane lipids: where they are and how they behave. Nat. Rev. Mol. Cell Biol. 9:112-124.

Veatch, S.L., and S.L. Keller. 2003. Separation of liquid phases in giant vesicles of ternary mixtures of phospholipids and cholesterol. Biophysical journal. 85:3074-3083.

Veatch, S.L., and S.L. Keller. 2005. Seeing spots: Complex phase behavior in simple membranes. Biochimica et Biophysica Acta (BBA) - Molecular Cell Research. 1746:172-185.

Veatch, S.L., P. Cicuta, P. Sengupta, A. Honerkamp-Smith, D. Holowka, and B. Baird. 2008. Critical Fluctuations in Plasma Membrane Vesicles. ACS Chemical Biology. 3:287-293.

Verkleij, A.J., R.F. Zwaal, B. Roelofsen, P. Comfurius, D. Kastelijn, and L.L. van Deenen. 1973. The asymmetric distribution of phospholipids in the human red cell membrane. A combined study using phospholipases and freeze-etch electron microscopy. Biochim. Biophys. Acta. 323:178–93.

Vernay, A., S. Schaub, I. Guillas, M. Bassilana, and R.A. Arkowitz. 2012. A steep phosphoinositide bis-phosphate gradient forms during fungal filamentous growth. J Cell Biol. 198:711-730.

Vicidomini, G., H. Ta, A. Honigmann, V. Mueller, M.P. Clausen, D. Waithe, S. Galiani, E. Sezgin, A. Diaspro, S.W. Hell, and C. Eggeling. 2015. STED-FLCS: An Advanced Tool to Reveal Spatiotemporal Heterogeneity of Molecular Membrane Dynamics. Nano letters. 15:5912-5918.

Vind-Kezunovic, D., C.H. Nielsen, U. Wojewodzka, and R. Gniadecki. 2008. Line tension at lipid phase boundaries regulates formation of membrane vesicles in living cells. Biochimica et biophysica acta. 1778:2480-2486.

Visser, D., M. Langeslag, K.M. Kedziora, J. Klarenbeek, A. Kamermans, F.D. Horgen, A. Fleig, F.N. van Leeuwen, and K. Jalink. 2013. TRPM7 triggers Ca2+ sparks and invadosome formation in neuroblastoma cells. Cell calcium. 54:404-415.

Wachtler, V., S. Rajagopalan, and M.K. Balasubramanian. 2003. Sterol-rich plasma membrane domains in the fission yeast Schizosaccharomyces pombe. J Cell Sci. 116:867-874.

Waheed, A.A., Y. Shimada, H.F.G. Heijnen, M. Nakamura, M. Inomata, M. Hayashi, S. Iwashita, J.W. Slot, and Y. Ohno-Iwashita. 2001. Selective binding of perfringolysin O derivative to cholesterol-rich membrane microdomains (rafts). Proc. Natl. Acad. Sci. 98:4926–4931. doi:10.1073/pnas.091090798.

Wang, T.Y., and J.R. Silvius. 2000. Different sphingolipids show differential partitioning into sphingolipid/cholesterol-rich domains in lipid bilayers. Biophys. J. 79:1478–89.

Wang, Y.-H., A. Collins, L. Guo, K.B. Smith-Dupont, F. Gai, T. Svitkina, and P.A. Janmey. 2012. Divalent Cation-Induced Cluster Formation by Polyphosphoinositides in Model Membranes. J. Am. Chem. Soc. 134:3387–3395.

Waugh, R.E. 1996. Elastic energy of curvature-driven bump formation on red blood cell membrane. Biophys J. 70:1027-1035.

Wei, C., X. Wang, M. Chen, K. Ouyang, L.S. Song, and H. Cheng. 2009. Calcium flickers steer cell migration. Nature. 457:901-905.

Willekens, F.L.A., J.M. Werre, Y.A.M. Groenen-Döpp, B. Roerdinkholder-Stoelwinder, B. de Pauw, and G.J.C.G.M. Bosman. 2008. Erythrocyte vesiculation: a self-protective mechanism? Br. J. Haematol. 141:549–556.

Windschiegl, B., A. Orth, W. Römer, L. Berland, B. Stechmann, P. Bassereau, L. Johannes, and C. Steinem. 2009. Lipid reorganization induced by shiga toxin clustering on planar membranes. PLoS ONE. 4:e6238-e6238.

Woon, L.A., J.W. Holland, E.P.W. Kable, and B.D. Roufogalis. 1999. Ca2+sensitivity of phospholipid scrambling in human red cell ghosts. Cell Calcium. 25:313–320. doi:10.1054/ceca.1999.0029.

Wu, M., X. Wu, and P. De Camilli. 2013. Calcium oscillations-coupled conversion of actin travelling waves to standing oscillations. Proc Natl Acad Sci U S A. 110:1339-1344.

Yanez-Mo, M., O. Barreiro, M. Gordon-Alonso, M. Sala-Valdes, and F. Sanchez-Madrid. 2009. Tetraspanin-enriched microdomains: a functional unit in cell plasma membranes. Trends Cell Biol. 19:434-446.

Yang, S.-T., V. Kiessling, and L.K. Tamm. 2016. Line tension at lipid phase boundaries as driving force for HIV fusion peptide-mediated fusion. Nat. Commun. 7:11401. doi:10.1038/ncomms11401.

Yeung, T., G.E. Gilbert, J. Shi, J. Silvius, A. Kapus, and S. Grinstein. 2008. Membrane Phosphatidylserine Regulates Surface Charge and Protein Localization. Science (80-.). 319:210–213.

Yoon, Y.Z., J. Kotar, G. Yoon, and P. Cicuta. 2008. The nonlinear mechanical response of the red blood cell. Phys Biol. 5:036007.

Yu, H., N. Wang, X. Ju, Y. Yang, D. Sun, M. Lai, L. Cui, M.A. Sheikh, J. Zhang, X. Wang, and X. Zhu. 2012. PtdIns (3,4,5) P3 Recruitment of Myo10 Is Essential for Axon Development. PLOS ONE. 7:e36988.

Yu, J., D.A. Fischman, and T.L. Steck. 1973. Selective solubilization of proteins and phospholipids from red blood cell membranes by nonionic detergents. J. Supramol. Struct. 1:233–248.

Yuana, Y., A. Sturk, and R. Nieuwland. 2013. Extracellular vesicles in physiological and pathological conditions. Blood reviews. 27:31-39.

Zachowski, A. 1993. Phospholipids in animal eukaryotic membranes: transverse asymmetry and movement. Biochem J. 294 (Pt 1):1-14.

Zanetti, G., K.B. Pahuja, S. Studer, S. Shim, and R. Schekman. 2012. COPII and the regulation of protein sorting in mammals. Nat Cell Biol. 14:20-28.

Zhao, H., A. Michelot, E.V. Koskela, V. Tkach, D. Stamou, D.G. Drubin, and P. Lappalainen. 2013. Membrane-sculpting BAR domains generate stable lipid microdomains. Cell Rep. 4:1213-1223.

Zheng, C., and G. Vanderkooi. 1992. Molecular origin of the internal dipole potential in lipid bilayers: calculation of the electrostatic potential. Biophysical Journal. 63:935-941.

Zheng, Y., J. Nguyen, Y. Wei, and Y. Sun. 2013. Recent advances in microfluidic techniques for single-cell biophysical characterization. Lab on a chip. 13:2464-2483.

Zimmerberg, J., and M.M. Kozlov. 2006. How proteins produce cellular membrane curvature. Nat Rev Mol Cell Biol. 7:9-19.

Zwaal, R.F., and A.J. Schroit. 1997. Pathophysiologic implications of membrane phospholipid asymmetry in blood cells. Blood. 89:1121–32.

Annex

α-Hederin Induces Apoptosis, Membrane Permeabilization and Morphologic Changes in Two Cancer Cell Lines Through a Cholesterol-Dependent Mechanism

Authors Joseph H. Lorent[1,2], Catherine Léonard[1], Marthe Abouzi[1], Farida Akabi[1], Joëlle Quetin-Leclercq[2], Marie-Paule Mingeot-Leclercq[1]

Affiliations
[1] Université catholique de Louvain, Louvain Drug Research Institute, Cellular and Molecular Pharmacology, Bruxelles, Belgium
[2] Université catholique de Louvain, Louvain Drug Research Institute, Pharmacognosy, Bruxelles, Belgium

Key words
- saponin
- triterpenic acid
- apoptosis
- membrane permeabilization
- cholesterol

received March 18, 2016
revised July 21, 2016
accepted August 4, 2016

Bibliography
DOI http://dx.doi.org/10.1055/s-0042-114780
Published online August 30, 2016
Planta Med 2016; 82: 1532–1539 © Georg Thieme Verlag KG Stuttgart · New York · ISSN 0032-0943

Correspondence
Prof. Dr. Marie-Paule Mingeot-Leclercq
UCL B1.73.05
Université catholique de Louvain – Louvain Drug Research Institute
Cellular and Molecular Pharmacology – Pharmacognosy
Avenue E. Mounier 73
B-1200 Bruxelles
Belgium
Phone: + 32 27 64 73 74
marie-paule.mingeot@uclouvain.be

Abstract

In perspective of reducing the mortality of cancer, there is a high interest in compounds which act on multiple cellular targets and therefore prevent the appearance of cancer resistances. Saponins and α-hederin, an oleanane-type saponin, induce cancer cell death through different pathways, including apoptosis and membrane permeabilization. Unfortunately, the mechanism by which cell death is induced is unknown. We hypothesized that the activity of α-hederin mainly depends on its interaction with membrane cholesterol and therefore investigated the cholesterol and saponin-structure dependency of apoptosis and membrane permeabilization in two malignant monocytic cell lines. Apoptotic cell death and membrane permeabilization were significantly reduced in cholesterol-depleted cells. Permeabilization further depended upon the osidic side chain of α-hederin and led to extracellular calcium influx and nuclear fragmentation, with only the latter being susceptible to caspase inhibitors. Membrane order, measured by laurdan generalized polarization imaging, was neither reduced by α-hederin nor its aglycone hederagenin suggesting that their activity was not related to membrane cholesterol extraction. However, a radical change in morphology, including the disappearance of pseudopodes was observed upon incubation with α-hederin. Our results suggest that the different activities of α-hederin mainly depend on its interaction with membrane cholesterol and consequent pore formation.

Abbreviations

AO/EB:	acridine orange/ethidium bromide
BCA:	bicinchonic acid
BSA:	bovine serum albumin
DAPI:	4′,6-diamidino-2-phenylindole
EGTA:	ethylene glycol-bis(β-aminoethyl ether)-N,N,N′,N′-tetraacetic acid
FCS:	fetal calf serum
MβCD:	methyl-β-cyclodextrin
SDS:	sodium dodecyl sulfate

Supporting information available online at http://www.thieme-connect.de/products

Introduction

Cancer is becoming an increasing problem of public health especially in developed countries. The appearance of cancer resistance towards conventional chemotherapy diminishes the chances of successful treatment and is therefore a major challenge in cancer research [1]. A way to prevent chemotherapeutic resistance in cancer cells is to act on multiple targets. Saponins, natural amphiphilic compounds have shown the potential to induce cancer cell death by multiple pathways and to increase the activity towards common chemotherapeutic agents or radiotherapy [2–5]. α-Hederin (kalopanaxsaponin A, **Fig. 1S**, Supporting Information), an oleanane type saponin extracted from *Hedera helix*, showed a promising activity *in vivo* against colon and lung cancer [5]. It has been shown that α-hederin possesses a selective cytotoxic activity towards cancer cells most probably by activating on apoptotic pathways via cytosolic increase of reactive oxygen species and Ca^{2+} [6,7]. We recently showed that α-hederin and its aglycone hederagenin (**Fig. 1S**, Supporting Information) were able to induce pore formation in liposomal systems in a cholesterol dependent manner [8]. Because cholesterol plays a critical role for both the activity on cancer cells and hemolysis by saponins [9], the characterization of the interaction between α-hederin and cholesterol in cell

		Non-depleted	Depleted
U937	Cholesterol/proteins	13.13 ± 1.30 µg/mg	4.49*** ± 0.24 µg/mg
	Cholesterol/phospholipids	150.90 ± 14.98 µg/µM	40.26*** ± 2.16 µg/µM
THP-1	Cholesterol/proteins	11.29 ± 0.39 µg/mg	6.54*** ± 0.72 µg/mg
	Cholesterol/phospholipids	129.93 ± 4.17 µg/µM	60.07*** ± 6.67 µg/µM

Three independent experiments have been performed, Statistical analysis: One-way ANOVA. ***p < 0.001

Table 1 Ratios of cholesterol/proteins and cholesterol/phospholipids in non-depleted and cholesterol depleted U937 and THP-1 cells.

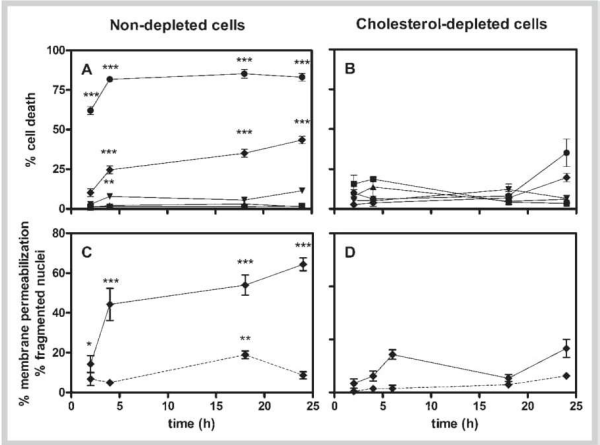

Fig. 1 Cytotoxicity induced by α-hederin in non-depleted (**A, C**) and cholesterol-depleted U937 cells (**B, D**). Panels **A** and **B** show trypan blue assay of cells incubated with increasing concentrations of α-hederin: Control (■), 10 µM (▲), 15 µM (▼), 20 µM (♦) and 25 µM (●). Panels **C** and **D** display acridine orange/ethidium bromide assay of cells incubated with 20 µM of α-hederin. Straight line: Cells with permeabilized plasma membrane, dashed line: cells with fragmented nuclei. Three independent experiments were performed. Statistical analysis: Two-way ANOVA between non-depleted and cholesterol depleted conditions. *P < 0.5; **p < 0.1; ***p < 0.01.

membranes is a key for the understanding of the mechanisms involved in saponin induced cell death. The interaction of α-hederin with membraneous cholesterol could also have repercussions on the chemotherapeutic resistance of cancer cells since its regulatory function on the membrane order has been put into relationship with the activity of drug expelling channels [10]. However, several saponins changed the lipid order in cell membranes but no consistency was observed among those compounds regarding an increase or decrease of membrane fluidity or whether this change was cholesterol related or not [11, 12]. Interestingly, ginsenoside Rg3 induced changes in the membrane order responsible for a reduction of chemotherapeutic resistance in multidrug resistant cancer cells [13].

Hence, the activity of saponins and α-hederin might depend on their interaction with cholesterol in the plasma membrane. We therefore decided to analyze the importance of cholesterol in α-hederin induced cell death in cancer cells and the effects of the saponin on plasma membrane integrity and order. As a model, we used two monocytic cell lines depleted or not in cholesterol: U937, a cholesterol auxotroph cell line [14] and THP-1 cells, able to synthesize their own cholesterol [15]. In addition, we established the importance of the sugar moiety for those effects, by comparing the effect of α-hederin with that obtained with its aglycone, hederagenin.

Results

MβCD was very efficient in reducing the cholesterol/protein and cholesterol/phospholipid ratio in U937 and THP-1 cells (**Table 1**). The phospholipid amount was not influenced by MβCD (data not shown), indicating a selective depletion of cholesterol. The measured cholesterol concentrations of non-depleted cells corresponded almost to values reported in literature [16, 17].

Cell death was rapidly observed in α-hederin treated U937 cells by trypan blue assay. It increased upon α-hederin concentration. At the highest concentration investigated (25 µM; **Fig. 1 A**), α-hederin induced 62 ± 5.2% of cell death after 2 h of incubation. Depletion of cholesterol by MβCD effectively reduced α-hederin induced cell death in U937 cells upon 18 h of incubation (**Fig. 1 B**). These observations agree with those previously obtained on THP-1 cells [8]. SDS, conversely to α-hederin induced cell death preferentially in cholesterol-depleted cells (**Fig. 2S**, Supporting Information). This confirms that only the saponin toxicity was inhibited by cholesterol depletion.

Monitoring the cholesterol-dependency of α-hederin induced cell death by acridine orange/ethidium bromide staining (**Fig. 1 C, D**) allowed us to follow the permeabilization of the plasma membrane in parallel with changes of the nucleus' morphology. The fragmentation of the nucleus is usually regarded as a sign of apoptotic cell death but might also occur to a lesser extend in necrosis [18]. Membrane permeabilization and the subsequent influx of ethidium bromide were induced long before the appearance of nucleus fragmentation. More than 40% of the cells lost their membrane integrity after 4 h of incubation with 20 µM

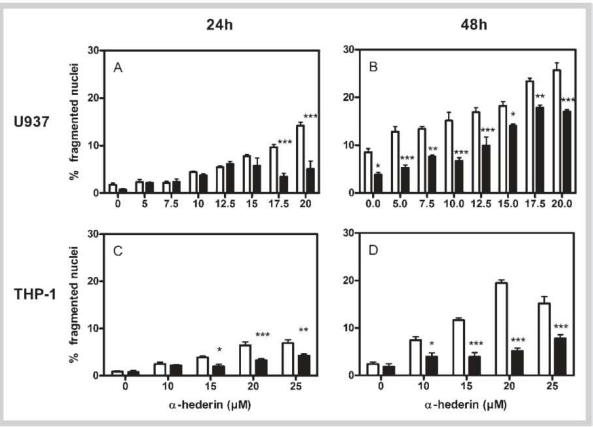

Fig. 2 Apoptosis induced by α-hederin in U937 (**A, B**) and THP-1 (**C, D**) cells, depleted or non- depleted in cholesterol. Fragmentation of nucleus of depleted (black bars) or non-depleted (white bars) cells incubated for 24 (**A, C**) and 48 h (**B, D**) with increasing concentrations of α-hederin. Statistical analysis: One-way ANOVA: depleted vs. non-depleted cells. *P < 0.05; **p < 0.01; ***p < 0.001.

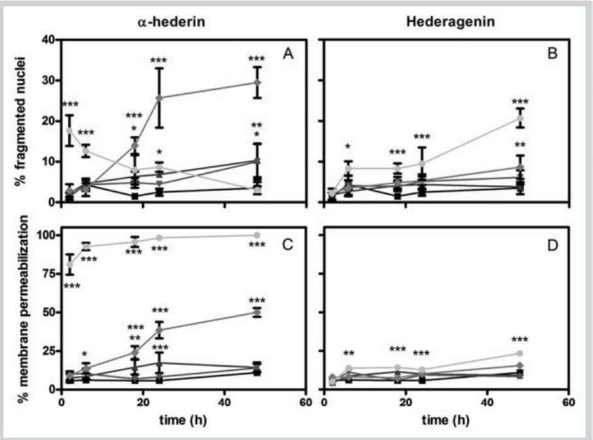

Fig. 3 Apoptosis (% fragmentated nuclei) and cell necrosis (% membrane permeabilization) induced by α-hederin and its aglycone, hederagenin. Panels **A, B, C, D**: U937 cells incubated for 2, 6, 18, 24 and 48 h with α-hederin (**A, C**) or hederagenin (**B, D**). Control (■, black), 10 μM (▲, very dark grey), 15 μM (▼, dark grey), 20 μM (♦, grey) and 40 μM (•, light grey). Statistical analysis: Two-way ANOVA: vs. control. *P < 0.05; **p < 0.01; ***p < 0.001.

of α-hederin in non-depleted cells. Nucleus fragmentation became significant after 18 h of incubation. Depletion of cholesterol reduced the fragmentation of the nucleus. Membrane defects were also reduced in depleted cells (**Fig. 1 D**) which confirmed the results obtained with trypan blue assay (**Fig. 1 A**).

Fragmentation of nuclei was further investigated in a concentration-dependent manner by DAPI assay for 24 and 48 h. Fragmentation increased upon α-hederin concentration in U937 (**Fig. 2 - A, B**) and THP-1 cells (**Fig. 2 C, D**). In THP-1, as well as in U937 (not shown), a maximum of fragmentation could be observed at concentrations around 20 μM. In all conditions investigated, depletion of cholesterol reduced the fragmentation of the nuclei.

The osidic side chain of α-hederin has been shown to play an important role in the formation of pores in giant unilamellar vesicles (GUV) [19]. We therefore investigated the critical role of sugars in the membrane permeabilization and cell death (**Fig. 3**). Hederagenin has the same triterpenoid backbone as α-hederin but lacks the sugar moiety. We compared the effects of α-hederin (**Fig. 3 A, C**) and hederagenin (**Fig. 3 B, D**) on U937 cells using AO/EB assay.

Consistently with results shown for the trypan-blue assay (**Fig. 1 A**), α-hederin induced a very rapid cytosolic ethidium bromide influx at higher concentrations (**Fig. 3 C**). This effect was not observed with hederagenin even at very long incubation periods (**Fig. 3 D**). Condensation and fragmentation of nuclei was induced very soon after addition of 40 μM of α-hederin but decreased for longer incubation periods. The cells presenting nuclear fragmentation at this concentration systematically presented ethidium bromide influx. The highest effect on fragmentation was observed with 20 μM of α-hederin for 24 and 48 h of incubation (**Fig. 3 A**). Hederagenin only induced fragmentation after

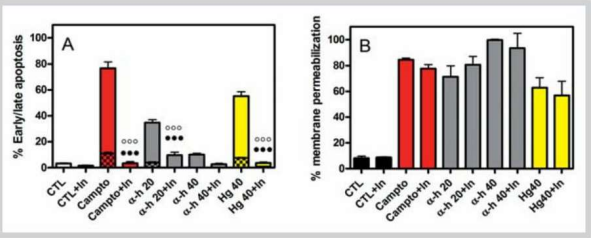

Fig. 4 Effect of caspase inhibitor on apoptosis and membrane permeabilization. Panels **A, B** U937 cells were incubated for 48 h with camptothecine (Campto, red), α-hederin (α-h, grey), hederagenin (Hg, yellow) with or without pan-caspase inhibitor Q-Vd-OPh (In). **A** Early (patterned bar)/late (not patterned bar) apoptosis and **B** membrane permeabilization. CTL is the control. Statistical analysis: One-way ANOVA; symbols: • = Early apoptosis ± inhibitor ○ = Late apoptosis ± inhibitor; three symbols: $p < 0.001$.

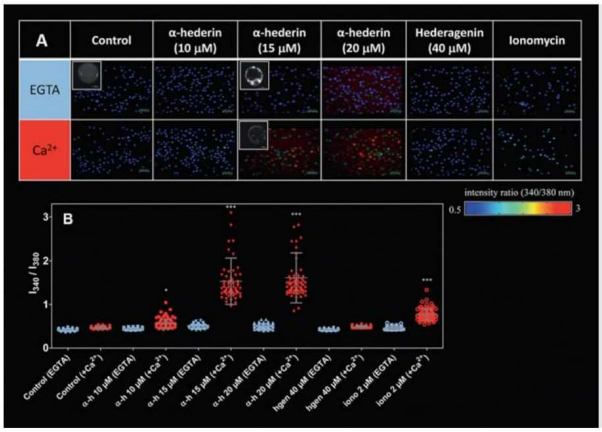

Fig. 5 Calcium influx: U937 cells have been labeled with Fura-2 AM and further incubated for 30 min at room temperature in KREBS media containing 250 µM EGTA or 1.5 mM $CaCl_2$ and α-hederin, hederagenin or ionomycin as positive control. In panel **A**, cells are pseudocolored upon the intensity ratio of Fura-$2_{bound\ to\ Ca^{2+}}$/Fura-$2_{unbound}$ (I_{340}/I_{380}). The colors range from 0.3 (deep blue) to 2.5 (red) and scale bars are equal to 50 µm. Inserts show a biphoton microscopy slide (scale bars are 5 µm) of a representative cell for the control and conditions where a significant change has been observed. Panel **B** represents the intensity ratio of at least 70 cells from two independent experiments for each condition. Blue symbols represent EGTA and red symbols the Ca^{2+}-containing condition. Statistical analysis: One way ANOVA has been performed separately for EGTA and Ca^{2+}-containing media. $^{*}P < 0.05$, $^{***}p < 0.001$ compared to the control.

48 h at 40 µM which is close to the solubility limit of the compound (**Fig. 3B**).

Moving on the mechanism involved in cell death and fragmentation of the nucleus by α-hederin and hederagenin, we investigated the role of caspases by preincubating cells with the pan-caspase inhibitor Q-VD-OPh (**Fig. 4A, B** and **Fig. 3S**, Supporting Information). After 48 h of incubation with α-hederin and hederagenin, Q-VD-OPh effectively inhibited fragmentation of the nucleus but did not significantly reduce the cytosolic ethidium bromide influx for both compounds. In addition, the proportion of early apoptosis compared to all cells with fragmented nuclei was very low also for shorter incubation periods (**Fig. 4A** and **Fig. 3S** (**C, D**), Supporting Information). Camptothecine induced nuclear fragmentation and cell death was efficiently reduced by Q-VD-OPh especially at shorter incubation times (**Fig. 3S**, Supporting Information) and agrees with data obtained on HL-60 cells [20]. At 4 h of incubation and 40 µM α-hederin, caspase inhibition by Q-VD-OPh did not reduce the membrane permeabilization, suggesting a caspase independent cell death at high saponin concentrations (**Fig. 3S** (**B**), Supporting Information).

Calcium influx in monocytes has been compared for α-hederin, hederagenin and ionomycin. α-Hederin induced calcium influx in a concentration- and time-dependent manner. After 30 min of incubation with α-hederin, no significant calcium influx was observed at 10 µM, but several cells showed a higher intensity ratio of FURA-2 (I_{340}/I_{380}) which reflects a higher intracytosolic Ca^{2} $^{+}$-concentration compared to the control. This was only observed in media containing extracellular Ca^{2+} (**Fig. 5A, B**). The cytosolic Ca^{2+}-influx induced a significant change of the intensity ratio at 15 and 20 µM of α-hederin in Ca^{2+}-containing media. Extracellular EGTA reduced effectively the intensity ratio in α-hederin incubated cells suggesting an extracellular influx. The overall intensity of the FURA-2 signal was reduced at 15 and 20 µM, reflecting a leak of the fluorescent marker out of the cells. Interestingly, several cells treated with α-hederin concentrated FURA-2 into spots whereas a homogenous distribution of the marker was kept in other conditions (**Fig. 5A**). Biphoton microscopy (insets) revealed that this effect occurred even in the presence of EGTA suggesting it did not exclusively depend on extracellular Ca^{2+}. Hederagenin (40 µM) did not induce an increase of the intensity ratio, indicating a lack of cytosolic Ca^{+2}-increase.

At 40 µM, α-hederin induced rapid (less than 5 min) intracytosolic calcium influx (**Fig. 4S**, Supporting Information). The intensity ratio increased from 0.5 for control cells to 1.5 after 5 min treatment. Conversely to ionomycin, this increase did not depend on extracellular calcium (1.5 mM) which suggests that, at this concentration, α-hederin induces not only the influx of extracellular calcium but also the release of intracellular calcium stores. Additionally, the signal intensity of FURA-2 decreased, reflecting a leak out of FURA-2 from the cell. After 30 min of incubation and 40 µM of α-hederin, all the FURA-2 had been leaked from cells and they were no longer fluorescent (data not shown).

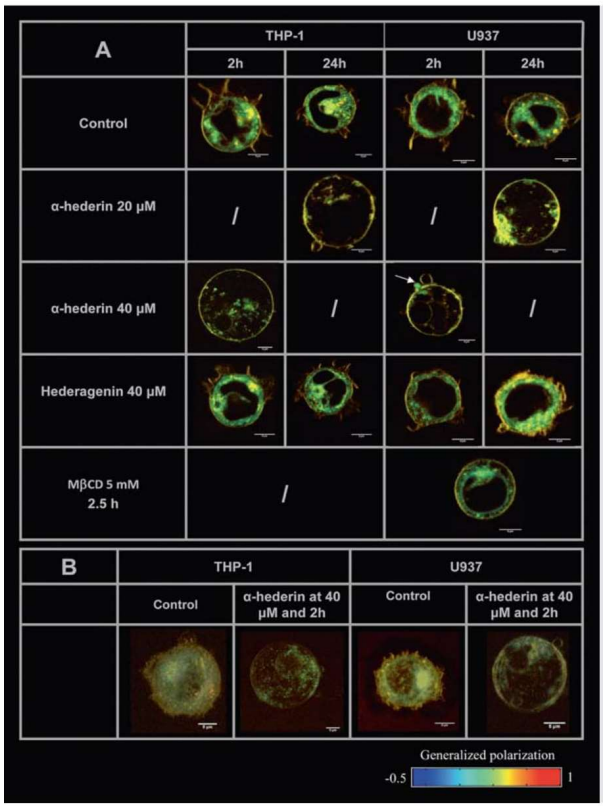

Fig. 6 GP-images of THP-1 and U937 cells, incubated with α-hederin (20, 40 µM) or hederagenin (40 µM) for 2 and 24 h. **A** Confocal sections in the middle plane of the cell. As a control, cells have been incubated with MβCD (5 mM) for 2.5 h. **B** 3D-reconstructions of GP-confocal sections for negative controls and at 2 h and 40 µM of α-hederin. GP-images are pseudocolored ranging from − 0.5 (blue) to 1 (red). Scale bar = 5 µM.

At a glance, intracytosolic calcium is significantly increased by α-hederin and at high concentrations, FURA-2 leak out is observed suggesting the formation of larger non Ca^{2+}-selective pores even at short incubation times. Hederagenin itself was not able to increase Ca^{2+}-influx at 40 µM and 30 min of incubation.

We further investigated the effect of α-hederin and hederagenin on morphology as well as on membrane order in macrophages. We used laurdan biphoton microscopy to determine generalized polarization (GP) of cell membranes. Laurdan-GP is an indicator of membrane order at the water-membrane interface. Higher GP-values reflect a lower polarity of the microenvironment of the fluorescent probe and can generally be associated with higher lipid packing in the membrane.

The GP of plasma membranes in U937 and THP-1 cells was always higher than the GP of intracellular membranes. This particularity has been shown in other cell lines and might be attributed to the higher content of cholesterol and saturated lipids of the plasma membrane, compared to intracellular organelles [21]. Hence, it permits to distinguish between the plasma membrane and intracellular membrane material (**Fig. 6**). GP values from the plasma membranes are represented as GP_{high} and all other GP values are represented as GP_{low} (**Fig. 5S**, Supporting Information).

Membrane morphology of U937 and THP-1 cells was radically changed upon incubation with α-hederin (**Fig. 6**). After 2 h of incubation with 40 µM, pseudopodes disappeared which gave the impression of a 'flat'-spherical plasma membrane (**Fig. 6A, B**). This effect was also observed at 24 h incubation with 20 µM of α-hederin (**Fig. 6A**). MβCD induced a similar effect which might indicate a cholesterol dependence of this effect. In addition, we observed the formation of plasma membrane blebs with 20 and 40 µM of α-hederin after 24 and 2 h of incubation, respectively. Those changes on the plasma membrane were accompanied by a release of intracellular membrane material to the extracellular media (see arrow) which made the cells resemble ghost cells. The shape of the nucleus was transformed from bilobar to spherical, which was occasionally accompanied by nuclear fragmentation.

In parallel, upon α-hederin incubation, we observed an overall increase of GP values in both cell types but this effect seemed to be more important for GP_{low} and GP_{mean} values (**Fig. 5S**, Supporting Information). This was most probably due to the fact that the intracellular membrane material was either disintegrated or re-

leased to the membrane exterior. The plasma membrane order (GP_{high}) in U937 cells remained unchanged. This was different to THP-1 cells, where plasma membrane order (GP_{high}) seemed to increase compared to the control. As a positive control for plasma membrane order reduction (GP_{high}), we used 5 mM of MβCD in RPMI media containing 1 mg/mL BSA and exempt of FCS. In those conditions, GP values (low, high and mean) were significantly reduced and generally attributed to the depletion of membrane cholesterol (**Fig. 5S**, Supporting Information) [22].
Hederagenin did neither have an effect on cell membrane morphology nor on membrane order for at least 24 h of incubation at its solubility limit of 40 µM.

Discussion

In the past, α-hederin has been shown to induce apoptotic features like DNA fragmentation and caspase dependent cell death. It has been assumed that the saponin would be able to induce apoptotic pathways via activation of specific Ca^{2+}-channels and depletion of antioxidant species in the cytoplasm [6, 7]. In addition to this effect, direct pore formation was observed but a link between both activities was so far missing [23].
Through our results it emerges that the main component of α-hederin induced cell death can be attributed to its membrane permeabilizing activity, especially at high concentrations, which seems to be related to the presence of cholesterol in the membrane. Several results point into this direction: (i) treated cells with fragmented nuclei present mostly a compromised cell membrane and ethidium bromide influx. They might still be seen as "late apoptotic" cells but at 2 h of incubation with 40 µM, the percentage of ethidium bromide influx is already at 75%. (ii) Total cell death is not reduced by general caspase inhibitors at short incubation times, conversely to campthotecin (**Fig. 3S**, Supporting Information). (iii) Depletion of cholesterol confers resistance towards α-hederin induced cell death. Pore formation in liposomal membranes by α-hederin has been shown to be cholesterol dependent [8] and lysis of red blood cells by saponins was explained by a cholesterol dependent mechanism [24]. The depletion of cholesterol in the plasma membrane of cancer cells should hence refer resistance to pore formation. (iv) Cytosolic Ca^{2+}-influx is concentration- and time-dependent. At 15 and 20 µM, influx depends mainly on extracellular calcium. It has been shown previously that pores formed by α-hederin in GUV and LUV increased their size through a concentration and time-dependent way [8, 19]. This is also supported by the fact that FURA-2, a larger molecule than Ca^{2+}, only escapes from the cells at high saponin concentrations (**Fig. 5S** (**A**), Supporting Information). Calcium influx might also be the trigger for several apoptotic hallmarks as it was proposed previously [6]. Apoptosis induction would in this case depend, at least in part, on pore formation by α-hederin. At 40 µM, α-hederin induced cytosolic Ca^{2+}-influx even when no Ca^{2+} was present in the extracellular media. This means that the saponin is also able to perforate membranes of intracellular calcium stores at high concentration. (v) Cells loose their intracellular organelles upon incubation with high concentrations of α-hederin. A part of the intracellular membrane material was released to the cell exterior which suggests relatively large pores (**Fig. 6**). (vi) The direct morphological changes on the plasma membrane as well as the flattening or the formation of blebs might indicate a direct effect on the membrane. Inhibition of pseudopodia formation by α-hederin and MβCD accounts for a cholesterol-dependency of this effect. It has been shown on macrophages, that the formation of pseudopodes is a cholesterol dependent mechanism [25, 26]. Formation of blebs is an apoptotic hallmark [27] but could be related to the curvature stress which is generated by α-hederin [8].
Despite all the data, it is not exactly clear which type of pore, membrane hole or instability is induced by α-hederin. Our recent studies on membrane models showed that α-hederin can induce the formation of large toroidal pores at high concentration, but it was also shown that at lower concentrations the saponin induced rather the formation of lipid aggregates in the membrane, which were composed of phospholipids and sterols. The formation of those aggregates might deplete the membrane of its lipid material and create transient or permanent membrane instabilities and holes [8, 19]. The increase of laurdan generalized polarization in the plasma membrane might indicate the formation of similar aggregates (**Fig. 5S**, Supporting Information) but to resolve this issue, it would require further investigation. Both mechanisms coexist most probably and might depend on the critical micellar concentration of the saponin [19]. Similarly, amphotericin, an antifungal compound, induced the formation of pores and a "sponge"-like phase, which was able to sequester membrane ergosterol and thereby decrease membrane stability [28]. However, since the effects of α-hederin were not accompanied by a decrease of plasma membrane order, as it has been observed with MβCD, an extraction of cholesterol from the membrane into the surrounding media is less probable (**Fig. 5S**, Supporting Information).
We further wanted to point out the importance of the sugar chain in cell death induction. Regarding the structure of the saponin, we showed that the presence of the sugar chain was critical for rapid cell death induction but didn't seem necessary for cell death induction at longer incubation periods. Without the sugar chain (hederagenin), there was neither a rapid cell death nor membrane permeabilization observed at concentrations up to 40 µM. This can probably be put into relationship with the results obtained in GUV at high concentration, where an immediate permeation to dextran at 4 kDa was observed with α-hederin whereas the effect with hederagenin became only evident at 48 h of incubation [8]. Induction of cell death required longer incubation periods and higher concentrations with hederagenin compared to α-hederin.
Despite the effect on membrane permeabilization, the extrinsic apoptotic pathway could also play a role, especially at lower concentrations. For avicin D, another saponin, depletion of membrane cholesterol by MβCD inhibited activation of death receptors in cancer cells [29]. Activation of death receptors via coalescence or disruption of lipid rafts has also been shown for some other saponins and cholesterol binding toxins [30, 31]. The induction of phase separation in GUVs mimicking nanoscopic raft domains by α-hederin supports this hypothesis [19].
Regarding the potential use of both drugs as anticancer agents, the present study shows that α-hederin induces cell death in cancer cells very efficiently. However, the question arises how the present mechanism could be in any way specific towards cancer cells. Some specificity might arise from an overproduction of cholesterol in several types of cancer cells as a higher membrane cholesterol content would mean a more efficient membrane destabilization or apoptosis induction by the saponin [32, 33]. Since α-hederin given intraperitoneal had an effective anticancer activity in mice against two very resilient cancer types, its limitation

due to hemolytic effects [34] might only apply when administered directly into the blood stream.
At a glance, α-hederin induces cell death via cholesterol dependent pore formation followed by cytosolic Ca^{2+}-influx mostly from extracellular media. The pore formation involves the release of intracellular membrane material from the cell. The pore forming activity would not be due to a cholesterol extraction from the membrane but rather due to the formation of cholesterol/saponin aggregates in the membrane which do not involve a general change of membrane order. This effect might further lead to the inhibition of pseudopodia formation. We also show that the caspase-dependent fragmentation of the nucleus is most probably due to the increase of cytosolic Ca^{2+} after membrane permeabilization of cancer cells [35].

Material and Methods

Chemicals, biochemicals and cell lines

α-hederin and hederagenin (purity ≥ 98%) were purchased from Extrasynthèse. The compounds were dissolved in ethanol. After evaporation of the solvent, the residue was resolubilized in RPMI media containing 0,1% of DMSO in an ultrasonic bath for 5 min. Corresponding controls were used. Cells were purchased from ATCC. RPMI medium was ordered by Life technologies. BCA protein assay, FURA-2 AM, ionomycin (purity > 90%) and Amplex red cholesterol assay kit were purchased from ThermoFisher Scientific. MβCD, SDS, DAPI, acridine orange and ethidium bromide were ordered from Sigma-Aldrich. All other reagents were ordered from E. Merck AG.

Cell culture, cholesterol depletion and incubation with α-hederin and hederagenin

All our experiments were performed on cells which were freshly defrozen from a stock, that had been established directly after purchasing the cells from ATCC. Cell cultures were never kept longer than 3 weeks in culture. Cells were cultivated in RMPI medium containing 10% FCS in 95% air and 5% CO_2.
For cholesterol depletion, cells (10^6 cells/mL) were incubated for 2.5 h in RPMI medium containing 1 mg/mL BSA and 5 mM MβCD. Cell counting was performed in a Burker chamber. After incubation, cells were washed 3 times with RPMI medium without serum.
At this time, a part of the cells were quantified for their cholesterol, phospholipid and protein contents. For cholesterol and phospholipid quantification, cellular lipids were first extracted [36] and further quantified by Amplex red cholesterol assay and phosphorus assay [37]. Proteins were quantified by the BCA protein assay kit.
For further incubation with α-hederin, hederagenin or SDS, cholesterol-depleted cells were incubated in RPMI media containing 10% FCS.

Determination of cell death

Cell death was quantified by the trypan blue assay using a phase contrast microscope and results were expressed in % of total cells [38].

Determination of cell nucleus fragmentation and integrity of the plasma membrane

We used DAPI assay to determine nuclear fragmentation [39]. A total of 500 cells was counted.
To distinguish between living, death cells and early and late apoptosis, we used the AO/EB assay [40]. Both stains label the nucleus but only acridine orange can diffuse through an intact plasma membrane. After incubation, cells were harvested and washed in PBS medium. They were then put in contact with the AO/EB (100 µg/mL) solution and observed by fluorescence microscopy. Early apoptotic cells had a fragmented nucleus and presented no EB influx. All the cells showing EB influx were counted as cells with a defect membrane. Cells presenting both EB influx and nucleus fragmentation were considered as late apoptotic. A total of 200 cells were counted.

Determination of extracellular calcium influx by microspectrofluorimetry

U937 cells were loaded with FURA-2 AM for 1 h at 20 °C in RPMI medium containing 10% FCS. They were further washed with KREBS-HEPES media (+BSA 1 mg/mL) adjusted at pH = 7.4 and incubated in the same media containing 1.5 mM $CaCl_2$ or 250 µM EGTA. α-hederin and hederagenin were resuspended in the corresponding buffer solution with 0.1% DMSO. For microscopy, cells were transferred into non coated IBIDI slides and alternatively excited at 340 and 380 nm. Emission fluorescence was monitored at 510 nm using a Deltascan spectrofluorimeter (Photon Technology International) coupled to a Nikon Diaphot inverted microscope (Fluar 20×, objective; numerical aperture, 0.75). Fluorescence intensity was recorded over the surface of each single cell and intracytosolic $[Ca^{2+}]$ was evaluated from the ratio of the fluorescence emission intensities excited at both wavelengths. A minimum of 30 cells have been analyzed for each condition.

Biphoton microscopy of laurdan in monocytes

After incubation, cells were washed with RPMI media and labeled with laurdan at 2 µM and 37 °C for 30 min in RPMI media (+ 1 mg/mL BSA). They were further washed with PBS at pH = 7.4 and transferred in the same buffer to IBIDI slides. Excitation was done at 780 nm (0.5% intensity) and cells were observed using a C-Apochromat 63×/1.2 water immersion objective. Emission intensity was recorded upon two channels ($I_1 = I_{404-457}$ nm and $I_2 = I_{468-528}$ nm) on entire cells. Generalized polarization (GP) was calculated using the formula: $GP = (I_1 - G.I_2)/(I_1 + G.I_2)$. The G-factor (G) is instrument dependent and was determined through a calibration method previously described [41]. Generalized polarization (GP) images (HSV images) were created with a own Matlab routine based on principles previously established [41]. Briefly, all GP-values of an obtained GP-image were fitted to a double Gaussian function. The centre of both functions were represented by two GP values (GP_{high} and GP_{low}), reflecting approximately the GP-values of the plasma membrane and the intracellular membranes, respectively (see results). GP_{mean} represented the total average of all GP-values in a cell. A total of 15 entire cells was analyzed for each condition.

Supporting information

Structures of α-hederin and hederagenin as well as results and additional data are available as Supporting Information.

Acknowledgements

We thank the laboratory of cell biology for the disposition of their biphoton microscope (LSM 510 NLO, Zeiss) and especially Patrick Van Der Smissen for his skillful help. We also appreciated the

work of Nicolas Tajeddine for the calcium release assays and Marie-Claire Cambier for her help on cell culture. We also thank the Université Catholique de Louvain for the "Bourse du patrimoine" grant which permit part of this work.

Conflict of Interest

The authors declare no conflict of interest.

References

1 *Holohan C, Van Schaeybroeck S, Longley DB, Johnston PG.* Cancer drug resistance: an evolving paradigm. Nat Rev Cancer 2013; 13: 714–726
2 *Lee SJ, Sung JH, Lee SJ, Moon CK, Lee BH.* Antitumor activity of a novel ginseng saponin metabolite in human pulmonary adenocarcinoma cells resistant to cisplatin. Cancer Lett 1999; 144: 39–43
3 *Jiang H, Zhao P, Feng J, Su D, Ma S.* Effect of Paris saponin I on radiosensitivity in a gefitinib-resistant lung adenocarcinoma cell line. Oncol Lett 2014; 7: 2059–2064
4 *Huang C, Xu D, Xia Q, Wang P, Rong C, Su Y.* Reversal of p-glycoprotein-mediated multidrug resistance of human hepatic cancer cells by astragaloside II. J Pharm Pharmacol 2012; 64: 1741–1750
5 *Park HJ, Kwon SH, Lee JH, Lee KH, Miyamoto K, Lee KT.* Kalopanaxsaponin A is a basic saponin structure for the anti-tumor activity of hederagenin monodesmosides. Planta Med 2001; 67: 118–121
6 *Choi JH, Lee HW, Park HJ, Kim SH, Lee KT.* Kalopanaxsaponin A induces apoptosis in human leukemia U937 cells through extracellular Ca^{2+} influx and caspase-8 dependent pathways. Food Chem Toxicol 2008; 46: 3486–3492
7 *Swamy SM, Huat BT.* Intracellular glutathione depletion and reactive oxygen species generation are important in alpha-hederin-induced apoptosis of P388 cells. Mol Cell Biochem 2003; 245: 127–139
8 *Lorent J, Le Duff CS, Quetin-Leclercq J, Mingeot-Leclercq MP.* Induction of highly curved structures in relation to membrane permeabilization and budding by the triterpenoid saponins, alpha- and delta-hederin. J Biol Chem 2013; 288: 14000–14017
9 *Shany S, Bernheimer AW, Grushoff PS, Kim KS.* Evidence for membrane cholesterol as the common binding site for cereolysin, streptolysin O and saponin. Mol Cell Biochem 1974; 3: 179–186
10 *Gelsomino G, Corsetto PA, Campia I, Montorfano G, Kopecka J, Castella B, Gazzano E, Ghigo D, Rizzo AM, Riganti C.* Omega 3 fatty acids chemosensitize multidrug resistant colon cancer cells by down-regulating cholesterol synthesis and altering detergent resistant membranes composition. Mol Cancer 2013; 12: 137
11 *Jiang YS, Jin ZX, Umehara H, Ota T.* Cholesterol-dependent induction of dendrite formation by ginsenoside Rh2 in cultured melanoma cells. Int J Mol Med 2010; 26: 787–793
12 *Ishida H, Hirota Y, Nakazawa H.* Effect of sub-skinning concentrations of saponin on intracellular Ca^{2+} and plasma membrane fluidity in cultured cardiac cells. Biochim Biophys Acta 1993; 1145: 58–62
13 *Kwon HY, Kim EH, Kim SW, Kim SN, Park JD, Rhee DK.* Selective toxicity of ginsenoside Rg3 on multidrug resistant cells by membrane fluidity modulation. Arch Pharm Res 2008; 31: 171–177
14 *Billheimer JT, Chamoun D, Esfahani M.* Defective 3-ketosteroid reductase activity in a human monocyte-like cell line. J Lipid Res 1987; 28: 704–709
15 *Kritharides L, Christian A, Stoudt G, Morel D, Rothblat GH.* Cholesterol metabolism and efflux in human THP-1 macrophages. Arterioscler Thromb Vasc Biol 1998; 18: 1589–1599
16 *De Pace DM, Esfahani M.* The effects of cholesterol depletion on cellular morphology. Anat Rec 1987; 219: 135–143
17 *Wang Y, Chen Z, Liao Y, Mei C, Peng H, Wang M, Guo H, Lu H.* Angiotensin II increases the cholesterol content of foam cells via down-regulating the expression of ATP-binding cassette transporter A1. Biochem Biophys Res Commun 2007; 353: 650–654
18 *Martelli AM, Zweyer M, Ochs RL, Tazzari PL, Tabellini G, Narducci P, Bortul R.* Nuclear apoptotic changes: an overview. J Cell Biochem 2001; 82: 634–646
19 *Lorent J, Lins L, Domenech O, Quetin-Leclercq J, Brasseur R, Mingeot-Leclercq MP.* Domain formation and permeabilization induced by the saponin alpha-hederin and its aglycone hederagenin in a cholesterol-containing bilayer. Langmuir 2014; 30: 4556–4569
20 *King MA, Radicchi-Mastroianni MA.* Effects of caspase inhibition on camptothecin-induced apoptosis of HL-60 cells. Cytometry 2002; 49: 28–35
21 *Parasassi T, Gratton E, Yu WM, Wilson P, Levi M.* Two-photon fluorescence microscopy of laurdan generalized polarization domains in model and natural membranes. Biophys J 1997; 72: 2413–2429
22 *Sanchez SA, Gunther G, Tricerri MA, Gratton E.* Methyl-beta-cyclodextrins preferentially remove cholesterol from the liquid disordered phase in giant unilamellar vesicles. J Membr Biol 2011; 241: 1–10
23 *Gauthier C, Legault J, Girard-Lalancette K, Mshvildadze V, Pichette A.* Haemolytic activity, cytotoxicity and membrane cell permeabilization of semi-synthetic and natural lupane- and oleanane-type saponins. Bioorg Med Chem 2009; 17: 2002–2008
24 *Bangham AD, Horne RW, Glauert AM, Dingle JT, Lucy JA.* Action of saponin on biological cell membranes. Nature 1962; 196: 952–955
25 *Kay JG, Murray RZ, Pagan JK, Stow JL.* Cytokine secretion via cholesterol-rich lipid raft-associated SNAREs at the phagocytic cup. J Biol Chem 2006; 281: 11949–11954
26 *Petrovic N, Schacke W, Gahagan JR, O'Conor CA, Winnicka B, Conway RE, Mina-Osorio P, Shapiro LH.* CD13/APN regulates endothelial invasion and filopodia formation. Blood 2007; 110: 142–150
27 *Kroemer G, Galluzzi L, Vandenabeele P, Abrams J, Alnemri ES, Baehrecke EH, Blagosklonny MV, El Deiry WS, Golstein P, Green DR, Hengartner M, Knight RA, Kumar S, Lipton SA, Malorni W, Nunez G, Peter ME, Tschopp J, Yuan J, Piacentini M, Zhivotovsky B, Melino G.* Classification of cell death: recommendations of the nomenclature committee on cell death 2009. Cell Death Differ 2009; 16: 3–11
28 *Anderson TM, Clay MC, Cioffi AG, Diaz KA, Hisao GS, Tuttle MD, Nieuwkoop AJ, Comellas G, Maryum N, Wang S, Uno BE, Wildeman EL, Gonen T, Rienstra CM, Burke MD.* Amphotericin forms an extramembranous and fungicidal sterol sponge. Nat Chem Biol 2014; 10: 400–406
29 *Xu ZX, Ding T, Haridas V, Connolly F, Gutterman JU.* Avicin D, a plant triterpenoid, induces cell apoptosis by recruitment of Fas and downstream signaling molecules into lipid rafts. PLoS One 2009; 4: e8532
30 *Yi JS, Choo HJ, Cho BR, Kim HM, Kim YN, Ham YM, Ko YG.* Ginsenoside Rh2 induces ligand-independent Fas activation via lipid raft disruption. Biochem Biophys Res Commun 2009; 385: 154–159
31 *Garcia-Saez AJ, Buschhorn SB, Keller H, Anderluh G, Simons K, Schwille P.* Oligomerization and pore formation by equinatoxin II inhibit endocytosis and lead to plasma membrane reorganization. J Biol Chem 2011; 286: 37768–37777
32 *Montero J, Morales A, Llacuna L, Lluis JM, Terrones O, Basanez G, Antonsson B, Prieto J, Garcia-Ruiz C, Colell A, Fernandez-Checa JC.* Mitochondrial cholesterol contributes to chemotherapy resistance in hepatocellular carcinoma. Cancer Res 2008; 68: 5246–5256
33 *Li YC, Park MJ, Ye SK, Kim CW, Kim YN.* Elevated levels of cholesterol-rich lipid rafts in cancer cells are correlated with apoptosis sensitivity induced by cholesterol-depleting agents. Am J Pathol 2006; 168: 1107–1118
34 *Chwalek M, Lalun N, Bobichon H, Ple K, Voutquenne-Nazabadioko L.* Structure-activity relationships of some hederagenin diglycosides: haemolysis, cytotoxicity and apoptosis induction. Biochim Biophys Acta 2006; 1760: 1418–1427
35 *Juin P, Pelletier M, Oliver L, Tremblais K, Gregoire M, Meflah K, Vallette FM.* Induction of a caspase-3-like activity by calcium in normal cytosolic extracts triggers nuclear apoptosis in a cell-free system. J Biol Chem 1998; 273: 17559–17564
36 *Gamble W, Vaughan M, Kruth HS, Avigan J.* Procedure for determination of free and total cholesterol in micro- or nanogram amounts suitable for studies with cultured cells. J Lipid Res 1978; 19: 1068–1070
37 *Bartlett GR.* Phosphorus assay in column chromatography. J Biol Chem 1959; 234: 466–468
38 *Tennant JR.* Evaluation of the trypan blue technique for determintion of cell viability. Transplantation 1964; 2: 685–694
39 *Servais H, Van Der Smissen P, Thirion G, Van der Essen G, Van Bambeke F, Tulkens PM, Mingeot-Leclercq MP.* Gentamicin-induced apoptosis in LLC-PK1 cells: involvement of lysosomes and mitochondria. Toxicol Appl Pharmacol 2005; 206: 321–333
40 *Hathaway WE, Newby LA, Githens JH.* The acridine orange viability test applied to bone marrow cells. I. Correlation with trypan blue exclusion and eosin dye exclusion and tissue culture transformation. Blood 1964; 23: 517–525
41 *Owen DM, Rentero C, Magenau A, Abu-Siniyeh A, Gaus K.* Quantitative imaging of membrane lipid order in cells and organisms. Nat Protoc 2012; 7: 24–35

7.1 Supplementary material

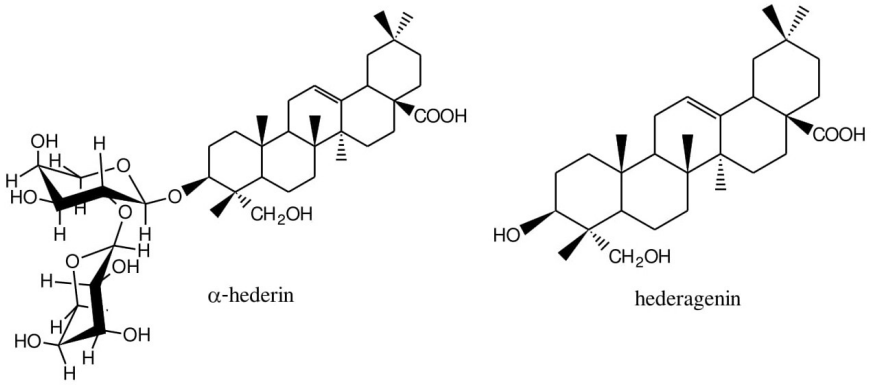

Fig. 1S Molecular structures of α-hederin and its aglycone hederagenin.

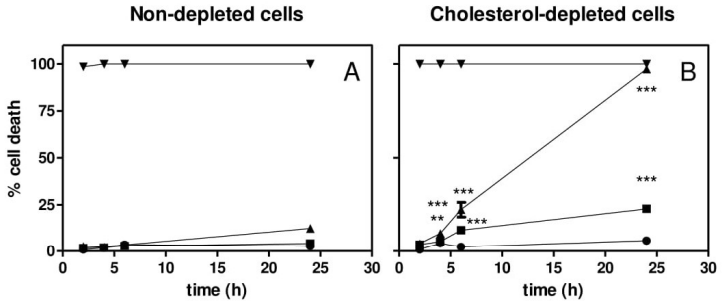

Fig. 2S Trypan blue assay in non-depleted (**A**) and cholesterol-depleted U937 cells (**B**) of increasing concentrations of sodium dodecyl sulfate (SDS): Control (●), 100 µM (■), 250 µM (▲) and 500 µM (▼). Statistical analysis: Two-way ANOVA between non-depleted and cholesterol depleted conditions. **P < 0.1, ***p < 0.01.

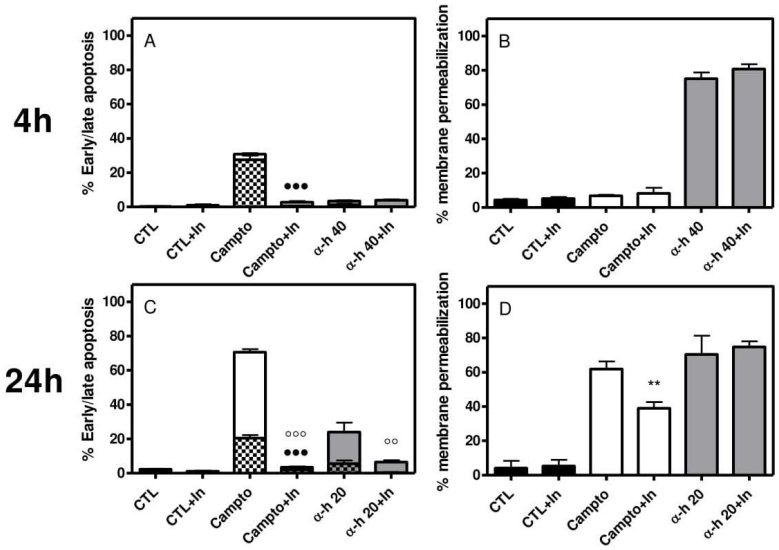

Fig. 3S Acridine orange/ethidium bromide assay of U937 cells. Early/late apoptosis (**A**, **C**) and membrane permeabilization (**B**, **D**) for cells incubated with or without general caspases inhibitor Q-VD-OPh. Camptothecine (Campto, white) has been used as a positive control for apoptosis induction. α-Hederin (α-h, grey) has been used at 20 µM and 40 µM for 24h and 4h of incubation, respectively. Statistical analysis for conditions with or without inhibitor: One way ANOVA. Symbols: ● = early apoptosis, ○ =late apoptosis, * =membrane permeabilization; two symbols : $p < 0.01$, three symbols: $p < 0.001$.

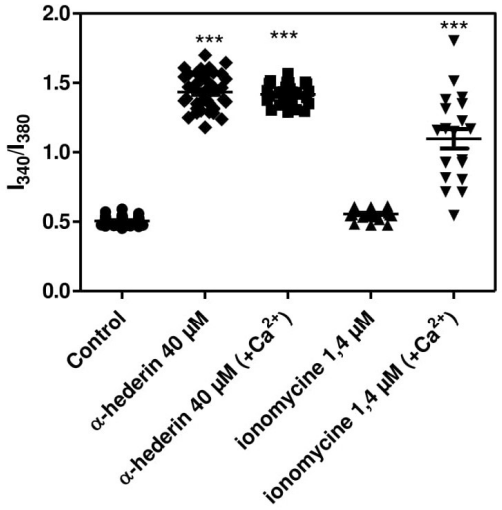

Fig. 4S Intensity ratio of Ca^{2+} bound vs. unbound FURA-2 in U937 cells after 5 min of incubation with α-hederin in media containing Ca^{2+} ions ($+Ca^{2+}$) or not. Statistical analysis: One way ANOVA was used to compare intensity ratios to the control. ***$P < 0.001$.

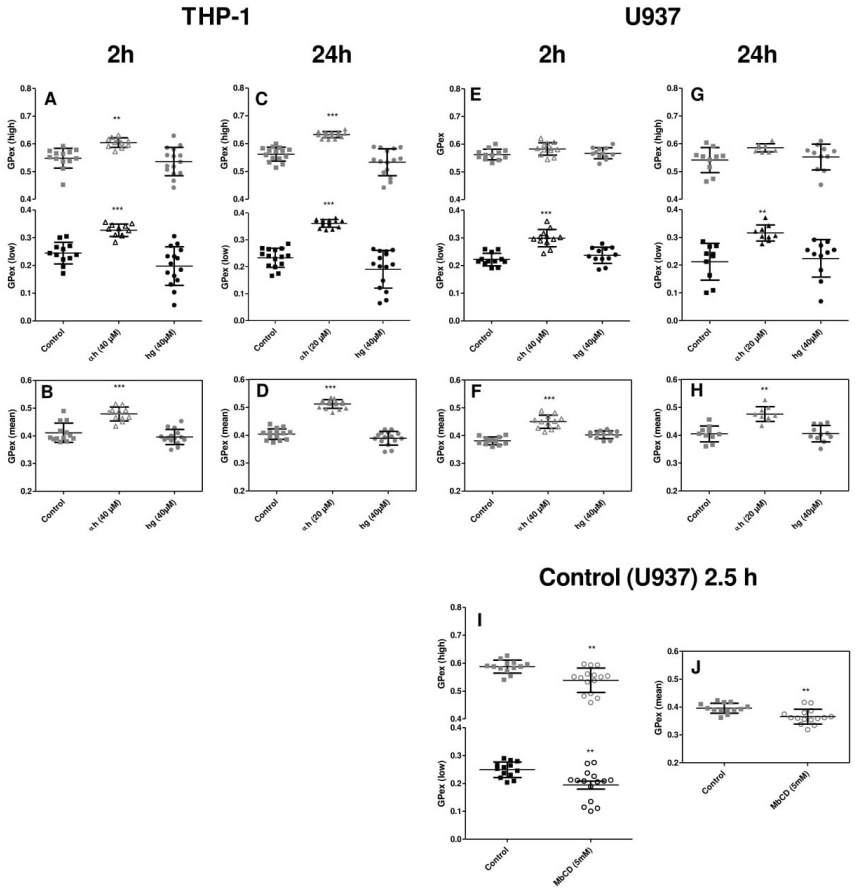

Fig. 5S GP-data of THP-1 (**A**, **B**, **C**, **D**) and U937 (**E**, **F**, **G**, **H**) cells. Panel **A**, **C**, **E**, **G**, **I**: GP-values of a GP image have been fitted to a double Gaussian function centered at GPex (low), black colors and GPex (high), grey colors. Panel **B**, **D**, **F**, **H**, **J**: Average of all GP-values in a GP-image. Statistical analysis, two-way ANOVA compared to control. **P < 0.01, ***p < 0.001.